University of Louisville

ThinkIR: The University of Louisville's Institutional Repository

Electronic Theses and Dissertations

5-2023

Development of nonorthogonal wavefunction theories and application to multistate reaction processes.

Emily Michelle Kempfer
University of Louisville

Follow this and additional works at: https://ir.library.louisville.edu/etd

Part of the Computational Chemistry Commons

Recommended Citation

Kempfer, Emily Michelle, "Development of nonorthogonal wavefunction theories and application to multistate reaction processes." (2023). *Electronic Theses and Dissertations.* Paper 4049.
Retrieved from https://ir.library.louisville.edu/etd/4049

This Doctoral Dissertation is brought to you for free and open access by ThinkIR: The University of Louisville's Institutional Repository. It has been accepted for inclusion in Electronic Theses and Dissertations by an authorized administrator of ThinkIR: The University of Louisville's Institutional Repository. This title appears here courtesy of the author, who has retained all other copyrights. For more information, please contact thinkir@louisville.edu.

DEVELOPMENT OF NONORTHOGONAL WAVEFUNCTION THEORIES AND APPLICATION TO MULTISTATE REACTION PROCESSES

By
Emily Michelle Kempfer

B.S. in Chemistry, Missouri State University, 2017
M.S. in Chemistry, University of Louisville, 2020

A Dissertation
Submitted to the Faculty of the
College of Arts and Sciences of the University of Louisville
in Partial Fulfillment of the Requirements
for the Degree of

Doctor of Philosophy
in Chemistry

Department of Chemistry
University of Louisville
Louisville, Kentucky

May 2023

Copyright 2023 by Emily Michelle Kempfer

All rights reserved

DEVELOPMENT OF NONORTHOGONAL WAVEFUNCTION THEORIES AND APPLICATION TO MULTISTATE REACTION PROCESSES

By

Emily Michelle Kempfer
B.S. in Chemistry, Missouri State University, 2017
M.S. in Chemistry, University of Louisville, 2020

Dissertation approved on

February 24th, 2023

by the following Dissertation Committee:

Dissertation Director
Dr. Lee Thompson

Dr. Pawel Kozlowski

Dr. Sachin Handa

Dr. Vance Jaeger

DEDICATION

I would like to dedicate this work to my grandfather, Arnold Montgomery, a devoted lifelong learner. From him, I learned that once you find your passion, it is hard to stop without wanting to understand more.

ACKNOWLEDGMENTS

First, I want to express my sincerest gratitude to my supervisor Dr. Lee Thompson for all of his help and support. I have greatly enjoyed my time as a student working with you, and I am honored to be one of the first of many to come from your research group. I also want to thank the professors in the Chemistry Department at the University of Louisville for their mentorship and support during the past five years.

With a project of this kind, there is also an enormous list of resources, services, and software to acknowledge, but I would specifically like to acknowledge the Cardinal Research Cluster and the admin Harrison (James) Simrall, for all of his assistance throughout my years at the University of Louisville.

I have also had the pleasure of sharing an office space with several people; Clint Evrard, Spancer (Xinju) Dong, Dr. Andrew Mahler, Adam Kinyua, Zihui Song, Hoang An Tran, Saurav Paumer, and Saptarshi Saha. My daily interactions with them have been so enjoyable, and I am grateful for my time with them. Many undergraduates have made their way through the Thompson research group, but I would like to thank a handful that I have directly worked with: Irma Avdic, Meagan Haase, Thomas Dane Pike, Jonathan Bersson, and Erin Pidcock. Your assistance was unmatched, and I would not have achieved as much without you.

Finally, I would like to thank my dissertation committee: Prof. Pawel Kozlowski, Prof. Michael Nantz, Prof. Sachin Handa, and Dr. Vance Jaeger. Thank you for being willing to be a part of my doctoral journey and for reviewing this dissertation.

ABSTRACT

DEVELOPMENT OF NONORTHOGONAL WAVEFUNCTION THEORIES AND APPLICATION TO MULTISTATE REACTION PROCESSES

Emily Michelle Kempfer

February 24, 2023

Many prominent areas of technological development rely on exploiting the photochemical response of molecules. An application that has been of particular interest to our research group is the control of molecular switches through a combination of different external stimuli (light, electric field, deprotonation). However, despite significant advances in theoretical approaches and numerous cases of successful application of theory, simulating photochemical reactions remains a computational challenge. Theoretical methods for describing excited states can be broadly divided into two categories: single-reference response methods and multireference methods. Single reference methods provide reliable semiquantitative results for single excitations in molecules with a well-defined set of Aufbau occupied orbitals in the ground state. However, these methods cannot describe double excited states, Rydberg states, charge transfer states, systems with strongly correlated ground states, or regions of the potential energy surface with degeneracies between electronic states. Multireference methods are alternatives for studying excited states and can provide accurate and general results. However, multireference methods require significant technical and chemical insight, and become computationally costly as the system size increases. Here, I will discuss my work applying various types of excited state methods for understanding the electric field control of azobenzene isomerization. Due to the size and complexity of the π structure in azobenzene, I will highlight the limitations of the current excited state methodologies that prevent researchers from studying larger and more complex systems. I will then turn to discuss new methodological developments in projected double-hybrid density functional theory, which seeks to overcome several of the problems of single reference excited state models. I will illustrate the underlying ideas motivating the development of the method and its performance compared to more established theories. Despite its success, projected double-hybrid density functional theory is unable to account for ‘multiple correlation mechanisms’. As a result, I will also introduce concepts in multiple correlation mechanisms and how they can be exploited to perform nonorthogonal active space decomposition, along with applications and paths for future improvements.

TABLE OF CONTENTS

Dedication . . . iii

Acknowledgments . . . iv

Abstract . . . v

List of Tables . . . ix

List of Figures . . . xii

INTRODUCTION . . . 1

FOUNDATIONAL COMPUTATIONAL METHODOLOGY . . . 5
- Wavefunction Method . . . 5
- Electron Correlation Energy Problem . . . 8
- Post-Hartree-Fock Methods for Describing Electron Correlation . . . 10
- Density Functional Theory . . . 14

ELECTRIC FIELD CONTROL OF MULTISTATE PROCESSES . . . 18
- Electric Field Control . . . 18
- Unsubstituted Azobenzene . . . 19
- Substituted Azobenzene (Di-Hydroxy Azobenzene) . . . 33
- Overall Conclusions . . . 49
- Supporting Documents – Electric Field Control of Multistate Processes Unsubstituted Azobenzene . . . 50
- Supporting Documents – Electric Field Control of Multistate Processes Substituted (Di-Hydroxy) Azobenzene . . . 59

SYMMETRY BREAKING AND PROJECTION METHODS FOR EXCITED STATES . . . 72
- Introduction . . . 72
- Local Excited State Benchmarking Set . . . 80
- Single-Reference Challenge of Non-Local Excited States . . . 89
- Local, Charge Transfer, and Rydberg Excited State Benchmarking set . . . 89
- Supporting Documents – Symmetry Breaking and Projection Methods for Excited States . . . 103

APPLICATION OF NONORTHOGONAL METHODS FOR EFFICIENT MODELING OF STRONGLY CORRELATED SYSTEMS . . . 116
- Introduction . . . 116
- Theory and Computational Details . . . 117
- Results . . . 120

Conclusions 126
Supporting Documents – Application of Nonorthogonal Methods for Efficient Modeling of Strongly Correlated Systems 127
Effect of Natural Orbital Occupation Number Thresholds on Energy Discontinuities 139

CONCLUSIONS 140

REFERENCES 142

Appendix A: Commonly Used Acronyms 161

CURRICULUM VITA 163

LIST OF TABLES

3.1 Relative bare electronic and Gibbs energies, and dipole moments of optimized HO−AB−OH and HO−AB−O$^-$ S_0 stationary points under field-free conditions 37
3.2 Relative energies of S_1 and S_2 excitation energies from the optimized S_0 stationary points of anti HO−AB−OH, syn HO−AB−OH, and HO−AB−O$^-$ under field-free conditions 45
3.3 Structural parameters, relative energies, and dipole moments of optimized S_0 and S_1 stationary points of azobenzene under field-free conditions . . 50
3.4 Relative energies of optimized S_0 and S_1 stationary points of azobenzene under F_{dip} field 51
3.5 Relative energies of optimized S_0 and S_1 stationary points of azobenzene under F_{azo} field 52
3.6 Relative energies of optimized S_0 and S_1 stationary points of azobenzene under F_{phe} field 53
3.7 Relative energies of optimized S_0 stationary points of HO−AB−OH under F_{NN} field 59
3.8 Relative energies of optimized S_0 stationary points of ceHO-AB-OH under F_{OC} field 60
3.9 ceHO-AB-OH molecules ΔG relative barrier heights from the S_0 cis structure in kcal mol^{-1} for the three transition states examined in all two electric fields. 61
3.10 Relative energies of optimized S_0 stationary points of HO−AB−O$^-$ under F_{NN} field 62
3.11 Relative energies of optimized S_0 stationary points of HO−AB−O$^-$ under F_{OC} field 63
3.12 HO−AB−O$^-$ molecules ΔG relative barrier heights from the S_0 cis structure in kcal mol^{-1} for the three transition states examined in all two electric fields. 64
3.13 Relative energies of S_1 and S_2 transition energies from the relative S_0 stationary points of HO−AB−OH under F_{NN} field 65
3.14 Relative energies of S_1 and S_2 transition energies from the relative S_0 stationary points of HHO−AB−OH under F_{OC} field 66
3.15 Relative energies of S_1 and S_2 transition energies from the relative S_0 stationary points of deprotonated HO−AB−O$^-$ under F_{NN} field 67
3.16 Relative energies of S_1 and S_2 transition energies from the relative S_0 stationary points of deprotonated HO−AB−O$^-$ under F_{OC} field 68

4.1 Mean error of ΔPAV-DH-DFT/TZVP excitation energies with respect to CASPT2/TZVP results 81
4.2 Standard deviation of ΔPAV-DHDFT/TZVP excitation energies with respect to CASPT2/TZVP results for different classes of benchmark molecules 86

4.3 Mean error (ME) and standard deviation (SD) of benchmarked methods with respect to CASPT2/TZVP results 88
4.4 Mean error (ME), mean absolute error (MAE), and standard deviation (SD) for vertical excitation energies to local, charge transfer, and Rydberg electronic states 92
4.5 Mean error (ME), mean absolute error (MAE), and standard deviation (SD) in eV for vertical excitation energies to local, charge transfer, and Rydberg electronic states 93
4.6 Change in the Δ-PHF vertical excitation energy of charge transfer excitations as a function of number of annihilated spin states 99
4.7 ΔPAV-DSDPBEP86 results for local excitations with 69% HF Exchange 104
4.8 ΔPAV-DSDPBEP86 results for charge transfer excitations with 69% HF Exchange 105
4.9 ΔPAV-DSDPBEP86 results for Rydberg excitations with 69% HF Exchange 105
4.10 Local vertical excitation energy results for linear response methods, TD-DSDPBEP86 and TD-ωB2PLYP as well as inclusion of mean error, mean absolute error, and standard deviation. 106
4.11 Charge transfer vertical excitation energy results for linear response methods, TD-DSDPBEP86 and TD-ωB2PLYP as well as inclusion of mean error, mean absolute error, and standard deviation. 107
4.12 Rydberg vertical excitation energy results for linear response methods, TD-DSDPBEP86 and TD-ωB2PLYP as well as inclusion of mean error, mean absolute error, and standard deviation. 108
4.13 Mean error and standard deviation for ΔPAV-DSDPBEP86 excitation energies for local states in reference to gas phase and CASPT2/CC2 109
4.14 Mean absolute error for ΔPAV-DSDPBEP86 excitation energies for local states in reference to gas phase and CASPT2/CC2 values 109
4.15 Mean error and standard deviation for ΔPAV-DSDPBEP86 excitation energies for charge transfer states in reference to gas phase and CASPT2/CC2 values 110
4.16 Mean absolute error for ΔPAV-DSDPBEP86 excitation energies for charge transfer states in reference to gas phase and CASPT2/CC2 values 110
4.17 Mean error and standard deviation for ΔPAV-DSDPBEP86 excitation energies for charge transfer states without data in which the $\langle \hat{S}^2 \rangle$ of the reference increases upon projection in reference to gas phase and CASPT2/CC2 values 111
4.18 Mean error and standard deviation for ΔPAV-DSDPBEP86 excitation energies for rydberg states in reference to gas phase and CASPT2/CC2 values 111
4.19 Mean absolute error for ΔPAV-DSDPBEP86 excitation energies for Rydberg states in reference to gas phase and CASPT2/CC2 values 112

5.1 Number of Hamiltonian matrix elements and error in correlation energy with respect to full valence DMRG calculation for different methods in the calculation of ozone using the cc-pVTZ basis set. ^{a}Results from ref. 206. 123

5.2 Number of Hamiltonian matrix elements and error in correlation energy with respect to full valence DMRG calculation for different methods in the calculation of nickel-acetylene using the cc-pVTZ basis set. [a]Results from ref. 206. 125
5.3 Relative energies between **bis** and **per** geometries of μ-oxo dicopper ammonia calculated using different methods with cc-PVDZ basis set, except DMRG calculation using ANO-RCC basis set. [a]Results taken from ref. 235. [b]Results are obtained from the methodology of ref. 206. 126
5.4 Ozone cartesian coordinates 127
5.5 Ni-actylene cartesian coordinates 127
5.6 **Bis** (μ-oxo) dicopper ammonia cartesian coordinates 127
5.7 **Per** (μ-oxo) dicopper ammonia cartesian coordinates 128
5.8 Ozone total energies and occupation numbers for NO-ASD, average density UNO-CAS(CI and SCF), CASSCF, and DMRG 130
5.9 Nickel-Actelyene total energies and occupation numbers for NO-ASD, average density UNO-CAS(CI and SCF), CASSCF, and DMRG 132
5.10 Energy of NO-ASD(4e,4o;2e,2o) compared to averaged density UNO-CASCI with active spaces of increasing size. 133
5.11 **Bis** $\mu - oxo$ dicopper ammonia total energies and occupation numbers for NO-ASD and average density UNO-CAS(CI and SCF) 135
5.12 **Per** $\mu - oxo$ dicopper ammonia total energies and occupation numbers for NO-ASD and average density UNO-CAS(CI and SCF). 137

LIST OF FIGURES

2.1 Summary of HF-Roothan-Hall SCF Procedure 9
2.2 Potential energy curve of H_2 10
2.3 Illustration of Jacobs Ladder of DFT 16

3.1 Azobenzene molecular orbitals selected for the 10 electrons in 8 orbitals CASSCF calculation 21
3.2 Orientation of external fields applied to azobenzene 22
3.3 Optimized structures of azobenzene S_0 and S_1 potential energy surfaces . 23
3.4 Effect of +0.01 au and −0.01 au orientated external electric fields applied to photo and thermal isomerization pathways of azobenzene compared to field-free conditions 25
3.5 Excited state rotation photoisomerization pathway under applied electric fields 26
3.6 Derivative coupling and gradient difference vectors that define the branching space around S_0/S_1CI_{rot} 27
3.7 Potential energy surface of branching space around S_0/S_1CI_{rot} 28
3.8 Reaction coordinate between rotation, inversion, and inversion planar transition structures under applied electric fields 29
3.9 Effect of thermal isomerization reaction barrier under different field orientations and strength 31
3.10 Orientation of applied fields with respect to HO−AB−OH and HO−AB−O^- molecules 35
3.11 Azo bond length in rotation transition state at different F_{OC} field strengths for HO−AB−OH and HO−AB−O^- 38
3.12 Gibbs activation energies on S_0 of reaction pathways with applied electric fields 39
3.13 Half-life of protonated and deprotonated dihydroxyazobenzene upon application of F_{NN} and F_{OC} 41
3.14 Potential energy surface in the branching space of the protonated and deprotonated HO−AB−OH around the S_0/S_1 CI 43
3.15 Energy difference between the S_0 and S_1 potential energy surfaces in the branching space of protonated HO−AB−OH and deprotonated HO−AB−O^- molecules with F_{NN} 44
3.16 HO−AB−OH and HO−AB−O^- molecules relative energy gaps between S_0 and S_1 stationary points with applied electric fields 47
3.17 Effect of all orientated external electric fields applied to photo and thermal isomerization pathways of azobenzene 54
3.18 Projection of the S_0 cis/trans minimum to rotation/inversion transition structure field-free difference dipole moment on the F_{dip} axis 56
3.19 Projection of the S_0 cis/trans minimum to rotation/inversion transition structure field-free difference dipole moment on the F_{azo} axis 57

3.20 Projection of the S_0 cis/trans minimum to rotation/inversion transition structure field-free difference dipole moment on the F_{phe} axis 58
3.21 Gradient difference and derivative coupling vectors that define the branching space of the anti and syn protonated derivatives of azobenzene around the S_0/S_1 CI 69
3.22 Gradient difference and derivative coupling vectors that define the branching space of the anti and syn deprotonated derivatives of azobenzene around the S_0/S_1 CI 70
3.23 S_0 and S_1 potential energy surfaces of HO$-$AB$-$O$^-$ under F_{NN} field in the S_0/S_1 branching space 71

4.1 Histograms showing frequency of deviation and normal distribution of computed ΔPAV-DH-DFT/TZVP excitation energies from CASPT2/TZVP results 83
4.2 Correlation plots of computed ΔPAV-DHDFT/TZVP and CASPT2/TZVP excitation energies showing least squares regression line and associated coefficient of determination 85
4.3 Mean error and standard deviation of local excitation vertical excitation energies as a function of Hartree-Fock exchange percentage 95
4.4 Role of exact exchange in controlling the average excited state HOMO-LUMO energy difference and the correlation between mean error 95
4.5 Mean error and standard deviation of charge transfer vertical excitation energies as a function of Hartree-Fock exchange percentage 97
4.6 Mean error and standard deviation of charge transfer vertical excitation energies as a function of Hartree-Fock exchange percentage 98
4.7 Mean error and standard deviation of Rydberg vertical excitation energies as a function of Hartree-Fock exchange percentage 100
4.8 Mean error and standard deviation of all classes of vertical excitation energies as a function of Hartree-Fock exchange percentage 101
4.9 Mean error and standard deviation of local excitation vertical excitation energies as a function of Hartree-Fock exchange percentage without data in which $\langle \hat{S}^2 \rangle$ of the reference increases upon projection. 112
4.10 Mean error and standard deviation of Rydberg excitation vertical excitation energies as a function of Hartree-Fock exchange percentage without data in which $\langle \hat{S}^2 \rangle$ of the reference increases upon projection. 113
4.11 Role of exact exchange in controlling the average HOMO-LUMO energy difference and the correlation between mean error for local excitations . . 113
4.12 Role of exact exchange in controlling the average HOMO-LUMO energy difference and the correlation between mean error for charge transfer excitations 114
4.13 Role of exact exchange in controlling the average HOMO-LUMO energy difference and the correlation between mean error for Rydberg excitations 114

5.1 Schematic for formation of the nonorthogonal active space decomposition scheme Hamiltonian $\hat{H}_{ASD}$ and overlap N_{ASD} indicating diagonal block orthogonal and off-diagonal block nonorthogonal components. 119
5.2 Occupation numbers of valence natural orbitals in ozone compared with a full valence DMRG for different methods indicated in the legend with the cc-pVTZ basis set. 121
5.3 Occupation numbers of valence natural orbitals in nickel-acetylene compared with DMRG(18e,33o) for different methods indicated in the legend with the cc-pVTZ basis set. 124
5.4 **Bis** and **per** isomers of μ-oxo dicopper ammonia complex. 125
5.5 Pictorial Representation of the Natural Orbitals of Ozone's two UHF solutions 131
5.6 Pictorial Representation of the Natural Orbitals of Ni-Acetylene's two UHF solutions 134
5.7 Pictorial Representation of the Natural Orbitals of **Bis** $\mu - oxo$ dicopper ammonia's two UHF solutions 136
5.8 Pictorial Representation of the Natural Orbitals of **Per** $\mu - oxo$ dicopper ammonia's two UHF solutions 138
5.9 Selected natural orbital occupation numbers along the O-O-O bending coordinate of ozone. 139

CHAPTER 1

INTRODUCTION

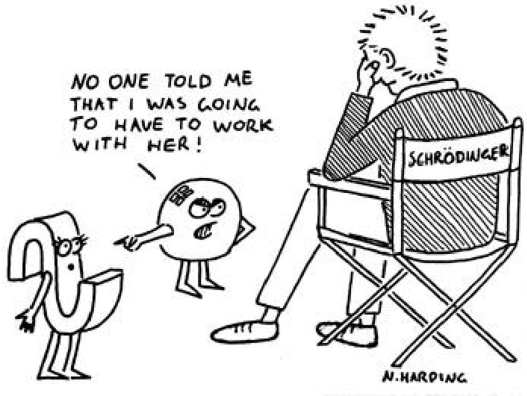
NO ONE TOLD ME THAT I WAS GOING TO HAVE TO WORK WITH HER!
SCHRÖDINGER
N. HARDING

The development of new light-based technologies (e.g. molecular switches) requires accurate and computationally efficient excited state methodologies to model medium and large systems. Examples of important processes which require an atomistic understanding of different photochemical pathways include light-harvesting (1; 2), biological fluorescence (3; 4), and solar cells (5; 6; 7). To understand the reactivity and nature of photo-active molecules, the reaction needs to be examined over multiple electronic states and points of degeneracy between states. Computationally, the chemical reactivity of a molecule can be examined using the potential energy surface (PES), which is a function describing the chemistry of the system, where the total function can be divided into separate smaller functions representing individual electronic states of the PES. The PES can describe many points of interest when examining chemical reactivity, like minima, first-order saddle points, and possible conical intersections. Locating these points allows us to computationally describe the kinetic, thermodynamic, and photochemical reactivity of the molecule of interest. As computational chemists, we aim to find a computationally efficient and accurate method to describe the function.

Most conventional electronic structure theories like Hartree-Fock (HF) and density functional theory (DFT) were created with the purpose of examining electronic ground state properties. The HF method is variational in the ground state, meaning the computed energy is always higher than the exact energy. The DFT methodology is also variational for an exact DFT functional however, functional approximation can change variational ability. However, for both single reference methodologies, in which approximations are used, the variational principle does not hold for excited states because the formulation only allows for the upper bound of the exact ground state energy to be determined. Consequently, excited states calculated by single determinantal techniques can be more challenging and less accurate than the ground state. Thus, there is a need for accurate and computationally efficient excited state methodologies.

One of the most common and accurate methodologies for excited states is configuration interaction (CI) method. The CI expansion is written as a linear combination of excited determinants constructed from excitations of electrons among the ground state optimized HF orbitals. Full CI is a method which includes any number of electron excitations in the CI expansion. While full CI is accurate, the expansion can become extremely long and complex, making this method too computationally costly even for the smallest of molecules. Truncation of the CI wavefunction can reduce computational cost however, the resulting wavefunction is not necessarily size consistent and converges slowly with the order of truncation. The simplest CI expansion for excited states is configuration interaction singles (CIS) in which the wavefunction is written as a linear expansion of singly excited determinants from the ground state HF orbitals. The most prominent issue with CIS is that it only includes single excited Slater determinants and thus, cannot describe states with multiple excitation character which are frequently needed for the description of the entire PES. Another prominent type of single reference methodology is the time-dependent density functional theory (TD-DFT) method in which, excited states can be calculated as a linear response of the ground state reference to a small time-dependent external electric field perturbation. The TD-DFT method is widely utilized due to its accuracy and computational efficacy for vertical excitation energies (VEEs) in large systems. Despite the utility of TD-DFT, well-known issues include inabilities to describe charge-transfer states, double-excited states, Rydberg states, and electronic degeneracies with the ground state (8; 9; 10; 11). TD-DFT can be improved upon using the rungs of Jacobs ladder or through different exchange-correlation functionals, which will be discussed further in the following chapter. One problematic issue with using single reference methods for describing the PES is that the orbitals for each excited state configuration are not optimized for the excited electronic configuration, which can cause significant errors in accuracy. Overall, however, with the improvement of CIS or TD-DFT, there is no easy 'fix' to the qualitative issues with these methodologies.

In comparison to single reference, multireference methods like complete active space self-consistent field (CASSCF) and complete active space second order perturbation theory (CASPT2), which are known to be much better at describing the entire PES, including points of degeneracy between states. Multireference methods are closely related to the CI methodology in which a multideterminantal expansion is used to express the total wavefunction where both the expansion coefficients and orbitals are optimized. The multideterminantal expansion is created through an active space (AS), comprised of occupied and virtual molecular orbitals of interest. Multireference methodologies can be some of the most accurate methods currently implemented; however, the accuracy of this method comes at a significant cost. Multireference methods are known for being difficult to use because they require the user to have chemical intuition and significant knowledge about the system of interest. After all, the resulting energies are utterly reliant on the user-selected orbitals in the AS. These methods are also extremely limited in terms of system size in which the AS selected cannot be larger than 16 electrons and 16 orbitals due to computational cost; thus, multireference methods cannot be used for large or medium-sized molecules like those in many photochemical reactions.

Current methodologies for studying medium to large excited state systems, like in the above examples, are extremely limited. Where DFT methodologies break down for large-scale systems due to the sizable charge-transfer character of the excitations and multireference character of the wavefunction (12). Highly accurate multireference methods like CASSCF or CASPT2 are limited to simulating a single chromophore due to the computational scaling of the methods themselves. The study of large-scale systems is usually treated via a quantum mechanical embedded molecular mechanics method, e.g. ONIOM or QM/MM (13). While these methods are beneficial in large-scale systems, the study of photochemical nonadiabatic systems needs a quantum mechanical description of the entire system due to the quantum nature of the light absorption process and thus the QM layer requires the presence of the entire photoactive region which can become quite large and computationally costly (14; 15). Thus, there is a need for a computationally efficient and accurate quantum mechanical methodology for simulating larger systems.

One approach generally overlooked for obtaining excited states is utilizing self-consistent field (SCF) solutions. This method has been overlooked due to some pitfalls, like the fact that nonvariational behavior is frequently observed or that solutions may be challenging to use because during energy convergence, they can converge with each other, disappear, or collapse to the ground state. These SCF solutions are also known to be non-variational and also non-orthogonal to one another making them complex to utilize. The disadvantages of this methodology can be overcome and have been a significant interest in the field of quantum chemistry, like the creation of techniques that address convergence issues for excited state optimization of SCF solutions: the maximum overlap method (MOM) method and the initial maximum overlap method (IMOM) method developed by Peter Gill and co-workers determine the set of occupied orbitals that have the greatest overlap with the previous iteration (16; 17), Van Voorhis and co-workers created the σ-SCF model in which they use a targeted energy approach in combination with the convergence criteria based on energy variance (18; 19). Neuscamman also created a method in which energy variation is used, and it also constructs Lagrangians for variational optimization of the excited states (20; 21). Regardless of the optimization procedure, orbital spin and spatial symmetry breaking is generally impossible to achieve if it is not included in the initial guess. Thus, some computational methods require a global search of the SCF solution space (22). The advantages of using SCF solutions for excited states are unique to the methodology itself. The method can capture orbital relaxation effects that are frequently missed in methods like CIS and TD-DFT. Methodologies using SCF solutions can also perform post-SCF procedures just like the ground state, allowing for the opportunity to capture additional correlation. Lastly, the process of identifying and using the solutions can be easily parallelized allowing the calculation to be utilized on larger systems without large computational cost unlike multireference methods. Currently, high-speed and efficient computers are being created, including the largest and fastest computer in the world, Frontier, located in Oak Ridge, Tennessee, which can deliver a quintillion calculations per second! Even with the utilization of these high-speed computers, older methodologies like multireference methods are not sped up by any significant amount of time because the incredible speed of calculations on newly developed computers relies on the methodology being parallelized. Thus, the advantage of the possible parallelization for SCF solution methodologies is significant due to the finding and using of many SCF solutions in a single calculation.

In this thesis, we want to explore current and new methodological treatments for examining excited states, taking time to highlight both advantages and disadvantages. Both wavefunction and density functional approaches are equally examined in this work, demonstrating an extensive investigation of methodologies for excited state systems. Overall, this thesis is divided into six main chapters beginning with the current chapter, ***Introduction***, in which we provide context and motivation for the entirety of this work. This is then followed by ***Chapter 2: Foundational Computational Methodology*** in which I briefly introduce the core tools of HF and DFT methodologies which will are used throughout this thesis. The following chapter, ***Chapter 3: Electric Field Control of Multistate Processes*** is our first investigation of excited state processes using preexisting methodologies. This chapter provides a basis for the capabilities of current multireference and single reference methodologies in exploring the azobenzene and azobenzene derivative PESs. ***Chapter 4: Symmetry Breaking and Projection Methods for Excited States*** and ***Chapter 5: Application of Nonorthogonal Methods for Efficient Modeling of Strongly Correlated Systems*** demonstrate introductory results demonstrating a new methodology for excited state examination with SCF solution methodologies for studying larger systems without the computational cost. Finally, ***Chapter 6: Conclusion*** outlines the results achieved in this work and discusses the relevance to the field of computational chemistry.

Several Appendices and references support the chapters in this thesis. Supporting documents are provided in the final section at the end of each chapter, supplying further information in tables and figures corresponding to the text. Appendix A contains all relevant acronyms and should be referred to throughout the text.

CHAPTER 2

FOUNDATIONAL COMPUTATIONAL METHODOLOGY

Wavefunction Method

The HF method assumes that a $\mathrm{N_{elec}}$-body wavefunction can be approximated by a single *Slater determinant (SD)* made up of $\mathrm{N_{elec}}$ spin-orbitals. Within the HF method, approximations are made for this method to be useful in application. This section takes the time to go through some of the core concepts of the HF methodology.
One of the core equations of describing molecular systems in quantum chemistry is the *time-independent Schrödinger equation*, which is an *eigenvalue equation* describing a chemical system composed of electrons and nuclei.

$$\hat{H}\Psi(\mathbf{r}_1, \mathbf{r}_2, ..., \mathbf{r}_{N_{elec}}, \mathbf{R}_1, \mathbf{R}_2, ..., \mathbf{R}_{N_{atom}}) = E\Psi(\mathbf{r}_1, \mathbf{r}_2, ..., \mathbf{r}_{N_{elec}}, \mathbf{R}_1, \mathbf{R}_2, ..., \mathbf{R}_{N_{atom}}) \tag{2.1.1}$$

where, $\mathbf{r}_{N_{elec}}$ and $\mathbf{R}_{N_{atom}}$ are the x,y,z coordinates of electron N_{elec} and nuclei N_{atom}. The properties of the system are described using the Hamiltonian operator, $\hat{H}$, and E and Ψ are the eigenvalues and eigenvectors, respectively. Where E is the energy corresponding with the wavefunction. The wavefunction, Ψ, is a function of all the electron and nuclear coordinates, which provides all information about the system. As stated previously, $\hat{H}$ is the Hamiltonian operator which operates on the wavefunction through,

$$\hat{H} = -\sum_{i=1}^{N_{elec}} \frac{1}{2}\hat{\nabla}_i^2 - \sum_{I=1}^{N_{atom}} \frac{1}{2M_I}\hat{\nabla}_I^2 - \sum_{i=1}^{N_{elec}}\sum_{I=1}^{N_{atom}} \frac{Z_I}{r_{iI}} + \sum_{i=1}^{N_{elec}}\sum_{j>i}^{N_{elec}} \frac{1}{r_{ij}} + \sum_{I=1}^{N_{atom}}\sum_{J>I}^{N_{atom}} \frac{Z_I Z_J}{R_{IJ}} \tag{2.1.2}$$

Equation 2.1.2 is expressed in atomic units, where i and j index electrons, $\mathrm{N_{elec}}$ is the number of electrons, I and J index nuclei, $\mathrm{N_{atom}}$ is the number of nuclei, Z_I is the charge of nucleus I, M_I is the mass of nucleus I, ∇_i^2 is the laplacian operator acting on the coordinates of particle i, r_{ij} is the distance between electrons i and j, and lastly, R_{IJ} is the distance between nuclei i and j. The first three terms are one electron operators, kinetic energy operator and electron-nuclear potential operator, which describe the kinetic energy of each particle. The last two terms are two-electron operators which describe the two-electron interaction between particles. The two-body operators in the Hamiltonian prevent calculation of the wavefunction analytically because it is no longer possible to decouple electron and nuclear degrees of freedom. Specifically, for the electron-nuclear coupling, it is assumed that nuclei are fixed in position relative to the motion of the electrons due to the large difference of mass between nuclei and electrons, which is known as the *Born-Oppenheimer approximation* (23). With this assumption, the kinetic energy terms of the nuclei are treated as having zero values and separately from electrons, allowing equations 2.1.1 and 2.1.2 to be reduced to only the electronic components.

$$\hat{H}_{elec}(\mathbf{R})\Psi(\mathbf{r}_1, \mathbf{r}_2, ..., \mathbf{r}_N; \mathbf{R}) = E(\mathbf{R})\Psi(\mathbf{r}_1, \mathbf{r}_2, ..., \mathbf{r}_N; \mathbf{R}) \tag{2.1.3}$$

$$\hat{H}_{elec} = -\sum_{i=1}^{N_{elec}} \frac{1}{2}\hat{\nabla}_i^2 - \sum_{i=1}^{N_{elec}} \sum_{I=1}^{N_{atom}} \frac{Z_I}{r_{iI}} + \sum_{i=1}^{N_{elec}} \sum_{j>i}^{N_{elec}} \frac{1}{r_{ij}} \tag{2.1.4}$$

Equation 2.1.4 can be further broken into the core Hamiltonian operator

$$\hat{h} = \frac{1}{2}\hat{\nabla}^2 - \sum_{I} \frac{Z_I}{r_I} \tag{2.1.5}$$

and the electron-electron repulsion operator.

$$\hat{v} = \frac{1}{r_{ij}} \tag{2.1.6}$$

The electronic Hamiltonian in equation 2.1.4 only depends on the spatial coordinates of the electrons, $\mathbf{r}$, however, to completely describe a system the spin of the electrons need to be specified. The Hamiltonian has no terms that depend on spin however, there are properties of the wavefunction that are dependent on spin. Thus, Wolfgang Pauli showed that within relativistic quantum field theory, particles with half-integral spin, electrons, require an antisymmetric wavefunction. In which, if two electrons switch positions in the wavefunction, that wavefunction is then equal to the negative original wavefunction.

$$\Psi(\mathbf{x}_1, \mathbf{x}_2, ..., \mathbf{x}_N) = -\Psi(\mathbf{x}_2, \mathbf{x}_1, ..., \mathbf{x}_N) \tag{2.1.7}$$

2.1.1 Orbital Picture

After discussing the general Schrödinger equation, it is now beneficial to take time to discuss the form of the wavefunction. However, before discussing more complex wavefunctions, the wavefunction for a single electron system must be examined in which, an orbital is a wavefunction for a single particle. A spatial orbital, $\psi_i(\mathbf{r})$ is a function of the position vector, $\mathbf{r}$, and describes the spatial distribution of an electron. The spatial wavefunction can be divided into radial and angular parts,

$$\psi(r, \theta, \phi) = R(r)\Theta(\theta, \phi)\Phi(\phi) \tag{2.1.8}$$

where, the angular part is obtained from spherical harmonics and the radial part is the exponential decay function. Each function has an associated quantum number from the boundary conditions; principle (n), angular (l), and magnetic ($\mathrm{m_l}$) quantum numbers. Firstly, the principle quantum number (n) describes the size of the orbital, by grouping the orbitals into their relative shells. The orbitals can then be further divided into sub-shells that describes the shape of the orbital by the angular quantum number (l). Orbitals have shapes that can be described as spherical ($\mathrm{l} = 0$), polar (l

= 1), or cloverleaf (l = 2). Orbitals can become much more complex shapes as the angular quantum number becomes larger. For orbitals with angular quantum numbers above l = 0, the shape of the orbitals allow for different orientations in space, thus the third quantum number, magnetic (m_l) quantum number, describes the orientation in space, where m_l=2l+1. Quantum numbers are important for uniquely describe each solution and thus assist in the proper description of the system.

It is well known that beyond the one-electron system, the wavefunction becomes a complicated function of all coordinates in the system. Thus, the N_{elec} wavefunction can be approximated as a product of 1-electron orbitals.

$$\psi(\mathbf{r}_1, \mathbf{r}_2, ..., \mathbf{r}_{N_{elec}}) = \psi(\mathbf{r}_1)\psi(\mathbf{r}_2)...\psi(\mathbf{r}_{N_{elec}}) \tag{2.1.9}$$

The above is exact for the hydrogen atom but for more than one electron the wavefunction does not have the properties required by equation 2.1.7 and thus must be modified to account for antisymmetry.

2.1.2 Slater Determinants

When constructing the many electron wavefunction from 1-electron orbitals, the correct spin properties must be accounted for. The most straightforward approach is to include spin explicitly in the orbital. A complete set for describing spin requires the two orthonormal orbitals, $\alpha(\omega)$ and $\beta(\omega)$ which accounts for spin up and spin down configurations of the electron. Thus, the spin orbital, $\chi(\mathbf{x})$ can account for both spin and space coordinates.

$$\chi(\mathbf{x}) = \begin{cases} \psi_i(\mathbf{r})\alpha(\omega) \\ \psi_i(\mathbf{r})\beta(\omega) \end{cases} \tag{2.1.10}$$

Furthermore, for cases consisting of more than two electrons an antisymmetric wavefunction can be formulated by arranging orbitals in a SD, as shown below.

$$\Psi(\mathbf{x}_1, \mathbf{x}_2, ..., \mathbf{x}_{N_{elec}}) = \frac{1}{\sqrt{N_{elec}!}} \begin{vmatrix} \chi_1(\mathbf{x}_1) & \chi_2(\mathbf{x}_1) & \cdots & \chi_{N_{elec}}(\mathbf{x}_1) \\ \chi_1(\mathbf{x}_2) & \chi_2(\mathbf{x}_2) & \cdots & \chi_{N_{elec}}(\mathbf{x}_2) \\ \vdots & \vdots & \ddots & \vdots \\ \chi_1(\mathbf{x}_{N_{elec}}) & \chi_2(\mathbf{x}_{N_{elec}}) & \cdots & \chi_{N_{elec}}(\mathbf{x}_{N_{elec}}) \end{vmatrix} \tag{2.1.11}$$

A SD will always satisfy the antisymmetry condition for any choice of the one electron functions. Another consequence of the antisymmetry principle that follows the SD is that if any 2 electrons have the same quantum numbers the wavefunction goes to zero. Therefore, the SD is the most straightforward wavefunction that has the correct spin properties. Use of the variational theorem to determine the best set of spin orbitals in the SD is known as the HF method.

2.1.3 Self-Consistent Field Method

Within the HF methodology, the energy associated with the trial state is given by

$$E_{HF} = \frac{\langle \Psi_{HF}|\hat{H}|\Psi_{HF}\rangle}{\langle \Psi_{HF}|\Psi_{HF}\rangle} \tag{2.1.12}$$

which demonstrates the *variational principle* in which the approximate HF wavefunction is always greater in energy than the exact ground state energy of the system. The wavefunction, Ψ_{HF}, is a description of the electronic configurations of atoms in the molecular orbital (MO) basis however, with this form, the equation of the wavefunction is a continuous function which a computer cannot represent. Thus, for the wavefunction to be adapted for computation, basis sets were introduced where a one-electron wavefunction is obtained by a linear combination of the basis sets. The basis set most commonly chosen is that of the atomic orbital (AO) basis thus creating the *linear combination of atomic orbitals (LCAO)* approach (24).

$$|\psi_i\rangle = \sum_{\mu}^{N_{basis}} C_{\mu i}|\phi_\mu\rangle \tag{2.1.13}$$

With the wavefunction in the AO basis, new coefficients arise, C, which have a direct dependence on the energy. Solving for the optimal C requires an iterative method called the *SCF procedure.* There are many ways one can optimize the energy functional via SCF methods in equation 2.1.12, the most well-known is the Roothan method. Where, an improved set of orbital coefficients can be found by solving the eigenvalue problem, $\mathbf{FC} = \mathbf{SC}\epsilon$ with an initial guess of orbital coefficients, C. Where ϵ is the diagonal matrix of eigenvalues, also known as the energies of the HF orbitals, and F is the Fock matrix,

$$F_{\mu\nu} = h_{\mu\nu} + \sum_{\lambda\sigma} P_{\lambda\sigma}(2(\mu\nu|\sigma\lambda) - (\mu\lambda|\sigma\nu)) \tag{2.1.14}$$

The second term of the Fock matrix equation is reliant on the input orbitals or density, P, demonstrating the non-linearity of the equation. Where, the density is:

$$P_{\lambda\sigma} = \sum_{i} C_{\lambda i}C^*_{i\sigma} \tag{2.1.15}$$

A schematic version of the HF-Roothan-Hall SCF methodology can be observed in figure 2.1. Where an energy solution is found when the coefficients, C, obtained by the Fock matrix eigenvalue problem are unchanged between iterations (25).

ELECTRON CORRELATION ENERGY PROBLEM

While the HF approximation is very successful in many cases, it has limitations due to the fact that the approximate wavefunction never corresponds to the exact wavefunction. Thus, due to the variational principle, E_{HF} is always an upper-bound to the exact energy, $\mathcal{E}$, and the difference between the two energies is the correlation energy, E_{corr}.

$$E_{corr} = \mathcal{E} - E_{HF} \tag{2.2.1}$$

E_{corr} is noted as a negative value and is a measure of the error introduced through the HF approximation. The error then leads to the *correlation energy problem.*

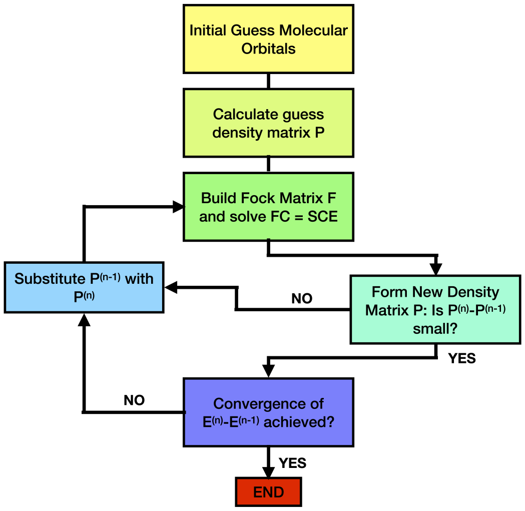
Initial Guess Molecular Orbitals
Calculate guess density matrix P
Build Fock Matrix F and solve FC = SCE
Form New Density Matrix P: Is P(n)-P(n-1) small?
NO
Substitute P(n-1) with P(n)
YES
Convergence of E(n)-E(n-1) achieved?
NO
YES
END

Figure 2.1. Summary of HF-Roothan-Hall SCF Procedure

One source of error in the correlation is caused by the instantaneous repulsions among electrons. In the standard HF methodology electron correlation is not fully described because the electrostatic interaction between electrons is accounted for in an averaged manner causing the electron-electron repulsion term of the Hamiltonian to not always correctly describe the system. This error in the correlation energy can be described as *dynamical* because it is the electron interactions that happen beyond the orbital picture where missing dynamical correlation is significant when electrons are in close proximity. In terms of the CI expansion dynamical correlation can be considered as the case where many determinants have small but non-negligible CI weights in the wavefunction. The second type of correlation energy is termed as *strong* or *static correlation*. Where static correlation is the electron interactions that occur due to degeneracies between orbitals, in which an electronic state does not have a well defined set of Aufbau occupied orbitals. As a result, the wavefunction is an entanglement of superposition of electron configurations, which represents permanent electron interactions that occur over longer distances. The missing static correlation is particularly significant when electrons are in different spatial orbitals which have similar orbital energies. When static correlation is present, the wavefunction will have few determinants with relatively large CI coefficients.

One of the most basic examples utilized to demonstrate the effect of correlation is that of the dissociation of the H_2 molecule, figure 2.2. At equilibrium distance, the HF method gives a relatively good approximation to the exact energy due to the correlation error being relatively small and caused exclusively by dynamical correlation. As the bond stretches, the correlation error proceeds to increase. here at large bond distances, the error is no longer due to dynamical but to static because of two independent hydrogens each containing one electron on its center with no interaction with each other. This causes there to be two different but energetically equal configurations at long distances. restricted Hartree-Fock (RHF) methodology fails to describe this behavior however, the unrestricted Hartree-Fock (UHF) method leads

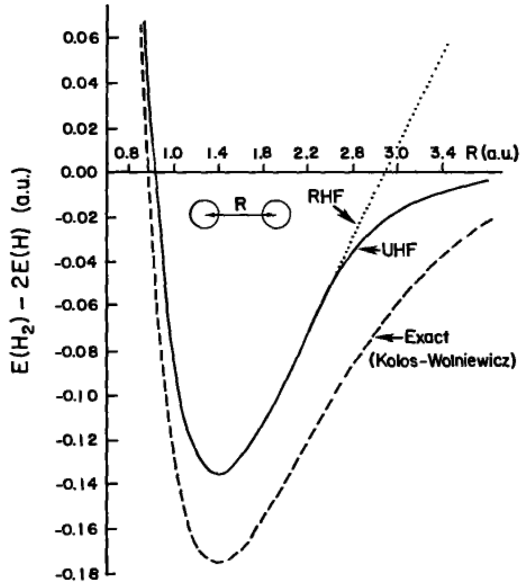

Figure 2.2. Potential energy curve of H$_2$ from reference (24)

to near exact behavior due to the separate treatment of α and β spins but gives the wrong wavefunction.

POST-HARTREE-FOCK METHODS FOR DESCRIBING ELECTRON CORRELATION

Due to the lack of correlation energy being one of the largest contributions of error in the SCF methodology, correlation energy can be added into the system by utilizing post-HF methodologies. Post-HF methodologies include electron correlation through incorporating excited state configurations after the SCF procedure in the HF methodology. Post-HF methods can be broadly divided into two categories: methods based upon perturbation theory and methods based on the variational principle. Both types of approaches are utilized throughout this thesis and thus more detailed descriptions will be provided.

2.3.1 Configuration Interaction

CI methods are one of the conceptually most straightforward methods for solving the many-body Hamiltonian. The CI method denotes that the exact many-body wavefunction can be written as a linear combination of SDs, where the exact wavefunction, also known as **full CI**, can be written in the following form.

$$|\Phi_{fullCI}\rangle = D_0|\Psi_0\rangle + \sum_{i<a} D_i^a|\Psi_i^a\rangle + \sum_{\substack{i<j\\a<b}} D_{ij}^{ab}|\Psi_{ij}^{ab}\rangle + \sum_{\substack{i<j<k\\a<b<c}} D_{ijk}^{abc}|\Psi_{ijk}^{abc}\rangle + ... \qquad (2.3.1)$$

Ψ_i^a is describing a single excitation from occupied orbital i to virtual orbital a, Ψ_{ij}^{ab} is describing double excitations etc:The individual Ψ's in the above equation can also be termed as *configuration state functions (CSFs).* In which, CSFs represent a linear combination of SDs. In many cases, a one determinantal wavefunction is sufficient for description of the system in question, however, in many cases it is not, which allows the linear combination of CSFs to be utilized. In the CI methodology the expansion coefficients, C, are optimized but the individual wavefunctions are not. CI methods provide an exact solution to the many-body problem; however, the number of N-electron determinants can be enormous even for small molecules. Thus, there is a necessity for truncating the CI wavefunction by including only single (CIS), double (CID), or single and double excitations (CISD) into the ground-state HF determinant. As stated in *Brillouin's theorem*, single excited determinants do not affect the ground state energy, so the CIS method is solely useful for obtaining single excitation excited states (24). The CI method is the simplest example of utilizing the variational principle and it will later assist in the understanding of multiconfigurational methods.

2.3.2 Coupled Cluster

Another variational post-HF methodology is the coupled cluster (CC) method, which uses the HF molecular orbital method and constructs the multi-electron wavefunction using an exponential cluster operator to account for additional electron correlation. The basic wavefunction can be written as;

$$|\Phi\rangle = e^{\hat{T}}|\Psi_0\rangle \tag{2.3.2}$$

where Ψ_0 is the reference wavefunction which is typically a SD constructed from the HF molecular orbitals. $\hat{T}$ is the cluster operator which operates on Ψ_0 to create a linear combination of excited determinants from the reference wavefunction.

$$\hat{T} = \hat{T}_1 + \hat{T}_2 + \hat{T}_3 + ... \tag{2.3.3}$$

where $\hat{T}_1$ is the operator of all single excitations, $\hat{T}_2$ is the double excitations operator, and so on.

Similarly to the CI methodology, the full CC wavefunction can become very computationally costly thus, truncation is most often needed. However, the largest difference between CI and CC methods is the utilization of the exponential ansatz. The exponential ansatz greatly assists in correcting problems that are normally caused by truncation like size extensivity, meaning that the energy of a dimer system is equal to the two systems individually added together.

2.3.3 Møller-Plessent Perturbation Theory

The Møller-Plessent (*MP*) perturbation theory method differs from the CI method in which the energy is solved by using perturbation theory instead of the variational principle. Where the total electronic Hamiltonian is the sum of the unperturbed Hamiltonian operator $\hat{H}_0$ and a small perturbation $\hat{H}^{'}$,

$$\hat{H} = \hat{H}_0 + \lambda\hat{H}^{'} \tag{2.3.4}$$

Where, λ is a small real number that weights the perturbation and regulates the order of perturbation, and $\hat{H}'$ are the relevent two-electron integrals. When using the shifted Fock operator as the unperturbed Hamiltonian operator, the *MP* equations can be derived where the first order *MP* energy is:

$$E_{MP1} = \langle \Psi_0 | \hat{H}' | \Psi_0 \rangle \tag{2.3.5}$$

Due to *Brillouin's theorem* mentioned previously in section 2.3.1, the first order *MP* energy is equal to HF. The first and major contribution to the electron correlation is through the second-order *MP* energy (MP2).

$$E_{MP2} = \sum_{\substack{a<b \\ r<s}} \frac{\langle \Psi_0 | \hat{H}' | \Psi_{ab}^{rs} \rangle \langle \Psi_{ab}^{rs} | \hat{H}' | \Psi_0 \rangle}{\epsilon_a + \epsilon_b - \epsilon_r - \epsilon_s} \tag{2.3.6}$$

Where the denominator is reliant on orbital energies of the relevant excitation. The *MP* method will be utilized in the difference projection-after-variation double-hybrid density functional theory (ΔPAV-DH-DFT) methodology in Chapter 4 and there we will discuss possible faults of the methodology.

2.3.4 Multiconfigurational Methods

Closely related to CI methods are multiconfigurational methods. Where, $|\Psi_0\rangle$ in equation 2.3.1, may not be a suitable wavefunction for the CI expansion due to the fact that it is a single determinant wavefunction. Thus, two or more references can be utilized to do the CI expansion, this method is noted as multi-reference configuration interaction (MRCI). However, one large issue with MRCI is the choice of determinants used for the reference to then build the expansion. CASSCF methodology provided an alternative through the use of an AS. In which, the AS is a selection of orbitals in which to do the expansion between, denoting the most important determinants for the calculation. The accuracy, of the method itself, is reliant on the users selection of the AS. The selection of the AS is known to be difficult due to the large amount of chemical intuition that is needed by the user. Further detail about this methodology will be presented in following chapters.

2.3.5 Nonorthogonal Configuration Interaction

The nonorthogonal configuration interaction (NOCI) methodology, details the CI method however, instead of the use of orthogonal SDs, they are nonorthogonal. The utilization of nonorthogonal determinants has been relatively recent in the computational community. However, the simplistic approach of allowing nonorthogonality between determinants can capture additional correlation in the system that cannot be captured in an orthogonal system. Because of the nonorthogonality between determinants the calculation of energy needs to be examined. The energy of electronic state A in the NOCI calculation is obtained from

$$E_A = \sum_{\mu\nu} h_{\mu\nu} \gamma_{\mu\nu}^A + \frac{1}{2} \sum_{\mu\nu\sigma\lambda} \langle \mu\nu || \sigma\lambda \rangle \Gamma_{\mu\nu\sigma\lambda}^A \tag{2.3.7}$$

In which, $\gamma^A_{\mu\nu}$ and $\Gamma^A_{\mu\nu\sigma\lambda}$ are the one-electron and two-electron density matrices for state A, respectively

$$\gamma^A_{\mu\nu} = S_A^{-1} \sum_{IJ} C^*_{IA} C_{JA} N_{IJ} P^{IJ}_{2\mu\nu} \tag{2.3.8}$$

$$\Gamma^A_{\mu\nu\sigma\lambda} = S_A^{-1} \sum_{IJ} C^*_{IA} C_{JA} N_{IJ} P^{IJ}_{1\mu\nu} P^{IJ}_{2\sigma\lambda} \tag{2.3.9}$$

The energy in equation 2.3.7 is expressed in the AO basis. This is the same equation that can be utilized in the orthogonal CI procedure, however, the main difference between these two procedures is the corresponding values of the MO form of the transition density matrices, P. In the orthogonal CI procedure these values are either 0 or 1 due to the *Slater Condon Rules*, however, in a nonorthogonal system the values can fall between 0 and 1, creating the dependence of the energy not only on the coefficients, C, but also the transition density matrices. The scaling factor, is the inverse of $\mathrm{S_A}$ which is a product of the overlap between two solutions, I and J.

$$S_A = \sum_{IJ} C^*_{IA} C_{JA} N_{IJ} \tag{2.3.10}$$

The matrix elements of $\mathrm{N_{IJ}}$ are computed from the determinant of the occupied-occupied (*oo*) overlap matrix, $N_{IJ} = det(^{IJ}M)$.

$$^{IJ}\mathbf{M} =^I \mathbf{C}^\dagger_{occ} \mathbf{S}^J \mathbf{C}_{occ} \tag{2.3.11}$$

Where, $\mathbf{C}_{\mathrm{occ}}$ is the occupied MO coefficient matrix and $\mathbf{S}$ is the AO overlap matrix. The *oo* overlap matrix gives the projection of orbitals in the bra (ket) configuration onto orbitals in the ket (bra) configuration. $^{IJ}\mathbf{M}$ is not necessarily symmetric due to the fact that the occupied orbitals in the bra and ket may differ. The Hamiltonian matrix elements $\mathrm{H_{IJ}}$ are computed using the transition density matrices.

$$H_{IJ} = \tilde{N}_{IJ} \langle I|\hat{H}|J\rangle = \tilde{N}_{IJ} \left(\langle \mathbf{h}\mathbf{P}_3 \rangle + \frac{1}{2} \langle \mathbf{P}_1 \mathbf{G}(\mathbf{P}_2) \rangle \right) \tag{2.3.12}$$

In which, $\mathbf{G}(\mathbf{P}_2)$ is the contraction of the transition density matrix with the two-electron resonance integrals (2ERIs) and $\tilde{N}$ is the psuedodeterminant of $^{IJ}\mathbf{M}$. The psuedodeterminant is the determinant of the product of nonzero eigenvalues, thus $\tilde{N}_{IJ}$ is equal to N_{IJ} when $^{IJ}\mathbf{M}$ is nonsingular. The form of the transition density matrices is dependent on the size of the null space of $^{IJ}\mathbf{M}$ which demonstrates the components of the bra determinant that are orthogonal to the ket determinant. To compute P, the null space must be separated using singular value decomposition (SVD) to transform the orbital basis.

$$^{IJ}\mathbf{M} = \mathbf{U}^{IJ}\mathbf{\Sigma}\mathbf{V}^\dagger \tag{2.3.13}$$

Where, in the new basis, $^I\tilde{\mathbf{C}} = {}^I\mathbf{CU}$ and $^J\tilde{\mathbf{C}} = {}^J\mathbf{CV}$ and the overlap between the two transformed orbitals is given by $^{IJ}\mathbf{\Sigma}$. The transition density matrices can then be computed using:

$$\mathbf{P}_1^{IJ} = \begin{cases} {}^{J}\mathbf{C}^{IJ}\mathbf{M}^{-1I}\mathbf{C} or {}^{J}\tilde{\mathbf{C}}^{IJ}\boldsymbol{\Sigma}^{-1I}\tilde{\mathbf{C}} & \text{for } \dim(\ker({}^{IJ}\mathbf{M})) = 0 \\ \sum_j {}^{J}\tilde{\mathbf{C}}_j {}^{I}\tilde{\mathbf{C}}_j^{\dagger}/\sigma_{jj} & \text{for } \dim(\ker({}^{IJ}\mathbf{M})) = 1 \\ {}^{J}\tilde{\mathbf{C}}_j {}^{I}\tilde{\mathbf{C}}_j^{\dagger} & \text{for } \dim(\ker({}^{IJ}\mathbf{M})) = 2 \\ 0 & \text{for } \dim(\ker({}^{IJ}\mathbf{M})) > 2 \end{cases} \tag{2.3.14}$$

$$\mathbf{P}_2^{IJ} = \begin{cases} \mathbf{P}_1^{IJ} & \text{for } \dim(\ker({}^{IJ}\mathbf{M})) = 0 \\ {}^{I}\tilde{\mathbf{C}}_i {}^{J}\tilde{\mathbf{C}}_i^{\dagger} & \text{for } \dim(\ker({}^{IJ}\mathbf{M})) \leq 2 \\ 0 & \text{for } \dim(\ker({}^{IJ}\mathbf{M})) > 2 \end{cases} \tag{2.3.15}$$

$$\mathbf{P}_3^{IJ} = \begin{cases} \mathbf{P}_1^{IJ} & \text{for } \dim(\ker({}^{IJ}\mathbf{M})) = 0 \\ {}^{I}\tilde{\mathbf{C}}_i {}^{J}\tilde{\mathbf{C}}_i^{\dagger} & \text{for } \dim(\ker({}^{IJ}\mathbf{M})) = 1 \\ 0 & \text{for } \dim(\ker({}^{IJ}\mathbf{M})) > 1 \end{cases} \tag{2.3.16}$$

where the diagonal elements of ${}^{IJ}\boldsymbol{\Sigma}$ are in ascending order starting with index i. It should be noted that the value of $\mathrm{H_{IJ}}$ is the same regardless of how the transition density matrices are computed. As stated earlier in this section, the equations above are in the AO basis, in a later chapter this methodology will be discussed in the MO basis.

DENSITY FUNCTIONAL THEORY

HF methodology is known to be one of the backbones of computational chemistry however, it does not stand alone. DFT methodologies are some of the most widely used computational procedures for electronic structure calculations. In comparison to HF methodologies, DFT methods are based on the electron density, which is experimentally measurable, unlike a wavefunction. The utilization of the electron density, in DFT methodologies allows for the method to be a function of position only, which is three variables (x, y, and z). In comparison, the wavefunction of an n-electron system is a function of 4n-variables, three spatial and one spin coordinate for every electron in the system. Regardless of the size of the system, DFT methodologies will always be reliant on only three variables while wavefunction methods grow in computational cost with every electron added into the system. The low computational cost of DFT has led to a steady increase of utilization in computational chemistry.

2.4.1 Kohn-Sham Formulation of Density Functional Theory

Current DFT calculations are based on the Kohn-Sham (KS) approach. However, before KS, two theorems were proposed by Hohenberg and Kohn which helped pave the path for current DFT based methods. The first Hohenberg-Kohn theorem states that all ground state properties of a molecule can be determined by the ground state electron density functional, $\rho_0(x, y, z)$.

$$E_0 = E[\rho_0] \tag{2.4.1}$$

The theorem states that given the electron density, the energy can be calculated. The second Hohenberg-Kohn theorem is the DFT counterpart of the wavefunction variational method, stating that any trial electron density function will give an energy higher than (or equivalent to, if it were exactly the true electron density function) the true ground state energy.

$$E_\nu[\rho_\nu] \geq E_0[\rho_0] \tag{2.4.2}$$

Where, ρ_ν is the trial electron density and $E_0[\rho_0]$ is the true ground state energy, corresponding to the true electron density ρ_0. The trial density must also satisfy the condition $\int \rho_\nu(r)dr = n$ where n is the total number of electrons in the n-representable system. Overall, Hohenberg and Kohn demonstrated that there is a universal functional of the density F, which does not depend on the details of the system and gives its energy,

$$E[\rho(r)] = \int \nu_n(r)\rho(r)dr + F[\rho(r)] \tag{2.4.3}$$

where, ν_n is the external Coulomb potential created by the nuclei. This functional of the energy is minimized by varying the electron density however, we do not have a good starting point for the electron density and we also do not know the exact functional F. The KS equations assists in combating both of these problems.

In the KS framework, the system is created with non-interacting electrons where the ground state density is the same of the physical system. Because the electrons do not interact, the wavefunction is denoted by a SD of orthonormal orbitals and the density is given by

$$\rho(r) = \sum_{i=1}^{N} \psi_i^{KS*}(r)\psi_i^{KS} \tag{2.4.4}$$

These orbitals are calculated by solving the KS equations.

$$\left[-\frac{1}{2}\nabla_i^2 + \nu_n(r) + \int \frac{\rho(r_2)}{|r_1 - r_2|} + \nu_{xc}(r)\right]\psi_i^{KS} = \epsilon_i\psi_i^{KS} \tag{2.4.5}$$

It is often easier to understand the KS equation by rewriting equation 2.4.5 in terms of energy,

$$E_{tot}[\rho] = E_T[\rho] + E_V[\rho] + E_J[\rho] + E_{XC}[\rho] \tag{2.4.6}$$

The exchange-correlation, ν_{xc} and E_{xc}, is a key piece to the KS equations. This term accounts of the correlated motion of electrons which the Coulombic term lacks to include. The exchange-correlation potential functional is a process of transforming the electron density into the exchange-correlation energy. This energy compensates for self-interaction error (*SIE*), in which, when the electrons interacting are assumed as a charge cloud. Within *SIE*, electrons can become much closer to one another than in reality. The energy also accounts for the deviations in the kinetic energy due to the non-interacting electrons. The exchange-correlation energy can be divided between the exchange and correlation functionals.

$$E_{xc}[\rho] = E_x[\rho] + E_c[\rho] \tag{2.4.7}$$

A good functional will handle not only exchange and correlation errors but also SIE and kinetic energy errors where, the E_x term corrects for the strongly correlated motion of electrons of the same spin and removes nonphysical self-repulsion terms in the potential energy term and E_c corrects the more weakly correlated motion of electrons of opposite spin.

SIE is an error that is a consistent problem throughout DFT functionals. In DFT the energy is a functional of the single-particle density so there is no way to distinguish between Coulomb interactions and self-interaction (26). In the DFT methodology, the interaction of each electron is characterized as an electron interacting with the entire electron density, which includes its own density, as the Coulomb energy. The self-interaction is removed from the Coulomb energy with the utilization of the approximate functionals discussed in the following subsection. However, the Coulomb should cancel with the exchange exactly but in approximate DFT functionals it does not thus causing the SIE. In comparison, HF methodologies do not experience SIE due to the fact that the exchange term in HF is exact thus, the SIE is not present in the calculation.

In DFT, the primary issue stems from devising a good exchange correlation functional, $E_{xc}[\rho]$. The sophistication of the $E_{xc}[\rho]$ has steadily increased and the hierarchy of theory has been termed as Jacobs Ladder, where the top of the ladder will culminate the divine functional, demonstrated in figure 2.3. In further sections, only functionals from the 3rd, 4th, and 5th rung of Jacobs ladder are used. However, a very brief description of each rung will be described below.

2.4.2 Jacobs Ladder: Including Electron Correlation into DFT

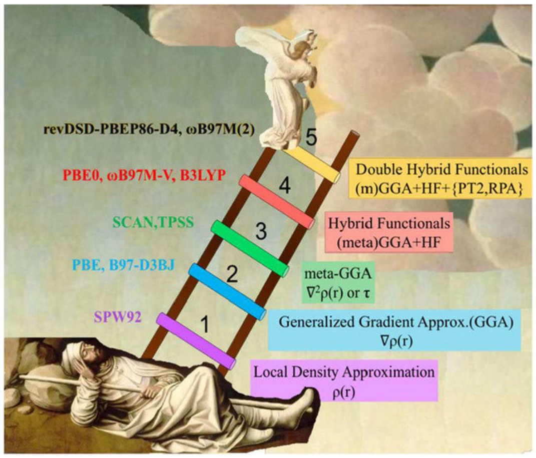

Figure 2.3. Illustration of Jacobs Ladder of DFT

The first rung and simplest approximation to the exchange-correlation energy is from the Local Density Approximation (LDA). In which one assumes that at every point in the molecule, the energy density has the value that would be given by a locally homogenous electron gas. LDA functionals are generally, not accurate enough for studying chemical systems due to the fact that the energy density can change drastically when moving across the molecular surface. However, these functionals are useful for large scale materials. Because LDA assumes a constant density, for an improved description of the exchange-correlation functional, a gradient is included in the second rung of Jacobs ladder known as Generalized Gradient Approximation (GGA) functionals. In GGA, the exchange functional utilizes both the electron density and the gradient, which is the first derivative of the density with respect to position. GGA corrections were a major advancement in practical DFT calculations, where equation 2.4.7 is taken advantage of in combination with the utilization of both the electron density and gradient, and the total exchange correlation energy functional can be divided into an exchange, ex. B88, and a correlation functional, ex. LYP. The 3rd rung of Jacobs ladder, termed meta-GGA, can provide further improvement on the GGA approach by utilizing the second derivative of the density. However, computing the second derivative can create some computational problems, but this can be avoided by making the functional dependent on the kinetic energy density rather than the electron density, by summing the squares of the gradients of the KS molecular orbitals.

The functionals in the 4th and 5th rung of Jacobs ladder utilize HF exchange in addition to the DFT exchange-correlation term. The justification lies in the *adiabatic connection* in which the exchange-correlation energy can be taken as a weighted sum of the DFT exchange correlation energy and the HF exchange energy. In hybrid DFT functionals, 4th rung of Jacobs Ladder, the HF exchange is computed using the KS orbitals of the non-interacting electrons. These electrons have no Coulomb interaction but they do show Pauli repulsion of electrons. The total hybrid DFT functional equation's main distinguishing characteristic is the percentage of HF exchange.

$$E_{xc} = (1 - a_x)E_x^{GGA} + a_x E_x^{HF} + bE_c^{GGA} \tag{2.4.8}$$

Even further improvements to DFT come from the 5th rung of Jacobs Ladder, which corresponds to double-hybrid (DH) methodologies, where the exchange contribution is a hybrid of GGA and HF exchange and the correlation is a hybrid of DFT and $MP2$-like correlation, computed with Kohn-Sham orbitals (27; 28).

$$E_{xc} = (1 - a_x)E_x^{GGA} + a_x E_x^{HF} + bE_c^{GGA} + c(\gamma_{\alpha\alpha} E_c^{\alpha\alpha PT2} + \gamma_{\alpha\beta} E_c^{\alpha\beta PT2}) \tag{2.4.9}$$

DH methods have shown their utility and accuracy for both ground (29; 30) and excited state systems (31; 32; 33; 34) showing that they are the most reliable density functional approximations that even rival wavefunction based approaches (35). The efficacy of DH methodologies are examined in more detail in Chapter 4.

CHAPTER 3

ELECTRIC FIELD CONTROL OF MULTISTATE PROCESSES

Electric Field Control

Control of chemical kinetics and thermodynamics is at the core of chemistry. While the role of macroscopic properties, such as temperature, pressure and concentration are routinely used, recent developments have sought to control chemical reactivity at the molecular level through the use of ultrafast lasers and electric fields (36; 37; 38; 39; 40; 41). In particular, there has been significant recent interest in electric field control of chemical reactions based on modifying the stability of different charge distributions in structures along reaction pathways. There are two modes by which electric field interaction with molecules can modify reactivity. Firstly, systems in which permanent multipole moments change significantly in direction and magnitude as the reaction proceeds display behavior that can be rationalized by classical electromagnetism. The effect of permanent electrostatics has been hypothesized as playing a key role in enzyme catalysis (42; 43). Secondly, recent work has demonstrated how relative contributions of valence bond structures to the molecular wavefunction can be modified depending on (de)stabilization of charge distributions within each configuration, demonstrating how systems with no net charge distribution interact with electric fields (44). Together, the mechanisms of electric field interaction with molecules modify reaction pathways and can be used to control chemical reactivity.

The control and manipulation of chemical reactions through applied electric fields have been demonstrated both experimentally and theoretically in a growing number of chemical systems (45; 46; 47; 48). Shaik *et al.* calculated that selectivity of Diels-Alder reactions could be controlled by the use of correctly oriented electric fields (49; 50), which was subsequently corroborated experimentally (51; 52). In addition, oriented external electric fields (OEEFs) have been investigated theoretically to control electron transfer reactions (53), reactions of iron porphyrins (54), substitution reaction mechanisms (55), nitromethane decomposition (56), electrochemical CO_2 reduction (57) and radical stability (58). Experimentally, electric fields have been shown to modulate component exchange in dynamic liquid crystals (59), selectivity in epoxide rearrangement on an Al_2O_3 surface (60), direct desulfurization on Cu(111) surfaces (61), and hydrogen evolution reactions on MoS_2 nanosheets (62). Despite growing understanding of electric field effects on molecular ground states, very few investigations of OEEFs on excited state reaction pathways have been performed. Coote *et al.* have examined electric field effects on vertical excitation energies of acetophenone (63), while Knoch *et al.* studied the effect of OEEFs on modifying accessibility of electronic state crossings in *p*-coumaric acid (64). The study was motivated by the identification that the electronic states responsible for photoisomerization across photobiological systems show charge separation that can be stabilized through the protein electrostatic environment (65; 66). In particular, *p*-coumaric acid is the chromophore of the photoactive yellow protein, where the electrostatic environment of the protein environment was identified as enabling trans-to-cis isomerization (67).

Unsubstituted Azobenzene

[1]

3.2.1 Introduction

In this chapter we seek to understand the role of OEEFs on modulating the thermal and photo-isomerization of azobenzene. The ultrafast photoisomerization of azobenzenes is well studied (68) and used to develop photochromic molecular switches in diverse applications including molecular machines (69), biomolecules and drug delivery systems (70; 71), and solar thermal fuels (72; 73) through functionalizing the azobenzene scaffold. Azobenzenes have several interesting properties that suggest the use of OEEFs as a design paradigm for developing advanced devices. In particular, azobenzene has among the largest dipole moments found in organic molecules (~ 3.5 D in the *cis* geometry compared to e.g. alkanes (< 1 D) and formaldehyde (2.33 D) (74)) and the orientation of the dipole is strongly dependent on the geometry, suggesting that OEEFs can selectively act on different regions of the PES. In addition to permanent electrostatics, the contributions of different resonance structures arising from conjugation in azobenzene can be modified through application of OEEFs. Azobenzene can be functionalized to obtain push-pull azobenzenes which can enhance the role of OEEFs, which will be further discussed in section 3.3.1. Before functionalization can be performed, it is necessary to understand how the scaffold itself responds to OEEFs. Several previous studies have examined the isomerization response of azobenzenes under electric fields, including using scanning tunneling microscopy over azobenzenes adsorbed on surfaces (75; 76; 77), electrochemical processes (78; 79), in polar liquids and liquid crystals (80), self-assembled monolayers of azobenzenes on gold (81), and as a recording medium for polarization holography (82). However, only cis-to-trans isomerization was observed to be enhanced and there has not been an examination of the response to concerted perturbation by electric fields and light. Furthermore, the shape of the PES around the intersection seam which is important for determining photochemical reactivity has never been examined under applied field conditions."

In this chapter we will demonstrate that the ground and exited-state PESs of azobenzene can be manipulated based on the direction and magnitude of an applied electric field enabling control of photoreaction products. Examination of different field-free isomerization pathways have indicated the presence of both rotation and inversion pathways on the S_1 surface which decay via the same extended seam to the S_0 surface (83; 84; 85). In addition, the less-studied thermal isomerization can proceed via either a rotation or inversion pathway, with recent work suggesting the inversion isomerzation pathway is more energetically favored (85). First, we examine the effect of OEEFs on the S_1 pathway, including how electric fields modify accessibility to the conical intersection (CI) as well as the shape of the branching space around the CI, and so changes observed photoproducts and quantum yields (86; 87; 88). Secondly, we demonstrate the effect of OEEFs on the accessibility of S_0 rotation and inversion pathways.

---

[1] Adapted with permission from Kempfer-Robertson, E. M., Avdic, I., Haase, M. N., Pike, T. D. & Thompson, L. M. Protonation State Control of Electric Field Induced Molecular Switching Mechanisms. Physical Chemistry Chemical Physics 55, 5251-5261 (2023). Copyright 2023 The Royal Society of Chemistry.

3.2.2 Theory and Computational Details

All calculations were performed using the CASSCF method within Gaussian 16 (89). Ideally, the whole π system of azobenzene, 18 electrons and 16 orbitals, should be included in the AS but computational expense necessitated truncation to 10 electrons in 8 orbitals, as was used by Casellas *et al* (85). The omitted π orbitals were excluded on the basis that the occupation numbers did not change significantly from two or zero over the relevant regions of the field-free potential energy surface, and that use of a 14 electron in 12 orbital AS did not result in a significant change geometries or relative energies of test calculations. Fig. 3.1 shows the 8 AS orbitals at the azobenzene trans geometry, containing π and π^* benzene ring orbitals, π and π^* azo group orbitals, and nonbonding nitrogen orbitals. Dynamic correlation has been shown to play an important role in obtaining quantitative agreement with experiment (84; 85). However, this study assumes that the CASSCF PES is qualitatively correct and focuses on the changes induced by OEEFs on such a surface. As the principle effect of OEEFs is on static correlation and the study is focused on the qualitative changes of the PES that occur upon application of OEEFs, the conclusions are likely to be valid even though we have not investigated the role of dynamic correlation. Our field-free results are in agreement with those obtained from CASSCF references used in CASPT2 studies suggesting that any discrepancy between our values and experiment is as a result of neglecting dynamic correlation (84).

The azobenzene ground state has C_{2h} symmetry in the trans isomer and C_2 symmetry in the cis isomer. In the absence of an electric field, the orbitals belong to an irreducible representation of the nuclear point group (indicated in Fig. 3.1 for the C_{2h} trans isomer). As a result of truncation of the AS, point group symmetry breaking was observed in the reference orbitals, which captures additional correlation missing in the multiconfigurational expansion. The results presented in this work are those that allow symmetry-broken reference orbitals where present, rather than symmetry adapted orbitals, although the relative energy difference between the approaches was only around 1-2 kcal mol^{-1}. The rationale for admitting a symmetry-broken reference is that the nuclear point group is C_1 at the S_0/S_1 CI so nuclear symmetry is not preserved across the reaction path, and applied OEEFs lower the molecular symmetry and so it would be inconsistent to require a higher symmetry of the field-free calculations (90).

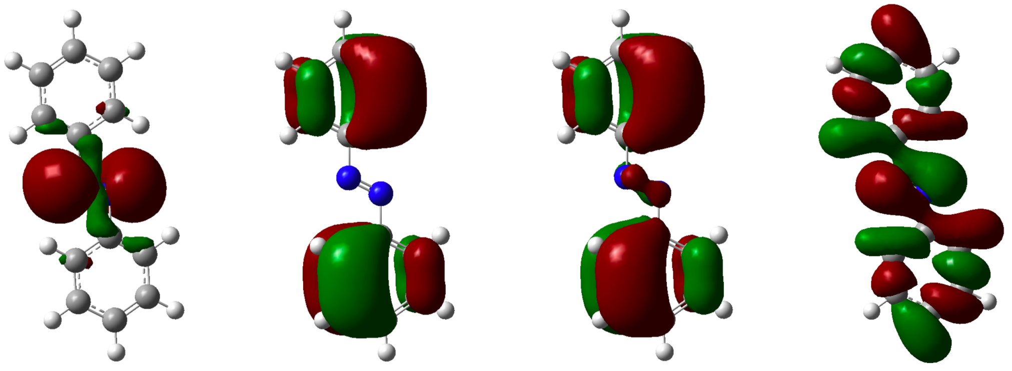

(a)Nonbonding (a_g) (b)Benzene π (b_g) (c)Benzene π (a_u) (d)Nonbonding (b_u)

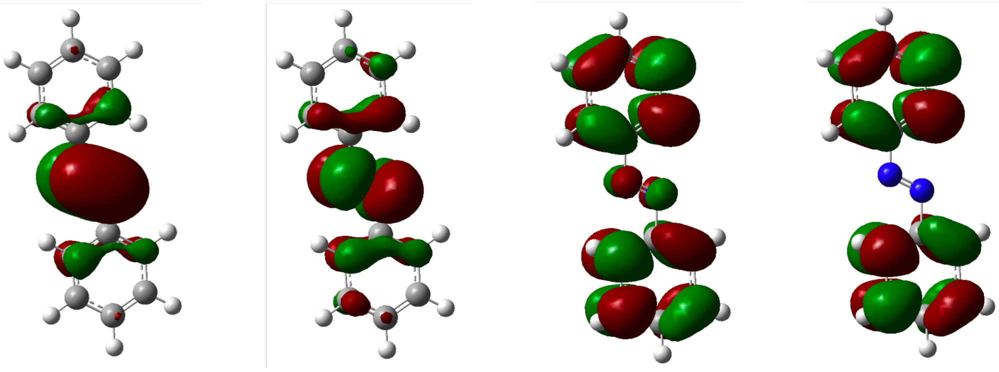

(e)Azo π (a_u) (f)Azo π^* (b_g) (g)Benzene π^* (b_g) (h)Benzene π^* (a_u)

Figure 3.1. Molecular orbitals selected for the 10 electrons in 8 orbitals CASSCF calculation, shown at the ground state trans structure. Irreducible representation labels shown are strictly only correct at the C_{2h} symmetry shown, but are used as labels throughout the text.

All stationary points along the rotation and rotation-inversion pathways were optimized using the 6-31G(d) basis set used in previous studies (84; 85). Although the S_2 surface is likely to play a role in the initial photoisomerization pathway, theoretical calculations have indicated that at low energies population of S_2 is transient and rapidly accesses the S_1 surface before reaching the S_0/S_1 CI (91; 83; 84; 85). Therefore, the present study is focused on the S_0 and S_1 electronic states. Geometry optimization was performed using field-free conditions and was re-run at all magnitudes of OEEFs applied along three different axes (fig. 3.2): the axis defined by the dipole moment (F_{dip}), the N=N axis (F_{azo}), and the axis defined by connecting the centroid of a phenyl ring to the nearest azo N atom (F_{phe}). Note that there are two F_{phe} axes which are usually degenerate due to symmetry. The electric field sign convention is the same as that used by Shaik and coworkers (45), where positive sign indicates that the field gradient along the specified axis points from the negative charge to the positive charge. Electric fields were applied in increments of ±0.0025 au along each axis up to a field strength of ±0.0100 au, which is $\sim 0.1\times$ the intensity of a typical laser field and the same order of magnitude as electric fields found inside protein active sites (92; 42; 93), at electrode surfaces (57; 94), and that result

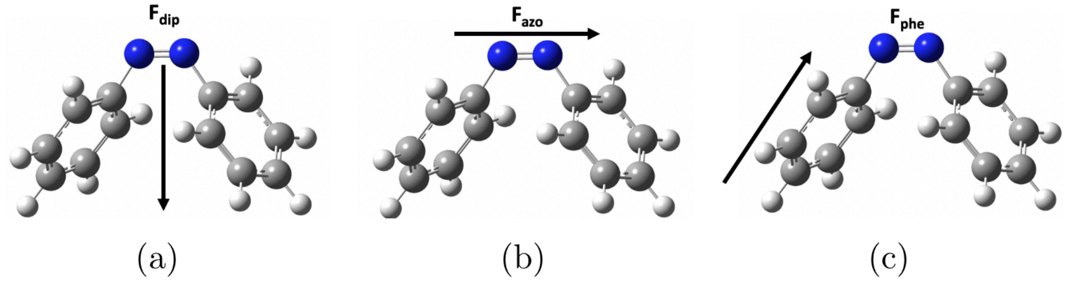

(a) (b) (c)

Figure 3.2. Orientation of external fields applied to azobenzene in this study showing a) F_{dip}, b) F_{azo} and c) F_{phe}.

from dipole-dipole and hydrogen bonding in molecular systems (95; 96; 97) (1 au = $5.14 \times 10^3\,\mathrm{MV\,cm^{-1}}$).

3.2.3 Results

Before discussion of the electric field effect on the isomerization of azobenzene, we first discuss the field-free reaction profile for comparison. The field-free results essentially reproduce the CASSCF results of Conti *et al*(84) and the relative energies and dipole moments are summarized in table 3.3. The optimized ground state cis and trans minima (S_0 (cis) and S_0 (trans) structures respectively) and the transition state structures of the rotation and inversion pathway (S_0 (rot ts) and S_0 (inv ts) respectively) are shown in fig. 3.3. The S_0 (trans) structure is planar and due to a center of inversion has zero dipole moment. Through thermal or photoisomerization, azobenzene is converted to the S_0 (cis) structure, which was computed to have a dipole of 3.4 D orientated between the phenyl groups and perpendicular to the azo bond. The S_0 (cis), S_0 (rot ts), and S_0 (inv ts) structures are 15.1, 59.0 and 47.9 kcal mol^{-1} less stable than the S_0 (trans) structure respectively suggesting thermal isomerization occurs through the inversion pathway. The stability of the inversion pathway transition state results from photoisomerization via inversion of an sp^2-hybridized orbital on one of the nitrogens which preserves the double bond character of the azo group, while in the rotation pathway the azo bond length increases 0.1 Å reducing π conjugation as the nonbonding and π-bonding orbtials on the azo group switch roles.

Starting from the S_0 (trans) structure, excitation to the S_1 state is then followed by relaxation to the S_0/S_1 seam of electronic degeneracy. The minimum energy conical intersection along the rotation pathway (S_0/S_1CI_{rot}) and S_1 structures optimized with CNNC angles constrained to 180° and 0° (S_1 (trans) and S_1 (cis) respectively) are shown in fig. 3.3. Motion orthogonal to trans-to-cis isomerization in the branching space around S_0/S_1CI_{rot} connects photodissociated (or vibrationally hot) products, corresponding to azo dissociation and formation of $2\,\mathrm{Ph}^{\cdot} + \mathrm{N}_2$. The S_1 (cis) and S_0/S_1CI_{rot} structures both contain permanent dipoles that are in the same direction as their relative ground state structures but the total dipole moment is smaller because the excitation is of $n\pi^*$ character and results in charge transfer into the phenyl rings opposing the ground state dipole (the S_1 (cis) and S_0/S_1CI_{rot} have dipoles of 1.4 D

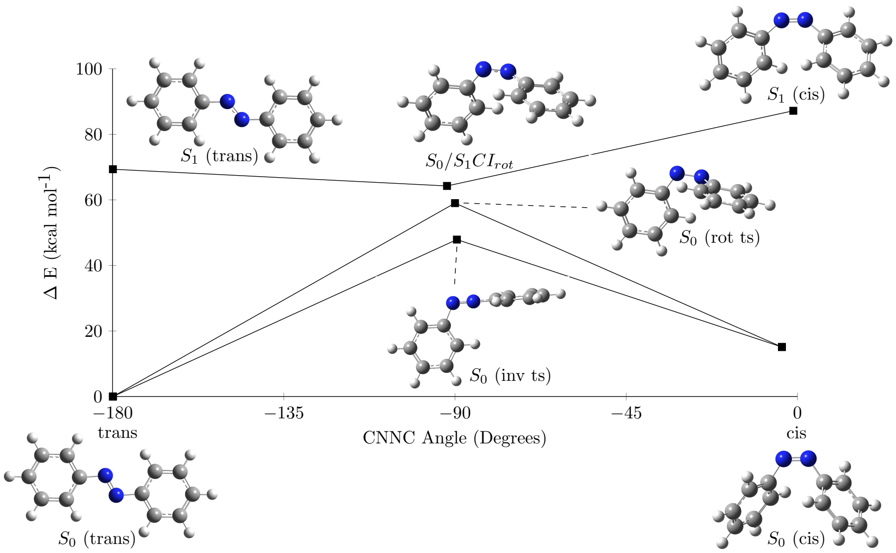

Figure 3.3. Optimized structures of azobenzene S_0 and S_1 potential energy surfaces showing both S_0 rotation and inversion pathways.

and 0.5 D smaller than their corresponding ground state structures (S_0 (cis) and S_0 (rot ts) rotation respectively). The S_0/S_1CI_{rot}, S_1 (trans), and S_1 (cis) structures are 64.3, 69.4, and 87.1 kcal mol^{-1} above the S_0 (trans) structure respectively. Unlike for the ground state, there is no alternative isomerization pathway via inversion under field-free conditions as this channel has a substantial barrier and the S_0/S_1 energy gap is large across the reaction path (83).

Use of CASSCF permits analysis of the wavefunction in terms of configuration weights. As each configuration has a different charge distribution, application of OEEFs will change the character of the wavefunction through configuration weight modification. To interpret the effect of OEEFs on wavefunction character, we first discuss the field-free wavefunctions. In the following discussion, orbitals are labelled by the character and irreducible representation at the C_{2h} geometry given in fig. 3.1. The trans S_0 minimum (S_0 (trans)) is dominated by a single configuration of squared (and thus normalized) CI weight 0.90 with double occupation of nonbonding a_g, benzene π b_g, benzene π a_u, nonbonding b_u and azo π a_u. The cis S_0 minimum (S_0 (cis)) is also dominated by a single configuration with weight 0.90, but the configuration corresponds to a $\pi^2\pi^{*2}$ excitation of orbitals at the trans geometry, with double occupation of azo π^* b_g instead of azo πa_u as a result of torsion around the π bond. We emphasize that the π^* label is only with respect to occupation of orbitals at the trans reference, but at the cis geometry the azo π^* b_g orbital is in fact occupied in the ground state and corresponds to a π bonding orbital.

In the S_0 transition structure wavefunctions (S_0 (rot ts) rotation and S_0 (inv ts) inversion) there are two important configurations that are common to both wavefunctions – the ground state configuration which dominates the S_0 (trans) wavefunction and a $n\pi^*$ configuration which corresponds to a single excitation from nonbonding b_u

to azo π^* b_g. In the rotation pathway transition structure S_0 (rot ts) the wavefunction displays significant $n\pi^*$ character (weight 0.44), although with the major contribution still from the ground state configuration (weight 0.59), while the inversion pathway transition structure S_0 (inv ts) wavefunction remains of greater ground state character (weight 0.90) with a much smaller contribution from the $n\pi^*$ configuration (weight 0.04). Excited state structures show greater multireference character than corresponding ground state structures. S_1 (cis) has four important configurations – two of $n\pi^*$ character which differ as a result of single excitation from nonbonding a_g or nonbonding b_u, with weights of 0.05 and 0.03 respectively, one $n^2\pi^{*2}$ excitation (double excitation from nonbonding b_u) with weight 0.44, and the previously discussed $\pi^2\pi^{*2}$ with weight 0.44. The S_1 (trans) wavefunction has two important configurations both describing the $n\pi^*$ excitation, with weights 0.90 (nonbonding a_g) and 0.05 (nonbonding b_u). Finally S_0/S_1CI_{rot} has three important configurations with closed shell ground state, $n\pi^*$ (nonbonding a_g), and $\pi^2\pi^{*2}$ character, with weights 0.40, 0.46 and 0.03 respectively.

3.2.3.1 Modification of photoisomerization pathways

Having examined the electronic structures and geometries of azobenzene S_0 and S_1 PESs under field free conditions, we now discuss the effect of OEEFs on the azobenzene S_1 PES. Application of negative F_{dip} (fig. 3.4a and 3.4b and table 3.4) stabilizes S_1 (cis) and S_0/S_1CI_{rot} and causes an increase in the dipole, while positive F_{dip} destabilizes charge separation and increases the energy at weak fields. In contrast, S_1 (trans) has no permanent dipole under field free conditions and so application of any field regardless of the orientation allows charge separation and results in relative stabilization compared to the field-free energy. At strong positive F_{dip} ($\geq 7.5 \times 10^{-3}$ au), we observed a strong-field dipole-inversion effect in S_1 (cis), in which the applied field is strong enough that charge barycenters realign to be antiparallel to the applied field. The result of the strong-field dipole-inversion effect is that the qualitative response of the PES to the applied field follows a significantly different trend to that at low-field strengths. With $F_{dip} = +0.01$ au, the strong-field dipole-inversion effect causes S_1 (cis) to be stabilized by 9.49 kcal mol^{-1}, which is in fact only 0.50 kcal mol^{-1} higher energy than when $F_{dip} = -0.01$ au. The geometry changes of S_0/S_1CI_{rot} are relatively small, with the largest coordinate change being the NNCC torsion under $F_{dip} = \pm 0.01$ au, which moves by $-10.5°$ when the field is applied in the negative direction and 13.2° when the field is applied in the negative direction. The effect of F_{dip} on the various structures combined is that negative and weakly positive F_{dip} cause the minimum energy rotation pathway CI to become more ‘peaked’ in character, while at large positive F_{dip}, the energetic ordering of S_0/S_1CI_{rot} and S_1 (trans) is reversed and the CI seam is energetically less accessible. Fig. 3.5 shows the minimum energy pathway between S_1 (trans) and S_0/S_1CI_{rot} which also demonstrates that the sign of F_{dip} can be used to change the qualitative shape of the PES around S_0/S_1CI_{rot}. In addition, fig. 3.5 shows that $+F_{dip}$ causes a minimum on the S_1 CNNC torsion coordinate at an angle of around 112.5° as a result of the strong-field dipole-inversion effect. As the shape of the potential energy surface leading to the CI plays a role in determining

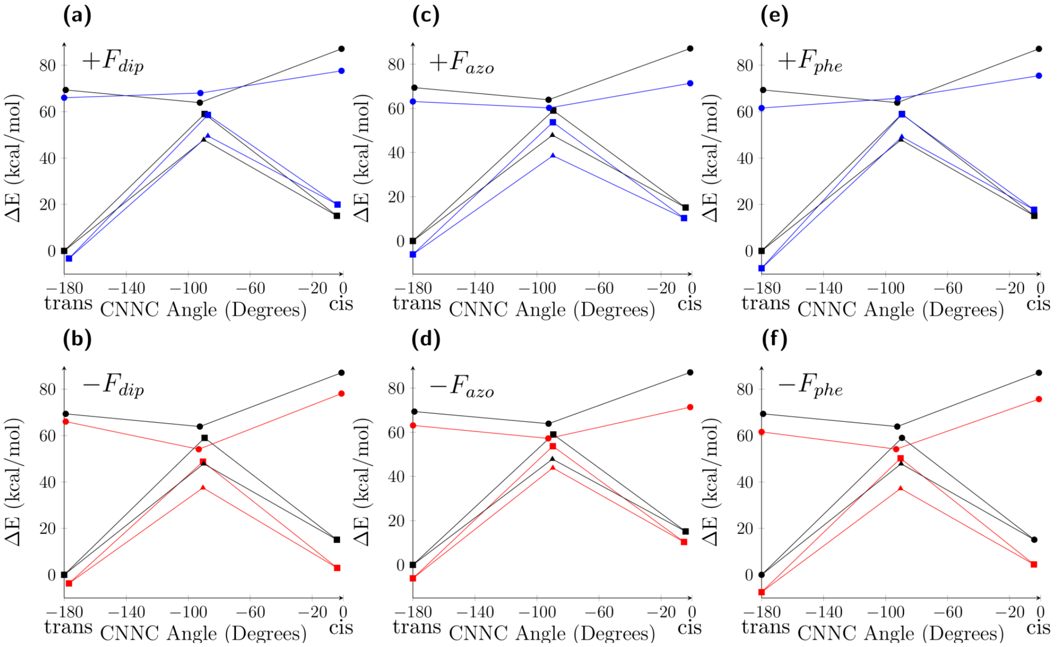

Figure 3.4. Effect of +0.01 au (gold) and −0.01 au (red) orientated external electric fields applied to photo and thermal isomerization pathways of azobenzene compared to field-free conditions (black). Panels a, c and e (top row) shows positive fields and panels b, d and f (bottom row) shows negative fields. Panels a and b (first column) shows F_{dip}, panels c and d (middle column) shows F_{azo} and panels e and f (right column) shows F_{phe} (△ – S_0 inversion pathway, □ – S_0 rotation pathway, ○ – S_1 rotation pathway). Energies are shown with respect to the field-free C_{2h} structure. Fig. 3.17 shows full results for all field strengths.

the excited state lifetime, which has traditionally been considered to correlate with quantum yield, it would be expected that the quantum yield of photoisomerization can be controlled by application of electric fields. Recent findings have demonstrated the importance of vibronic coherence in determining quantum yield which cannot be accounted for directly in our study (98; 99; 100). However, the changes in the shape of the potential energy surface leading to the CI as well as the branching space (see below) are likely to change the phase-matching mechanism required to yield the cis isomer and so modify the quantum yield compared to the experimentally determined field-free quantum yield on excitation to S_1 of ~ 0.2 (101).

We now discuss in more detail the effect of F_{dip} on the shape of the branching space around S_0/S_1CI_{rot}. The branching space coordinates that lift the electronic degeneracy involve PhNNPh torsional motion along the derivative coupling vector and symmetric NN stretching and PhNN bending along the gradient difference vector (fig. 3.6). From S_0/S_1CI_{rot}, coupled motion along both branching space vectors in the forward (positive) direction leads to the S_0 (cis) isomer, while motion in the reverse (negative) direction leads to the S_0 (trans) isomer. The PES defined by the branching space vectors is shown in fig. 3.7 under field-free, $F_{dip} = +0.01$ a.u., and $F_{dip} = -0.01$ a.u. conditions. The branching space PES under field free conditions shows

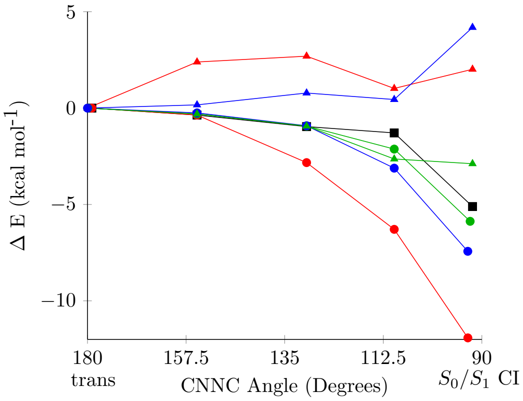

Figure 3.5. Excited state rotation photoisomerization pathway under applied electric fields of different orientations with strengths ±0.01 a.u. determined using CAS(10,8)/6-31G(d) with constrained CNNC optimizations from vertical excitation geometry (180°) to conical intersection(90°) (△ – positive fields, ○ – negative fields, black – field-free, red – F_{dip}, green – F_{azo} field, blue – F_{phe}).

that energetically downhill degeneracy breaking occurs along the (+1,+1) or (-1,-1) coordinate with an energy barrier along the (+1,-1) and (-1,+1) coordinates which lead to molecular dissociation of the azo group. Under negative F_{dip} orientation, the branching space is qualitatively similar to that under field-free conditions, although the S_0 surface is skewed with minima at (+1,+0.5) and (-1,-0.5) such that relaxation to the cis or trans S_0 minima involves a trajectory with vibrationally excited azo bond. However, under positive F_{dip} the S_0 surface is orientated 90° relative to the field-free conditions, such that the energetically favorable and unfavorable degeneracy lifting coordinates are now reversed. As a result, under strong positive fields the rotation photoisomerization pathway of azobenzene is inhibited and photoexcitation is channeled towards vibrationally hot NN and CN stretching modes.

Although the rotation pathway is now broadly accepted as the principle photoisomerization mechanism in azobenzene, the possibility of an inversion pathway has been strongly articulated (102). To determine if OEEFs could allow access to the inversion photoisomerization pathway, the S_0/S_1 energy gap was computed along the interpolated pathway between S_0/S_1CI_{rot} and the inversion thermal isomerization transition state $S_0(ts, C_2)$, which connect to each other through wagging of the out-of-plane phenyl group (fig. 3.8). In addition, the interpolated pathway between $S_0(ts, C_2)$ and a planar inversion structure obtained by rotation of the out-of-plane phenyl group was calculated. State averaged CASSCF calculations under field-free conditions demonstrated that although the planar inversion structure had a smaller energy gap than the nonplanar inversion structure, both structures had an S_0/S_1 energy gap of over 30 kcal mol^{-1}. Application of F_{dip} changes the energy gap at the nonplanar inversion structure by -4.21 kcal mol^{-1} under negative field orientations and by +4.00 kcal mol^{-1} under positive field orientations, while the inverse effect is observed at the planar inversion structure (+1.87 kcal mol^{-1} and -1.95 kcal mol^{-1} under negative and positive F_{dip} fields respectively). Thus, even though the change in

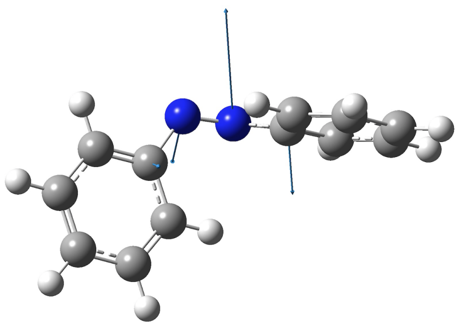

(a)Derivative Coupling (X_1)

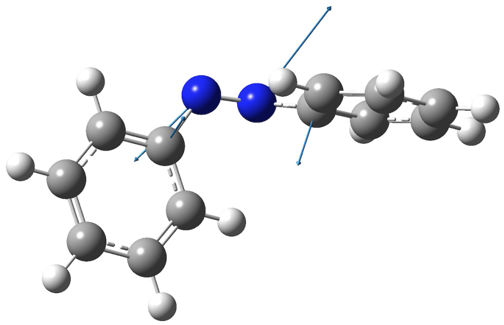

(b)Gradient Difference (X_2)

Figure 3.6. Derivative coupling (panel a) and gradient difference vectors (panel b) that define the branching space around S_0/S_1CI_{rot} computed using CAS(10,8)/6-31G(d).

S_0/S_1 energy gap along the inversion pathway is not trivial, the total gap is still substantial and so F_{dip} application does not permit photoisomerization via the inversion pathway.

Unlike F_{dip}, application of F_{azo} results in stabilization of excited state structures regardless of the orientation and strength of the applied field (fig. 3.4c and 3.4d and table 3.5). To understand the behavior of F_{azo}, the S_1 (cis) structure can be used as a representative example. The S_1 (cis) wavefunction has four important configurations – $\pi^2\pi^{*2}$, two $n\pi^*$ and $n^2\pi^{*2}$. The $n\pi^*$ configurations show charge transfer into the phenyl rings relative to the ground state, while the $n^2\pi^{*2}$ and $\pi^2\pi^{*2}$ configurations preserve electron density on the azo group. Therefore, the $n\pi^*$ configurations display charge separation along the same axis as the F_{azo} orientation. Application of F_{azo} breaks the C_2 symmetry of the two $n\pi^*$ configurations into a configuration that corresponds to charge separation favored by F_{azo} and another which is disfavoured by F_{azo}. The $\pi^2\pi^{*2}$ and $n^2\pi^{*2}$ configuration weights decrease slightly with F_{azo} application (to 0.27 and 0.28 respectively at $F_{azo} = -0.01$ au), while the stabilized $n\pi^*$ configuration weight increases (to 0.34 at $F_{azo} = -0.01$ au) and the destabilized $n\pi^*$ configuration weight decreases (to 0.00 at $F_{azo} = -0.01$ au), so that regardless of the orientation of F_{azo} the effect on the relative energy is the same.

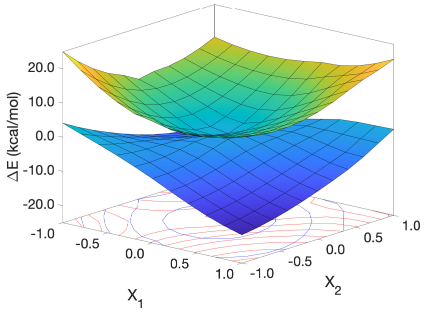

(a)$F_{dip} = +0.01$ au

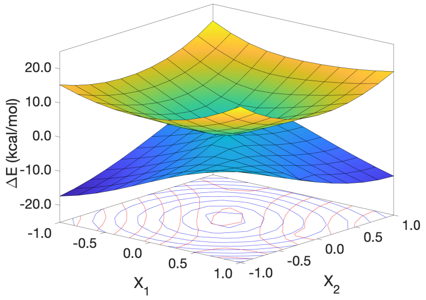

(b)Field-free conditions

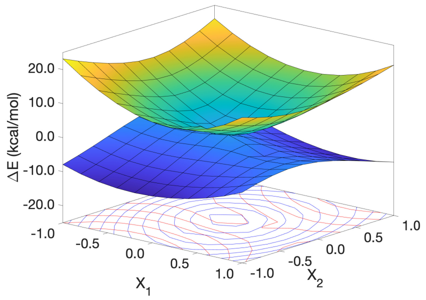

(c)$F_{dip} = -0.01$ au

Figure 3.7. Potential energy surface of branching space around S_0/S_1CI_{rot} computed using CAS(10,8)/6-31G(d) under $F_{dip} = +0.01$ au (panel a), field-free (panel b), and $F_{dip} = -0.01$ au (panel c) conditions. Coordinates are given by branching space vectors shown in fig. 3.6. Surfaces are colored by energy relative to S_0/S_1CI_{rot}, with contour maps of S_0 (red) and S_1 (blue) surfaces shown below.

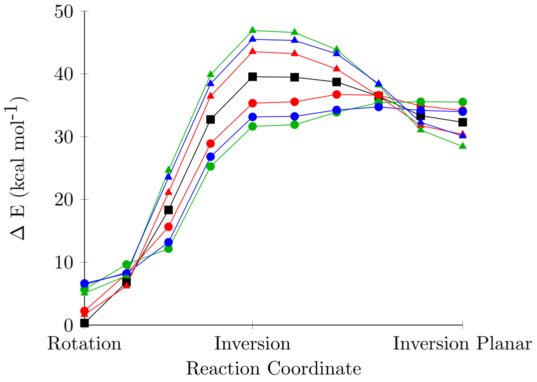

Figure 3.8. Reaction coordinate between rotation, inversion, and inversion planar transition structures under applied electric fields of different orientations with magnitude of ±0.01au determined using stateaveraged CAS(10,8)/6-31G(d)(△ – positive fields, ○ – negative fields, black – field-free, red – F_{dip}, green – F_{azo} field, blue – F_{phe}).

Whilst energy stabilization occurs regardless of applied F_{azo} orientation, S_0/S_1CI_{rot} is the only structure that has a different magnitude depending on F_{azo} orientation. When F_{azo} is negative, S_0/S_1CI_{rot} is 7% more stabilized than with positive field at ±0.0025 au and by 38% at ±0.0050 au. The differential stabilization results from the fact that the S_0/S_1CI_{rot} has reduced C_1 nuclear symmetry compared to other structures on S_1 as a result of distortion of PhNN angles, so that one of the azo nitrogens has a less negative partial charge than the other. Therefore, the resulting symmetry broken $n\pi^*$ configurations do not correspond to equal charge transfer and so are differentially stabilized or destabilized depending on F_{azo} orientation. As a result, fig. 3.5 demonstrates that both orientations of F_{azo} field preserve the peaked nature of the conical intersection along with differential stabilization of S_0/S_1CI_{rot}. As for F_{dip}, F_{azo} did not result in the closing of the S_0/S_1 energy gap at either the planar or nonplanar structures (fig. 3.8). However, of the three field axes examined, F_{azo} had the largest effect on the S_0/S_1 energy gap, as (similarly to S_0/S_1CI_{rot}) the inversion isomerization structures have asymmetric electron density distribution over the azo nitrogens.

The study of F_{phe} has two motivations. First, unlike F_{dip} the applied field is orientated along an internal coordinate of the molecule and so provides a more realistic simulation of an applied field that could be achieved in experiment, such as through tethering the azobenzene molecule to a support. Second, upon $n\pi^*$ excitation to the S_1 state, electron density moves from the azo group into the phenyl ring along the axis of F_{phe}, suggesting that application of F_{phe} may be able to tune the gap between S_0 and S_1. Application of F_{phe} results in similar relative energy modifications to F_{dip} results (fig. 3.4e and 3.4f and table 3.6). However, F_{phe} has a component that interacts with the charge redistribution that results from increased $n\pi^*$ configuration weights in S_1 that is orthogonal to the S_0 dipole. Negative F_{phe} applied to S_1 (cis) increases the weight of all important configurations except the $n\pi^*$ (nonbonding b_u) configuration (weight 0.00 at $F_{phe} = -0.01$ au), stabilizing the field-free charge distribution and increasing the permanent dipole to 7.45 D. However, positive F_{phe} stabilizes the $n\pi^*$

(nonbonding b_u) configuration (weight 0.18 at $F_{phe} = +0.01$ au) while destabilizing the $n\pi^*$ (nonbonding a_g), $n^2\pi^{*2}$ and $\pi^2\pi^{*2}$ configuration (weights 0.01, 0.36 and 0.35 respectively at $F_{phe} = +0.01$ au).

Regardless of the axis or orientation of the applied field the vertical excitation energy from S_0 (trans) remains essentially constant. F_{dip} causes similar charge redistribution in both electronic states as, owing to inversion symmetry, neither the S_0 or S_1 surfaces possess a permanent dipole. Application of a field in either orientation is symmetrically equivalent and reduces the symmetry of the wavefunction to allow charge separation. Similarly, stabilization of S_0 (trans) depends on the strength of F_{azo}, while in the S_1 state, F_{azo} aligns with the axis of charge separation in the two dominant $n\pi^*$ configurations that are equivalent but display opposite dipoles. Thus, depending on the F_{azo} orientation one of the $n\pi^*$ configurations is stabilized at the expense of the other, but as both configurations are equivalent the energy stabilization is identical. Application of F_{azo} shows the largest change in vertical excitation energy of any of the three orientations, but only differs by 1 kcal mol^{-1} from the field-free structure at ±0.01 au. F_{phe} similarly modifies the S_1 (trans) wavefunction by stabilizing one $n\pi^*$ orientation over the other depending on orientation.

3.2.3.2 Modification of thermal isomerization pathways

In this section the effect of OEEFs on thermal isomerization pathways is examined. First, we look at the F_{dip} applied to the S_0 PES (figs. 3.4a and 3.4b and table 3.4). Structures S_0 (cis), S_0 (rot ts), and S_0 (inv ts) are stabilized by a negative field and destabilized by a positive field; as the negative field vector stabilizes the zero-field charge distribution and causes an increase in the permanent dipole. As in S_1, the exception on the S_0 surface is S_0 (trans) which does not exhibit a permanent dipole and so application of the external field favors charge separation to counter the applied field and causes an opposing dipole moment regardless of the field orientation. Application of $-F_{dip}$ reduces the height of the rotation thermal trans-to-cis isomerization barrier by up to 6.55 kcal mol^{-1} at -0.01 au, which is 11% of the field-free barrier height. The inversion pathway follows a similar trend, with the trans-cis barrier decreasing by 6.66 kcal mol^{-1} when $F_{dip} = -0.01$ au (fig. 3.9). In contrast to the thermal trans-cis isomerization which is reduced, the height of the cis-trans reaction barrier increases under $-F_{dip}$, with the rotation barrier increasing by 1.91 kcal mol^{-1} and the inversion barrier increasing by 1.80 kcal mol^{-1} (fig. 3.9). Despite the significant energetic effect of F_{dip} on reaction barriers (in absolute terms, rather than as a fraction of the field-free barrier), the configuration weights of S_0 structures do not change significantly relative to the field-free wavefunction.

We now discuss the effect of F_{azo} application on the S_0 PES (figs. 3.4c and 3.4d and table 3.5). Application of F_{azo} causes smaller changes in relative energy and geometry in comparison to F_{dip}. Stabilization of structures is equivalent regardless of whether negative or positive F_{azo} is applied because there is no contribution to the permanent dipole along the NN bond in any structure. Thus, F_{azo} applied in either direction stabilizes charge separation across NN and lowers the overall energy. The exception is the S_0 (inv ts) transition structure where one phenyl ring moves while

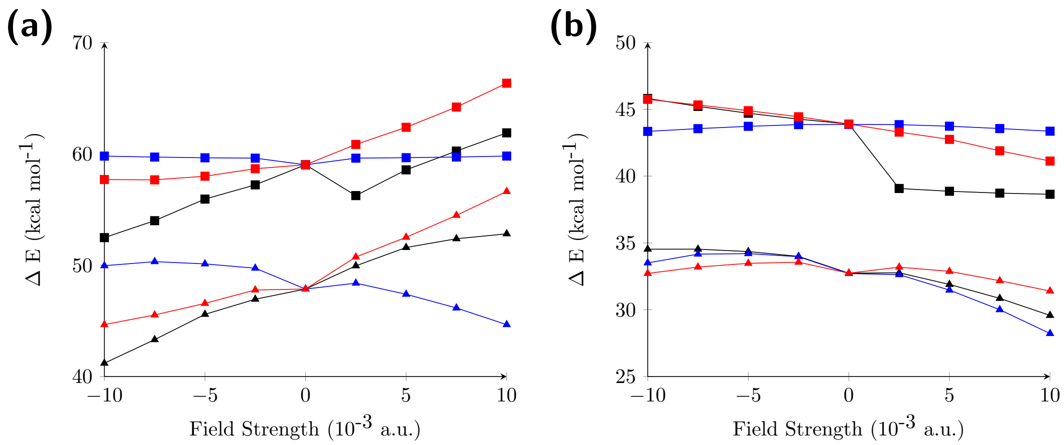

Figure 3.9. Effect of thermal isomerization reaction barrier computed using CAS(10,8)/6-31G(d) under different field orientations and strength. Panel a shows the trans-cis thermal isomerization reaction barrier and panel b shows the cis-trans thermal isomerization reaction barrier (□ – rotation pathway, △ – inversion pathway, black – F_{dip}, blue – F_{azo}, red – F_{phe}).

the other remains stationary, creating a small dipole contribution along the NN bond (1.09 D component compared to a total dipole of 2.41 D) that is favored by a positive F_{azo} and disfavored by negative F_{azo}. However, $F_{azo} = -0.0075$ au is strong enough to invert the orientation of NN dipole component and stabilize the energy of S_0 (inv ts). Similarly to F_{dip}, the wavefunction configuration weights in each S_0 structure do not change significantly upon application of F_{azo}. The projection of the dipole moments on the F_{azo} field for the S_0 reaction, shown in figure 3.19, demonstrate that the rotation barrier does not affect the dipole as much as it does for the inversion pathway and that is dependent on the contribution to the dipole moment coming from the same direction. The inversion pathway has much larger contribution to the dipole moment than the rotation pathway which is causing the discrepancy between the two pathways.

Application of F_{phe} to the S_0 ground state results in relative energy changes of a similar magnitude and direction to F_{dip} (fig. 3.4e and 3.4f and table 3.6). Application of negative F_{phe} stabilizes all ground state structures while destabilization occurs with positive F_{phe}. Although F_{phe} is not aligned with the permanent dipole, it is close in orientation in structures S_0 (cis), S_0 (rot ts), and S_0 (inv ts) resulting in similar, although smaller, energy changes. The reaction barrier for the trans-cis rotation pathway is lowered by 1.33 kcal mol^{-1} at $F_{phe} = -0.01$ au compared to 6.55 kcal mol^{-1} at $F_{dip} = -0.01$ au. Similarly, the trans-cis inversion pathway reaction barrier is stabilized by 3.18 kcal mol^{-1} at $F_{phe} = -0.01$ au compared to 6.66 kcal/mol at $F_{dip} = -0.01$ au. For the thermal cis-trans isomerization, $F_{phe} = -0.01$ au increases the rotation pathway barrier by 1.84 kcal mol^{-1} and reduces the inversion barrier pathway by 0.01 kcal mol^{-1}. At application of large positive F_{phe}, S_0 (rot ts) and S_0 (inv ts) structures are stabilized relative to application of medium positive F_{phe} as the dipole moment inverts to align with the field. The strong-field dipole-inversion effect causes the barrier to be reduced in height relative to the field-free barrier even though the field orientation destabilizes the structure with weak fields. For example, at $F_{phe} = +0.01$ au the thermal cis-trans rotation barrier is reduced by 2.77 kcal mol^{-1} as expected, while contrary to expectations based on the weak field response, the inversion barrier is also reduced by 1.33 kcal mol^{-1}. Therefore, the largest cis-trans thermal inversion barrier is in fact found in the weak-field limit. In figure 3.20, we show that the projection of the dipole on the F_{phe} field is somewhat similar to the F_{dip} field especially for the rotation pathway. Therefore this pathway would be a great alternative to the F_{dip} field which would be experimentally hard to achieve with the changing dipole direction throughout the isomerization process.

Examining the effect of F_{dip}, F_{azo} and F_{phe} on the S_0 PES, it is apparent that there is no selective control enabling switching between inversion and rotation pathways as both behave similarly regardless of the applied field, although it is possible to control the barrier heights of both pathways. For example, application of F_{dip} can be used to stabilize the S_0 (cis) structure and reduce the rate of cis-trans thermal isomerization, potentially providing a route to improved devices that use azobenzene as an energy storage medium. In addition, F_{dip} is dependent on molecular geometry and a fixed electric field that most favors stabilization of cis azobenzene would not stabilize the transition structures to the same extent. Based on the values in 3.4, an electric field which simultaneously stabilizes S_0 (cis) and destabilizes the transition structures by their ± 0.01 a.u. energies could increase the cis-trans thermal isomerization barrier by on the order of > 10 kcal mol^{-1}. Similarly, a field that stabilizes the transition structures while disfavoring S_0 (cis) could decrease the cis-trans isomerization barrier by > 10 kcal mol^{-1}. The projection of the dipole moments on the applied field axes (figs. 3.18–3.20) demonstrate the similarity of F_{phe} and F_{dip}, despite the fact that F_{phe} is defined by an internal coordinate of the molecule. Therefore, the results of F_{dip} could be reproduced (although requiring larger fields), by applying an external field along F_{phe}. Such an axis could be determined by tethering of azobenzene molecules to a surface attached by the para-position of one of the phenyl rings and applying fields parallel or perpendicular to the surface.(103) Thus electric fields provide a route for developing improved devices such as solar thermal fuels that utilize azobenzene to store energy, by reducing thermal autodischarge and so improving storage lifetime and facilitating thermal revision of the fuel form to produce heat.

3.2.4 Conclusions

The effect of orientation and magnitude of applied external electric fields on azobenzene PESs was explored theoretically to understand how OEEFs may provide a new approach in the design of azobenzene-based devices. Through calculation of the azobenzene S_0 and S_1 stationary points, it has been established that applied fields can modify the energy ordering of vertical excitation and S_0/S_1 minimum energy conical intersection geometries, such that the initial photorelaxation pathway on S_1 involves an energetic barrier along the isomerization coordinate. The branching space around the S_0/S_1 minimum energy conical intersection was found to be qualitatively different under applied fields compared to the field-free conditions, with strong positive fields changing the energetically favorable relaxation pathway on S_0 from an isomerization coordinate to an azo dissociation coordinate. Despite the changes to the S_1 PES, applied electric fields were unable to modify the S_0/S_1 energy gap such that photoisomerization could proceed though a competing inversion pathway. We conclude from our findings on the applied field response of the S_1 PES that the quantum yield of photoisomerization is likely to be significantly decreased or enhanced through application of electric fields of specific orientations and strengths. On S_0, the inversion and rotation pathway transition structures were found to follow the same trend in applied field response, and so there is no given field orientation or strength that could switch thermal isomerization mechanisms. However, the barrier heights of photoisomerization reactions could be modified by on the order of $\pm 5 - 15$ kcal mol^{-1} such that electric fields could be used as a design motif to enhance or inhibit thermal revision of the cis fuel form in solar energy devices. Finally, a strong-field dipole-inversion effect was observed that resulted in electric field response trends at strong fields being qualitatively different to that at weak fields. The dipole inversion effect also has a geometric dependence that can lead to formation of new minima in the PES that do not exist under field-free conditions. Future developments using azobenzene as a scaffold to exploit and enhance the electric field response has the potential to provide new directions in device design.

SUBSTITUTED AZOBENZENE (DI-HYDROXY AZOBENZENE)

[2]

3.3.1 Introduction

Now that we have examined the PES and the effect of OEEFs on the unsubstituted Azobenzene we will now examine the enhancement of azobenzene properties. In order to enhance the properties of azobenzene in its function as a molecular switch, a large number of azobenzene derivatives obtained by modification of aromatic rings and/or addition of substituent groups have been synthesized and studied (104). Push-pull azobenzenes, obtained through the addition of substituent groups to modify resonance behavior, are a common strategy for decreasing isomerization lifetimes as the polarization of the azo bond induces greater single-bond character. Related to push-pull azobenzenes are dihydroxyazobenzenes, in which push-pull behavior can be induced through protonation/deprotonation of the substituent groups providing control of the isomerization rate (105; 106; 107; 108; 109; 110). Similar to inducing push-pull character, OEEFs have also been demonstrated to modify isomerization rates through polarization of the azo bond (111; 112). In this work, we examine the use of OEEFs on dihydroxyazobenzene, in both protonated and deprotonated forms, to examine how OEEFs i) interact differently with push-pull azobenzene compared to other azobenzenes, and ii) how a practical switch controlled by both OEEFs and protonation state can be designed.

---

[2] Adapted with permission from Kempfer-Robertson, E. M. & Thompson, L. M. Effect of Oriented External Electric Fields on the Photo and Thermal Isomerization of Azobenzene. The Journal of Physical Chemistry A 124, 3520–3529 (2020). Copyright 2022 American Chemical Society.

Although our previous work on the electric field response of azobenzenes provided insight as to how OEEFs could be used as a control mechanism for molecular switches, the modification of electric field response by tuning of substituent groups has not been investigated. In this work we study protonated and deprotonated forms of dihydroxyazobenzene, which serves as a model system for understanding how push-pull moieties that polarize the azo bond change the behavior with respect to symmetric substituted species under electric fields. By performing a detailed mechanistic study dihydroxyazobenzene, we reveal physical insight that is valid for all push-pull species, even if the details may change depending on the exact nature of the substituents. Additionally, one of the hydroxyl groups serves as a moiety to enable surface attachment. As a result, pH can be used to modify the protonation state of the hydroxyl group exposed to the environment and consequently change the important resonance structures in the wavefunction by inducing push-pull character. The findings provide insight into application of OEEFs combined with protonation state and/or light to control electronic structure and hence modify the thermal and photoisomerization kinetics and thermodynamics in order to control the lifetime of switch states (107; 105).

3.3.2 Theory and Computational Details

Neutral and anionic forms of 4,4'-dihydroxyazobenzene were studied in which only one hydroxyl group was deprotonated. The other hydroxyl group remained protonated to simulate the situation where the oxygen is used as a linker to attach dihydroxybenzene to a surface, and so always has satisfied valencies. The calculations were performed in gas phase except for the application of the homogeneous OEEF, as direct solvent polarization of the molecule in a field addressable array device is not expected to be significant relative to the applied field effect, and we assume that the surface itself does not significantly perturb the molecule except for the applied field. Fig. 3.10 shows the molecular structures of protonated and deprotonated molecules. Depending on the relative orientation of the free hydroxyl group with respect to the azo group in HO−AB−OH, two possible geometries are possible. The *anti* HO−AB−OH structure has the hydroxyl O−H bond oriented parallel to the azo N=N bond so that the molecule has a center of inversion with C_{2h} symmetry, while the *syn* HO−AB−OH structure has the hydroxyls O−H bond oriented perpendicular to the azo N=N bond, giving C_s symmetry and no center of inversion. Preliminary calculations were performed and revealed that there is very little difference between the anti and syn HO−AB−OH molecules. As a result, we focus on syn HO−AB−OH and HO−AB−O$^-$ molecules in the remainder of this article. In addition to the structural differences between molecules, there is a dynamical difference depending on which aryl ring is rotated along the isomerization pathway. However, as it is assumed the molecule is tethered to a surface, only motion of the untethered ring is considered.

The Gaussian 16 suite of programs was used to perform all stationary point geometry optimizations (89). DFT and TD-DFT calculations were performed using

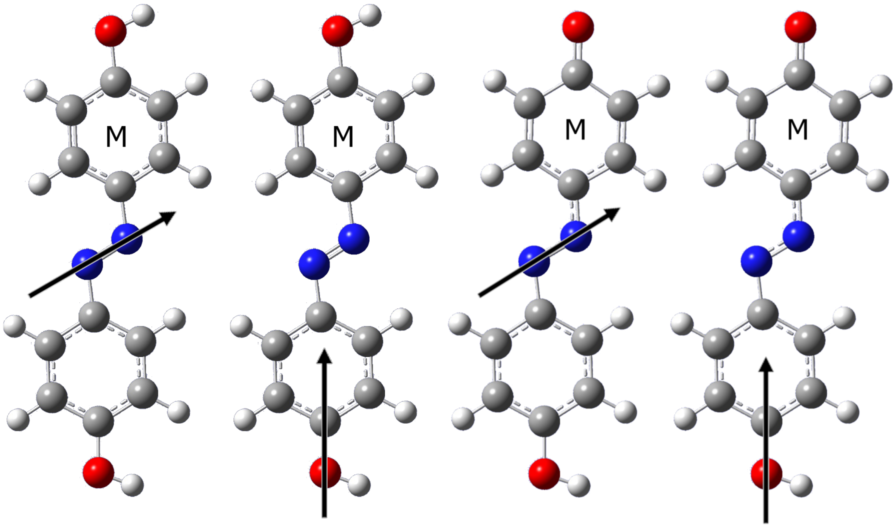

(a) HO-AB-OH F_{NN} (b) HO-AB-OH F_{OC} (c) HO-AB-O^- F_{NN} (d) HO-AB-O^- F_{OC}

Figure 3.10. Orientation of applied fields with respect to HO−AB−OH and HO−AB−O^- molecules. Arrows indicate the positive field direction and point from the positive charge to the negative charge, while the 'M' label denotes the ring in motion during isomerization.

B3LYP with the 6-311+G(d) basis set (113; 114). In order to study regions of the PES where nonadiabatic effects were possible due to near-degeneracy of the S_0, S_1, and S_2 electronic states, CASSCF was performed with 10 electrons in 8 orbitals with the 6-31+G(d) basis. All relevant geometries were first located under field-free conditions, and then recomputed at different magnitudes of the applied OEEF. Stationary points of the PES were confirmed by performing a normal mode analysis to ensure the correct number of modes with imaginary frequencies (one for transition structures (TSs) and zero for minima). The OEEF orientations are denoted as the F_{NN} and F_{OC} fields, where the F_{NN} field is applied along the azo bond of the molecule (fig. 3.10a for the protonated and fig. 3.10c for the deprotonated molecule) and the F_{OC} field is applied along the O−C bond of the phenyl ring attached to the surface that is stationary during isomerization (fig. 3.10b for the protonated and fig. 3.10d for the deprotonated molecule). The F_{NN} field is studied because it directly connects the two rings and so is most able to control push-pull behavior in the molecule, while the F_{OC} field is studied as it describes a field orientation perpendicular to a surface on which the molecule is tethered. The electric field sign convention used in this work is that a positive sign indicates the field gradient along a specified axis points from the positive charge to the negative charge (the opposite of the Gaussian). Electric fields were applied in increments of ±0.0025 a.u. up to ±0.0100 a.u. (1 a.u. = $5.14\text{x}10^3$ MV cm^{-1}) which are comparable to the electric field magnitudes found in scanning tunneling microscopy break junction (STM-BJ) or at protein active sites (115; 116). As the multipole moments of charged molecules are not invariant to the coordinate origin, the center of mass was used as the coordinate system origin when analyzing the field-response properties in terms of the dipole.

In order to study the kinetics of ground-state isomerization reactions, the Eyring equation was used to compute the rate constant for each isomerization mechanism k_i

$$k_i(\mathbf{E}, T) = \frac{k_B T}{h} \exp\left\{\frac{-\Delta^{\ddagger} G_i(\mathbf{E})}{RT}\right\} \tag{3.3.1}$$

where k_B is the Boltzmann constant, T is the temperature (298K was used in this study), h is Planck's constant, $\Delta^{\ddagger}G$ is the Gibbs activation energy computed in the rigid-rotor harmonic oscillator approximation, $\mathbf{E}$ is the electric field vector, and R is the gas constant. The total rate constant k_{total} is equal to the sum of the rate constants for each isomerization mechanism

$$k_{total}(\mathbf{E}, T) = \sum_i k_i(\mathbf{E}, T) \tag{3.3.2}$$

and the half-life $t_{1/2}$ could then be computed assuming that the isomerization mechanisms are first-order processes

$$t_{1/2}(\mathbf{E}, T) = \ln(2)/k_{total}(\mathbf{E}, T) \tag{3.3.3}$$

Eq. 3.3.2 gives the total rate constant of isomerization for a large number of molecules. However, for any single molecule, the average isomerization half-life is computed using the weighted average rate constant k_{av}

$$k_{av}(\mathbf{E}, T) = \sum_i p_i(\mathbf{E}, T) k_i(\mathbf{E}, T) \tag{3.3.4}$$

where $p_i(\mathbf{E}, T) = N \exp\{-\beta(T) E_i(\mathbf{E})\}$ is the normalized Boltzmann factor, with $\beta(T) = 1/k_B T$. The expected half-life for the isomerization of any single molecule is then obtained using eq. 3.3.3 with k_{av} instead of k_{total}.

3.3.3 Results

In this section we examine the behavior of the thermal and photo isomerization pathways of 4,4'-dihydroxyazobenzene. First, we will discuss the field free thermal isomerization pathways for both the protonated and deprotonated species. We will then discuss and compare the thermal isomerization under the F_{NN} and F_{OC} fields. In the following section, we detail the photochemical behavior of the protonated and deprotonated forms by first examining the CI branching space and OEEF effects. Finally, we will discuss the influence of the co mbination of pH and applied OEEFs on the photochemical pathway.

3.3.3.1 Thermal Isomerization Pathways of 4,4'-dihydroxyazobenzene

3.3.3.1.1 Field-Free Ground State Potential Energy Surface Before discussing the application of OEEFs, we first detail the PES and dipole moments under

Structure	HO−AB−OH			HO−AB−O$^-$		
	ΔE	ΔG	Dipole	ΔE	ΔG	Dipole
S_0 Trans	0.0	0.0	2.89	0.0	0.0	11.73
S_0 Rot TS	45.2	45.5	3.83	29.9	28.3	3.63
S_0 Rot Inv TS	44.2	43.1	4.43	41.9	40.7	9.69
S_0 Inv TS	46.8	46.6	2.77	41.6	40.5	9.68
S_0 Cis	17.1	17.0	4.37	17.0	17.0	8.86

Table 3.1. Relative bare electronic and Gibbs energies (kcal mol^{-1}), and dipole moments (Debeye) of optimized HO−AB−OH and HO−AB−O$^-$ S_0 stationary points under field-free conditions computed with B3LYP/6-311+G(d).

field free conditions, summarized in table 3.1. The thermal isomerization of azobenzene and its derivatives can occur through multiple different pathways: rotation, rotation-inversion, and inversion pathways, where the inversion pathway has been found to be the lowest energy pathway (117; 85). The rotation pathway involves torsion of the CNNC dihedral concurrently with azo bond stretching. In contrast, the inversion pathway moves along the NNC angle until it reaches 180° at the TS. Last, the rotation-inversion pathway is a combination of both the rotation and the inversion pathways, simultaneously moving along both CNNC dihedral and NNC angle coordinates.

In HO−AB−OH, all three isomerization mechanisms have similar *cis*-to-*trans* thermal isomerization Gibbs free energy activation barriers. The lowest Gibbs activation barrier is along the rotation-inversion pathway ($\Delta^{\ddagger}G = 26.1$ kcal mol^{-1}), while the rotation barrier is 2.4 kcal mol^{-1} higher, which is much closer to the inversion-rotation pathway than in unsubstituted azobenzene (111). The activation energy barriers for all three isomerization pathways are lower for dihydroxy azobenzene than for unsubstituted azobenzene by 6.0 kcal mol^{-1} for rotation inversion, 18.9 kcal mol^{-1} for inversion, and 15.7 kcal mol^{-1} for rotation pathways. The lower activation energy suggests that HO−AB−OH can achieve faster *cis*-to-*trans* isomerization (118). The results are also in agreement with Crecca *et al.* (119) and confirm the preference for the rotation-inversion pathway with functionalized azobenzenes. For the reaction energy, *cis* dihydroxy azobenzene is less stable than the *trans* structure by 1.9 kcal mol^{-1}, in comparison to unfunctionalized azobenzene.

Deprotonation yields HO−AB−O$^-$ which, in comparison to the protonated counterpart, gives lower energy activation barriers along all three pathways. The most significant change in activation barrier upon deprotonation is along the rotation isomerization pathway. The reason for the change in the rotation pathway activation energy is that this pathway requires a reduction in bond order in order to reach the transition state, which reduces conjugation within the molecule and so is energetically unfavorable. The available resonance structures for delocalization of the negative charge on the oxygen upon deprotonation reduce the bond order of the azo bond and so decrease the penalty for reducing conjugation to reach the TS (120). The increase in bond length upon deprotonation is illustrated in fig. 3.11. In con-

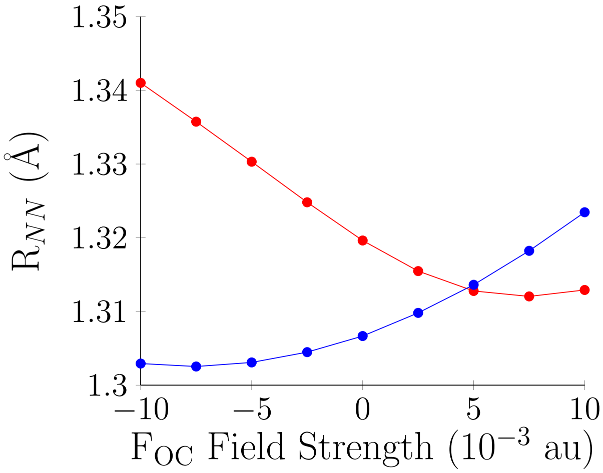

Figure 3.11. Azo bond length in rotation transition state at different F_{OC} field strengths for HO−AB−OH (blue) and HO−AB−O^{-} (red), indicating electric-field induced azo dissociation is not responsible for the reduced barrier height of inversion via the rotation transition state.

trast, the inversion and rotation-inversion pathways do not require a reduction in the bond order of the azo group, and so are not as affected by deprotonation as the rotation pathway. The dipole moments of the deprotonated molecule are larger for all structures than in the protonated molecule with the exception of the rotation TS, suggesting the deprotonated molecule will show enhanced sensitivity to OEEFs. However, as different structures show different size changes in the dipole moment upon deprotonation, it is expected that deprotonation will not only enhance the effect of OEEFs, but fundamentally change the topology of the PES.

3.3.3.1.2 Electric Field Modification of the Ground State Potential Energy Surface Having explored the S_0 PES and associated charge distribution under field-free conditions, we now study the electric-field response. Examining the effect of the applied F_{NN} field on the *cis*-to-*trans* thermal isomerization barrier heights (fig. 3.12a), it can be seen that positive fields cause a decrease in the rotation-inversion activation energies (blue triangles), while negative fields increase the barrier height. In comparison, the rotation pathway activation barrier (red circles) decreases in both the positive and negative directions of the applied field because, although both the *cis* minimum and rotation TS are stabilized with both directions of the applied field, the rotation TS is stabilized to greater extent. Both the *cis* minimum and rotation TS are stabilized regardless of the field orientation as the component of the dipole along the applied field axis is small and changes direction to minimize the field-dipole interaction energy. In contrast, the inversion barrier height (black squares) shows the opposite behavior to rotation-inversion with respect to the field sign. As a result, the inversion pathway is lowest energy with negative fields ($\Delta^{\ddagger}G = 18.8$ kcal mol^{-1} at $F_{NN} = -10.0 \times 10^{-3}$ a.u.), and the rotation-inversion pathway is lowest energy

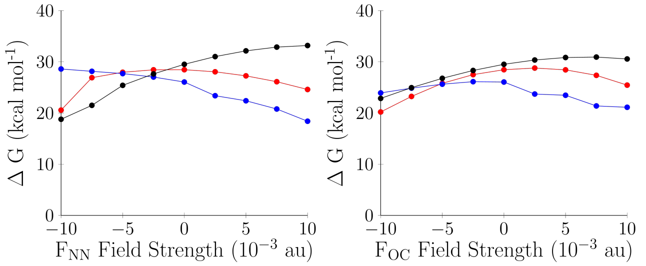

(a) HO-AB-OH F_{NN} (b) HO-AB-OH F_{OC}

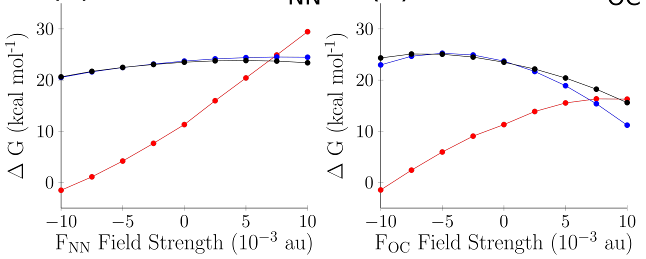

(c) HO-AB-O- F_{NN} (d) HO-AB-O- F_{OC}

Figure 3.12. Gibbs activation energies on S_0 of reaction pathways leading from the protonated (panels a and b) and deprotonated (panels c and d) *cis* structure (rotation – red circles; rotation-inversion – blue triangles; inversion – black squares). Panels a and c correspond to application of F_{NN} and panels b and d correspond to application of F_{OC}.

with positive fields ($\Delta^{\ddagger}G = 18.4$ kcal mol^{-1} at $F_{NN} = 10.0 \times 10^{-3}$ a.u.), while at -2.5×10^{-3} a.u., all three pathways have almost the same barrier height.

Applying F_{OC} to the protonated molecule (fig. 3.12b) gives similar results to the F_{NN} field, but with several small but significant differences. The rotation-inversion pathway (blue triangles) follows the same trend with both fields, with lower activation barriers at positive fields and a higher activation barriers at negative fields, but with larger magnitude negative F_{OC} fields the trend reverses and the barrier height starts to decrease slightly. As a result, it is not possible to increase the activation barrier along the rotation-inversion pathway using the F_{OC} field to the same extent as with the F_{NN} field. The inversion pathway (black squares) also gives a very similar trend regardless of the field applied, but with F_{OC}, the activation barrier field response is smaller than with F_{NN}. The reaction pathway that is most different between F_{OC} and F_{NN} fields is the rotation pathway (red circles), which has a much larger field response with negative F_{OC}. The reason for the difference is that at the rotation TS, the azo bond takes on more single bond character, and so increasing the single bond character of the *cis* minimum decreases the reaction barrier. The F_{OC} orientation is almost perpendicular to the azo bond at the *cis* minimum, and so positive F_{OC} increases electron density on the azo group, while negative F_{OC} decrease the electron density of the azo group. As a result, negative F_{OC} enhances the single bond character of the azo group at the *cis* minima, and so reduces rotation barrier heights. For the inversion and rotation-inversion TSs, the azo bond maintains its double bond character across the reaction pathway and so negative F_{OC} more equally destabilizes the *cis* minima and TSs.

We now discuss how deprotonation changes the OEEF response of the S_0 surface. The dipole of HO−AB−O$^-$ molecules is oriented from the hydroxyl ring (most positive) to the deprotonated ring (most negative) so negative F_{NN} is antiparallel to the molecular dipole and hence most stabilizing. The *cis* structures have notably larger field sensitivity than other geometries, leading to substantial changes in barrier height (fig. 3.12c). The effect of the F_{NN} field on barrier heights demonstrates the thermal pathway can be switched depending on the direction and magnitude of the field applied. Under field-free conditions and with a negative field, the rotation pathway is the preferred *cis*-to-*trans* isomerization pathway. At large negative fields, the energy barrier along the rotation pathway is removed. As demonstrated in fig. 3.11, which shows the N=N bond length in the rotation TS of HO−AB−O$^-$ at different field strengths, the reduced barrier is not a result of field-induced azo bond dissociation. Therefore, through the use of applied OEEFs, our results suggest it is possible to induce rapid thermal isomerization from *cis*-to-*trans* forms of dihydroxy azobenzene. Furthermore, with positive F_{NN}, the preferred isomerization pathway can be switched from the rotation to the inversion mechanism. As for the protonated species, the F_{OC} field response of HO−AB−O$^-$ barrier heights (fig. 3.12d) is similar to the F_{NN} field response. The key similarity is that application of negative F_{OC} fields can also drastically reduce the *cis*-to-*trans* isomerization activation energy. At positive F_{OC} fields, all three reaction pathways have a smaller activation barrier than with the equivalent F_{NN} field, although the change in energy ordering of TSs is preserved.

In conclusion, application of the F_{OC} can reproduce the behavior of the F_{NN} field which best controls the push-pull behavior of the isomer. In the protonated molecule, barrier heights can be modified by up to 10 kcal mol^{-1} at the examined field strengths and the preferred isomerization pathway can be modified depending upon the field origin. Upon deprotonation, the rotation pathway is significantly stabilized, and combined with a large field-response, it is possible to remove the energetic barrier for *cis*-to-*trans* isomerization.

3.3.3.1.3 Kinetic Effects Resulting from Electric Field Modification Despite the small size of azobenzene and its derivatives, including dihyroxy azobenzene, the mechanism of isomerization is complicated owing to the number of different possible reaction pathways. As illustrated in fig. 3.12, OEEFs can be used, not only to control the activation barrier of a single pathway, but also to control the particular isomerization mechanism that is favored. From a kinetics perspective, the important feature is the activation barrier, regardless of the particular isomerization mechanism. However, at certain electric field strengths and orientations, several isomerization mechanisms have similar activation barriers. In such a situation, the kinetics of isomerization is not defined by a single reaction pathway, but must account for the presence of multiple energetically viable pathways. As a result, OEEFs can potentially be used to control the kinetics by increasing or decreasing the number of routes for azobenzene to isomerize. Fig. 3.13 shows the half-lives of *cis*-to-*trans*

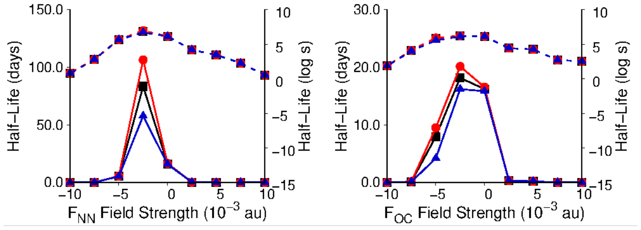

(a) HO-AB-OH F_{NN} (b) HO-AB-OH F_{OC}

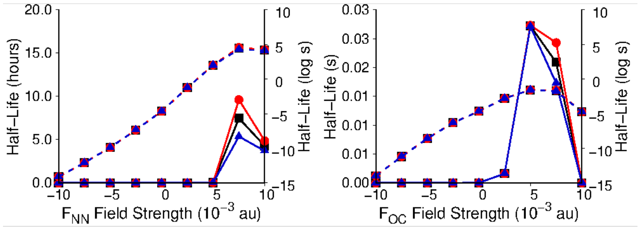

(c) HO-AB-O$^-$ F_{NN} (d) HO-AB-O$^-$ F_{OC}

Figure 3.13. Half-life of protonated (panels a and b) and deprotonated (panels b and c) dihydroxyazobenzene upon application of F_{NN} (panels a and c) and F_{OC} (panels b and d). Solid lines give the half-life on the left-axis (scale is different between panels) and dashed lines give the log of the half-life on the right axis (scale is comparable between panels). Blue triangles give the half-life computed using the total isomerization rate constant (eq. 3.3.2), black squares give the half-live computed using the rate constant of the fastest isomerization mechanism, and red circles give the average isomerization half-life (eq. 3.3.4).

isomerization for the protonated and deprotonated molecules under F_{NN} and F_{OC} fields. Note that the left axis shows raw half-life values (solid lines) on the most suitable scale for the particular molecule and field plotted, while the right axis shows logarithmic half-life values (dashed lines) in seconds on an axis that is common to all four panels so different molecules and fields can be compared.

From fig. 3.13, it is apparent that deprotonation causes the half-life to decrease substantially from months to fractions of a second. In addition, application of either field orientation or sign to the protonated molecule can decrease the half-life from months to seconds. For the protonated species, the presence of energetically similar isomerization mechanisms affects the kinetics at the field-free conditions, causing the total half-life to be 8 days shorter and the average half-life to be 7 days longer than if only the lowest energy pathway (rotation-inversion) is considered. Application of the F_{OC} field always reduces the half life regardless of the field orientation, even though the field orientation switches the most favorable isomerization mechanism from the rotation pathway with negative orientation and the rotation-inversion pathway with positive orientation (fig. 3.13b). At -0.5×10^{-3} a.u. F_{OC}, the rotation and rotation-inversion activation barriers differ by 0.2 kcal mol^{-1}, leading to a significant difference between the total isomerization rate constant, average isomerization rate constant, and the rate constants for each mechanism. As a result, the predicted total half-life is 15 days and the average half-life is 17 days, instead of 16 days computed using the largest rate individual rate constant. The F_{NN} field applied to the protonated molecule (fig. 3.13a) gives a field response that mirrors that of the F_{OC} field, although at -2.5×10^{-3} a.u., all three activation barriers are within 1.5 kcal mol^{-1}, causing the total half-life to be 57 days and the average half-life to be 106 days, instead of 83 days for the fastest individual isomerization process. For the deprotonated molecule, the sign of the field can be used to control the switching half-life (figs. 3.13c and 3.13d). The field-free half life is on the order of milliseconds, but both negative F_{NN} and F_{OC} fields are able to remove the rotation barrier to give rapid isomerization. With positive fields, due to the fact that F_{OC} leads to greater stabilization of all three reaction barriers compared to F_{NN}, the isomerization half-life can be increased to on the order of a second with F_{OC}, while F_{NN} can be used to increase the half-life to almost one hour. As a result, in terms of half-life, the F_{OC} field cannot exactly reproduce the F_{NN} field. However, the combination of deprotonation and electric field yields a switch in which the half-life can be controlled from months to instantaneous.

3.3.3.2 Photoinduced Isomerization Pathways of 4,4'-dihydroxyazobenzene

3.3.3.2.1 Modification of Photoisomerization Branching Space Pathways

To understand how deprotonation and applied OEEFs modifiy photochemical behavior, the location of minimum energy CIs and surrounding branching space topology can provide insight into the available branching pathways and a qualitative discussion of branching ratios, even though dynamics simulations are required to provide a quantitative prediction. Mapping the field-response of the branching space topology enables the change in branching pathways to be determined. In this section, the S_0/S_1 minimum energy CI is discussed, providing a description of how the nonradiative decay mechanisms along the rotation pathway are modified by OEEFs.

For the protonated molecule, the field-free PESs of the S_0/S_1 branching space is shown in fig. 3.14a. The branching space coordinates involve NN stretching and PhNN bending (bond-length alternation) along the derivative coupling vector, and PhNNPh torsional motion along the gradient difference vector (fig. 3.21). The energetically steepest descent path on the S_0 surface leads from the CI to the (-1,+0.5) coordinate, or in the opposite direction to (+1,-0.3), where the notation (x_1,x_2) gives the position along the X_1 and X_2 axes respectively shown in fig. 3.14. This steepest descent coordinate is closely aligned with the gradient difference vector, and is the *cis*-to-*trans* isomerization coordinate. A high energy ridge on S_0, which curves from (-0.7,-1), through the CI at (0,0), to (0,+1), contains two TSs at (-0.3,-0.7) and (0.0,+0.4), which are the two rotation TS structures. The S_1 surface of both conformers has a funnel-like topology, but where the energy rises less steeply along the torsional gradient difference coordinate than the bond-length alternation derivative coupling coordinate. Thus, in the field-free conditions, the nonradiative decay and subsequent branching pathways can be described using a single torsional coordinate.

To understand the effect of OEEFs on the CI branching space of the protonated molecule, fig. 3.15 shows the energy difference between S_0 and S_1 surfaces in the branching space upon application of F_{NN}. Due to the similar behavior of F_{NN} and F_{OC} fields, only results for the F_{NN} field are presented here. Negative fields are

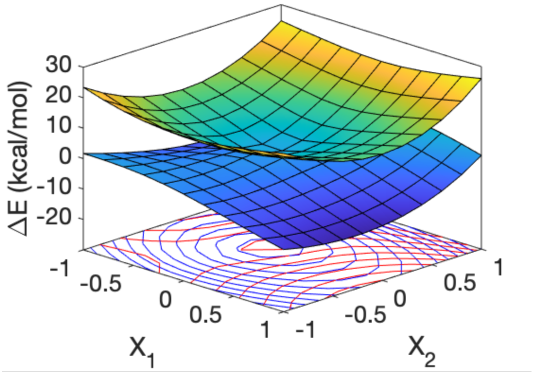

(a) HO-AB-OH

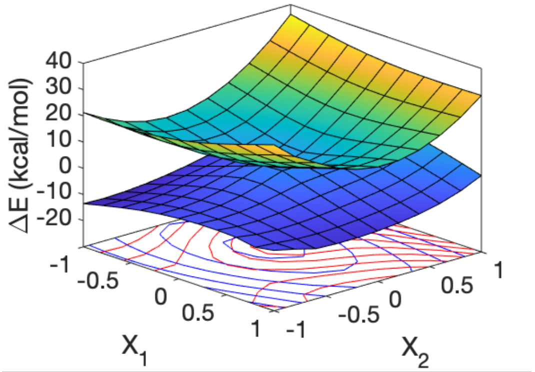

(b) HO-AB-O$^-$

Figure 3.14. Potential energy surface in the branching space of the (a) protonated (b) deprotonated HO−AB−OH around the S_0/S_1 CI computed using CAS(10,8)/6-31+G(d) under field free conditions.

observed to move the minimum energy CI along the high-energy ridge towards the (-0.3,-0.7) rotation TS geometry (fig. 3.15c). In contrast, positive fields move the minimum energy CI closer to the *cis* minimum (fig. 3.15a). The movement of the minimum energy closer to the *cis* minimum under positive fields indicates that the branching space takes on a more sloped character and will funnel the molecule back to the *cis* structure after photo-excitation, while the negative field preserves the peaked topology of the field-free conditions. As a result, application of positive F_{NN} can be used to control the photodynamic equilibrium by reducing cis-to-*trans* photoisomerization.

Turning to the effect of deprotonation, the field-free branching space vectors do not differ significantly from those of the protonated molecule (fig. 3.22). However, the deprotonated species differs in regard to the branching pathway towards the *cis* minimum, which is at (-1,-0.9) instead of (-1,+0.5) in the protonated molecules (fig. 3.14b). As a result, the role of bond-length alternation in the rotation pathway is opposite to the protonated molecule, moving from -0.9 to -0.4 along X_2 instead of

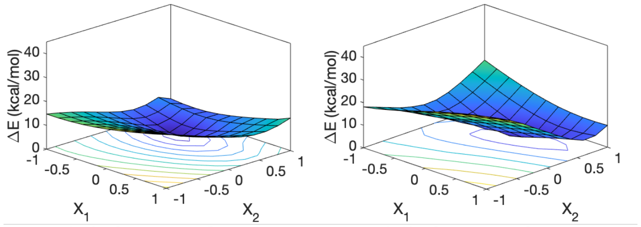

(a) OH-AB-OH
F_{NN} = +0.01 au

(d) OH-AB-O$^-$
F_{NN} = +0.01 au

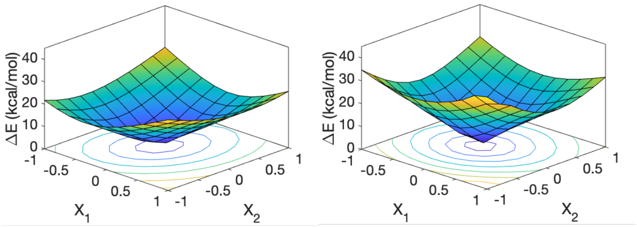

(b) OH-AB-OH
F_{NN} = 0.00 au

(e) OH-AB-O$^-$
F_{NN} = 0.00 au

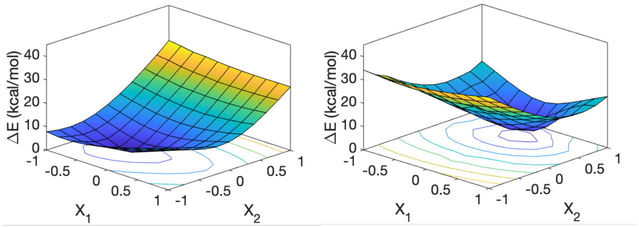

(c) OH-AB-OH
F_{NN} = -0.01 au

(f) OH-AB-O$^-$
F_{NN} = -0.01 au

Figure 3.15. Energy difference between the S_0 and S_1 potential energy surfaces in the branching space of protonated HO−AB−OH (a-c) and deprotonated HO−AB−O$^-$ (d-f) molecules with F_{NN} computed using CAS(10,8)/6-31+G(d).

from +0.5 to -0.3. The increase in the azo bond length is justified by the increased mesomeric resonance upon deprotonation reducing the double bond character of the azo group. The change in the position of S_0 minima upon deprotonation also leads to a substantial change in the location of the high-energy ridge and the rotation TS, which is at (0,-0.8). As a result, the rotation TS at (0,-0.8) is substantially lower in energy than the rotation TS at (0,+0.4) and explains the large decrease in rotation activation barrier upon deprotonation. On S_1, deprotonation increases the restoring force associated with displacement along the bond-length alternation coordinate. Examining the effect of F_{NN} on the branching space around the HO−AB−O$^-$ CI, positive fields provide a similar response to the protonated molecule, with the CI shifting to more positive X_2 indicating more single bond character of the azo bond (fig. 3.15d). Application of a negative field also shifts the position of the CI so that the azo bond has more single bond character, which is in contrast to the protonated molecules which are shifted towards more double-bond character.

Structure	Δ E (kcal mol^{-1})	
	HO−AB−OH	HO−AB−O$^-$
S_1 Trans	62.0	64.6
S_1 Rot Ts	50.2	40.2
S_1 Rot Inv Ts	63.6	73.6
S_1 Inv Ts	70.1	74.1
S_1 Cis	74.9	76.8
S_2 Trans	78.6	64.7
S_2 Rot Ts	114.1	85.2
S_2 Rot Inv Ts	108.1	96.4
S_2 Inv Ts	113.7	96.3
S_2 Cis	106.5	82.7

Table 3.2. Relative energies in kcal mol^{-1} of S_1 and S_2 excitation energies from the optimized S_0 stationary points of anti HO−AB−OH, syn HO−AB−OH, and HO−AB−O$^-$ under field-free conditions computed with B3LYP/6-311+G(d). HO−AB−OH energies are shown relative to HO−AB−OH S_0 *trans* structure for protonated species and to the HO−AB−O$^-$ S_0 *trans* structure for the deprotonated species.

3.3.3.2.2 Relative energies of S_0, S_1 and S_2 Field-Free Potential Energy Surfaces Before discussing the effect of the applied OEEFs on the photochemical pathways, we first summarize the field-free response of the S_1 and S_2 surfaces. The S_1 state is characterized by a $n \rightarrow \pi^*$ transition from the azo nonbonding orbital to the phenyl π^* orbital, while the S_2 state is characterized by a $\pi \rightarrow \pi^*$ transition. The reason for investigating the S_2 surface is that in unsubstituted azobenzenes, excitation to S_2 subsequently decays to S_1 via inversion of one of the phenyl rings, reminiscent of the thermal inversion pathway (121). As the photochemical pathways involves the same coordinates as the thermal pathways, an understanding of the effect of deprotonation and applied electric fields on the photoisomerization mechanisms can be determined from the vertical excitation energies of ground state geometries (114). The energies of the S_1 and S_2 surfaces at the S_0 HO−AB−OH and HO−AB−O$^-$ geometries, energies are relative to their respective S_0 *trans* structure, are summarized in table 3.2. Deprotonation increases the energy of S_1 surface relative to the S_0 *trans* minimum in comparison to the protonated structure, except for at the S_0 rotation TS geometry. For the S_2 surface, deprotonation substantially decreases the energy due to the mesomeric effect reducing the energy gap between π and π^* orbitals by increasing the single bond character of the azo bond.

Examining the energy gaps between electronic states for the HO−AB−OH molecules, the smallest $S_0 \rightarrow S_1$ energy gap is at the S_0 rotation TS geometry at 4.93 kcal mol^{-1}, owing to the close proximity of the S_1/S_0 CI. As the HO−AB−OH rotation TS is geometrically close to the S_1/S_0 CI, it can be used it determine the field-response of the rotation photoisomerization pathway. The HO−AB−OH S_0 rotation-inversion TS and S_0 inversion TS vertical excitation energies to S_1 are 19.4 and 23.3 kcal mol^{-1}

respectively. All HO−AB−OH S_0 TS structures have a relatively large $S_1 \rightarrow S_2$ vertical excitation energy (43.58 kcal mol^{-1} for the inversion pathway, 44.5 kcal mol^{-1} for the rotation inversion pathway, and 64.0 kcal mol^{-1} for the rotation pathway) indicating the presence of a CI between S_1 and S_2 along the inversion pathway is unlikely. In terms of relative $S_0 \rightarrow S_1$ and $S_1 \rightarrow S_2$ energy gaps for the deprotonated species, deprotonation increases the $S_0 \rightarrow S_1$ energy gap (32.5 kcal mol^{-1} for the inversion pathway, 31.7 kcal mol^{-1} for the rotation inversion pathway, and 10.3 kcal mol^{-1} for the rotation pathway) but decreases the $S_1 \rightarrow S_2$ energy gap (22.2 kcal mol^{-1} for the inversion pathway, 22.9 kcal mol^{-1} for the rotation inversion pathway, and 45.0 kcal mol^{-1} for the rotation pathway) as a result of the how mesomeric donation impacts the different electronic states.

3.3.3.2.3 Electric Field Modification of Nonadiabatic Decay Mechanisms

In order to understand how applied OEEFs can be used to modify the energy gaps between electronic states along each isomerization pathway, fig. 3.16 illustrates the vertical excitation energy at each S_0 TS geometry between S_0 and S_1 (panels a-d) and S_1 and S_2 (panels e-h). The effect of F_{NN} on the HO−AB−OH $S_0 \rightarrow S_1$ energy gap is shown in fig. 3.16a. The energy gap at the rotation TS (red circles) decreases with both field directions for HO−AB−OH, to the extent that the $n \rightarrow \pi^*$ transition energy is negative at -10.0×10^{-3} a.u. At the rotation-inversion TS geometry (blue triangles), positive fields increase the $S_0 \rightarrow S_1$ energy gap while negative fields decrease the $S_0 \rightarrow S_1$ energy gap. However, the inversion TS (black squares) demonstrates inverse behavior in which the negative fields increase and positive fields decrease the $S_0 \rightarrow S_1$ energy gap, although with lower field-sensitivity than at the rotation-inversion TS. Although the rotation-inversion $S_0 \rightarrow S_1$ energy gap can be significantly reduced using negative F_{NN}, it remains large at 9.3 kcal mol^{-1}, while the inversion TS $S_0 \rightarrow S_1$ vertical energy gap also remains large (22 kcal mol^{-1}). As a result, it is not possible to use F_{NN} to control nonadiabatic decay between S_0 and S_1 along either the inversion or rotation-inversion pathways. The F_{OC} field induces a similar $S_0 \rightarrow S_1$ change to F_{NN} (fig. 3.16b).

Upon deprotonation, a very different field response is observed, although F_{NN} and F_{OC} are again observed to be very similar (figs. 3.16c and 3.16d). Deprotonation increases the energy gap at the rotation TS under field-free conditions, but by applying a $+1.0 \times 10^{-3}$ a.u. field, a nonadiabatic decay process between S_0 and S_1 can be induced along the rotation pathway. This response appears to contradict the energy difference plot in fig. 3.15d which shows the CI moves away from the lowest energy TS in the branching space. However, as shown in fig. 3.23a, application of positive fields to the deprotonated molecule significantly changes the S_0 topology in the branching space such that the TS at positive X_2 is lowest in energy, explaining the observed field effect on the rotation pathway. For the inversion and rotation-inversion pathways, the field response of the S_0/S_1 energy gap in the deprotonated molecule is essentially the same. Positive fields have very little effect on the energy gap, which remains similar to the field-free value of 31.2 kcal mol^{-1} for the rotation-inversion barrier and 32.0 kcal mol^{-1} for the inversion TS. Only larger negative fields have a significant effect on

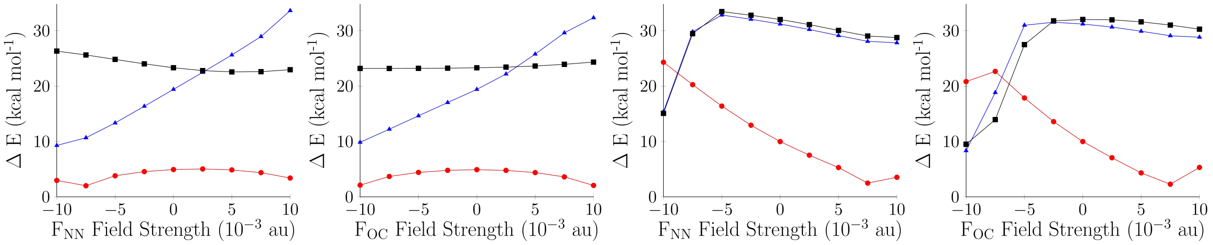

(a) S_0/S_1 HO-AB-OH F_{NN} (b) S_0/S_1 HO-AB-OH F_{OC} (c) S_0/S_1 HO-AB-O- F_{NN} (d) S_0/S_1 HO-AB-O- F_{OC}

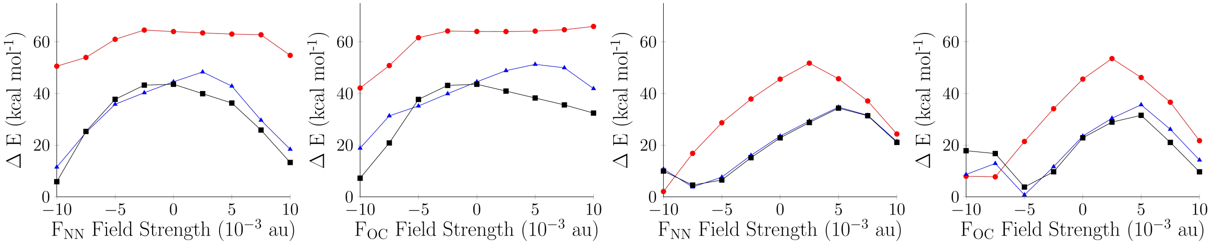

(e) S_1/S_2 HO-AB-OH F_{NN} (f) S_1/S_2 HO-AB-OH F_{OC} (g) S_1/S_2 HO-AB-O- F_{NN} (h) S_1/S_2 HO-AB-O- F_{OC}

Figure 3.16. HO−AB−OH and HO−AB−O$^-$ molecules relative energy gaps between S_0 and S_1 stationary points (a)HO−AB−OH with F_{NN}, (b) HO−AB−OH F_{OC}, (c) HO−AB−O$^-$ F_{NN}, and (d) HO−AB−O$^-$ F_{OC} and between S_1 and S_2 (e)HO−AB−OH with F_{NN}, (f) HO−AB−OH F_{OC}, (g) HO−AB−O$^-$ F_{NN}, and (h) HO−AB−O$^-$ F_{OC} for the rotation (red circles), rotation inversion (blue triangles), and inversion (black squares) for the three fields examined.

the S_0/S_1 energy gap, which at -1.0×10^{-3} a.u. decreases to 15.4 kcal mol^{-1} and 8.3 kcal mol^{-1} for the rotation-inversion pathway under F_{NN} and F_{OC} fields respectively, and to 15.1 kcal mol^{-1} and 9.5 kcal mol^{-1} for the inversion pathway under F_{NN} and F_{OC} fields respectively. As the lowest energy barriers observed for the deprotonated molecule are similar to the protonated molecule, the findings indicate that there is no nonadiabatic decay mechanism possible along the inversion or inversion-rotation pathway regardless of the protonation state.

Examining the S_1/S_2 energy gap, the F_{NN} field gives the same trends for the vertical excitation energy at all three S_0 TS structures, with large magnitude fields of either sign giving the smallest energy gap (fig. 3.16e). The S_1/S_2 energy gaps of the the HO−AB−OH molecule, at F_{NN} field magnitude of -10.0×10^{-3} a.u., is 10.96 kcal mol^{-1} at the rotation-inversion TS and 12.04 kcal mol^{-1} at the inversion TS. While these energy gaps are much lower than that of the field free gaps, which are 44.52 and 43.58 kcal mol^{-1} for the rotation inversion and inversion pathways respectively, they are still large enough to suggest that it is not possible to induce S_1/S_2 nonadiabatic decay using an applied electric field in the protonated molecule. Compared to the F_{NN} field response, the F_{OC} field induces a similar S_1/S_2 energy gap change (fig.3.16f). The effect of deprotonation on the S_1/S_2 energy gap is not as dramatic as for the S_0/S_1 energy, with the energy gap decreasing regardless of the field direction for all three isomerization pathways. However, with large negative F_{NN} or F_{OC}, it is possible to induce a nonadiabatic decay mechanism along all three isomerization pathways. For the inversion and rotation-inversion mechanisms, the nonadiabatic decay can be induced with -7.5×10^{-3} a.u. fields, while -10×10^{-3} a.u. is required to allow S_1/S_2 nonadibatic decay along the rotation pathway. In conclusion to this section, we have demonstrated that OEEFs can influence the energy gaps between electronic states that govern the photochemical reaction pathways. As a result, it is possible to control the possibility of S_1/S_2 nonadiabatic decay which plays an important role in the non-Kasha behavior observed in the photochemistry of azobenzene (85).

3.3.4 Conclusions

In this work, we examined the role of applied OEEF, deprotonation and photon absorption on the thermal and photo isomerization pathways of dihydroxyazobenzene. The protonated HO-AB-OH molecule was found to prefer thermal isomerization via the rotation-inversion pathway upon application of positive fields and the rotation pathway with negative fields. For the deprotonated molecule, thermal isomerization occurs via the rotation pathway with all fields except high positive fields, in which all three possible pathways are competitive. Our work demonstrates that it is possible to remove the *cis*-to-*trans* isomerization barrier through the combined action of deprotonation and applied OEEF. The finding that rapid *cis*-to-*trans* isomerization can be achieved on the ground state has application, not only for molecular switches, but for solar thermal batteries that utilize azobenzene, where *cis*-to-*trans* isomerization is required to recover energy from the charged device. Owing to the observed ability of OEEFs to tune the number of energetically viable isomerization pathways, we examined how the kinetics of thermal isomerization can be modified. Although half-lives could be reduced by up to 50%, there was no qualitative change in the reaction kinetics when considering the multiple viable pathways. However, although it was not observed in this system, the extent to which half-lives can be modified suggests that there may be other systems for which the electric field does not modify the kinetics by changing the barrier height of the lowest energy reaction pathway, but by lowering the barrier height of other pathways so that there are multiple energetically viable reaction pathways.

Considering the role of OEEFs and deprotonation on the excited state behavior, this work also demonstrated the S_0/S_1 and S_1/S_2 nonadiabatic decay mechanisms could be controlled. First, the branching space of the S_1/S_0 CI in HO−AB−OH could be modified by a positive field such that the minimum energy point on the seam was displaced towards the *cis* minimum. As a result, we hypothesized that an electric field could be used to shift the photodynamic equilibrium towards the *cis* minimum. From a device-design perspective, shifting the photodynamic equilibrium is useful for selectively populating the *cis* minimum via excitation to S_1 while avoiding the reverse photoisomerization caused by overlapping absorption bands of *cis* and *trans* minima. Examination of the energy gaps between the three lowest energy singlet states along each of the thermal isomerization pathways was used to establish whether electric fields could be used to induce or inhibit nonadiabatic decay mechanisms. In the protonated molecule, it was not possible to change the qualitative field-free behavior of the S_0/S_1 energy gap, with the rotation pathway always giving a small energy gap and the inversion and rotation-inversion pathways always giving an large energy gap, indicating that there was a state crossing in the vicinity of the rotation pathway only. However, deprotonation increased the S_0/S_1 energy gaps along all isomerization pathways and this effect could be enhanced by applying negative fields, while positive fields could be used to induce nonadiabatic decay along the rotation pathway. The S_1/S_2 energy gap is large for both the protonated and deprotonated molecules under field-free conditions. Application of either field sign was found to significantly decrease the S_1/S_2 energy gap, but only when the molecule was deprotonated and a negative field was used did the gap decrease to the extent that it indicated the possibility of a nonadiabatic decay mechanism along all three isomerization pathways. Overall, we established that OEEFs and protonation state can be used in concert to achieve large changes in thermal and photo-isomerization behavior which are valuable in the design of molecular-scale devices.

Overall Conclusions

Overall, through our investigations of azobenzene with both CASSCF and TD-DFT methodologies interesting behavior was observed with applied electric fields. To continue this work we wanted to examine larger systems like bis-azobeznenes, where two azobenzene units are bonded covalently at the para position. Bis-azobenzenes are of interest because these types of molecules can enhance the photoreactivity of an azobenzene molecule by up to twice the amount of a single azobenzene. However, these molecules have not been able to be studied computationally due to the computational cost of multireference methods and/or the inability to describe the full PES with DFT methodologies. In our first examination of azobenzene an AS of 10 electrons in 8 orbitals was utilized with the CASSCF methodology. If the same orbitals were utilized for a CASSCF calculation of bis-azobenzenes, the AS would be twice the size, consisting of 20 electrons and 16 orbitals. Single reference methods, like DFT, could be used for studying this molecule however, these methods fail to describe the entire PES especially around points of degeneracy and as our studies concluded above. For azobenzene systems, one of the most important interesting points of the PES is the CI, which is, in itself, a point of degeneracy between electronic states, which cannot be described by single reference methods. Overall, new methodologies, like the utilization of SCF solutions for excited states, are needed for describing systems like azobenzene efficiently and accurately.

The utilization of SCF solutions for studying excited states have many advantages, like the capturing of orbital relaxation effects which are often missed in methods like CIS and TD-DFT. SCF solution methodologies can also be easily parallelized allowing for utilization with larger molecules without computational cost. Generally, SCF solutions can be described as a single determinantal wavefunction that is optimized to describe particular electronic configurations. SCF solutions can be employed in a variety of ways however, the two methods in which SCF solutions will be utilized for examining excited states in the following chapters are with difference self-consistent field (ΔSCF) and NOCI methodologies.

3.5.0.1 Structural parameters, relative energies and dipole moments under field-free conditions

Structure	Distance (Å)		Angle (degrees)			ΔE (kcal mol^{-1})	Dipole Moment (D)
	r(NN)	r(CN)	CNN	CNNC	NNCC		
S_0(trans)	1.24	1.43	115.0	-179.9	179.9	0.00	0.00
S_0(rot ts)	1.35	1.40	115.8	-89.5	176.8	59.02	2.89
S_0(inv ts)	1.22	1.45	116.7	-90.0	178.5	47.90	2.41
S_0(cis)	1.24	1.44	122.9	-4.1	126.0	15.12	3.42
S_1(trans)	1.26	1.38	127.3	-179.9	179.9	69.36	0.00
S_0/S_1CI_{rot}	1.28	1.38	131.1	-92.1	173.7	64.26	2.28
S_1(cis)	1.24	1.39	139.1	-1.1	152.2	87.10	1.95

Table 3.3. Structural parameters, relative energies in kcal mol^{-1}, and dipole moments in Debeye of optimized S_0 and S_1 stationary points of azobenzene under field-free conditions computed with CAS(10,8)/6-31G(d). Energies are shown relative to $S_0(C_{2h})$.

3.5.0.2 Relative energies under applied F_{dip}

Structure	F_{dip} field (10^{-3} a.u.)								
	10.0	7.5	5.0	2.5	0.0	-2.5	-5.0	-7.5	-10.0
S_0(trans)	-3.27	-2.09	-1.25	-0.17	0.00	-0.17	-1.25	-2.07	-3.70
S_0(rot ts)	58.61	58.16	57.31	56.01	59.02	57.04	54.68	51.93	48.77
S_0(inv ts)	49.55	50.28	50.34	49.77	47.85	46.77	44.34	41.25	37.49
S_0(cis)	19.97	19.4	18.45	17.01	15.12	12.78	9.98	6.72	2.96
S_1(trans)	66.03	67.49	68.53	69.16	69.36	69.16	68.53	67.49	66.03
S_0/S_1CI_{rot}	68.04	67.62	66.79	65.61	63.89	62.34	60.21	57.46	54.11
S_1(cis)	77.61	78.74	88.45	88.04	87.10	85.64	83.66	81.17	78.11

Table 3.4. Relative energies in kcal mol^{-1} of optimized S_0 and S_1 stationary points of azobenzene under F_{dip} field computed using CAS(10,8)/6-31G(d). Energies are shown relative to zero-field $S_0(C_{2h})$.

3.5.0.3 Relative energies under applied F_{azo}

Structure	F_{azo} field (10^{-3} a.u.)								
	10.0	7.5	5.0	2.5	0.0	-2.5	-5.0	-7.5	-10.0
S_0(trans)	-6.09	-3.68	-1.96	-0.92	0.00	-0.92	-1.96	-3.68	-6.09
S_0(rot ts)	53.71	56.04	57.70	58.69	59.02	58.68	57.69	56.03	53.71
S_0(inv ts)	38.57	42.48	45.43	47.46	47.85	48.80	48.16	46.64	43.87
S_0(cis)	10.35	12.48	13.96	14.84	15.12	14.83	13.96	12.48	10.36
S_1(trans)	63.10	65.85	67.80	68.97	69.36	68.97	67.80	65.85	63.10
S_0/S_1CI_{rot}	60.22	62.28	63.62	64.22	63.89	63.30	62.62	59.98	57.23
S_1(cis)	71.36	75.52	78.66	80.80	87.10	80.81	78.66	75.53	71.37

Table 3.5. Relative energies in kcal mol^{-1} of optimized S_0 and S_1 stationary points of azobenzene under F_{azo} field computed using CAS(10,8)/6-31G(d). Energies are shown relative to zero-field $S_0(C_{2h})$.

3.5.0.4 Relative energies under applied F_{phe}

Structure	F_{phe} field (10^{-3} a.u.)								
	10.0	7.5	5.0	2.5	0.0	-2.5	-5.0	-7.5	-10.0
S_0(trans)	-7.48	-4.44	-2.29	-1.01	0.00	-1.01	-2.29	-4.44	-7.48
S_0(rot ts)	58.87	59.75	60.09	59.83	59.02	60.98	55.70	53.22	50.21
S_0(inv ts)	49.14	50.03	50.21	49.72	47.85	46.76	44.27	41.09	37.19
S_0(cis)	17.74	17.86	17.34	16.54	15.12	13.21	10.80	7.89	4.47
S_1(trans)	61.58	65.01	67.44	68.88	69.36	68.88	67.44	65.01	55.90
S_0/S_1CI_{rot}	65.77	66.15	66.02	65.32	63.89	62.38	60.27	57.52	54.15
S_1(cis)	75.53	78.44	80.47	81.63	87.10	85.86	83.21	79.85	75.72

Table 3.6. Relative energies in kcal mol^{-1} of optimized S_0 and S_1 stationary points of azobenzene under F_{phe} field computed using CAS(10,8)/6-31G(d). Energies are shown relative to zero-field $S_0(C_{2h})$.

3.5.1 Potential energy surfaces at different field sizes and orientations

3.5.1.1 Full results of potential energy surface electric fields response

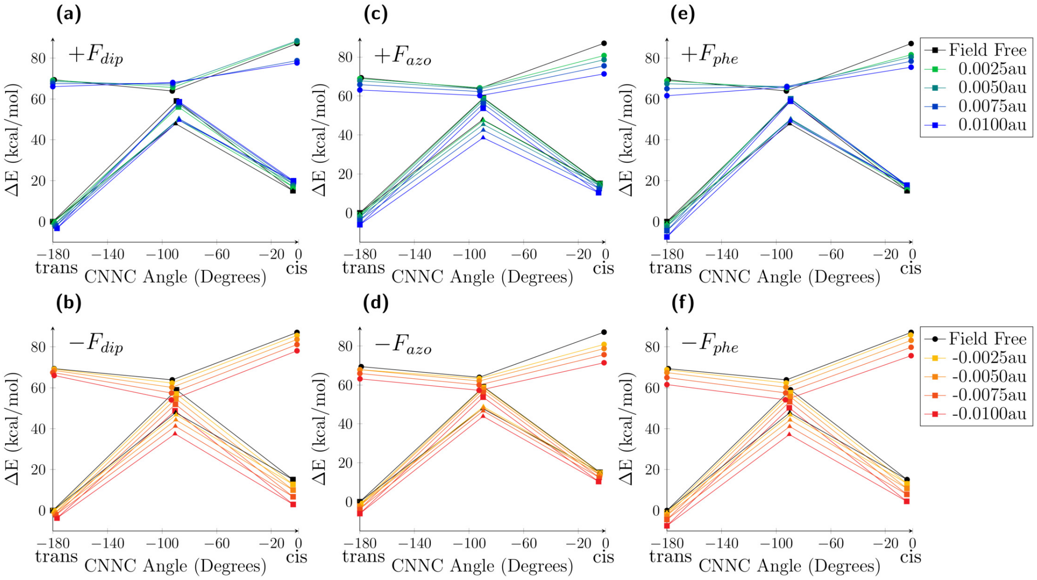

Figure 3.17. Effect of all orientated external electric fields applied to photo and thermal isomerization pathways of azobenzene (see legend for colors identifying field strength). Panels a, c and e (top row) shows positive fields and panels b, d and f (bottom row) shows negative fields. Panels a and b (first column) shows F_{dip}, panels c and d (middle column) shows F_{azo} and panels e and f (right column) shows F_{phe} (△ – S_0 inversion pathway, □ – S_0 rotation pathway, ○ – S_1 rotation pathway). Energies are shown with respect to the field-free C_{2h} structure.

3.5.2 Projected dipole moments on field axes

The change in the topology of the potential energy surface under an applied field can be rationalized in terms of a dipole-dipole interaction. Considering that the energy of point 1 on the potential energy surface is

$$E_1 = E_1^0 - \mathbf{F}.\boldsymbol{\mu}_1 \tag{3.5.1}$$

and the energy of point 2 on the potential energy surface is

$$E_2 = E_2^0 - \mathbf{F}.\boldsymbol{\mu}_2 \tag{3.5.2}$$

where $\mathbf{F}$ is the applied electric field vector, $\boldsymbol{\mu}$ is the molecular dipole vector, E^0 is the energy under field free conditions, and E is the total energy. Subtracting these two equations gives an expression for the energy difference as a result of an applied electric field

$$\Delta E = \Delta E^0 - \mathbf{F}.\Delta\boldsymbol{\mu} \tag{3.5.3}$$

so that the projection of the difference dipole on the axis of the applied field $|P(\boldsymbol{\mu}_1 - \boldsymbol{\mu}_2)|$ defines the energy change when the field is applied. According to eq. 3.5.3 the change in the energy between two points on the potential energy surface should be linear with respect to the size of the applied field. However, such an expression does not take account of changes to the electronic structure or geometry in response to the applied field. The following figures show the projection of the difference dipole moment on the three different field axis and so demonstrate how a field applied along one of the axes studied is able to modify the potential energy surface of the S_0 surface, up to the approximations just outlined.

3.5.2.1 Projection of dipole moments on F_{dip} electric field

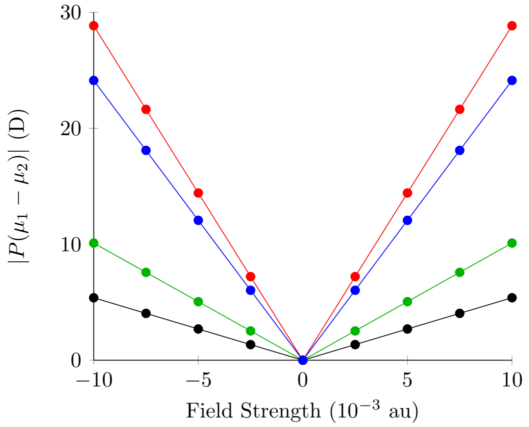

Figure 3.18. Projection of the S_0 cis/trans minimum to rotation/inversion transition structure field-free difference dipole moment on the F_{dip} axis (cis/rotation TS – black, cis/inversion TS – green, trans/rotation TS – red, trans/inversion TS – blue)

3.5.2.2 Projection of dipole moments on F_{azo} electric field

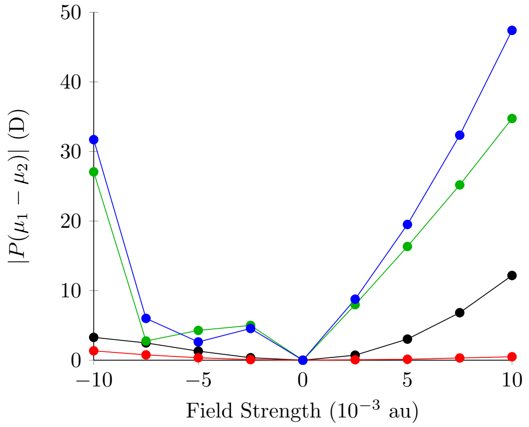

Figure 3.19. Projection of the S_0 cis/trans minimum to rotation/inversion transition structure field-free difference dipole moment on the F_{azo} axis (cis/rotation TS – black, cis/inversion TS – green, trans/rotation TS – red, trans/inversion TS – blue)

3.5.2.3 Projection of dipole moments on F_{phe} electric field

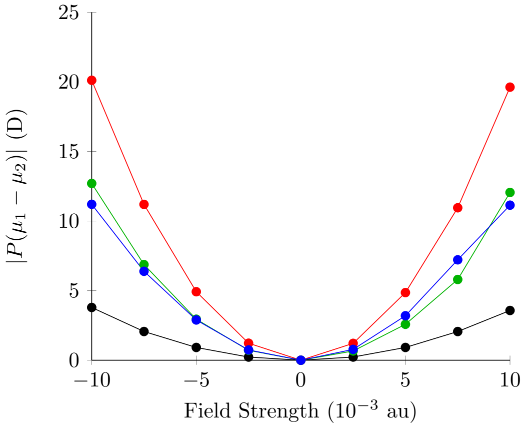

Figure 3.20. Projection of the S_0 cis/trans minimum to rotation/inversion transition structure field-free difference dipole moment on the F_{phe} axis (cis/rotation TS – black, cis/inversion TS – green, trans/rotation TS – red, trans/inversion TS – blue)

SUPPORTING DOCUMENTS – ELECTRIC FIELD CONTROL OF MULTISTATE PROCESSES SUBSTITUTED (DI-HYDROXY) AZOBENZENE

3.6.1 Thermal Isomerization Pathways of 4,4'-dihyroxyazobenzene

3.6.1.1 Electric Field Modification of the Ground State Potential Energy Surface of HO−AB−OH

Structure	F_{NN} field (10^{-3} a.u.)								
	-10.0	-7.5	-5.0	-2.5	0.0	2.5	5.0	7.5	10.0
S_0 trans	-1.78	0.18	1.12	1.06	0.00	-2.05	-5.10	-9.15	-14.23
S_0 rot ts	32.99	42.71	45.13	45.93	45.22	43.00	39.27	34.01	27.19
S_0 rot inv ts	42.45	45.18	46.24	45.89	44.21	41.19	36.80	31.00	23.59
S_0 inv ts	32.36	38.32	42.66	45.47	46.78	46.60	44.90	41.60	36.65
S_0 cis	12.58	15.52	17.21	17.71	17.05	15.23	12.23	8.02	2.54

Table 3.7. Relative energies in kcal mol^{-1} of optimized S_0 stationary points of ceHO-AB-OH under F_{NN} field computed using B3LYP. Energies are shown relative to the zero-field S_0 trans.

Structure	F_{OC} field (10^{-3} a.u.)								
	-10.0	-7.5	-5.0	-2.5	0.0	2.5	5.0	7.5	10.0
S_0 trans	-13.48	-7.51	-3.34	-0.86	0.00	-0.75	-3.11	-7.17	-13.03
S_0 rot ts	38.68	42.66	45.03	45.88	45.22	43.02	39.24	33.82	26.70
S_0 rot inv ts	43.23	45.22	46.05	45.72	44.21	41.34	36.99	30.84	23.38
S_0 inv ts	40.91	44.23	46.31	47.16	46.79	45.17	42.26	38.01	32.34
S_0 cis	17.92	19.11	19.35	18.67	17.05	14.50	11.01	6.55	1.11

Table 3.8. Relative energies in kcal mol^{-1} of optimized S_0 stationary points of ceHO-AB-OH under F_{OC} field computed using B3LYP. Energies are shown relative to the zero-field S_0 trans.

Structure	Field Strength (10^{-3} a.u.)								
	-10.0	-7.5	-5.0	-2.5	0.0	2.5	5.0	7.5	10.0
F_{NN} S_0 rot ts	20.56	26.90	27.96	28.44	28.46	28.05	27.26	26.11	24.59
F_{NN} S_0 rot inv ts	28.60	28.14	27.70	27.02	26.05	23.38	22.39	20.78	18.39
F_{NN} S_0 inv ts	18.78	21.50	25.40	27.64	29.51	31.02	32.14	32.88	33.18
F_{OC} S_0 rot ts	20.20	23.24	25.80	27.49	28.46	28.78	28.43	27.36	25.45
F_{OC} S_0 rot inv ts	23.92	24.86	25.63	26.12	26.05	23.70	23.47	21.38	21.12
F_{OC} S_0 inv ts	22.85	24.95	26.78	28.31	29.51	30.35	30.84	30.93	30.56

Table 3.9. ceHO-AB-OH molecules ΔG relative barrier heights from the S_0 cis structure in kcal mol^{-1} for the three transition states examined in all two electric fields.

3.6.1.2 Electric Field Modification of the Ground State Potential Energy Surface of HO−AB−O^{-}

Structure	F_{NN} field (10^{-3} a.u.)								
	-10.0	-7.5	-5.0	-2.5	0.0	2.5	5.0	7.5	10.0
S_0 trans	3.27	4.42	4.25	2.77	0.00	-4.05	-9.35	-15.91	-23.70
S_0 rot ts	23.55	27.07	29.32	30.28	29.89	28.09	24.81	19.92	13.29
S_0 rot inv ts	46.24	48.03	47.85	45.78	41.89	36.22	28.79	19.61	8.55
S_0 inv ts	46.29	48.05	47.79	45.61	41.58	35.75	28.14	18.74	7.43
S_0 cis	24.34	25.08	24.10	21.40	17.02	10.95	3.24	-6.10	-17.14

Table 3.10. Relative energies in kcal mol^{-1} of optimized S_0 stationary points of HO−AB−O^{-} under F_{NN} field computed using B3LYP. Energies are shown relative to the zero-field S_0 trans.

Structure	F_{OC} field (10^{-3} a.u.)								
	-10.0	-7.5	-5.0	-2.5	0.0	2.5	5.0	7.5	10.0
S_0 trans	10.09	11.17	9.82	6.08	0.00	-8.37	-18.95	-31.69	-46.54
S_0 rot ts	24.19	27.88	30.07	30.77	29.89	27.33	22.93	16.46	7.69
S_0 rot inv ts	49.27	50.66	49.75	46.79	41.89	35.11	26.47	15.96	3.49
S_0 inv ts	50.33	51.09	49.48	46.28	41.58	35.44	27.83	18.71	8.01
S_0 cis	24.55	24.44	23.13	20.65	17.02	12.24	6.32	-0.75	-9.02

Table 3.11. Relative energies in kcal mol^{-1} of optimized S_0 stationary points of HO$-$AB$-$O$^-$ under F_{OC} field computed using B3LYP. Energies are shown relative to the zero-field S_0 trans.

Structure	Field Strength (10^{-3} a.u.)								
	-10.0	-7.5	-5.0	-2.5	0.0	2.5	5.0	7.5	10.0
F_{NN} S_0 rot ts	-1.52	1.10	4.18	7.64	11.31	15.97	20.41	24.89	29.45
F_{NN} S_0 rot inv ts	20.52	21.61	22.45	23.13	23.71	24.14	24.38	24.51	24.46
F_{NN} S_0 inv ts	20.63	21.70	22.47	23.04	23.49	23.76	23.82	23.71	23.38
F_{OC} S_0 rot ts	-1.46	2.41	5.95	9.05	11.31	13.86	15.53	16.33	16.28
F_{OC} S_0 rot inv ts	22.96	24.66	25.24	24.90	23.71	21.68	18.90	15.38	11.19
F_{OC} S_0 inv ts	24.32	25.09	25.05	24.49	23.49	22.16	20.41	18.22	15.60

Table 3.12. HO−AB−O$^-$ molecules ΔG relative barrier heights from the S_0 cis structure in kcal mol^{-1} for the three transition states examined in all two electric fields.

3.6.2 Photoisomerization Pathways of 4,4'-dihydroxyazobenzene

3.6.2.1 Electric Field Modification of Excited State Potential Energy Surfaces of HO−AB−OH

Structure	F_{NN} field (10^{-3} a.u.)								
	-10.0	-7.5	-5.0	-2.5	0.0	2.5	5.0	7.5	10.0
S_1 trans	59.72	61.91	63.02	63.06	62.03	59.94	56.79	52.57	47.25
S_1 rot ts	35.96	44.72	48.93	50.49	50.15	48.04	44.14	38.38	30.59
S_1 rot inv ts	51.74	55.86	59.58	62.25	63.62	63.67	62.43	59.95	57.23
S_1 inv ts	58.68	63.94	67.48	69.49	70.10	69.40	67.47	64.21	59.61
S_1 cis	70.84	73.83	75.33	75.65	74.85	72.98	70.03	65.94	60.62
S_2 trans	59.14	75.78	78.21	79.17	78.51	76.19	72.26	66.88	60.16
S_2 rot ts	86.52	98.67	109.91	115.03	114.12	111.48	107.14	101.11	85.34
S_2 rot inv ts	63.23	80.77	95.41	102.54	108.14	112.01	105.27	89.59	75.63
S_2 inv ts	64.56	89.25	105.23	112.73	113.68	109.33	103.77	90.06	72.92
S_2 cis	71.79	89.15	102.19	105.61	106.53	103.16	97.48	89.64	78.21

Table 3.13. Relative energies in kcal mol^{-1} of S_1 and S_2 transition energies from the relative S_0 stationary points of HO−AB−OH under F_{NN} field computed using TD-B3LYP. Energies are shown relative to the zero-field S_0 trans.

Structure	F_{OC} field (10^{-3} a.u.)								
	-10.0	-7.5	-5.0	-2.5	0.0	2.5	5.0	7.5	10.0
S_1 trans	39.97	53.52	58.29	61.09	62.03	61.14	58.40	53.71	39.39
S_1 rot ts	40.79	46.34	49.45	50.67	50.13	47.80	43.62	37.43	28.77
S_1 rot inv ts	53.08	57.44	60.68	62.75	63.62	63.52	62.77	60.46	55.72
S_1 inv ts	64.10	67.42	69.52	70.40	70.10	68.60	65.90	61.95	56.68
S_1 cis	75.79	76.97	77.19	76.47	74.85	72.33	68.92	64.61	59.35
S_2 trans	46.70	63.38	71.80	76.64	78.51	76.99	72.47	62.90	46.99
S_2 rot ts	86.62	99.37	111.05	114.84	114.13	111.77	107.77	102.11	94.72
S_2 rot inv ts	67.29	84.45	95.83	102.66	108.13	112.36	114.05	110.42	97.61
S_2 inv ts	77.46	94.47	107.22	113.53	113.68	109.53	104.15	97.53	89.10
S_2 cis	86.42	98.60	106.55	108.36	106.53	102.35	96.71	90.22	82.98

Table 3.14. Relative energies in kcal mol^{-1} of S_1 and S_2 transition energies from the relative S_0 stationary points of HO−AB−OH under F_{OC} field computed using TD-B3LYP. Energies are shown relative to the zero-field S_0 trans.

3.6.2.2 Electric Field Modification of Excited State Potential Energy Surfaces of HO−AB−O$^-$

Structure	F_{NN} field (10^{-3} a.u.)								
	-10.0	-7.5	-5.0	-2.5	0.0	2.5	5.0	7.5	10.0
S_1 trans	34.11	48.23	57.62	62.39	64.49	60.75	55.74	49.39	31.66
S_1 rot ts	47.86	47.33	45.71	43.21	39.87	35.62	30.10	22.39	16.83
S_1 rot inv ts	61.65	77.85	80.69	77.85	73.10	66.44	57.92	47.70	36.38
S_1 inv ts	61.36	77.52	81.25	78.41	73.61	66.86	58.19	47.79	36.20
S_1 cis	51.09	62.88	71.45	77.63	75.24	69.73	61.76	51.52	39.23
S_2 trans	45.79	54.32	64.22	66.91	64.96	63.00	58.43	49.47	41.80
S_2 rot ts	49.91	64.15	74.38	81.09	85.44	87.36	75.80	59.50	41.15
S_2 rot inv ts	72.41	81.65	88.31	93.91	96.62	95.79	92.65	79.25	57.81
S_2 inv ts	71.33	82.07	87.76	93.57	96.45	95.62	92.52	79.19	57.28
S_2 cis	58.16	70.88	78.81	78.82	83.34	85.04	81.18	62.54	40.70

Table 3.15. Relative energies in kcal mol^{-1} of S_1 and S_2 transition energies from the relative S_0 stationary points of deprotonated HO−AB−O$^-$ under F_{NN} field computed using TD-B3LYP. Energies are shown relative to the zero-field S_0 trans.

Structure	F_{OC} field (10^{-3} a.u.)								
	-10.0	-7.5	-5.0	-2.5	0.0	2.5	5.0	7.5	10.0
S_1 trans	16.82	31.86	44.86	55.88	64.51	56.16	45.40	32.27	16.86
S_1 rot ts	45.00	50.53	47.94	44.35	39.88	34.40	27.25	18.75	13.00
S_1 rot inv ts	57.61	69.50	80.75	78.33	73.11	65.78	56.38	45.06	32.32
S_1 inv ts	59.82	65.05	76.98	78.06	73.62	67.41	59.43	49.73	38.29
S_1 cis	43.09	54.41	65.02	74.66	75.26	71.46	65.88	58.50	47.11
S_2 trans	40.31	57.46	70.44	70.11	64.98	59.10	49.58	37.83	19.66
S_2 rot ts	52.97	58.29	69.36	78.47	85.44	87.92	73.45	55.37	34.74
S_2 rot inv ts	66.26	82.41	81.50	89.99	96.62	96.20	92.01	71.19	46.55
S_2 inv ts	77.68	81.81	80.76	87.77	96.48	96.33	90.99	70.79	47.97
S_2 cis	68.63	76.49	77.87	77.52	83.34	85.35	82.51	66.08	49.51

Table 3.16. Relative energies in kcal mol^{-1} of S_1 and S_2 transition energies from the relative S_0 stationary points of deprotonated HO$-$AB$-$O$^-$ under F_{OC} field computed using TD-B3LYP. Energies are shown relative to the zero-field S_0 trans.

3.6.2.3 S_0/S_1 Branching Space Normal Modes

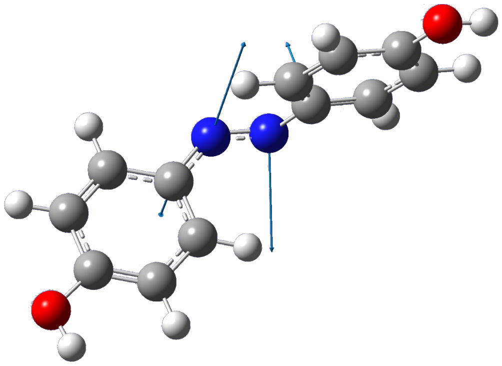

(a) Gradient Difference X_1

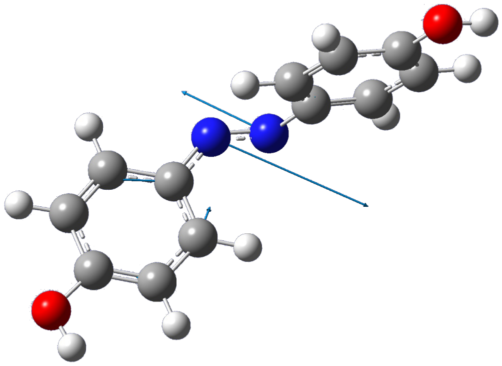

(b) Derivative Coupling X_2

Figure 3.21. Gradient difference (a) and derivative coupling (b) vectors that define the branching space of the anti and syn protonated derivatives of AB around the S_0/S_1 CI computed using CAS(10,8)/6-31+G(d)

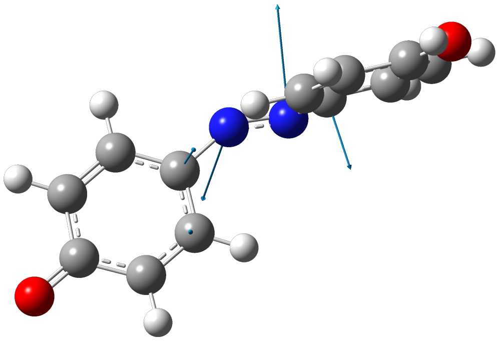

(a) Gradient Difference X_1

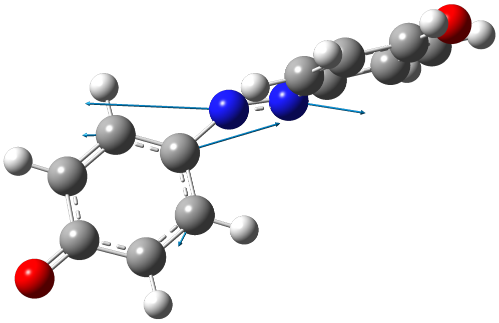

(b) Derivative Coupling X_2

Figure 3.22. Gradient difference (a) and derivative coupling (b) vectors that define the branching space of the anti and syn deprotonated derivatives of AB around the S_0/S_1 CI computed using CAS(10,8)/6-31+G(d).

3.6.2.4 Potential Energy Surfaces of Deprotonated Molecule Under Applied Field

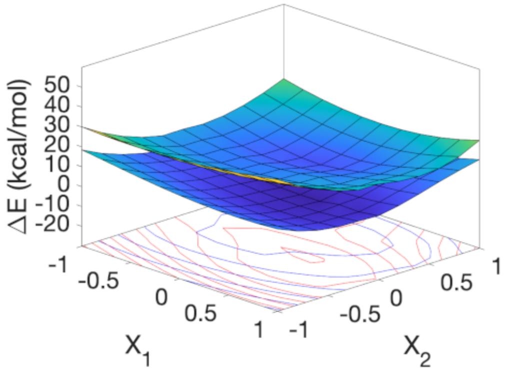

(a) OH-AB-O$^-$ F_{NN} = + 0.01 au

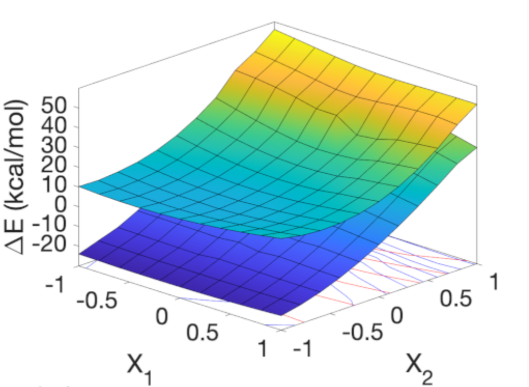

(b) OH-AB-O$^-$ F_{NN} = - 0.01 au

Figure 3.23. S_0 and S_1 potential energy surfaces of HO−AB−O$^-$ under F_{NN} field in the S_0/S_1 branching space. The difference between potential energy surfaces are shown in fig. 3.15.

CHAPTER 4

SYMMETRY BREAKING AND PROJECTION METHODS FOR EXCITED STATES

Introduction

[1,2] Excited-state methodologies can be broadly divided into two categories – multireference approaches based on the explicit construction of the wavefunction (122) and single-reference response-based approaches (123), both of which were demonstrated in chapter 3. Alternatively, ΔSCF based models are a third approach in which electronic states of interest are individually optimized. However, due to the individual optimization the treatment of correlation is not equivalent in ground and excited states.

The most widely used approaches for recovering dynamic correlation are DFT and second-order Møller-Plesset theory (MP2). The unification of the two approaches proposed by Grimme resulted in the formulation of double-hybrid density functional theory (DH-DFT) (124; 125), which was found to give improved results over hybrid DFT in ground-state calculations. Inclusion of MP2 correlation has the advantage that it can be obtained noniteratively, although it requires integral transformation to the MO basis and so scales as $\mathcal{O}(N^5)$. Extension of DH-DFT to the study of excited states has been reported via linear response (LR) on the underlying hybrid functional followed by an additive perturbative correction (126; 127; 128; 129; 130; 131; 132). However, because DH-DFT recovers a very limited amount of strong correlation, a naïve application to compute excited state energies through a difference double-hybrid density functional theory (ΔDH-DFT) approach is likely to give poor results. Despite the apparent limitations of DH-DFT, the nature of excited electronic states with singly-occupied MOs suggests that symmetry breaking of the reference SCF solution will be common, and that remaining strong correlation can be recovered by subsequent symmetry restoration. Spin-symmetry restoration has experienced a significant amount of recent interest, with the projected HF work of Scuseria and coworkers (133; 134) based on the Wheeler-Hill coordinate generator method (135; 136; 137; 138; 139) providing the basis for a number of subsequent developments, including projected MP2 method (140).

---

[1] Reprinted from Kempfer-Robertson, E. M., Pike, T. D. & Thompson, L. M. Difference projection-after-variation double-hybrid density functional theory applied to the calculation of vertical excitation energies. J Chem Phys 153, 074103 (2020), with the permission of AIP Publishing.

[2] Adapted with permission from Kempfer-Robertson, E. M., Haase, M. N., Bersson, J. S., Avdic, I. & Thompson, L. M. Role of Exact Exchange in Difference Projected Double-Hybrid Density Functional Theory for Treatment of Local, Charge Transfer, and Rydberg Excitations. J Phys Chem 126, 8058–8069 (2022). Copyright 2022 American Chemical Society.

Although focus in recent years has been on variational optimization of orbitals after projection, a noniterative projection on top of the variationally optimized wavefunction is easier to implement, has a much smaller computational prefactor, and does not affect iterative convergence behavior. Additionally, projection-after-variation (PAV) recovers only strong correlation, and so permits separation of correlation types. When used in combination with perturbation theory, PAV has been shown to give good quality PESs, free from the distortions and spurious minima present when projection is applied to a mean-field wavefunction (141; 142; 143; 144). In this work, we test the performance of ΔPAV-DH-DFT as a method for exploring the photophysics and photochemistry of molecules. In the remainder of this work, we first discuss the details of the ΔPAV-DH-DFT implementation, how it relates to other excited-state computational approaches, and the workflow for obtaining benchmark data. We then discuss in detail the performance of the model in comparison to results from CASPT2 calculations. The analysis first examines how each term in ΔPAV-DH-DFT contributes to the accuracy of the model, before detailing the performance for specific classes of molecules. In the final results subsection, we show that ΔPAV-DH-DFT can achieve standard deviations for the benchmark molecular excitations similar to linear response coupled cluster (LR-CC) methods.

4.1.1 Symmetry Breaking in Hartree-Fock

When performing HF calculations one can choose to either preserve or break symmetries of the Hamiltonian. It has been demonstrated that for a stretched hydrogen molecule, the broken symmetry HF solution can achieve an energy closer to that of the exact solution. This phenomenon relates to the energetic ordering of orbitals as the distance changes, where at the equilibrium distance, the antibonding and bonding orbitals are well-separated energetically. However, at long distances the antibonding and bonding orbitals become degenerate. Thus, the electronic configuration of the double occupation of the antibonding orbital and the double occupation of the bonding orbital exhibit similar configuration weights in the exact wavefunction. The symmetry-adapted HF solution does not give a good description of this due to the fact that it assumes the solution is only described by the double occupation of the bonding orbital, thus giving an incorrect approximation to the exact solution.

Symmetry broken solutions are prevalent in many systems, but can be demonstrated in mostly open-shell systems. A symmetry broken solution is detected during the SCF optimization procedure where near degeneracies are identified. The SCF optimization procedure then locates an SCF minima by breaking the symmetry of the Hamiltonian. The broken-symmetry solution can partially account for the additional correlation needed to describe the degeneracies of the system. Broken symmetry SCF states can become solutions of the HF procedure, however this can only be achieved by utilizing an initial broken symmetry state to reach that SCF solution. So, if the initial solution does not contain broken symmetries, the resulting SCF solution will also lack the broken symmetry. With broken symmetry solutions one can recover correlation that otherwise would not be built into the wavefunction. However, there are problems that arise with the utilization of broken symmetry SCF solutions like the existence of bad quantum numbers due to the spin contamination in the system.

4.1.1.1 Construction of projection operators

The projection-after-variation double-hybrid density functional theory (PAV-DH-DFT) method applied in this work has been described in ref. 144. This section serves to provide some background to projection methods, highlight specific features of the implementation used, and describe how the implementation differs from alternative formulations. Although difference projected double-hybrid density functional theory (Δ-Proj-DH-DFT) uses a KS determinant, the formulation is analogous to methods constructed from a HF determinant, and so in this section, we describe in general terms the construction of projection operators in the context of the wavefunction. Further modifications for projection of KS based methods are then developed in the following section.

Projectors can be used to recover good quantum numbers from symmetry-broken approximate wavefunctions $|\Phi_0\rangle$ by removing terms with incorrect S and M_S quantum numbers resulting from spin contamination. Generally, any wavefunction (including post-SCF) can be written in terms of the contributions from eigenfunctions with different S and M_S quantum numbers

$$|\Phi_0\rangle = \sum_S \sum_{M_S} c_{S,M_S} |S, M_S\rangle \tag{4.1.1}$$

where c_{S,M_S} are expansion coefficients. For spin-adapted wavefunctions, all but one of the c_{S,M_S} are zero, while for wavefunctions that have spin polarization (collinear and noncollinear), only c_{S,M_S} with the same M_S are nonzero. In the case that electron spins are not confined along a common spin axis (coplanar or noncoplanar), all c_{S,M_S} may be nonzero. If only the component of the wavefunction with spin quantum numbers S' and M'_S is desired, undesired components can be removed by acting on the wavefunction with the projector $\hat{P}_{S',M'_S}$

$$|S', M'_S\rangle = \hat{P}_{S',M'_S}|\Phi_0\rangle = \mathcal{N} \sum_S \sum_{M_S} c_{S,M_S} |S', M'_S\rangle\langle S', M'_S|S, M_S\rangle \tag{4.1.2}$$

where $\mathcal{N}$ normalizes the wavefunction, and due to the orthonormality of spin eigenfunctions, $\langle S', M'_S|S, M_S\rangle = \delta_{SS'}\delta_{M_S M'_S}$, thus selecting only the desired spin component of the wavefunction. In the remainder of this text we deal only with projection of collinear SCF solutions. One approach to realize the projection expressed in eq. 4.1.2 is to diagonalize the Hamiltonian built from a determinant expansion in the space of biorthogonal orbital pairs which have non-unit overlap. The eigenvectors then provide the coefficients that indicate how each spin-adapted eigenfunction of the Hamiltonian contributes to the symmetry-broken wavefunction. The projected energy E^P can then be obtained from

$$E^P = \frac{\sum_{I\in\langle\hat{S}^2\rangle=S_z(S_z+1)} c_I^* c_I E_I}{\sum_{I\in\langle\hat{S}^2\rangle=S_z(S_z+1)} c_I^* c_I} \tag{4.1.3}$$

where the summations only include pure-spin states of the desired $\langle \hat{S}^2 \rangle$ value and the denominator normalizes the wavefunction. While the formalism of eq. 4.1.3 is useful for conceptually understanding how projection works, the factorial scaling of the size of the determinant expansion in terms of the number of biorthogonal orbital pairs with non-unitary overlap undermines its practical utility.

Instead of explicitly constructing and diagonalizing the Hamiltonian in the basis of the biorthogonal determinant expansion, Löwdin proposed a projector that, while not resolving the factorial scaling required to fully project the wavefunction, can be used to project only the spin states that most contaminate the wavefunction (145)

$$\hat{P}_S = \prod_{K_z=S_z+1}^{\frac{1}{2}(N_\alpha+N_\beta)} \frac{\hat{S}^2 - K_z(K_z+1)}{S_z(S_z+1) - K_z(K_z+1)} \tag{4.1.4}$$

where $S_z = \frac{1}{2}(N_\alpha - N_\beta)$, i.e. the total electron spin projected along the axis of spin quantization, and N_α and N_β are the number of α and β electrons respectively. In the case of single excitations where a single electron pair is broken, the $S_z + 1$ spin state contaminates to a far greater extent than any other. As a result, the projector in eq. 4.1.4 can be truncated at $K_z = S_z + 1$ and the resulting projector is known as the annihilation operator

$$\hat{A}_{\mathrm{S}+1} = \frac{\hat{S}^2 - (S_z+1)(S_z+2)}{S_z(S_z+1) - (S_z+1)(S_z+2)} \tag{4.1.5}$$

Alternatively, the Wheeler-Hill coordinate generator formulation (146; 134) leads to a projector that ensures invariance of the wavefunction with respect to the axis of spin quantization

$$\hat{P}_S = \frac{2S_z+1}{2} \int_0^\pi d\beta \sin(\beta) d^S_{M_S M_S}(\beta) e^{i\beta\hat{S}_y} \tag{4.1.6}$$

where $d^S_{M_S M_S}(\beta)$ is the Wigner small d matrix and $e^{i\beta\hat{S}_y}$ is the collective rotation of the angle of spin quantization by an angle β. The advantage of the approach in eq. 4.1.6 is that projection of all contaminating spin states is possible at mean-field cost, and so resolves the factorial scaling or truncation of the Löwdin projector.

4.1.1.2 Projection-after-variation double-hybrid density functional theory

In the Δ-Proj-DH-DFT approach, the ground and excited states are computed by local optimization of two SCF solutions representing each state of interest which are generally symmetry broken. For the excited state, breaking an orbital pair always results in spin contamination at the SCF level that requires projection to resolve, while low spin open shell electronic structure in the ground state will also require projection. In the current implementation, the projector of eq. 4.1.5 is used to provide a corrected energy using

$$E^P = \frac{\langle \Phi_0 | \hat{H} \hat{A}_{S+1} | \Phi_0 \rangle}{\langle \Phi_0 | \hat{A}_{S+1} | \Phi_0 \rangle} \tag{4.1.7}$$

where as above, the exact nature of $|\Phi_0\rangle$ depends upon the specific methodology being used. The projector in eq. 4.1.5 is strictly valid only when one electron spin-pair is broken in the excitation and when the remaining orbitals are closed shell in both the ground and excited state. However, our previous work indicated that severe degradation of VEEs does not occur until $\langle\hat{S}^2\rangle$ closely approaches $(S_z+1)(S_z+2)$, which is indicated by an increase in $\langle\hat{S}^2\rangle$ upon annihilation. An additional source of error is the inability of symmetry breaking and projection to describe more than a single correlation mechanism, in which natural orbitals from several different symmetry-broken SCF solutions are required to capture the static correlation (147; 148).

In the case where $|\Phi_0\rangle$ is a HF or KS determinant, inserting eq. 4.1.5 into eq. 4.1.7 yields the projected SCF energy E^{PSCF}

$$E^{PSCF} = \langle\Phi_0|\hat{H}|\Phi_0 + \tilde{\Phi}_1\rangle \tag{4.1.8}$$

where

$$|\tilde{\Phi}_1\rangle = \sum_{ijab} \frac{|\Phi_{ij}^{ab}\rangle\langle\Phi_{ij}^{ab}|\hat{S}^2|\Phi_0\rangle}{\langle\hat{S}^2\rangle - (S_z+1)(S_z+2)} \tag{4.1.9}$$

is the correction to the SCF solution, in which $|\Phi_{ij}^{ab}\rangle$ are determinants obtained from double substitution of electrons with respect to $|\Phi_0\rangle$, with indices $i, j, k \ldots$ referring to occupied orbitals and $a, b, c \ldots$ referring to virtual orbitals. In the case of MP2, the projected energy E^{PMP2} is

$$E^{PMP2} = \langle\Phi_0|\hat{H}|\Phi_0 + \Phi_1 + \tilde{\Phi}_1'\rangle \tag{4.1.10}$$

where $|\tilde{\Phi}_1'\rangle$ is obtained by Gram-Schmidt orthogonalization of the first order correction

$$|\Phi_1\rangle = -\sum_{ijab} \frac{|\Phi_{ij}^{ab}\rangle\langle\Phi_{ij}^{ab}|\hat{H}|\Phi_0\rangle}{\Delta_{ijab}} \tag{4.1.11}$$

where ε is the orbital energy and $\Delta_{ijab} = \varepsilon_a + \varepsilon_b - \varepsilon_i - \varepsilon_j$, with $|\tilde{\Phi}_1\rangle$, yielding

$$|\tilde{\Phi}_1'\rangle = |\tilde{\Phi}_1\rangle\left(1 + \frac{\sum_{ijab}\langle\Phi_0|\hat{S}^2|\Phi_{ij}^{ab}\rangle t_{ij}^{ab}\{\langle\hat{S}^2\rangle - (S_z+1)(S_z+2)\}}{\sum_{ijab}|\langle\Phi_0|\hat{S}^2|\Phi_{ij}^{ab}\rangle|^2}\right) \tag{4.1.12}$$

where t_{ij}^{ab} are the MP2 amplitudes

$$t_{ij}^{ab} = \frac{\langle ij||ab\rangle}{\Delta_{ijab}} \tag{4.1.13}$$

Owing to the singularities in t_{ij}^{ab} due to the small orbital energy gaps in the denominator, which is particularly acute when performing MP2 corrections to excited states (and with low amounts of exact exchange in the case of DH-DFT), we have further investigated the use of regularized amplitudes $\tilde{t}_{ij}^{ab}$ (149)

$$\tilde{t}_{ij}^{ab} = t_{ij}^{ab}(1 - \exp\{-\lambda\Delta_{ijab}\})^2 \tag{4.1.14}$$

which goes to zero as $\Delta_{ijab} \to 0$ and where λ is a parameter that controls the regularization strength. The regularized amplitudes are used in both $|\Phi_1\rangle$ and $|\tilde{\Phi}_1'\rangle$ components of the DH-DFT functional.

Using a double-hybrid Kohn-Sham density in eq.4.1.10 , the projected double-hybrid density functional theory (PDH-DFT) energy can be written as

$$E^{PDH} = \langle \Phi_0 | \hat{H} | \Phi_0 + \gamma(\Phi_1 + \tilde{\Phi}_1') \rangle \tag{4.1.15}$$

where γ is the parameter than governs the amount of MP2 correlation in the double-hybrid functional. The exchange-correlation components of eq. 4.1.15 can be written as

$$E_{xc}^{PDH} = (1 - a_x)E_x^{GGA} + a_x E_x^{HF} + bE_c^{GGA} + c(\gamma_{\sigma\sigma} E_c^{\sigma\sigma PT2} + \gamma_{\alpha\beta} E_c^{\alpha\beta PT2} + \gamma_{\alpha\beta} E_c^{Proj}) \tag{4.1.16}$$

where the first three terms are standard exchange and correlation terms from hybrid DFT, the fourth and fifth terms are the MP2 correlation terms, which can be broken into same-spin ($\sigma\sigma$) and opposite-spin ($\alpha\beta$) components, and the final term is the projection contribution accounting for symmetry breaking in the reference Kohn-Sham orbitals. The coefficients a_x, b, c and γ are free parameters which can be fitted to a training set. An advantage of projection is that it does not increase the number of empirical parameters in the functional. As a result, in our previous work, we were able to examine the use of three functionals (PBEQIDH, B2PLYP and DSDPBEP86), along with MP2, without having to determine a suitable parameter for the projection term. Although a significant improvement was found upon use of a Kohn-Sham reference, there was no significant difference in the performance of different functionals. However, all functionals tested used a large amount of HF exchange, with a_x between 0.53 and 0.69, which raised the question about whether the apparent failure of difference projected density functional theory (Δ-Proj-DFT) observed in our previous study resulted from a combination of suboptimal parameters. In addition, high HF exchange character leads to greater symmetry breaking of the reference, and so may over-emphasize the importance of projection.

4.1.2 Connection to Other Excited State Methods

Having introduced the form of the difference projection-after-variation double-hybrid density functional theory (ΔPAV-DH-DFT), in this section we examine how the proposed method compares with other approached to facilitate the discussion of the performance of different methods. In particular, we discuss the connection between LR-CC methods difference second-order Møller-Plesset theory (ΔMP2), as well as additional correlations obtained using projection combined with a density functional reference.

Combining LR with CC methods provide a systematic route to the investigation of excited states (150). Except for relatively small systems, including the effect of triple substitutions that describe the simultaneous interaction of three electrons is unfeasible. Therefore, application of LR-CC to medium and large molecular systems is essentially limited to inclusion of single and double substitutions only – equation-of-motion coupled cluster singles and doubles (EOM-CCSD) (151) or linear-response coupled cluster singles and approximate doubles (LR-CC2) (152). The motivation for this work is that in several benchmark studies (153; 154), the LR-CC2 method is frequently found to perform as well as or better than EOM-CCSD approach despite coupled cluster singles and approximate doubles (CC2) being an approximation to coupled cluster singles and doubles (CCSD) in which the doubles amplitudes are correct to first order in the fluctuation potential rather than to second order. However, CC2 is iterative $\mathcal{O}(N_{basis}^5)$ cost and generally provides energies of similar quality to noniterative $\mathcal{O}(N_{basis}^5)$ MP2, with both giving the correct energy to second order in the fluctuation potential. The advantage of CC2 over MP2 is in the computation of properties as it includes orbital relaxation through single substitution terms (which is the basis for its use in LR formalisms).

The difference between CC2 and MP2 can be analyzed directly in terms of the cluster operators. The CC and MP2 energy corrections to a HF reference $|\Phi_0\rangle$ can be written as (using the linked cluster formalism rather than the similarity transformed Hamiltonian)

$$E_2^{CC} = \langle\Phi_0|\hat{\Phi}(\hat{T}_2 + \frac{1}{2}\hat{T}_1^2)|\Phi_0\rangle \tag{4.1.17}$$

$$E_2^{MP2} = \langle\Phi_0|\hat{\Phi}\hat{T}_2^{(1)}|\Phi_0\rangle \tag{4.1.18}$$

where $\hat{\Phi}$ is the electron-electron fluctuation potential and $\hat{T}_1$ and $\hat{T}_2$ are single and double substitution cluster operators respectively. The cluster operators are written

$$\hat{T}_1 = \sum_{ia} t_i^a \hat{E}_i^a \tag{4.1.19}$$

$$\hat{T}_2 = \frac{1}{2}\sum_{ijab} t_{ij}^{ab} \hat{E}_i^a \hat{E}_j^b \tag{4.1.20}$$

where $i, j, k \ldots$ denote occupied orbitals, $a, b, c \ldots$ denote virtual orbitals, $\{t\}$ are the cluster amplitudes, and $\hat{E}_{ia} = a_a^\dagger a_i$ is an electron excitation operator that annihilates an electron in orbital i and creates an electron in orbital a. The cluster amplitudes $\{t\}$ are determined by projection onto the set of substituted bra determinants in which approximation depends on the order of truncation in the cluster operator $\hat{T}$. In MP2 the doubles amplitudes are obtained from

$$t_{ij}^{ab} = -\frac{\langle\Phi_{ij}^{ab}|\hat{\Phi}|\Phi_0\rangle}{\varepsilon_a + \varepsilon_b - \varepsilon_i - \varepsilon_j} \tag{4.1.21}$$

where ε_p is energy of orbital p and Φ_{ij}^{ab} is a doubly substituted determinant, while in CC2 relaxation is permitted in the HF reference

$$t_{ij}^{ab} = -\frac{\langle\Phi_{ij}^{ab}|\hat{\Phi}\exp(\hat{T}_1)|\Phi_0\rangle}{\varepsilon_a + \varepsilon_b - \varepsilon_i - \varepsilon_j} \tag{4.1.22}$$

where the single substitution cluster amplitudes t_i^a are determined through a modified set of coupled cluster singles (CCS) amplitude equations involving the double amplitudes, and hence is solved iteratively until self-consistency. Thus the distinction between CC2 and MP2 is in the former methods ability to account for large changes in the reference orbitals such as those which may occur upon excitation or other type of perturbation.

Although MP2 cannot account for orbital relaxation explicitly, where two different HF references are used for ground and excited states, correlation is introduced through Thouless' theorem (155) and can be shown to of essentially the same type as the additional correlation in CC2

$$E_2^{\Delta SCF} = \langle \Phi_1 | \hat{H} \{\exp(\hat{T}_1) - 1\} | \Phi_1 \rangle \tag{4.1.23}$$

where $|\Phi_1\rangle$ is the unoptimized HF reference of the excited state obtained by occupied-virtual (ov) orbital swaps in the ground state reference $|\Phi_0\rangle$. Note the presence of the second term in eq. 4.1.23 results from the fact the correction is to the difference between two states, as opposed to eq. 4.1.22 which gives the correction to a single state. Unlike CC2, the orbital relaxation in ΔMP2 is not directly coupled to the perturbation (there is no orbital relaxation resulting from the inclusion of electron-electron correlation at second order in the fluctuation potential). However, orbital relaxation resulting from electron-electron correlation is expected to be negligible in comparison to relaxation in response to an external perturbation (photon absorbtion) which is included in ΔMP2. Thus, the conclusion of this paragraph is that a ΔMP2 approach should provide similar quality excitation energies to LR CC2 but with noniterative $\mathcal{O}(N^5)$ cost.

Although ΔMP2 is expected to provide similar performance to CC2, the LR formalism has several advantages. First, LR does not, in principle, require any additional user input parameters beyond those for the ground state (a black-box approach); second, an orthogonal set of solutions are obtained such that identification of electronic states is unambiguous; and third, zeroth-order references are not required for each state of interest. However, in reality, the main issue that has prevented the widespread adoption of difference methods is the variational collapse of the excited state optimization. As discussed in section 4.1, recent developments have resolved many of the issues in variationally optimizing to excited state SCF solutions to the extent that we have been able to perform benchmark studies of ΔSCF and post-ΔSCF methods in this work. An additional issue of LR-CC is that it is based on a HF wavefunction reference. Alternative KS references have the advantage of incorporating correlation with low-order scaling through parameterization of the exchange-correlation functional rather than through the cluster expansion that must be truncated due to computational expense. Through using a KS reference, we can define a ΔDH-DFT model for the study of excited states. Therefore, in addition to capturing long-range correlations through the MP2 correction, the KS reference introduces a limited amount of static correlation and an improved description of the short-range exchange-correlation hole.

Finally, we comment on the last correlation contribution absent from ΔDH-DFT, which is that arising from a significant difference in the strong correlations present between the ground and excited states. Despite the use of a KS reference combined with permitting symmetry breaking to mimic static correlation to an extent, DFT is still unable to fully account for strong correlations. While multireference perturbation theories (e.g. CASPT2) have been developed and successfully applied (156), explicit construction of the wavefunction places significant technical demands on the user and frequently cannot be applied to correlate sufficiently large orbital subspaces for molecular problems. Alternatively one can opt for an empirical approach like that of density functional theory with modified on-site repulsion (DFT+U) in which an on-site repulsion penalty can be added to tune DFT and capture the remaining static correlation (157). Recently, work using the on-top pair density has been developed to recover the remaining correlations in DFT (158). Another approach, and theDPAVHF option we have chosen in this work, is to use projection of the symmetry broken KS reference determinant to restore quantum numbers (see section 4.1.1.2). In the results, we demonstrate that spin projection is required for bringing errors in ΔDH-DFT into line with LR-CC, although the use of projection means that the method is no longer size extensive or size consistent for individual states. However, provided the projector is able to recouple the required number of electrons, projection is size intensive and so the quality of excitation energies does not deteriorate with system size.

Local Excited State Benchmarking Set

In this section, we examine the performance of ΔPAV-DH-DFT calculations of VEEs specifically examining local excitations. We first discuss the terms within the model (eq. 4.1.16) and the relative importance in improving agreement with benchmark CASPT2 results. Subsequently, we discuss how the model performs for different molecule types represented in the benchmark set and explain why the nature of certain molecule classes result in less satisfactory performance. Finally, we compare the ΔPAV-DH-DFT model to other types of methods used to study the excited states of molecules.

In this study, the performance of the ΔPAV-DH-DFT approach is examined using the local excited state benchmark of Schreiber and coworkers (153). The test set comprises 28 organic molecules covering important classes of chromophores in organic photochemistry. Within the test set, there are 7 unsaturated aliphatic hydrocarbons, 11 aromatic hydrocarbons and heterocycles, 6 carbonyl compounds, and 4 nucleobases. Geometries for each molecule were the same MP2/6-31(d) optimized structures as used in the original study. All calculations in this work used the TZVP basis set to compare directly with the previously reported CASPT2 results. Ground states were determined by computing the lowest energy real restricted (RR) solution with a standard direct inversion of the iterative subspace (DIIS) procedure using Aufbau occupations, followed by optimization along the eigenvectors corresponding to *ov* rotation instabilities until a stable real unrestricted (RU) solution was obtained. Excited states were obtained by swapping the relevant *ov* orbital pair in the lowest energy RR determinant and then optimizing with RU symmetry using DIIS with orbital occupation determined by MOM (159). All subsequent DH-DFT calculations

Functional component	MP2	PBEQIDH	B2PLYP	DSDPBEP86
PDH	-0.1228 (1.1278)	-0.2703 (0.5417)	-0.4933 (0.5024)	-0.2945 (0.5295)
DH	-0.7690 (1.1294)	-0.3450 (0.6615)	-0.6083 (0.6320)	-0.3999 (0.6636)
PRef.	0.8454 (2.4164)	0.0126 (1.1436)	-0.0182 (0.9846)	-0.0414 (1.1501)
Ref.	0.0843 (1.0875)	-0.1290 (0.8440)	-0.3159 (0.7677)	-0.1696 (0.8635)

Table 4.1. Mean error in eV of ΔPAV-DH-DFT/TZVP excitation energies with respect to CASPT2/TZVP results. The standard deviation in eV is shown in parenthesis. Results for four double-hybrid functionals are shown (MP2, PBEQIDH, B2PLYP, DSDPBEP86) broken down into the reference hybrid functional (Ref.), the projected reference hybrid functional (PRef.), the double hybrid functional (DH), and the projected double hybrid functional (PDH).

were performed on top of the reference wavefunctions. The double-hybrid density functional examined in this study were B2PLYP (124), PBEQIDH (160), and DSDPBEP86 (161; 162), in addition to standard MP2. Calculations were performed using a modified version of Gaussian 16 (89).

4.2.1 Overall performance

In table 4.1, we show the performance of each of the difference methods examined in terms of the mean error and standard deviation with respect to CASPT2 results. As the number of terms included in the functional decreases with descending rows in the table, it is expected that the methods in the bottom row give poorer results than methods in the top row. In terms of standard deviation, the expected pattern is generally observed, with the exception being that difference projection-after-variation density functional theory (ΔPAV-DFT) (table 4.1, row 3) gives substantially poorer results than difference density functional theory (ΔDFT) (table 4.1, row 4). Such a result suggests that projection should not be used with ΔDFT calculations because of reduced error cancellation. The addition of MP2 correlation to the reference functional to give ΔDH-DFT (table 4.1, row 2) shows that the additional correlation energy improves the standard deviation by around 0.2 eV for all reference models compared to the reference functional ΔDFT (table 4.1, row 4). Subsequent projection of the double hybrid functional to give ΔPAV-DH-DFT improves the standard deviation by 0.1 eV.

Different double hybrid functionals are represented in each of the columns of table 4.1. The exception is the first column that shows MP2 results. Between the three double hybrids (PBEQIDH, B2PLYP, DSDPBEP86), the trends are very similar, suggesting that the result is relatively insensitive to the underlying functional. The main difference between functionals is in the mean error, the magnitude of which is inversely correlated with HF exchange (B2PLYP – 53%, PBEQIDH – 69% and DSDPBEP86 – 69%). However, the standard deviations are very similar, showing a small positive correlation with HF exchange. Thus, ΔPAV-B2PLYP gives the largest mean error (0.49 eV) but the smallest standard deviation (0.50 eV). Additionally, there is no apparent distinction between standard double hybrids and those that use scaled component spin (DSDPBEP86). The double hybrids are a clear improvement over the results using a HF reference (table 4.1, column 1). While the difference Hartree-Fock (ΔHF) results are worse than ΔDFT results by around 0.2 eV in the standard deviation, ΔMP2 does not improve on ΔHF while ΔDH-DFT gives significantly better results than ΔDFT. Additionally, the use of projection only gives a marginal improvement in the ΔMP2 results.

Fig. 4.1 shows in greater detail the distribution of VEEs reported in table 4.1. Inspection of how the distribution changes as different terms are added gives a better sense of how each term corrects errors in the model. As an initial point, we first discuss the reference functions (fig. 4.1, row R4) in which the distribution of VEEs shows an approximately normal distribution. Comparing ΔHF (row R4 column C1) results with ΔDFT (row R4, columns C2-C4), it is apparent that the number of outliers that overestimate the VEE in HF are reduced by correlation introduced through the density functional reference. Examining the effect of including correlation through perturbation (comparing rows R2 and R4 of fig. 4.1) gives a similar trend as the effect of using a density functional reference, with fewer overestimated VEEs. It is somewhat unexpected that the inclusion of dynamic correlation through MP2 correlation generally decreases the VEE, as one would expect that there is a greater amount of dynamic correlation in the ground state than the excited state. As a result, the ground state should be stabilized to a greater extent than the excited state and so the VEE should increase. However, MP2 is not variational and may increase the energy of the ground state relative to the excited state resulting in a smaller VEE. Besides, the excited state reference is obtained via nonlinear optimization, and so is not necessarily variational, in which case it is unknown how the MP2 correction applied to the excited state will affect the VEE.

The effect of projection can be determined by examining the change in the distribution between rows R3 and R4 of fig. 4.1. Regardless of the reference, the standard deviation deteriorates when projection is applied, generally because the number of overestimated excitation energies increases significantly, causing ΔPAV-DFT to have the best mean VEE but the worst standard deviation. The spread in VEE as a result of projection can be understood by considering that while projection in the ground state will generally reduce the energy, in the excited state projection is more likely to increase the energy as the high spin contaminating spin state in the symmetry-broken wavefunction is generally below the low spin energy. However, while in most cases projection increases VEEs, the VEE decreases in some cases due to the contaminating high spin state lying above the low spin energy. Projection of the double-hybrid density functional also results in VEEs shifting in either direction depending on the relative energy of the contaminating triplet state. As for projection of the reference, the overall shift causes the mean VEE to increase (fig. 4.1, row R1 and R2). However, owing to a balanced description in correlation types, the standard deviation decreases upon changes in VEE due to projection.

Fig. 4.2 shows the correlation plots between the various difference methods tested in this work and CASPT2 results along with the coefficient of determination (R^2) values. The ΔPAV-DH-DFT results display the best correlation, while there is little

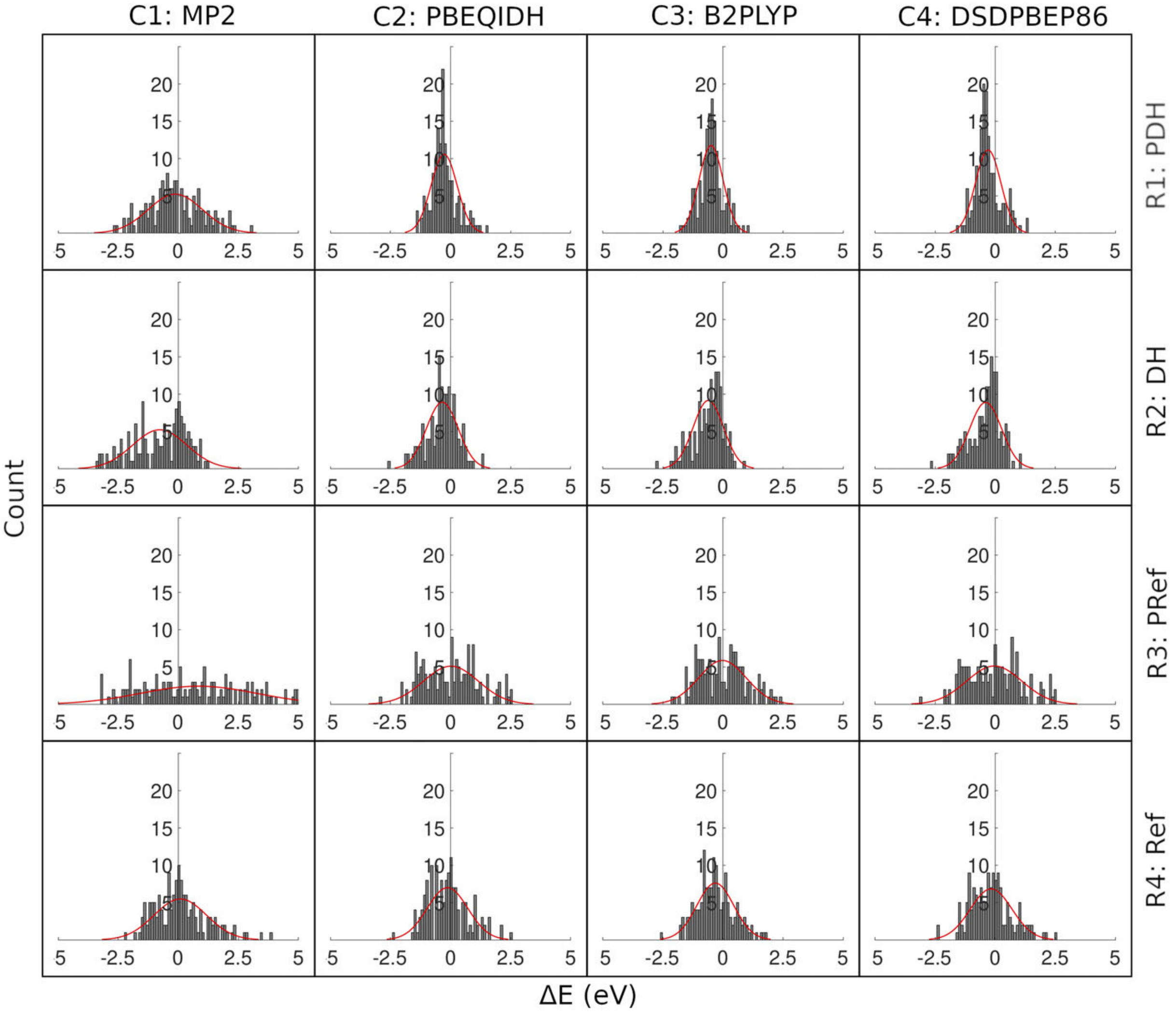

Figure 4.1. Histograms showing frequency of deviation (bin width 0.1 eV) and normal distribution of computed ΔPAV-DH-DFT/TZVP excitation energies from CASPT2/TZVP results. Four double-hybrid functionals are shown in columns (MP2, PBEQIDH, B2PLYP, DSDPBEP86), while rows show the frequency of deviation for the reference hybrid functional, the projected reference hybrid functional, the double hybrid functional, and the projected double hybrid functional.

to distinguish different double hybrids. The correlation for all methods improves as more terms are added into the model, except for difference projection-after-variation Hartree-Fock (ΔPAV-HF). Even though the standard deviation of ΔPAV-DFT is larger than ΔDFT, there no difference in correlation of either method with CASPT2 results. Generally, the trend lines show overestimated low-energy excitations and underestimated high-energy excitations. Therefore, it is possible to apply an energy-dependent scaling factor that may further reduce the standard deviation, although such a parameter has no obvious physical significance. Fig. 4.2 also demonstrates that the mean error of ΔPAV-B2PLYP is larger than the other double hybrids because it performs better in computing high energy excitations. Thus, slightly less HF exchange appears to result in a better overall performance at the expense of larger systematic energy shifts.

4.2.2 Performance for molecule classes and illustrative examples

We now turn to discuss the performance of the difference methods examined for different classes of molecules in the test set. For clarity and readability, we do not provide a detailed analysis of all molecules examined, but give illustrative examples and refer the reader to tables S1-S16 in reference (163) for detailed results. Table 4.2 shows the standard deviation for the various molecule classes. The general trend within each molecular class is the same as the overall trend, with the performance of the models improving as the number of terms in the energy expression increases. The poorest performance for ΔPAV-DH-DFT was in the unsaturated aliphatic hydrocarbons class, in which the addition of MP2 correlation to the reference functional does not improve the model, although projection reduces the standard deviation by around 0.2 eV. Examining the VEE of individual states reveals that the linear unsaturated aliphatic hydrocarbons have a much larger standard deviation than the cyclic molecules. We now focus on two illustrative examples of linear polyenes that demonstrate where the ΔPAV-DH-DFT model performs well and where caution should be used.

First, the ethene 1^1B_{1u} state has been well-studied both computationally and experimentally, where the VEE has been found hard to predict due to the mixed-valence and Rydberg character. The CASPT2 (2 electrons, 2 orbitals active space) results of Schreiber and coworkers gave a VEE of 8.62 eV, while LR-CC methods give energies in the range of 8.37-8.51 eV. Enlargement of the basis set from TZVP to d-aug-cc-pV5Z the linear-response coupled cluster singles, doubles and approximate triples (LR-CC3) gave a VEE of 7.88 eV, while a multi-state CASPT2 result with a much larger 8 electrons, 20 orbital active space gave a value of 7.83 eV. Experimentally, the VEE is believed to lie between 7.7 and 8.0 eV, with Schreiber suggesting a value of 7.8 eV as the best estimate. The ΔPAV-DH-DFT results show a functional dependence, with MP2 giving 9.06 eV, B2PLYP 6.85 eV, PBEQIDH 7.19 eV and DSDPBEP86 7.68 eV, demonstrating that although the overall results are similar for different functionals, there are variations for individual calculations. Therefore, even though the ΔPAV-DH-DFT ethene 1^1B_{1u} states are in larger error than LR-CC with respect to the CASPT2 results, the ΔPAV-DH-DFT values are actually in closer

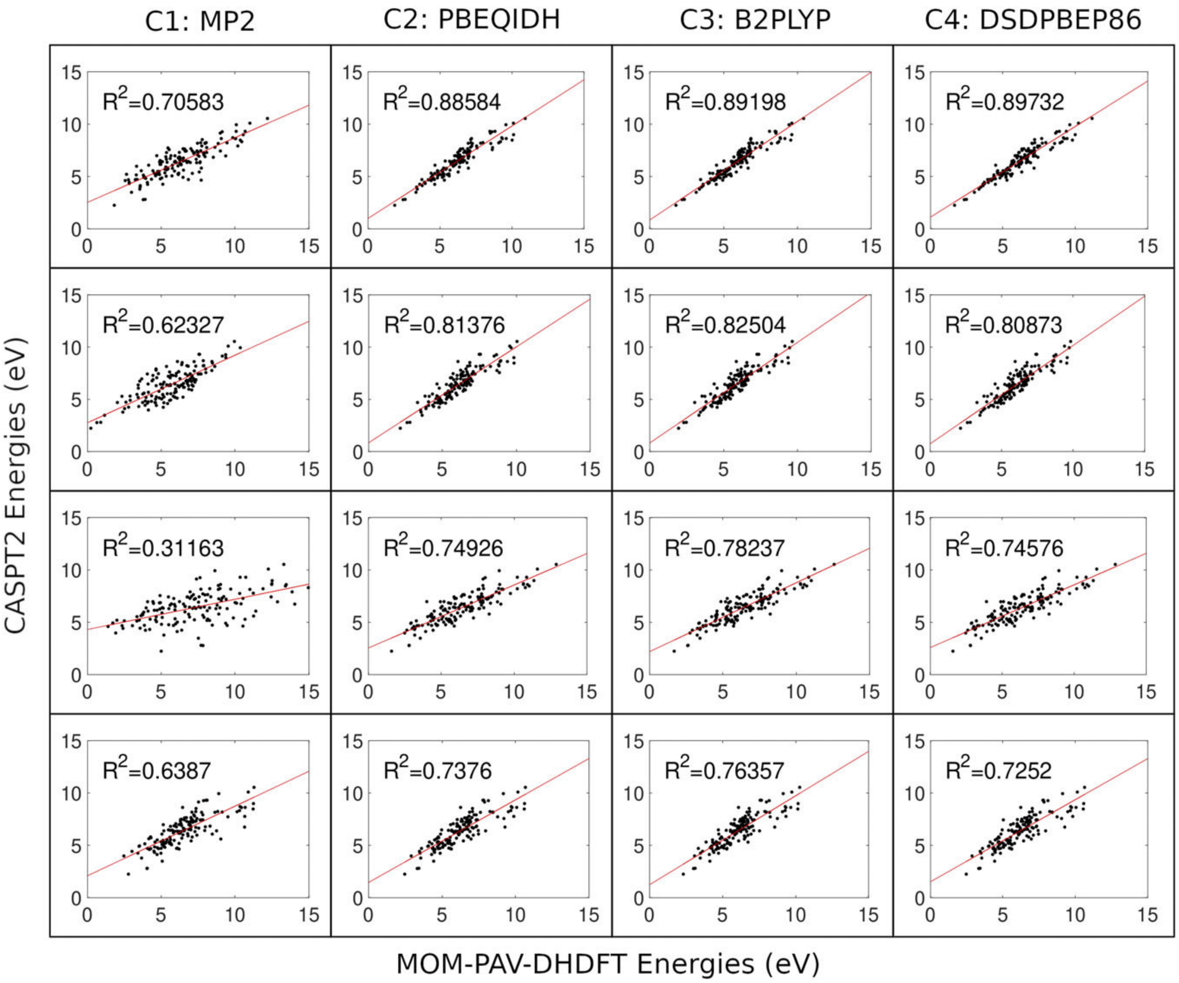

Figure 4.2. Correlation plots of computed ΔPAV-DHDFT/TZVP and CASPT2/TZVP excitation energies showing least squares regression line and associated coefficient of determination. Four double-hybrid functionals are shown in columns (MP2, PBEQIDH, B2PLYP, DSDPBEP86), while rows show the frequency of deviation for the reference hybrid functional, the projected reference hybrid functional, the double hybrid functional, and the projected double hybrid functional.

Functional component	MP2	PBEQIDH	B2PLYP	DSDPBEP86
Unsaturated Aliphatic Hydrocarbons				
PDH	1.0505	0.7201	0.7140	0.6317
DH	0.9407	0.9288	0.9006	0.9376
PRef.	1.8449	0.7434	0.6920	0.7481
Ref.	1.1242	0.9786	0.9383	0.9802
Aromatic Hydrocarbons and Heterocycles				
PDH	1.0739	0.5922	0.5413	0.5983
DH	1.0979	0.6650	0.6231	0.6560
PRef.	2.1466	1.1347	0.9828	1.1427
Ref.	1.0983	0.8720	0.7803	0.9125
Aldehydes, Ketones and Amides				
PDH	0.8894	0.3069	0.2810	0.3351
DH	1.1142	0.5249	0.5698	0.5987
PRef.	2.8806	1.3377	1.1000	1.3448
Ref.	1.2673	0.7248	0.5983	0.7343
Nucleobases				
PDH	0.6772	0.3709	0.3372	0.3554
DH	0.4093	0.4081	0.3793	0.3943
Pref.	0.9922	0.8180	0.7337	0.8093
Ref.	0.6949	0.5769	0.5667	0.5645

Table 4.2. Standard deviation in eV of ΔPAV-DHDFT/TZVP excitation energies with respect to CASPT2/TZVP results for different classes of benchmark molecules. Results for four double-hybrid functionals are shown (MP2, PBEQIDH, B2PLYP, DSDPBEP86) broken down into the reference hybrid functional (Ref.), the projected reference hybrid functional (PRef.), the double hybrid functional (DH), and the projected double hybrid functional (PDH).

correspondence with the likely experimental value. The unprojected methods (with or without the MP2 correlation added for all functionals including MP2) tended to significantly underestimate excitation energies giving a range of 5.86-6.44 eV. Projection on top of the reference tended to overestimate the VEE giving 8.90-9.01 eV, demonstrating that inclusion of dynamic and static correlation together is important for correctly reproducing experimental values.

Second, we examine the 1^1B_u and 2^1A_g states of E-butadiene of which Sundstrom and Head-Gordon have discussed the various theoretical results (164). To summarize, the ordering of the two states was inconsistent between different methods but has been determined as 1^1B_u at 6.21 eV followed by the 2^1A_g state at 6.41 eV, while the reference CASPT2 calculations gave 6.47 and 6.83 eV respectively. Obtaining the correct order of the two states requires a balance of correlation types as the two states are dominated by either dynamic (1^1B_u) or static (2^1A_g) correlation effects. The 2^1A_g state also includes a significant amount of double excitation character (HOMO→LUMO) in addition to multiple single-excitation determinants (HOMO-1→LUMO and HOMO→LUMO+1). For all difference methods, the correct ordering of 1^1B_u and 2^1A_g states was obtained (even ΔHF). The 1^1B_u state was underestimated by all functionals at the ΔPAV-DH-DFT level of theory (5.02-5.67 eV), but not when projected MP2 was used (6.68 eV). In contrast, the 2^1A_g state is typically overestimated (8.52 eV with MP2 and 6.98-7.42 eV with double-hybrids). However, the results of ΔPAV-DH-DFT are in line with LR-CC VEEs of 7.63 eV (LR-CC2) and 7.42 eV (EOM-CCSD) which indicate the importance of including triples (LR-CC3 gives 6.77 eV). The determinant used as the reference for the 2^1A_g state is the HOMO-1→LUMO as it has the correct symmetry, while the HOMO→LUMO+1 determinant has A_u symmetry. Therefore, rather than through direct *ov* orbital swapping, the HOMO→LUMO+1 character is incorporated entirely through orbital relaxation, while HOMO→LUMO double excitation is incorporated through disconnected terms in the orbital relaxation.

The other molecular class in which the error standard deviation was relatively large was the aromatic hydrocarbons and heterocycles. We discuss here the results from benzene as an example of the molecule in the aromatic class. The ground state of benzene is a model system for multireference behavior, with an open-shell singlet ground state as a result of the doubly degenerate e_{1g} HOMO. The low-lying $\pi \rightarrow \pi^*$ excited states of benzene involve single excitations into the degenerate e_{2u} LUMO and so are close in energy, with best estimates provided by Schreiber and coworkers of 5.08 eV (1^1B_{2u}), 6.54 eV (1^1B_{1u}) and 7.13 eV (1^1E_{1u}) (153). Additionally, the 2^1E_{2g} state is found at 8.41 eV and has HOMO→LUMO double excitation character. The VEE of 1^1B_{2u} is predicted reliably by all LR-CC methods (5.07-5.27 eV) compared to the CASPT2 result of 5.05 eV. ΔPAV-DH-DFT gave consistently higher energies for the 1^1B_{2u} state (5.51-5.64 eV), but were marginally better than the projected MP2 (5.72 eV). The LR-CC 1^1B_{1u} (6.68-6.74 eV) and 1^1E_{1u} (7.44-7.65 eV) were slightly above the best estimates, with LR-CC2 and LR-CC3 being essentially identical for both states. However, ΔPAV-DH-DFT underestimated the VEEs by around 1 eV for both states (5.52-5.66 eV for 1^1B_{1u} and 5.97-6.51 eV for 1^1E_{1u}) while projected MP2 actually gave the best results (5.94 eV for 1^1B_{1u} and 7.45 eV for 1^1E_{1u}), suggesting discrepancies in these states of ΔPAV-DH-DFT with best estimates result from an imbalance in the way correlation is introduced through the density functional. Finally, the double excited character of the 2^1E_{2g} state is apparent in the large difference between LR-CC2 and LR-CC3 (9.03 eV and 8.43 eV respectively), where LR-CC3 is believed to give an essentially correct answer. In the case of the 2^1E_{2g} state the projected MP2 value of 9.45 eV is similar in error to the LR-CC2 and EOM-CCSD (9.21 eV) results, while PAV-DH-DFT (8.65-9.08 eV) give a marginal improvement. In line with the findings in the 2^1A_g state of E-butadiene, we conclude that ΔPAV-DH-DFT suffers a similar inability to quantitatively determine the VEEs to electronic states with significant double excitation character, but that the numerical error is smaller in ΔPAV-DH-DFT.

	ΔMP2	ΔPMP2	ΔB2PLYP	ΔPB2PLYP	LR-CC2^{a}	EOM-CCSD^{a}	LR-CC3^{a}
ME	-0.77	-0.12	-0.61	-0.49	0.29	0.49	0.20
SD	1.13	1.13	0.63	0.50	0.41	0.58	0.27

Table 4.3. Mean error (ME) and standard deviation (SD) in eV of benchmarked methods with respect to CASPT2/TZVP results. ^{a}Results reproduced from ref. 153.

4.2.3 Comparison with other excited state methods

In order to ascertain how the difference models tested in this work compare to established computational methods, particularly LR-CC methods, we report the mean error and standard deviation of various computational methods for the same test set (table 4.3). In particular we focus on standard deviations as mean errors can be corrected by systematic shifts provided that the standard deviation is sufficiently small. First we briefly outline the results of LR-CC methods obtained in ref. 153. Although LR-CC2 is an approximation to EOM-CCSD, LR-CC2 gave better performance in both mean error and standard deviation, implying some amount of error cancellation. LR-CC3 was found to give the closest agreement with CASPT2, with standard deviation of 0.27 eV – less than half the standard deviation of EOM-CCSD. The performance of LR-CC3 is a result of an improved description of double excitations. We sought to corroborate the relative performance of LR-CC methods by examining the standard deviations with respect to CASPT2 of a more recent benchmark by Azarias and coworkers for $n \rightarrow \pi^*$ excitations (154). Although the standard deviations of LR-CC2 (0.41 eV in ref. 153 and 0.40 eV in ref. 154) and EOM-CCSD (0.58 eV in ref. 153 and 0.68 eV in ref. 154) are consistent, the LR-CC3 results (0.27 eV in ref. 153 and 0.40 eV in ref. 154) show that LR-CC3 does not consistently give VEEs in closer agreement to CASPT2 than LR-CC2, although depending on the system, LR-CC3 results may be superior to CASPT2 in reproducing experiment.

Turning to the results of the difference methods, the average VEE is underestimated in both projected and unprojected difference MP2 and DH-DFT while LR-CC methods overestimate the mean VEE. ΔDH-DFT has a standard deviation (0.63 eV) similar to that of EOM-CCSD (0.58 eV). The decent performance of unprojected ΔDH-DFT is useful because it is size extensive. However, the additional correlation energy obtained through projection in the ΔPAV-DH-DFT approach enables the standard deviation (0.50 eV) to improve to an intermediate level between EOM-CCSD and LR-CC2. As LR-CC2 is an approximation to EOM-CCSD there is no reason that LR-CC2 should have superior performance, and so the ΔPAV-DH-DFT standard deviation indicates similar performance to LR-CC methods including up to double excitation cluster operators. The ΔMP2 and ΔPMP2 method have over double the standard deviation (1.13 eV) compared to LR-CC2 despite the similarities in the underlying physics discussed in section 4.1.2 showing the importance of the double hybrid reference functional in obtaining accuracy comparable to LR-CC values.

Single-Reference Challenge of Non-Local Excited States

The most popular methodology for studying the excited states of large systems is TD-DFT, which provides a semiquantitative description of local excitations in the vertical excitation region (165; 166). Despite the utility of TD-DFT, well known issues include inabilities to describe charge-transfer states, double-excited states, Rydberg states, and electronic degeneracies with the ground state (8; 9; 10; 11). Numerous improvements to the TD-DFT methodology have partially resolved some issues, including range separated functionals to describe charge transfer (167; 168; 169) and inclusion of select double-substituted determinants to describe conical intersections (170). In addition, improved accuracy can be obtained using a double-hybrid TD-DFT formalism (34; 132; 131; 33; 32; 31) or within a wavefunction formalism using LR-CC2 or EOM-CCSD approaches (171; 152).

Although DH approaches increase the computational scaling of TD-DFT approaches to noniterative $\mathcal{O}(N^5)$, they can often rival the accuracy of more expensive wavefunction-based approaches (35; 163) while correcting TD-DFT errors in systems such as singlet-singlet valence excitations in large organic dyes (172; 173), electronic circular dichroism spectra (174), and excited states in polycyclic aromatic hydrocarbons (175). Despite the successes of DH methods, they give an unsatisfactory description of charge transfer and Rydberg states (176; 177; 178; 179), which can be partially ameliorated through use of range separation (180; 181; 167; 182; 183). However, the range separation parameter is system-dependent (184) and although the exact exchange parameter has been investigated for ground state transition metal complexes (185), there was yet to be a study of how exact exchange affects the accuracy of charge transfer, Rydberg, and local vertical excitation energies within a difference formalism.

Local, Charge Transfer, and Rydberg Excited State Benchmarking set

In the previous section, we have described an alternative DH-DFT approach for modeling local excited states which was found to give results of similar quality to LR-CC2 or EOM-CCSD despite the lower computational scaling (163). The previous section focused only on local excitations and revealed surprisingly that ΔPAV-DFT gave significantly worse performance than ΔDFT. As a result, in this section we examine a broader class of excitation types, including local, charge-transfer, and Rydberg states. We investigate how inclusion of exact exchange affects the relative performance of ΔPAV-DH-DFT and underlying methodologies. The goal of this study is to provide a systematic understanding of how the exact exchange parameter can be tuned for different excitation types, as well as establish if the previous failures of ΔDFT are a result of the functional parameterization. The exchange parameter is investigated due to the understanding of spin contamination where it is relevant to note that DFT suffers from spin contamination to a lesser extent than HF wavefunctions, although for low-spin open shell systems, any single-reference methodology will eventually exhibit symmetry breaking (186). In the context of excited electronic states, the breaking of an electron pair will always lead to large contributions from contaminating spin states, while the amount of HF exchange may modulate the extent of symmetry breaking in the remaining $N-2$ electrons. Correlation generally reduces spin contamination (although not always (187)), although the presence of spin contamination is known to significantly impact the convergence of the Møller-Plesset perturbation series (188; 189).

In the remainder of the section, we first discuss the overall performance of ΔPAV-DH-DFT on three types of vertical excitation energies – local, charge transfer and Rydberg excitations, and compare the results with conventional time-dependent double-hybrid density functional theory (TDDHDFT). The local excitations tested are a different set to those used in our previous work, so our goal is to ensure our previous findings are transferrable as well as provide additional data on the models performance. As our previous work found insignificant difference between functionals, we only use the DSDPBEP86 functional throughout this study. Second, we examine the role of the HF exchange contribution for improving the description of difference VEEs, particularly for Rydberg and charge transfer excitations which from linear-response TD-DFT are known to require nonlocal exchange to correct for self-interaction error and describe the long-range component of the exchange correlation hole. Lastly, we conclude by describing the successes, limitations and future directions of the ΔPAV-DH-DFT methodology.

In order to ascertain the role of HF exchange on the accuracy of ΔPAV-DH-DFT calculations, we first examined the performance using the benchmark set of Tozer etål:(190) The benchmark set consists of 32 local excitations, 14 charge transfer excitations, and 13 Rydberg excitations. Owing to the similarity in the performance of different functionals previously observed, only DSDPBEP86 was used, as spin-component scaled terms have been implicated in separating the parameterization of long-range (same-spin) and short-range (opposite-spin) interactions important for a balanced description of correlation energy change upon excitations (191; 192; 193). The basis sets used were: cc-pVTZ for dipeptide, β-dipeptide, tripeptide, N-phenylpyrrole (PP), 4-(N,N-dimethylamino)benzonitrile (DMABN) and HCl; and d-Aug-cc-pVTZ for N_2, CO and H_2CO. The use of diffuse functions when studying N_2, CO, and H_2CO was due to the Rydberg character of the excited electronic states. Ground states were determined by computing the lowest energy real restricted solution and then performing analysis of the orbital-rotation Hessian to ensure no instabilities with respect to ov rotations were present. All molecules were found to have stable restricted SCF solutions in the ground state. Excited states were obtained by swapping relevant ov orbital pairs in the real-restricted determinant, and then optimizing using MOM (159; 194) or state-targeted energy projection (STEP) (195) with real-unrestricted symmetry. A more detailed description of the workflow required to determine the SCF solutions corresponding to both ground and excited states is outlined in section 4.5.6 of the supplementary information. Both ground and excited state energies were calculated using the reference functional (PBEP86), the projected reference functional (projected PBEP86), the double-hybrid functional (DSDPBEP86), and the projected double-hybrid functional (projected DSDPBEP86). To ascertain the role of HF exchange, the value of a_x in eq. 4.1.16 was varied in increments of

0.1 from zero to one. Vertical excitation energies were also computed using TD-DSDPBEP86 in order to compare the performance of linear response and difference DH-DFT. All calculations were performed using a modified version of Gaussian 16 (89), other than TDDHDFT calculations which used Orca (196), and the Wheeler-Hill coordinate generator projection method which was implemented in a stand-alone code using the MQCPack library (197) interfaced with Gaussian. Difference vertical excitations energies were compared to benchmark reference values determined in ref. 190 from gas-phase experimental data, state specific CASPT2 and LR-CC2 computational data.

First, we discuss the performance of ΔPAV-DH-DFT VEEs for different excitation types using original parameterization for the ground state (69% HF exchange) used in our original study and compare the result with state-of-the-art conventional TDDHDFT. We then discuss how the performance of ΔPAV-DH-DFT VEEs changes depending on the percentage of HF exchange. Our analysis breaks the performance down into local, charge transfer and Rydberg excitations, as well as overall performance.

4.4.1 DSDPBEP86 Vertical Excitation Energies Using Original Parameterization

The standard deviations and mean errors of difference unprojected and projected hybrid and double-hybrid functionals for computing VEEs of local, charge transfer, and Rydberg states using the original parameterization (69% HF exchange) are shown in table 4.4. We first comment on the performance of the local excitations in the Tozer benchmark set (ref. 190) and contrast the results with our previous study, in which the Thiel benchmark set (ref. 153) consisting of only local excitations was used. Subsequently, we examine the results of difference unprojected and projected functionals for computing charge transfer and Rydberg states, which have not previously been explored using difference methods. Results using a difference formalism are compared to TDDHDFT results with the same functional.

The results shown in column 3 of table 4.4, which detail the local excitations of the Tozer benchmark, are broadly in agreement with the results using the Thiel benchmark in column 6, with decreasing mean error and standard deviation with the number of terms in the functional (163). In terms of standard deviations, all methods gave slightly better results in the Tozer benchmark than the Thiel benchmark, improving by 0.09 – 0.26 eV depending on the number of terms included in the functional. ΔDFT gave the largest improvement in standard deviation between benchmarks by 0.26 eV, although still performed worse than either of the two MP2 corrected methods. As was observed in the Thiel test set, the Tozer test set also revealed ΔPAV-DFT gave a worse standard deviation than the unprojected ΔDFT, indicating that without MP2 correlation, projection should not be used with ΔDFT results. In terms of mean error, the Tozer benchmark corroborated the findings using the Thiel benchmark that difference methods systematically underestimate VEEs. MP2 corrected methods give improved mean errors in the Tozer benchmark, while the reference functionals give worse mean errors. As a result, the Tozer benchmark gives the expected order of improvement in mean error with the number of terms in

Method/Functional		This work (Tozer)			Ref. 163 (Thiel)
		Type of Excitation			
		Local	Charge Transfer	Rydberg	Local
Δ-Proj-DSDPBEP86	ME	-0.19	-0.66	-0.16	-0.29
	MAE	0.37	0.75	0.51	0.58
	SD	0.44	0.57	0.61	0.53
Δ-DSDPBEP86	ME	-0.31	-0.31	-0.24	-0.40
	MAE	0.47	0.52	0.33	1.09
	SD	0.53	0.44	0.37	0.66
Δ-Proj-PBEP86[a]	ME	-0.35	-1.02	-0.27	-0.04
	MAE	0.82	1.12	1.14	0.69
	SD	1.07	0.67	1.37	1.15
Δ-PBEP86[a]	ME	-0.50	-0.35	-0.35	-0.17
	MAE	0.67	0.47	0.53	0.94
	SD	0.61	0.46	0.60	0.86

Table 4.4. Mean error (ME), mean absolute error (MAE), and standard deviation (SD) in eV for vertical excitation energies to local, charge transfer, and Rydberg electronic states compared to benchmark values in refs. 190 and 153, computed using Δ-Proj-DSDPBEP86 and underlying methods. [a]Methods use nonstandard 69% exact exchange.

the functional. The fact that functionals without MP2 correlation give worse results is likely a result of the larger standard deviation, so that the anomalously low mean error of ΔPAV-DFT in the Thiel benchmark (-0.04 eV) was a consequence of sign cancellation. Despite the fact that both the Tozer and the Thiel benchmark sets showed projection increased the standard deviation of ΔDFT, both benchmarks showed projection reduced the mean error, even though the mean error of ΔPAV-DFT was inconsistent between benchmarks. In comparison to the TD-DFT results (table 4.5), the DFT difference methods result in larger standard deviations than those obtained using TD-DFT except for TD-DSDPBEP86, which surprisingly had greater standard deviation that any of the lower-rung density functionals (TD-PBE standard deviation is 0.27 eV, TD-B3LYP is 0.26 eV, TD-CAM-B3LYP is 0.27 eV, and TD-DSDPBEP86 is 0.43 eV). The performance of TDDHDFT in terms of standard deviation, was almost identical to ΔPAV-DH-DFT, and yet better than unprojected ΔDH-DFT. While the mean error of ΔDFT is larger than any of the functionals tested using TD-DFT, ΔPAV-DFT and ΔDH-DFT give similar mean errors to TD-PBE (-0.31 eV), while ΔPAV-DH-DFT gives a mean error similar to TD-B3LYP (-0.15 eV) and TD-DSDPBEP86 (-0.19 eV) for local excitations. The competitiveness of TD-DFT with difference methods is perhaps unsurprising as TD-DFT is known to perform well for local excitations.

Method/Functional		Type of Excitation		
		Local	Charge Transfer	Rydberg
TD-DSDPBEP86	ME	-0.19	-1.52	-0.21
	MAE	0.38	1.68	0.49
	SD	0.43	1.42	0.54
TD-CAM-B3LYP[a]	ME	0.02	-0.81	-0.50
	MAE	0.20	0.27	0.50
	SD	0.27	0.31	0.18
TD-B3LYP[a]	ME	-0.15	-1.35	-1.11
	MAE	0.22	1.36	1.11
	SD	0.26	0.86	0.23
TD-PBE[a]	ME	-0.31	-2.60	-1.84
	MAE	0.33	2.60	1.84
	SD	0.27	1.37	0.30

Table 4.5. Mean error (ME), mean absolute error (MAE), and standard deviation (SD) in eV for vertical excitation energies to local, charge transfer, and Rydberg electronic states compared to benchmark values in ref. 190, computed using time-dependent density functional theory with different functionals. [a]Results from ref. 190.

We now turn to discuss the Rydberg and charge transfer excitations which were not included in the Thiel benchmark set, and so it is not possible to evaluate results from the Tozer benchmark in the context of previous results. A key finding of ref. 190 is that additional HF exchange improves the performance of all excitations in linear-response TD-DFT, particularly for Rydberg and charge transfer states, and so the high HF exchange of double-hybrid functionals is likely to give good performance in difference methods. All difference methods, (table 4.4, column 4) give results for charge transfer excitations that are better than TD-PBE, TD-B3LYP, and TD-DSDPBEP86 in terms of both mean error and standard deviation. Only unprojected methods – with or without the MP2 correction – are able to approach the standard deviation of TD-CAM-B3LYP, although TD-CAM-B3LYP has a much larger mean error. The standard deviations and mean errors of charge transfer states show unprojected methods give better results than projected methods, regardless of whether MP2 correlation is included in the functional. Using difference methods to compute VEEs of Rydberg states, all methods gave better mean errors than TD-CAM-B3LYP or TD-DSDPBEP86, with the number of terms in the functional correlating with a decrease in the mean error. However, difference methods gave a larger standard deviation than linear-response approaches, with projection diminishing the performance of hybrid and double-hybrid functionals. Based on these findings, while projection improves the performance of difference methods for studying local excitations, for charge transfer and Rydberg excitations, the use of projection can lead to reduced accuracy and/or precision. As a result, we seek to understand the origin of the failure of projection when applied to Rydberg and charge transfer states, and whether the performance can be improved by alternative parameterizations.

4.4.2 Effect of Exact Exchange Parameter on Δ-Proj-DH-DFT Vertical Excitation Energies

In this section, we seek to establish the role of the value of a_x in tuning the performance of Δ-Proj-DH-DFT methods for local, charge transfer and Rydberg excitations.

4.4.2.1 Local Excitations

The mean error and standard deviation of local excitation VEEs as a function of HF exchange percentage are shown in fig. 4.3, with numerical values provided in table 4.13. The results in table 4.4, with the original HF exchange parameter, are indicated by squares, while circles indicate results with differing values of HF exchange ranging between 0% and 100%. The mean error of ΔPAV-DH-DFT, shown in fig. 4.3a (red), does not change significantly between 40% and 80%, with values between -0.31 eV and -0.17 eV. At 60% and 70% ΔPAV-DH-DFT is the best performing functional in terms of mean error, although the smallest ΔPAV-DH-DFT mean error is actually obtained at 50% HF exchange (-0.17 eV). Therefore, the standard HF exchange value of most double-hybrid functionals, which typically lie between 50% and 70%, is likely to be a reasonable choice for calculating local VEEs. At low amounts of HF exchange, both projected and unprojected double-hybrid methods rapidly degrade in performance and the hybrid functionals become the best performing methods. ΔPAV-DFT (blue) is the best performing method at 50% HF exchange and below. In fact, the global minimum mean error in terms of functional and HF exchange percentage is ΔPAV-DFT with 40% HF exchange, which gives a value of -0.11 eV. At 20% HF exchange, ΔPAV-DFT is competitive with the best performing double-hybrid parameterization in terms of both mean error and standard deviation. However, as will be demonstrated below and is observed in TD-DFT, the performance of hybrid functionals is not transferable to charge transfer and Rydberg VEEs.

The reason the double hybrids systematically fail with low HF exchange contributions is a result of double counting static correlation through both the DFT exchange and MP2 correlation parts, which has previously been highlighted by Grimme (27). Additionally, recent findings by Santra and coworkers have indicated that double-hybrid functionals parameterized with lower HF exchange, which results in a smaller frontier orbital energy gap (198), may benefit from regularization (199), indicating that the reduced performance of double-hybrids with low HF exchange is also in-part due to the numerical consequences of the smaller orbital energy gap. The effect of the HOMO-LUMO energy gap on the relative performance of hybrid and double hybrid functionals is illustrated in fig. 4.4 for all excitation types, while figs. 4.11, 4.12, and 4.13 show the same trend broken down by excitation type. At low amounts of

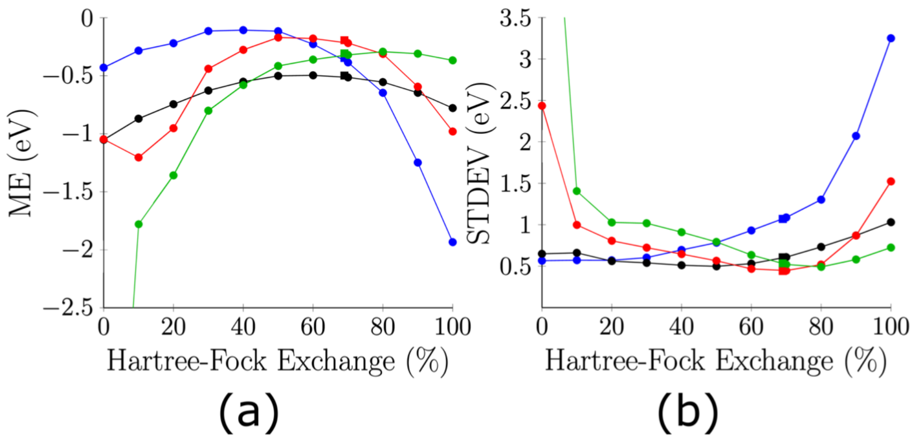

Figure 4.3. Mean error (panel a) and standard deviation (panel b) of local excitation vertical excitation energies as a function of Hartree-Fock exchange percentage for ΔPAV-DH-DFT (red), ΔDH-DFT (green), ΔPAV-DFT (blue), and ΔDFT (black) compared to benchmark values. Squares show the results at 69% Hartree-Fock exchange.

HF exchange the average frontier orbital energy gap rapidly approaches zero (black line, left axis), resulting in the mean error of both projected and unprojected double hybrid functionals (green and red lines respectively, right axis) increasing to a greater extent than either unprojected or projected hybrid functionals (black and blue respectively). Using regularization at low amounts of exact exchange, in which eq. 4.1.14 is employed with $\lambda = 1.45$, changes the mean error of ΔPAV-DH-DFT to -0.41 eV from -1.05 eV, suggesting the presence of small HOMO-LUMO gaps has an effect on the methods performance.

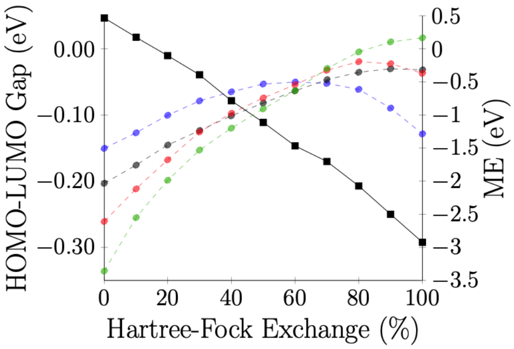

Figure 4.4. Role of exact exchange in controlling the average excited state HOMO-LUMO energy difference (black squares, left axis) and the correlation between mean error (right axis) in ΔPAV-DH-DFT (red), ΔDH-DFT (green), ΔPAV-DFT (blue), and ΔDFT (black). Graph shows results for all excitation types (local, charge transfer and Rydberg).

At high amounts of HF exchange, the projected methods drop off in performance, whether the projection is performed on the hybrid or double-hybrid functional. At

80% HF exchange and above, the unprojected ΔDH-DFT becomes the best performing methodology, while at the same HF exchange value, ΔDFT overtakes ΔPAV-DFT in performance. One reason for the failure of projection at high HF exchange values is due to the fact that symmetry breaking is greater when more HF exchange is included, potentially cause the Löwdin annihilator to fail when spin polarization of electron pairs that are not involved in the excitation occurs. When the analysis is performed excluding states where the $\langle \hat{S}^2 \rangle$ increases upon annihilation (fig. 4.9), the projected methods are found to improve slightly, but not change the qualitative results when including these ill-behaved states. The robustness of the Löwdin annihilation operator to multiple spin contaminants in both the Thiel and the Tozer benchmarks is somewhat surprising, as it is known to lead to completely incorrect behavior in the dissociation of linear H_4 (200). However, while annihilation of the $(S_z + 1)$ contaminating state that leads to an increase in $\langle \hat{S}^2 \rangle$ is a clear indicator of failure of the projection, it is also possible that even in cases where projection $\langle \hat{S}^2 \rangle$ does not increase, the contamination of unprojected higher-order spin multiplicities may still adversely affect performance. As demonstrated below for charge-transfer excitations, higher order contamination can still pay a significant role even in cases where $\langle \hat{S}^2 \rangle$ does not increase upon annihilating the $(S + 1)$ contaminating state. As a result, the reduced performance of the projected methods at high HF exchange is a consequence of the limitations of the particular form of the projector used, rather than projection generally.

The trend in standard deviation (fig. 4.3b) follows almost exactly the same trends as the mean error, with MP2 correlation corrected functionals performing worse at low HF exchange percentage and projected functionals performing worse at high HF exchange percentages. All four methods are, at some HF exchange percentage, the best performing method in terms of standard deviation. Interestingly, despite being the better performing method in terms of mean error, ΔPAV-DFT has significantly worse standard deviation than ΔDFT at all but low HF exchange percentages. The lowest standard deviation of ΔPAV-DH-DFT is achieved when the HF exchange is at 69%, indicating the default parameters are the most suitable for calculating VEEs of local excitations. As a result, the combination of low mean error and standard deviation indicates that ΔPAV-DH-DFT is the functional that will deliver the most accurate and precise results.

4.4.2.2 Charge Transfer Excitations

In this section we discuss the performance of ΔPAV-DH-DFT in describing charge transfer excitations as a function of HF exchange (fig. 4.5). In terms of mean error, the best performing functional is unprojected ΔDH-DFT (green) at 80% exact exchange, which gives a value of -0.01 eV (fig. 4.5a). The mean error of unprojected ΔDH-DFT does not change significantly from 80-100% HF exchange, and in fact at 90% the VEEs are slightly overestimated in contrast to the general trend which underestimates VEEs. At low HF exchange values, the poor performance of MP2 corrected methods that was apparent in the local excitations is also present in charge transfer excitations, causing the hybrid functionals to become the better performing functionals between

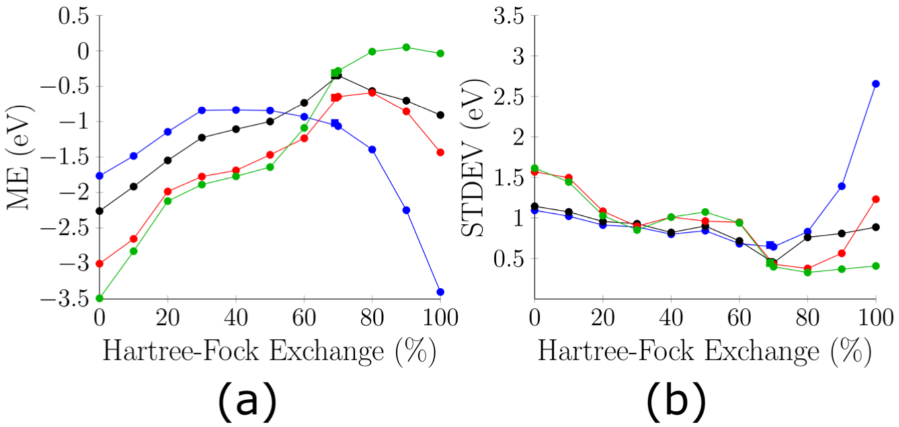

Figure 4.5. Mean error (panel a) and standard deviation (panel b) of charge transfer vertical excitation energies as a function of Hartree-Fock exchange percentage for ΔPAV-DH-DFT (red), ΔDH-DFT (green), ΔPAV-DFT (blue), and ΔDFT (black) compared to benchmark values. Squares show the results at 69% Hartree-Fock exchange.

0% and 60% HF exchange. Below 60% HF exchange, projection improves the VEE of charge transfer excitations, while at 60% HF exchange and above, projection gives worse performance as was also observed for local excitations. While the performance of ΔPAV-DFT (blue) diminishes rapidly at 60% exact exchange and above, ΔPAV-DH-DFT (red) reaches a minimum mean error of -0.59 eV at 80% HF exchange before performance diminishes. At around 70% HF exchange, the performance of hybrid and double-hybrid functionals cross, so that at 69% HF exchange (squares) used in the standard parameterization, ΔDH-DFT gives a slightly smaller mean error than ΔDFT.

In terms of standard deviation (fig. 4.5b), projection does not result in a significant change in performance below 70% HF exchange. Above 70% HF exchange, the projected hybrid functional (blue) standard deviation rapidly deteriorates, while the projected double-hybrid (red) performance is slightly worse than the unprojected functionals. For both projected and unprojected double-hybrid functionals, the standard deviation is minimized with 80% HF exchange, while for hybrid functionals, the best standard deviation is at 70%. As for local excitations, diminished performance of projection methods at high HF exchange is partly due to the limitations of the Löwdin annihilation operator used as a projector in this work. In order to establish the extent to which the projector choice affects the functional performance, the analysis was recomputed excluding excitations to states in which $\langle \hat{S}^2 \rangle$ increased upon projection (fig. 4.6). At 70% HF exchange, one data point was removed, at 80%, five data points were removed, while at 90% seven data points were removed, and at 100% eight data points were removed. As shown in fig. 4.6a, both the projected hybrid and double-hybrid mean error and standard deviation improve at 70-100% once the anomalous data points are removed. However, even removing the anomalous data points, projection still resulted in larger mean error at high HF exchange.

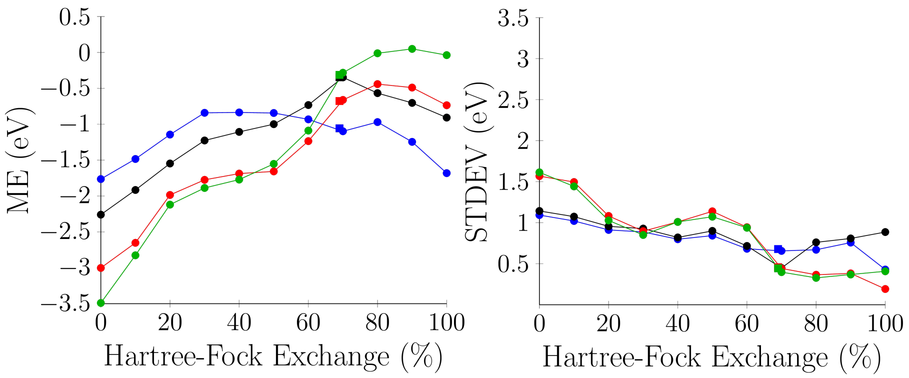

(a) (b)

Figure 4.6. Mean error (panel a) and standard deviation (panel b) of charge transfer vertical excitation energies as a function of Hartree-Fock exchange percentage for ΔPAV-DH-DFT (red), ΔDH-DFT (green), ΔPAV-DFT (blue), and ΔDFT (black) compared to benchmark values, without data in which $\langle \hat{S}^2 \rangle$ of the reference increases upon projection. Squares show the results at 69% Hartree-Fock exchange.

To further assess if the increased mean error upon projection at high exact exchange is a result of higher-order contaminating states that cannot be projected by the Löwdin annihilator, even when the value of $\langle \hat{S}^2 \rangle$ does not increase upon projection, table 4.6 shows the energy change as a result of increasing numbers of projected spin states on the unrestricted Hartree-Fock charge-transfer excited state energy. It is expected that, as higher spin states generally contribute less to contamination of symmetry-broken states, the energy change should decrease with each term in eq. 4.1.4 as higher spin states are projected, i.e. the magnitude of the values should decrease across the row from column 3 to column 6 of table 4.6. Indicated in the final column of table 4.6 is the percentage exact exchange at which the excited PBE calculation showed an increase in the value of $\langle \hat{S}^2 \rangle$ upon annihilation of the triplet state. It is expected that states for which $\langle \hat{S}^2 \rangle$ increases at some amount of exact exchange would show larger energy changes when higher spin states are projected, than states for which $\langle \hat{S}^2 \rangle$ never increases upon projection. Analyzing table 4.6 it can be seen that states for which $\langle \hat{S}^2 \rangle$ increased for some amount of Hartree-Fock exchange in the projected DFT calculations displayed greater energy change upon projection of any contaminating spin state than states for which $\langle \hat{S}^2 \rangle$ always decreased. For example, $\langle \hat{S}^2 \rangle$ always decreases upon triplet annihilation of the dipeptide $n_1 \rightarrow \pi_2^*$ state, which shows smaller energy change upon projection than in the $\pi_1 \rightarrow \pi_2$ state, for which $\langle \hat{S}^2 \rangle$ increases at 80% and above. However, even for states where $\langle \hat{S}^2 \rangle$ decreases regardless of the amount of exact exchange, the energy change upon annihilation of the $(S+2)$ contaminating state (table 4.6, column 4) is comparable to the energy change upon annihilation of the $(S+1)$ contaminating state (table 4.6, column 3). Using the dipeptide $n_1 \rightarrow \pi_2^*$ as an example again, annihilation of the (S+1) state changes the energy by -14.66 kcal mol^{-1}, while further projecting the (S+2) state increases the energy by 10.23 kcal mol^{-1} over the (S+1) annihilated state. The large

Molecule	Excitation	Energy change on annihilation of indicated spin states (kcal mol^{-1})				% exact exchange at which excited state PBE $\langle \hat{S}^2 \rangle$ increases
		$\Delta E^{\hat{A}(S+1)}_{UHF}$	$\Delta E^{\hat{A}(S+1,S+2)}_{\hat{A}(S+1)}$	$\Delta E^{\hat{A}(S+1,S+2,S+3)}_{\hat{A}(S+1,S+2)}$	$\Delta E^{\hat{A}(S+1 \ldots S+\infty)}_{\hat{A}(S+1,S+2,S+3)}$	
Dipeptide	$n_1 \rightarrow \pi_2^*$	-14.66	10.23	-0.18	-0.39	
	$\pi_1 \rightarrow \pi_2^*$	-57.31	45.30	-2.56	-0.13	80, 90, 100
β-Dipeptide	$n_1 \rightarrow \pi_2^*$	-15.12	10.53	-0.18	-0.09	
	$\pi_1 \rightarrow \pi_2^*$	-62.12	49.48	-3.12	-0.13	90, 100
PP	$2\ ^1B_2$	-12.84	19.86	-1.05	-0.06	90, 100
	$3\ ^1A_1$	-45.42	37.25	-3.43	-0.06	80, 90, 100
DMABN	^1A	-51.74	56.77	-7.31	0.18	70, 80, 90, 100
HCL	$^1\Pi$	-2.67	6.70	-0.04	-0.04	
Tripeptide	$\pi_1 \rightarrow \pi_2^*$	-9.85	16.77	-0.76	-0.07	100
	$\pi_2 \rightarrow \pi_3^*$	-57.48	45.56	-2.72	-0.13	80, 90, 100
	$\pi_1 \rightarrow \pi_3^*$	-66.01	52.72	-3.37	-0.13	80, 90, 100
	$n_1 \rightarrow \pi_3^*$	-16.41	11.31	-0.19	-0.08	
	$n_2 \rightarrow \pi_3^*$	-16.23	11.30	-0.21	-0.06	
	$n_1 \rightarrow \pi_2^*$	-16.59	11.55	-0.22	-0.53	

Table 4.6. Change in the Δ-PHF vertical excitation energy of charge transfer excitations as a function of number of annihilated spin states in kcal mol^{-1}. The final column shows the exact exchange percentages at which $\langle \hat{S}^2 \rangle$ of the excited state PBE calculation increased upon triplet annihilation $\hat{A}(S+1)$.

energy changes upon annihilation of both $(S+1)$ and $(S+2)$ demonstrates the large role these two states play in the contamination of the charge transfer excited states. Annihilation of the $(S+3)$ state, (table 4.6, column 5), has little effect on the energy for all but the most contaminated charge transfer states, eg. DMABN, while full projection reveals that contamination beyond the $(S+3)$ state is small for all states (table 4.6, column 6). Although it is not possible to directly compare the results in table 4.6 which use a symmetry broken HF determinant instead of PBE like the results in fig. 4.6, it is apparent that even in cases where $\langle \hat{S}^2 \rangle$ does not increase upon annihilation of the $(S+1)$ state, it is still possible that the $(S+2)$ state can play a large role. The use of DFT generally reduces the effect of spin contamination and so will decrease the importance of annihilating $(S+2)$ and higher states. However, the findings illustrated by fig. 4.6 and table 4.6 imply that improved performance of ΔPAV-DH-DFT requires use of a more general projector that can recouple arbitrary numbers of symmetry broken electron spin pairs.

4.4.2.3 Rydberg Excitations

Rydberg excitations are known to be challenging for TD-DFT owing to the diffuse nature of the virtual orbitals which accept an electron and are not properly described due the incorrect asymptotic behavior of the exchange-correlation contribution to the density (201). Use of exact HF exchange has been found to significantly improve the prediction of VEEs in TD-DFT calculations, although there has been little investigation of difference approaches for studying Rydberg states. Fig. 4.7 shows the performance of the four difference methods in describing VEE to Rydberg states. Examining the mean error with respect to HF exchange in fig. 4.7, it can be seen that Rydberg states show a different trend to local and charge transfer excitations, with little difference between projected and unprojected functionals, or between hy-

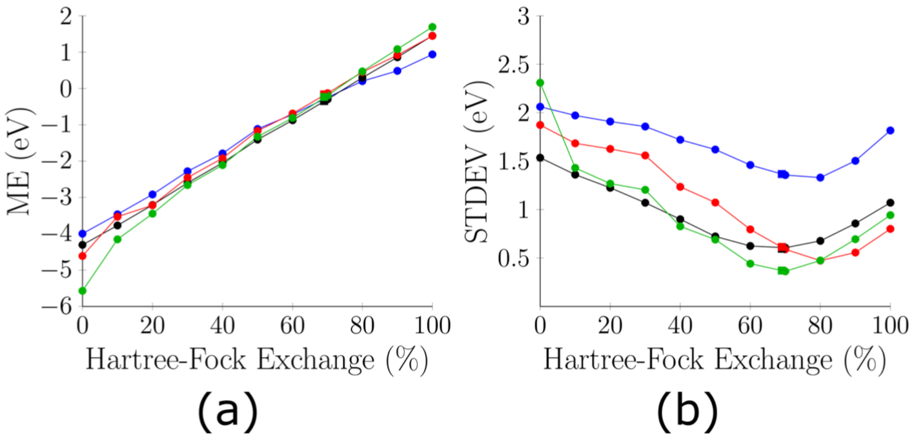

(a)

(b)

Figure 4.7. Mean error (panel a) and standard deviation (panel b) of Rydberg vertical excitation energies as a function of Hartree-Fock exchange percentage for ΔPAV-DH-DFT (red), ΔDH-DFT (green), ΔPAV-DFT (blue), and ΔDFT (black) compared to benchmark values, without data in which $\langle \hat{S}^2 \rangle$ of the reference increases upon projection. Squares show the results at 69% Hartree-Fock exchange.

brid and double-hybrid functionals, and a linear correlation between VEE and HF exchange. As a result, all functionals cross the zero mean error line between 70% and 80% HF exchange, with the MP2 corrected functionals crossing at slightly lower values (72.2% for ΔPAV-DH-DFT and 72.9% for ΔDH-DFT) than the hybrid functionals (75.5% for ΔPAV-DFT and 75.0% for ΔDFT). Due to the similar performance of all functionals in terms of mean error, the best performing functional for computing Rydberg excitations can be selected using the lowest standard deviation at the point that the mean error crosses zero (fig. 4.7b). The performance of ΔPAV-DFT is poor at all amount of HF exchange, while ΔPAV-DH-DFT only performs well at high HF exchange. MP2 correlation significantly improves the standard deviation of projected functionals, while unprojected functionals only give a noticeable difference in performance above 60% exact exchange. The best standard deviation is achieved at 70% exact exchange for unprojected methods, and at 80% exact exchange for projected methods. However, even though above 80% exact exchange, ΔPAV-DH-DFT gives the best results, which is the opposite behavior to charge transfer and local excitations, increasing HF exchange causes the performance of all functionals to diminish.

4.4.2.4 Overall Performance

The performance for all three excitation types in the Tozer benchmark is shown in fig. 4.8. The trend in mean error reflects that of local and charge transfer excitations, with projection giving better performance at low HF exchange, while the use of perturbation theory improves the result at high HF exchange. At 60-70% HF exchange, the crossover between the two effects leads to a very similar mean error in all four methods tested. Increasing the HF exchange to around 80% in unprojected double-hybrid density functional theory will lead to the lowest mean error, and the

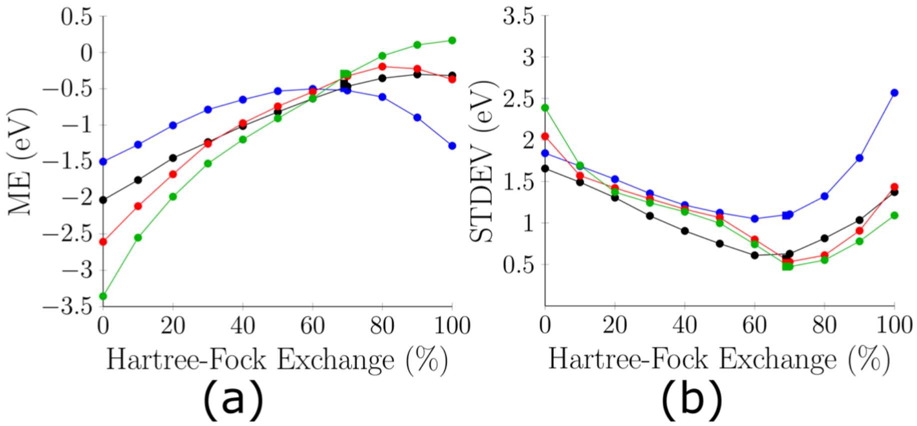

Figure 4.8. Mean error (panel a) and standard deviation (panel b) of all classes of vertical excitation energies as a function of Hartree-Fock exchange percentage for ΔPAV-DH-DFT (red), ΔDH-DFT (green), ΔPAV-DFT (blue), and ΔDFT (black) compared to benchmark values. Squares show the results at 69% Hartree-Fock exchange.

unprojected double-hybrid is the only method that crosses the zero mean error axis. The mean error for the projected double-hybrid functional is also minimized at 80% HF exchange. For unprojected hybrid functionals, the best HF exchange parameter is 100%, although this value is a consequence of error cancellation where Rydberg excitations overestimate the VEE, while local and charge transfer excitations underestimate the VEE. Projected hybrid functionals are the best choice for low HF exchange, particularly at the 15-30% range of many common hybrid functionals. However, even projected hybrid functionals would benefit from a larger amount HF exchange, around 60%, in order to minimize error in the calculation of Rydberg VEEs.

Although it is possible to tune all four functionals to obtain mean errors of -0.5 eV below the benchmark value, the standard deviation gives good reason to use double-hybrid functionals over hybrid functionals. Fig. 4.8b shows that the minimum standard deviation for double-hybrid functionals is at 70% HF exchange, while for hybrid functionals, the lowest standard deviation is at 60%. However, for unprojected hybrid functionals, the lowest mean error is at 100%, where all four functionals show increased standard deviation. For the projected hybrid functional, even though the lowest mean error and standard deviation coincide at the same HF exchange, the standard deviation is twice as large as for all three other methods. The double-hybrid functionals give similar mean error and standard deviation at both 70% and 80% HF exchange, indicating the advantage of double hybrid functionals in providing low mean error and standard deviation at the same value of HF exchange. For ΔDH-DFT, the performance limit is a mean error of 0 eV with a standard deviation of 0.5 eV. While projection gives better performance for local excitations, the failures for charge transfer states at high HF exchange means that overall it does not improve the performance. However, as the failure of projection appears to be a result of multiple contaminating states at high HF exchange which cannot be accounted for with the Löwdin annihilator, development of alternative projection formalisms may further improve the performance and yield better results than the unprojected approach across all excitation types.

The failure of the Löwdin projector at high amount of exact exchange can be emphasized by examination of the average $\langle \hat{S}^2 \rangle$ for the excited state calculation. With the standard parameterization (69%) where ΔPAV-DH-DFT performs best, the average $\langle \hat{S}^2 \rangle$ is 1.04 for local excited states, 1.07 for charge transfer states, and 1.02 for Rydberg states. These results indicate that regardless of the character of the excited state, all excitations could be characterized as breaking a single electron pair where the Löwdin projector should work well, with very little spin polarization of the remaining N-2 electrons in response to the excitation. Increasing the exact exchange to 100% gives average $\langle \hat{S}^2 \rangle$ of 1.18 for local excitations, 1.22 for charge transfer, and 1.08 for Rydberg states. As a result, it is apparent that higher amounts of exact exchange lead to greater spin contamination, although it appears that Rydberg states are less affected, suggesting that local and charge transfer states are most likely to lead to failure of the Löwdin projector.

4.4.3 Conclusions

In this section we performed a systematic investigation of the performance of difference approaches for studying different types of electronic excitations (local, charger transfer, and Rydberg). In particular, we examined how hybrid and double-hybrid functionals performed, along with the importance of including projection to account for strong correlation from breaking an electron pair in the excitation. Through evaluation using the test set of Schreiber and coworkers (exclusively local excitations), ΔPAV-DH-DFT was found to give similar quality results to LR-CC2 and EOM-CCSD. Additionally, ΔDH-DFT, which has the advantage of being size extensive, performed only marginally worse than EOM-CCSD. The advantage of ΔPAV-DH-DFT is that the scaling is noniterative $\mathcal{O}(N^5)$, compared to iterative $\mathcal{O}(N^5)$ for LR-CC2 and iterative $\mathcal{O}(N^6)$ for EOM-CCSD. Therefore ΔPAV-DH-DFT can be applied to larger systems than other approaches that give similar accuracy. It appears that ΔPAV-DH-DFT can describe excited states that are described by multiple single excitations and, although significant double excitation character appears to limit the performance of ΔPAV-DH-DFT, its performance was superior to LR-CC2 and EOM-CCSD. However, for excitations with leading double-excitation character, it is possible to use a reference that reflects the double excitation at zeroth order. A further advantage of ΔPAV-DH-DFT is that all developments applicable to the ground state for the computation of properties are also available to excited states.

Furthermore, given the known importance of using exact HF exchange for properly describing charge transfer and Rydberg excitations within the Tozer benchmarking set, we examined the role of the HF exchange parameter on controlling the mean error and standard deviation. Overall, the local excitation VEEs corroborated the findings from both benchmarking sets, which demonstrated that projected double-hybrid functionals give the smallest standard deviation. However, in the previous section, detailing the local excitations, the default HF exchange of the double-hybrid functional was used for all functionals tested. As a result, the poor performance of hybrid functionals may have been a reflection of the poor parameterization used.

When examining how different terms in the functional change the performance as a function of HF exchange, two clear trends were observed. First, at low amounts of HF exchange, MP2 correlation significantly degrades the performance of local and charge transfer VEEs. The poor double-hybrid performance with low amounts of exact exchange is a result of double counting of strong correlation, as the low amount of exact exchange implies a high amount of DFT exchange, which accounts for static correlation through inclusion of an exchange hole. In addition, low HF exchange contribution reduces the frontier orbital energy gap causing numerical issues in the correlation term, which may be partially fixed by regularization. Second, projection degrades the performance of functionals at high amounts of HF exchange due to the increased contributions of higher-order contaminating spin states which the Löwdin projector is unable to account for. Implementation of the method using alternative forms of the projector that can recouple arbitrary numbers of electron pairs may improve the performance and extend the applicability of the model to multi-electron excitations and open-shell ground states. Future work should also involve developing transition dipole moments to enable spectral simulation and work in the group is currently progressing in this direction. One of the other disadvantages of ΔPAV-DH-DFT include the requirement to identify and optimize individual excited state reference determinants and the nonorthogonality of electronic states. With the development of additional techniques for locating reference determinants and improved understanding of the global self-consistent field solution space (202), we anticipate reduced difficulties with identifying relevant excited state reference wavefunctions. The fact that we have been able to identify references associated with each of the electronic states in the test set demonstrates that many of the issues associated with finding excited state references have been partially resolved. However, the approach still requires an understanding of the character of relevant excited states, and so is not black-box like LR-CC methods. Resolving the issue of orthogonality between electronic states is more problematic. One could abandon the difference method altogether and apply linear response to the reference function and then add the correlation resulting from perturbation theory and projection. However, such an approach is likely to suffer from many of the issues that limit linear-response methods. Alternatively, it may be possible to exploit the connection between nonorthogonal configuration interaction and the projection operator, although the extension to density functional references may prove problematic due to the uncontrolled double-counting of correlation.

SUPPORTING DOCUMENTS – SYMMETRY BREAKING AND PROJECTION METHODS FOR EXCITED STATES

4.5.1 ΔPDSDPBEP86 Vertical Excitation Energies

Molecule	Excitation	Ref.	PDSDPBEP86	DSDPBEP86	PPBEP86	PBEP86	$\langle \hat{S}^2 \rangle_0$	$\langle \hat{S}^2 \hat{P} \rangle_0$	$\langle \hat{S}^2 \rangle_1$
Dipeptide	$n_1 \rightarrow \pi_1^*$	5.62	5.36	5.60	4.29	4.77	1.0167	0.1342	1.0108
	$n_2 \rightarrow \pi_2^*$	5.79	5.59	5.85	4.51	5.00	1.0176	0.1413	1.0105
β-Dipeptide	$n_1 \rightarrow \pi_1^*$	5.40	5.36	5.62	4.26	4.76	1.0189	0.1515	1.0097
	$n_2 \rightarrow \pi_2^*$	5.10	5.43	5.68	4.33	4.81	1.0189	0.1517	1.0108
PP	$1\ {}^1B_2$	4.85	5.07	4.95	5.23	5.00	1.0847	0.6733	1.2245
	$2\ {}^1A_1$	5.13	4.72	4.90	4.67	5.00	1.1027	0.8224	1.2139
DMABN	${}^1B$	4.25	4.01	4.53	3.46	4.47	1.1617	1.2357	1.1738
Tripepitde	$n_1 \rightarrow \pi_1^*$	5.74	5.41	5.67	4.33	4.82	1.0189	0.1516	1.0096
	$n_2 \rightarrow \pi_2^*$	5.61	5.61	5.87	4.54	5.03	1.0192	0.1544	1.0103
	$n_3 \rightarrow \pi_3^*$	5.91	5.67	5.92	4.57	5.06	1.0193	0.1553	1.0103
H_2CO	${}^1B_1$	8.68	8.55	8.60	7.70	7.81	1.0150	0.1198	1.0346
	${}^1A_2$	3.94	3.43	3.68	2.38	2.85	1.0228	0.1830	1.0180
N_2	${}^1\Delta_u$	10.27	12.05	9.66	14.13	10.44	1.0009	0.0074	1.4975
	${}^1\Sigma_u^-$	9.92	9.62	9.66	8.37	8.44	1.0097	0.0777	1.0315
	${}^1\Pi_g^-$	9.31	8.73	8.63	8.68	8.50	1.0182	0.1447	1.0820
CO	$D^1\Delta$	10.23	9.73	9.83	8.48	8.67	1.0093	0.0744	1.0167
	$I^1\Sigma^-$	9.88	9.73	9.83	8.48	8.67	1.0093	0.0744	1.0167
	$A^1\Pi^-$	8.51	7.89	7.27	8.21	7.09	1.0178	0.1425	1.1557
Acene (n=1)	${}^1B_{2u}$	4.88	4.43	3.97	5.19	4.39	1.0383	0.3054	1.3106
	${}^1B_{3u}$	4.46	4.53	4.72	4.54	4.91	1.1034	0.8298	1.2066
Acene (n=2)	${}^1B_{2u}$	3.69	3.26	2.90	3.89	3.27	1.0443	0.3553	1.3042
	${}^1B_{3u}$	3.89	3.81	4.20	3.56	4.31	1.1353	1.0913	1.1994
Acene (n=3)	${}^1B_{2u}$	2.90	2.48	2.18	3.03	2.49	1.0507	0.4076	1.3069
	${}^1B_{3u}$	3.52	3.84	4.00	4.12	4.43	1.0826	0.6709	1.1423
Acene (n=4)	${}^1B_{2u}$	2.35	1.96	1.69	2.43	1.95	1.0557	0.4480	1.3122
	${}^1B_{3u}$	3.27	3.15	3.34	3.35	3.71	1.0912	0.7386	1.1539
Acene (n=5)	${}^1B_{2u}$	1.95	1.56	1.30	1.99	1.54	1.0598	0.4820	1.3188
	${}^1B_{3u}$	3.09	2.58	2.80	2.71	3.13	1.1014	0.8275	1.1577
PA oligomer (n=2)	$1\ {}^1B_u$	5.92	5.71	4.65	6.76	5.07	1.0054	0.0429	1.4372
PA oligomer (n=3)	$1\ {}^1B_u$	4.95	4.67	3.87	5.54	4.25	1.0116	1.4132	0.0924
PA oligomer (n=4)	$1\ {}^1B_u$	4.41	3.99	3.40	4.70	3.73	1.0184	0.1474	1.3841
PA oligomer (n=5)	$1\ {}^1B_u$	4.27	3.52	3.09	4.11	3.38	1.0262	0.2095	1.3556

Table 4.7. ΔPAV-DSDPBEP86 results for local excitations with 69% HF Exchange where $\langle \hat{S}^2 \rangle_0$ is the $\langle \hat{S}^2 \rangle$ value from the reference, $\langle \hat{S}^2 \hat{P} \rangle_0$ is the reference $\langle \hat{S}^2 \rangle$ value after projection and $\langle \hat{S}^2 \rangle_1$ is the double hybrid $\langle \hat{S}^2 \rangle$ value

4.5.2 Linear-Response Double-Hybrid Vertical Excitation Energies

4.5.2.1 Excitation Energies of Local Excitations

Molecule	Excitation	Ref.	PDSDPBEP86	DSDPBEP86	PPBEP86	PBEP86	$\langle \hat{S}^2 \rangle_0$	$\langle \hat{S}^2 \hat{P} \rangle_0$	$\langle \hat{S}^2 \rangle_1$
Dipeptide	$n_1 \rightarrow \pi_2^*$	8.07	6.61	6.92	7.08	7.68	1.0216	0.1735	1.0093
	$\pi_1 \rightarrow \pi_2^*$	7.18	6.75	7.46	5.60	6.98	1.1011	0.7638	1.0607
β-Dipeptide	$n_1 \rightarrow \pi_2^*$	9.13	8.39	8.69	7.71	8.29	1.0216	0.1745	1.0001
	$\pi_1 \rightarrow \pi_2^*$	7.99	7.12	7.48	7.20	7.89	1.0816	0.6405	1.1087
PP	$2\ {}^1B_2$	5.47	5.56	5.63	5.66	5.79	1.0270	0.2001	1.1650
	$3\ {}^1A_1$	5.94	5.47	6.15	4.34	5.69	1.1490	1.1391	1.0719
DMABN	${}^1A$	4.56	4.11	4.34	4.01	4.44	1.1660	1.2725	1.3019
HCL	${}^1\Pi$	8.23	7.70	7.72	7.36	7.39	1.0106	0.0844	1.0362
Tripepitde	$\pi_1 \rightarrow \pi_2^*$	7.01	7.07	7.12	7.51	7.61	1.0521	0.4176	1.1366
	$\pi_2 \rightarrow \pi_3^*$	7.39	6.97	7.61	5.96	7.21	1.1038	0.7900	1.0582
	$\pi_1 \rightarrow \pi_3^*$	8.74	7.52	8.12	7.20	8.37	1.0988	0.7660	1.0667
	$n_1 \rightarrow \pi_3^*$	9.30	7.27	7.60	7.78	8.43	1.0334	0.2694	1.0055
	$n_2 \rightarrow \pi_3^*$	8.33	7.49	7.78	7.00	7.56	1.0222	0.1787	1.0038
	$n_1 \rightarrow \pi_2^*$	8.12	7.26	7.58	6.72	7.36	1.0248	0.1998	1.0012

Table 4.8. ΔPAV-DSDPBEP86 results for charge transfer excitations with 69% HF Exchange where $\langle \hat{S}^2 \rangle_0$ is the $\langle \hat{S}^2 \rangle$ value from the reference, $\langle \hat{S}^2 \hat{P} \rangle_0$ is the reference $\langle \hat{S}^2 \rangle$ value after projection and $\langle \hat{S}^2 \rangle_1$ is the double hybrid $\langle \hat{S}^2 \rangle$ value

Molecule	Excitation	Ref.	PDSDPBEP86	DSDPBEP86	PPBEP86	PBEP86	$\langle \hat{S}^2 \rangle_0$	$\langle \hat{S}^2 \hat{P} \rangle_0$	$\langle \hat{S}^2 \rangle_1$
H_2CO	${}^1A_2$	9.22	8.16	8.44	7.09	7.63	1.0316	0.2517	1.0112
	${}^1A_2$	8.38	7.94	8.17	6.91	7.36	1.0232	0.1889	1.0116
	${}^1B_2$	8.12	7.79	8.01	6.85	7.27	1.0252	0.2008	1.0150
	${}^1A_1$	7.97	9.12	7.41	10.43	7.70	0.9423	0.0136	1.3388
	${}^1B_2$	7.09	7.01	7.24	6.04	6.48	1.0226	0.1812	1.0122
N_2	${}^1\Pi_u$	13.24	13.18	12.29	14.79	13.21	1.0148	0.1171	1.2139
	${}^1\Sigma_u^+$	12.98	12.53	12.75	12.68	13.10	1.0110	0.0876	0.9985
	${}^1\Pi_u$	12.90	12.60	12.80	12.76	13.15	1.0109	0.0869	1.0025
	${}^1\Sigma_u^+$	12.20	11.88	11.99	12.18	12.39	1.0055	0.0791	1.0165
CO	$F^1\Sigma^+$	12.40	13.47	12.89	14.06	13.02	1.0135	0.1072	1.1715
	$E^1\Pi$	11.53	11.10	11.35	10.61	11.09	1.0653	0.5156	1.0478
	$C^1\Sigma^+$	11.40	10.91	11.24	10.30	10.93	1.0826	0.6541	1.0571
	$B^1\Sigma^+$	10.78	10.39	10.57	10.00	10.36	1.0639	0.5806	1.0653

Table 4.9. ΔPAV-DSDPBEP86 results for Rydberg excitations with 69% HF Exchange where $\langle \hat{S}^2 \rangle_0$ is the $\langle \hat{S}^2 \rangle$ value from the reference, $\langle \hat{S}^2 \hat{P} \rangle_0$ is the reference $\langle \hat{S}^2 \rangle$ value after projection and $\langle \hat{S}^2 \rangle_1$ is the double hybrid $\langle \hat{S}^2 \rangle$ value

4.5.2.2 Excitation Energies of Charge Transfer Excitations

Molecule	Excitation	Ref.	TD-DSDPBEP86
Dipeptide	$n_1 \rightarrow \pi_1^*$	5.62	4.89
	$n_2 \rightarrow \pi_2^*$	5.79	5.11
β-Dipeptide	$n_1 \rightarrow \pi_1^*$	5.4	4.85
	$n_2 \rightarrow \pi_2^*$	5.1	4.96
PP	$1\ {}^1B_2$	4.85	4.90
	$2\ {}^1A_1$	5.13	4.86
DMABN	${}^1B$	4.25	4.59
Tripepitde	$n_1 \rightarrow \pi_1^*$	5.74	4.86
	$n_2 \rightarrow \pi_2^*$	5.61	5.08
	$n_3 \rightarrow \pi_3^*$	5.91	5.16
H_2CO	${}^1B_1$	8.68	8.74
	${}^1A_2$	3.94	3.51
N_2	${}^1\Delta_u$	10.27	11.17
	${}^1\Sigma_u^-$	9.92	9.23
	${}^1\Pi_g^-$	9.31	9.23
CO	$D^1\Delta$	10.23	10.37
	$I^1\Sigma^-$	9.88	10.59
	$A^1\Pi^-$	8.51	8.53
Acene (n=1)	${}^1B_{2u}$	4.88	4.80
	${}^1B_{3u}$	4.46	3.91
Acene (n=2)	${}^1B_{2u}$	3.69	3.36
	${}^1B_{3u}$	3.89	3.46
Acene (n=3)	${}^1B_{2u}$	2.9	2.64
	${}^1B_{3u}$	3.52	3.03
Acene (n=4)	${}^1B_{2u}$	2.35	2.10
	${}^1B_{3u}$	3.27	3.21
Acene (n=5)	${}^1B_{2u}$	1.95	1.73
	${}^1B_{3u}$	3.09	2.69
PA oligomer (n=2)	$1\ {}^1B_u$	5.92	6.43
PA oligomer (n=3)	$1\ {}^1B_u$	4.95	5.24
PA oligomer (n=4)	$1\ {}^1B_u$	4.41	4.51
PA oligomer (n=5)	$1\ {}^1B_u$	4.27	3.99
ME			-0.19
MAE			0.38
STDDEV			0.43

Table 4.10. Local vertical excitation energy results for linear response methods, TD-DSDPBEP86 and TD-ωB2PLYP as well as inclusion of mean error, mean absolute error, and standard deviation.

Molecule	Excitation	Ref.	TD-DSDPBEP86
Dipeptide	$n_1 \rightarrow \pi_2^*$	8.07	8.54
	$\pi_1 \rightarrow \pi_2^*$	7.18	7.88
β-Dipeptide	$n_1 \rightarrow \pi_2^*$	9.13	8.20
	$\pi_1 \rightarrow \pi_2^*$	7.99	6.13
PP	$2\ ^1B_2$	5.47	4.19
	$3\ ^1A_1$	5.94	4.30
DMABN	^1A	4.56	3.73
HCL	$^1\Pi$	8.23	7.91
Tripepitde	$\pi_1 \rightarrow \pi_2^*$	7.01	6.18
	$\pi_2 \rightarrow \pi_3^*$	7.39	5.93
	$\pi_1 \rightarrow \pi_3^*$	8.74	5.68
	$n_1 \rightarrow \pi_3^*$	9.3	7.64
	$n_2 \rightarrow \pi_3^*$	8.33	4.59
	$n_1 \rightarrow \pi_2^*$	8.12	3.86
ME			-1.52
MAE			1.68
STDDEV			1.42

Table 4.11. Charge transfer vertical excitation energy results for linear response methods, TD-DSDPBEP86 and TD-ωB2PLYP as well as inclusion of mean error, mean absolute error, and standard deviation.

Molecule	Excitation	Ref.	TD-DSDPBEP86	TD-ωB2PLYP
H_2CO	${}^1A_2$	9.22	9.46	8.49
	${}^1A_2$	8.38	8.52	8.02
	${}^1B_2$	8.12	8.65	7.96
	${}^1A_1$	7.97	8.16	9.63
	${}^1B_2$	7.09	6.64	7.09
N_2	${}^1\Pi_u$	13.24	12.29	13.22
	${}^1\Sigma_u^+$	12.98	12.29	13.51
	${}^1\Pi_u$	12.9	11.86	13.73
	${}^1\Sigma_u^+$	12.2	12.00	13.73
CO	$F^1\Sigma^+$	12.4	13.08	14.09
	$E^1\Pi$	11.53	11.16	11.75
	$C^1\Sigma^+$	11.4	10.80	11.61
	$B^1\Sigma^+$	10.78	10.52	11.29
ME			-0.21	0.45
MAE			0.49	0.65
STDDEV			0.54	0.78

Table 4.12. Rydberg vertical excitation energy results for linear response methods, TD-DSDPBEP86 and TD-ωB2PLYP as well as inclusion of mean error, mean absolute error, and standard deviation.

4.5.2.3 Excitation Energies of Rydberg Excitations

Percentage of HF Exchange	Functional Component			
	PDSDPBEP86	DSDPBEP86	PPBEP86	PBEP86
0%	-1.05(2.44)	-6.38(7.38)	-0.43(0.57)	-1.05(0.65)
10%	-1.22(1.00)	-1.80(1.40)	-0.31(0.56)	-0.90(0.63)
20%	-0.95(0.81)	-1.36(1.03)	-0.22(0.57)	-0.75(0.56)
30%	-0.44(0.72)	-0.80(1.02)	-0.11(0.60)	-0.63(0.54)
40%	-0.28(0.65)	-0.58(0.91)	-0.11(0.70)	-0.55(0.51)
50%	-0.17(0.56)	-0.42(0.79)	-0.12(0.78)	-0.50(0.50)
60%	-0.18(0.47)	-0.36(0.63)	-0.23(0.93)	-0.50(0.53)
70%	-0.22(0.45)	-0.32(0.52)	-0.39(1.09)	-0.51(0.61)
80%	-0.31(0.52)	-0.29(0.49)	-0.65(1.30)	-0.55(0.73)
90%	-0.59(0.87)	-0.31(0.58)	-1.25(2.07)	-0.65(0.87)
100%	-0.98(1.52)	-0.37(0.72)	-1.93(3.25)	-0.78(1.03)

Table 4.13. Mean error and standard deviation (in parentheses), in eV, for ΔPAV-DSDPBEP86 excitation energies for local states in reference to gas phase and CASPT2/CC2 values from reference.

Percentage of HF Exchange	Functional Component			
	PDSDPBEP86	DSDPBEP86	PPBEP86	PBEP86
0%	1.81	6.49	0.55	1.05
10%	1.37	1.93	0.50	0.90
20%	1.11	1.51	0.47	0.77
30%	0.71	1.06	0.43	0.68
40%	0.61	0.90	0.47	0.63
50%	0.49	0.73	0.53	0.60
60%	0.37	0.56	0.67	0.63
70%	0.38	0.48	0.84	0.68
80%	0.47	0.49	1.13	0.76
90%	0.78	0.58	1.77	0.84
100%	1.22	0.68	2.61	0.96

Table 4.14. Mean absolute error, in eV, for ΔPAV-DSDPBEP86 excitation energies for local states in reference to gas phase and CASPT2/CC2 values from reference.

4.5.3 ΔPDSDPBEP86 Vertical Excitation Energy Mean Error and Standard Deviation

4.5.3.1 Mean Error and Standard Deviation for Local Excitations

Percentage of HF Exchange	Functional Component			
	PDSDPBEP86	DSDPBEP86	PPBEP86	PBEP86
0%	-3.00(1.57)	-3.49(1.61)	-1.76(1.09)	-2.26(1.14)
10%	-2.65(1.50)	-2.83(1.44)	-1.48(1.02)	-1.92(1.07)
20%	-1.99(1.08)	-2.12(1.03)	-1.14(0.91)	-1.55(0.96)
30%	-1.77(0.90)	-1.89(0.85)	-0.84(0.89)	-1.23(0.93)
40%	-1.69(1.01)	-1.77(1.01)	-0.84(0.80)	-1.11(0.82)
50%	-1.47(0.96)	-1.64(1.07)	-0.84(0.84)	-1.00(0.90)
60%	-1.24(0.95)	-1.09(0.94)	-0.93(0.68)	-0.73(0.72)
70%	-0.65(0.43)	-0.28(0.40)	-1.06(0.64)	-0.35(0.45)
80%	-0.59(0.38)	-0.01(0.33)	-1.39(0.83)	-0.57(0.76)
90%	-0.86(0.56)	0.05(0.37)	-2.25(1.39)	-0.70(0.81)
100%	-1.43(1.23)	-0.04(0.41)	-3.40(2.66)	-0.91(0.89)

Table 4.15. Mean error and standard deviation (in parentheses), in eV, for ΔPAV-DSDPBEP86 excitation energies for charge transfer states in reference to gas phase and CASPT2/CC2 values from reference.

Percentage of HF Exchange	Functional Component			
	PDSDPBEP86	DSDPBEP86	PPBEP86	PBEP86
0%	3.00	3.49	1.84	2.26
10%	2.65	2.83	1.57	1.92
20%	1.99	2.12	1.23	1.55
30%	1.99	2.12	1.23	1.55
40%	1.69	1.77	0.93	1.14
50%	1.66	1.64	1.01	1.06
60%	1.24	1.09	0.99	0.80
70%	0.66	0.38	1.13	0.69
80%	0.63	0.26	1.46	0.71
90%	0.90	0.32	2.30	0.85
100%	1.48	0.34	3.40	1.06

Table 4.16. Mean absolute error, in eV, for ΔPAV-DSDPBEP86 excitation energies for charge transfer states in reference to gas phase and CASPT2/CC2 values from reference.

4.5.3.2 Mean Error and Standard Deviation for Charge Transfer Excitations

Percentage of HF Exchange	Functional Component			
	PDSDPBEP86	DSDPBEP86	PPBEP86	PBEP86
0%	-2.05(1.82)	-2.54(1.85)	-1.27(1.26)	-1.48(1.12)
10%	-2.35(0.92)	-2.51(0.89)	-1.36(0.94)	-1.59(0.72)
20%	-1.15(1.31)	-1.24(1.23)	-0.54(1.50)	-0.67(1.42)
30%	-1.28(1.18)	-1.39(1.20)	-0.27(1.50)	-0.43(1.50)
40%	-1.40(1.03)	-1.49(1.000)	-0.32(1.65)	-0.45(1.55)
50%	-0.86(1.39)	-0.87(1.33)	-0.14(1.32)	-0.15(1.15)
60%	-0.80(0.77)	-0.69(0.69)	-0.40(1.01)	-0.18(0.72)
70%	-0.66(0.44)	-0.28(0.40)	-1.10(0.66)	-0.36(0.42)
80%	-0.47(0.35)	0.00(0.34)	-1.13(0.81)	-0.35(0.46)
90%	-0.49(0.38)	0.05(0.37)	-1.25(0.76)	-0.49(0.52)
100%	-0.74(0.19)	-0.04(0.41)	-1.68(0.43)	-0.69(0.59)

Table 4.17. Mean error and standard deviation (in parentheses), in eV, for ΔPAV-DSDPBEP86 excitation energies for charge transfer states, without data in which the $\langle \hat{S}^2 \rangle$ of the reference increases upon projection in reference to gas phase and CASPT2/CC2 values.

Percentage of HF Exchange	Functional Component			
	PDSDPBEP86	DSDPBEP86	PPBEP86	PBEP86
0%	-4.61(-1.87)	-5.57(-2.31)	-4.00(-2.06)	-4.30(-1.54)
10%	-3.53(-1.68)	-4.15(-1.43)	-3.46(-1.97)	-3.77(-1.36)
20%	-3.22(-1.63)	-3.45(-1.27)	-2.92(-1.91)	-3.21(-1.22)
30%	-2.45(-1.56)	-2.66(-1.20)	-2.28(-1.86)	-2.60(-1.07)
40%	-1.92(-1.23)	-2.11(-0.83)	-1.79(-1.72)	-2.05(-0.90)
50%	-1.17(-1.07)	-1.33(-0.69)	-1.12(-1.62)	-1.41(-0.72)
60%	-0.69(-0.80)	-0.81(-0.44)	-0.71(-1.46)	-0.87(-0.62)
70%	-0.13(-0.59)	-0.20(-0.36)	-0.25(-1.36)	-0.30(-0.61)
80%	0.45(-0.47)	0.47(-0.47)	0.20(-1.33)	0.30(-0.68)
90%	0.92(-0.56)	1.08(-0.69)	0.48(-1.50)	0.86(-0.86)
100%	1.45(-0.80)	1.69(-0.94)	0.94(-1.82)	1.45(-1.07)

Table 4.18. Mean error and standard deviation (in parentheses), in eV, for ΔPAV-DSDPBEP86 excitation energies for rydberg states in reference to gas phase and CASPT2/CC2 values from reference.

4.5.3.3 Mean Error and Standard Deviation for Rydberg Excitations

4.5.4 ΔPDSDPBEP86 Local and Rydberg Vertical Excitation Energy Mean Error and Standard Deviation Excluding Excitations where $\langle \hat{S}^2 \rangle$ Increases After Annihilation of $S + 1$ State

Percentage of HF Exchange	Functional Component			
	PDSDPBEP86	DSDPBEP86	PPBEP86	PBEP86
0%	4.61	5.57	4.15	4.30
10%	3.53	4.15	3.68	3.77
20%	3.27	3.45	3.18	3.21
30%	3.27	3.45	3.18	3.21
40%	2.12	2.11	2.28	2.05
50%	1.50	1.39	1.84	1.43
60%	0.99	0.86	1.48	0.94
70%	0.46	0.29	1.12	0.53
80%	0.51	0.61	1.14	0.58
90%	0.92	1.13	1.34	0.94
100%	1.45	1.72	1.69	1.46

Table 4.19. Mean absolute error, in eV, for ΔPAV-DSDPBEP86 excitation energies for Rydberg states in reference to gas phase and CASPT2/CC2 values from reference.

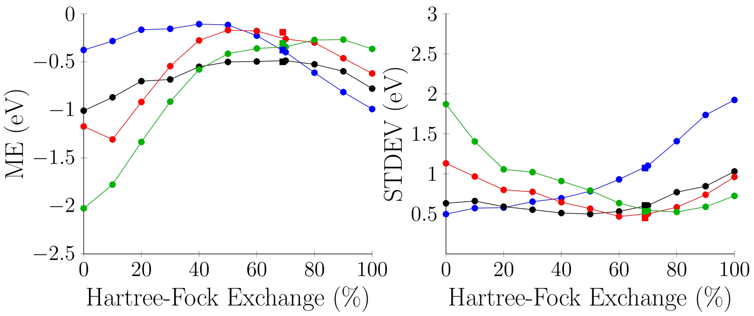

(a) (b)

Figure 4.9. Mean error (panel a) and standard deviation (panel b) of local excitation vertical excitation energies as a function of Hartree-Fock exchange percentage for ΔPAV-DH-DFT (red), ΔDH-DFT (green), ΔPAV-DFT (blue), and ΔDFT (black) compared to benchmark values, without data in which $\langle \hat{S}^2 \rangle$ of the reference increases upon projection. Squares show the results at 69% Hartree-Fock exchange.

4.5.5 Correlation Between Average HOMO-LUMO Gap and Mean Error in Difference Double Hybrid Functional Theory

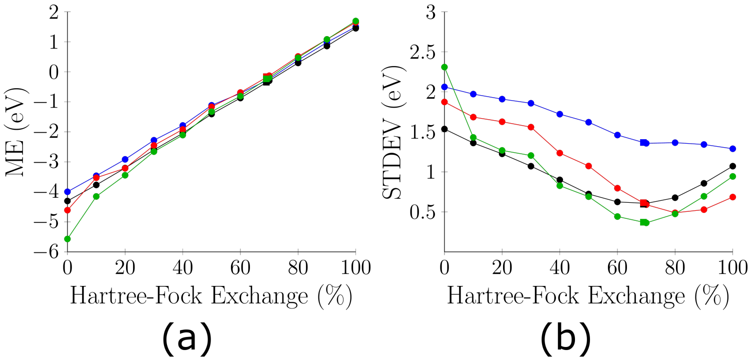

Figure 4.10. Mean error (panel a) and standard deviation (panel b) of Rydberg excitation vertical excitation energies as a function of Hartree-Fock exchange percentage for ΔPAV-DH-DFT (red), ΔDH-DFT (green), ΔPAV-DFT (blue), and ΔDFT (black) compared to benchmark values, without data in which $\langle \hat{S}^2 \rangle$ of the reference increases upon projection. Squares show the results at 69% Hartree-Fock exchange.

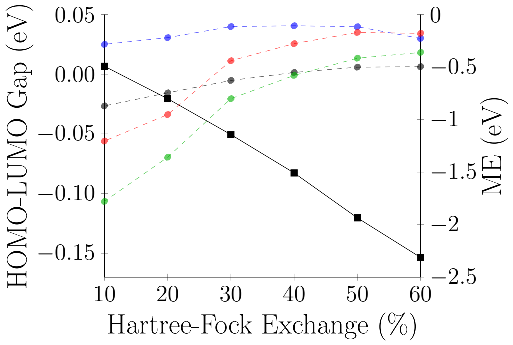

Figure 4.11. Role of exact exchange in controlling the average HOMO-LUMO energy difference (black squares, left axis) and the correlation between mean error (left axis) in ΔPAV-DH-DFT (red), ΔDH-DFT (green), ΔPAV-DFT (blue), and ΔDFT (black) for local excitations.

4.5.6 Workflow and Gaussian keywords for obtaining initial guesses in difference self-consistent field methods

To compute Δ SCF and Δ post-SCF vertical excitation energies, two different SCF must be obtained for each state of interest. Assuming one of the states is the ground state, the work flow for identifying these states is as follows:

1. Perform a restricted or restricted open-shell SCF optimization to find the closed shell representation of the ground state that preserves orbital symmetries where present.

2. Perform orbital swaps on the restricted representation of the ground state to obtain the restricted or restricted open-shell initial guess of the excited state of interest. In Gaussian, orbital swaps can be performed using the guess=alter keyword.

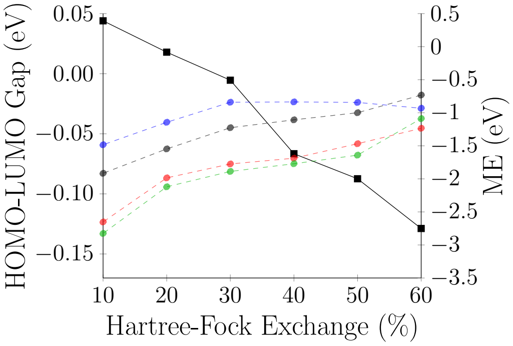

Figure 4.12. Role of exact exchange in controlling the average HOMO-LUMO energy difference (black squares, left axis) and the correlation between mean error (left axis) in ΔPAV-DH-DFT (red), ΔDH-DFT (green), ΔPAV-DFT (blue), and ΔDFT (black) for charge transfer excitations.

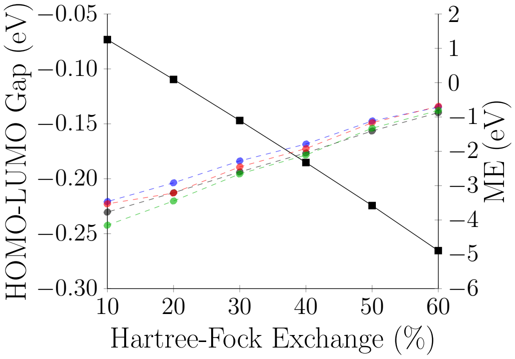

Figure 4.13. Role of exact exchange in controlling the average HOMO-LUMO energy difference (black squares, left axis) and the correlation between mean error (left axis) in ΔPAV-DH-DFT (red), ΔDH-DFT (green), ΔPAV-DFT (blue), and ΔDFT (black) for Rydberg excitations.

3. Perform a local SCF optimization of the restricted or restricted open shell excited state initial guess to obtain the unrestricted excited state SCF solution. A modified version of Gaussian is required to prevent variational collapse.

4. Perform analysis of the orbital rotation Hessian and follow any *ov* orbital rotation eigenvectors that lower the energy in order to obtain the unrestricted ground state SCF solution. In Gaussian, the stability eigenvector test and eigenvector following can be accomplished with the stable=opt keyword.

5. Projected double-hybrid density functional theory has been implemented in Gaussian 16 and subsequent versions. Performing projected double-hybrid density functional theory on excited states may require the Gaussian keyword IOp(8/11=1) to avoid errors in the case of negative frontier orbital energy gaps.

This keyword will only print a warning in the case of small orbital energy gaps which leads to divergences in the second order energy correction.

CHAPTER 5

APPLICATION OF NONORTHOGONAL METHODS FOR EFFICIENT MODELING OF STRONGLY CORRELATED SYSTEMS

Introduction

[1]

Strong correlation, otherwise known as non-dynamical or static correlation, arises when an electronic state does not have a well-defined set of occupied orbitals. As a result, the wavefunction is an entangled superposition of electron configurations, with permanent interactions between electrons at fractionally occupied sites that occur over long distances. A challenge in the development of electronic structure methods that are able to account for strong correlation is the identification of the relevant correlated orbital space $\{|\psi_i\rangle\}$ (203). Once the correct orbital subspace has been identified, accounting for the interactions between all N sites can be performed numerically by solving for the wavefunction in the Hilbert space $\mathcal{H}$ constructed as the tensor product of $\{|\psi_i\rangle\}$

$$\mathcal{H} = \bigotimes_{i}^{N} |\psi_i\rangle \tag{5.1.1}$$

which leads to $\mathcal{O}(N!)$ scaling in the dimensionality of $\mathcal{H}$. Due to the factorial scaling with the number of strongly correlated sites, it is desirable to minimize the value of N. Through *oo* and virtual-virtual (*vv*) orbital transformations, it is possible to minimize the expansion in eq. 5.1.1 by 'concentrating' the strong correlation in as small a subset of orbitals as possible. Löwdin was the first to recognize that the smallest possible orbital subset that recovers the strong correlation is the fractionally occupied natural orbitals (NOs) of the full configuration interaction (FCI) density (145). In order to establish the correct subset of orbitals without resorting to their explicit calculation, Pulay and coworkers developed unrestricted natural orbitals (UNO) approach, in which the fractionally occupied NOs of symmetry broken self-consistent field density matrices are used (204; 205). While it is known that symmetry breaking in mean-field wavefunctions is a marker of strong correlation, only recently has it been possible to demonstrate the validity of the UNO approach by comparison with the very large active spaces afforded by density matrix renormalization group (DMRG) (206).

Despite the success of the UNO approach, difficulties are encountered in the presence of multiple correlation mechanisms (MCMs). MCMs can be defined as situations in which one or more strongly correlated occupied orbitals has multiple correlation partners (205; 206). An alternative definition of MCMs is that all possible reference SCF solutions have fractionally occupied NOs that describe only a subspace of the FCI NOs, such that any determinant expansion in one of the SCF solution NOs is unable to span the strongly correlated subspace of the FCI Hilbert space. As a result, strong correlations in wavefunctions with MCMs cannot be treated by projection-after-variation methods or standard UNO approaches, because SCF symmetry breaking cannot fully reveal the set of strongly correlated orbitals. Early in the development of the UNO method, it was noted that multiple correlation mechanisms are signaled by the presence of several nearly-degenerate SCF solutions. To resolve this issue in the UNO framework, the NOs of the averaged density matrices were used (206). While the averaged-density UNO method enables the identification of the minimum required subset of orbitals to describe the strong correlation, the approach still has factorial scaling in the number of correlated orbitals according to eq. 5.1.1. A question that arises is whether the partitioning of the wavefunction indicated by different SCF solutions can be utilized in a different way that avoids the factorial scaling in the correlated orbital space. In other words, can interactions between correlated mechanisms be treated differently to interactions within correlation mechanisms in such a way that the method scales polynomially with the number of correlation mechanisms?

---

[1] This chapter is adapted with permission from Kempfer-Robertson, E. M., Mahler, A. D., Haase, M. N., Roe, P., & Thompson, L. M. Nonorthogonal Active Space Decomposition of Wave Functions with Multiple Correlation Mechanisms. The Journal of Physical Chemistry Letters 13, 12041-12048 (2022). Copyright 2022 American Chemical Society.

THEORY AND COMPUTATIONAL DETAILS

In this chapter, we propose to couple together separate UNO expansions through nonorthogonal Hamiltonian blocks, which can dramatically reduce the scaling of the required wavefunction expansion. The proposed nonorthogonal active space decomposition (NO-ASD) approach is related to several other methods, including active space decomposition (207), block-localized wavefunction (208), molecular orbital-valence bond theory (209), NOCI-F (210), and constrained constrained density functional theory configuration interaction (CDFTCI) (211), in that fragment wavefunctions are constructed and used to partition a CI active space. However, the proposed approach differs as the fragments are defined entirely self-consistently, rather than using arbitrary constraints or spatial partitioning of the molecule. Instead of solving for the wavefunction in the Hilbert space defined by eq. 5.1.1, the wavefunction is determined in the Hilbert space formed from the direct sum of the separate UNO expansions on each SCF solution

$$\mathcal{H} = \bigoplus_{I}^{N_{\mathrm{CM}}} \left(\bigotimes_{i}^{N_I} |{}^I\psi_i\rangle \right) \tag{5.2.1}$$

where the index I indicates the correlation mechanism. As a result, the formulation in eq. 5.2.1 properly treats entanglement between orbitals within each correlation mechanism, but gives an unentangled superposition of different correlation mechanisms. However, because each correlation mechanism is generally constructed from a set of orbitals that are nonorthogonal to the set of orbitals in other correlation mechanisms, orbitals in each correlation mechanism can be expressed as disconnected single excitation cluster operators acting to infinite order in the basis of a common set of orthogonal orbitals (155). As a result, entanglement between orbitals in different correlation mechanisms that is not formally included in the determinant expansion is implicitly wrapped in. Therefore, NO-ASD recovers entanglement through an effective Hamiltonian approach, in contrast to explicit tensor decomposition (212). It is important to note that the full tensor product in eq. 5.2.1 may produce larger determinant expansions than necessary, and these additional determinants may in fact lead to greater errors. As demonstrated in the context of multistate DFT, a minimal active space with half-projection of open-shell determinants is all that should be required (213; 214; 215). However, here we opt for complete active space (CAS) expansions is to ensure the connection with the active space decomposition philosophy embodied by eq. 5.2.1 and to enable direct comparison with CAS wavefunctions.

The workflow of performing the NO-ASD scheme is as follows: First, the relevant set of SCF solutions must be identified. In this regard, UNO and NO-ASD approaches are equivalent in the extent to which they are black-box. More generally, understanding and identifying relevant SCF solutions is still a challenge and an active area of research (216; 217), with several local SCF optimization techniques and global searching algorithms having been developed in recent years (218; 219; 147; 220; 221; 22; 195). Typically, the nearly-degenerate low-energy SCF solutions are the relevant set, which simplifies solution identification. Subsequently, from the identified SCF solutions, a determinant CAS expansion is constructed in the fractionally occupied set of NOs for each SCF solution. The resulting orthogonal determinant expansions are then coupled using NOCI (fig. 5.1). In section 2.3.5, the NOCI methodology is discussed in the AO basis. This work however, utilizes the MO basis where the molecular orbitals are fixed, and the CI coefficients are linearly optimized. As described in section 2.3.5, nonorthogonal Hamiltonian matrix elements can be computed according to the generalized Slater-Condon rules (222; 223) and the energy determined by solving the generalized eigenvalue problem

$$\mathbf{HD} = \mathbf{NDE} \tag{5.2.2}$$

where $\mathbf{H}$ is the Hamiltonian matrix, $\mathbf{N}$ is the Slater determinant or configuration state function overlap matrix, and $\mathbf{D}$ and $\mathbf{E}$ are the eigenvectors and eigenvalues respectively. The NO-ASD wavefunction for state A is then written as

$$\Psi_A = \sum_{I}^{N_{CM}} \left({}^{IA}D_0 |{}^{I}\Psi_0\rangle + \sum_{ux} {}^{IA}D_{ux} |{}^{I}\Psi_u^x\rangle + \sum_{uvxy} {}^{IA}D_{uvxy} |{}^{I}\Psi_{uv}^{xy}\rangle + \sum_{uvwxyz} {}^{IA}D_{uvxyz} |{}^{I}\Psi_{uvw}^{xyz}\rangle + \dots \right) \tag{5.2.3}$$

where $u, v, x \dots$ indicate active space orbitals that are occupied in the reference determinant $|{}^{I}\Psi_0\rangle$, $x, y, z \dots$ are active space orbitals that are virtual in the reference determinant, and $\{D\}$ are the CI coefficients. Evaluation in the AO basis yields a maximum $\mathcal{O}(N_{\text{basis}}^4)$ scaling for each matrix element, although in practice diagonal blocks can be computed using standard orthogonal CI techniques, and matrix elements in off-diagonal nonorthogonal blocks only need to be evaluated if the number of occupied orbitals with zero overlap between determinants is less than or equal to two, where the overlap can be evaluated at $\mathcal{O}(N_{\text{elec}}^3)$ cost.

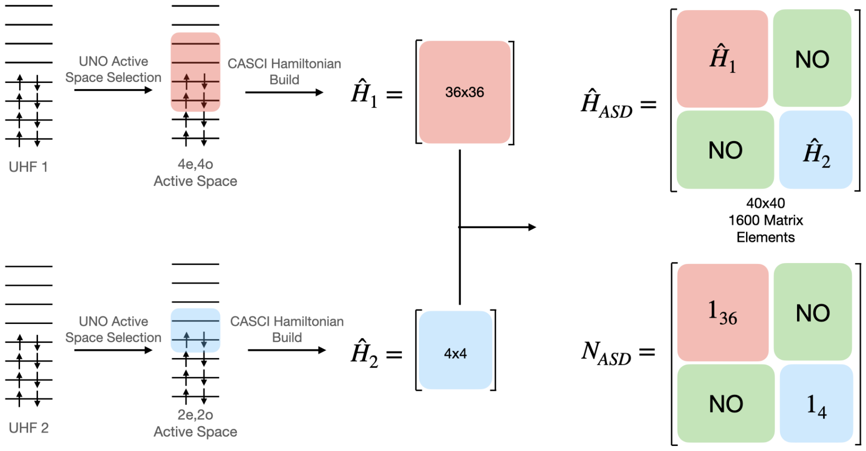
UNO Active Space Selection
CASCI Hamiltonian Build
$\hat{H}_1 =$
36x36
UHF 1
4e,4o Active Space
$\hat{H}_{ASD} =$
$\hat{H}_1$
NO
NO
$\hat{H}_2$
40x40 1600 Matrix Elements
UNO Active Space Selection
CASCI Hamiltonian Build
$\hat{H}_2 =$
4x4
UHF 2
2e,2o Active Space
$N_{ASD} =$
1_{36}
NO
NO
1_4

Figure 5.1. Schematic for formation of the nonorthogonal active space decomposition scheme Hamiltonian $\hat{H}_{ASD}$ and overlap N_{ASD} indicating diagonal block orthogonal and off-diagonal block nonorthogonal components.

Given the nature of the determinant expansion in NO-ASD, a more effective algorithm is to evaluate matrix elements in the nonorthogonal blocks in the MO basis, owing to the fact that only a single integral transformation at $\mathcal{O}(N_{\text{basis}}^5)$ cost is required for each pair of correlation mechanisms included in the calculation. The subsequent contractions required to compute matrix elements are then reduced to $\mathcal{O}(N_{\text{occ}}^4)$. The rules for matrix elements in the MO basis are as follows:

$$ {}^{IJ}H = \begin{cases} {}^{IJ}N\left(\sum_{ij} {}^{IJ}h_{ij} {}^{IJ}M_{ji}^{-1} + \frac{1}{2}\sum_{ijkl} {}^{IJ}\langle ij||kl\rangle {}^{IJ}M_{ki}^{-1} {}^{IJ}M_{lj}^{-1} \right) & \text{for } \dim(\ker({}^{IJ}\mathbf{M})) = 0 \\ {}^{IJ}\tilde{N}\left(\sum_{ij} {}^{IJ}h_{ij} U_{ip} V_{jp} + \sum_{ijkl} {}^{IJ}\langle ij||kl\rangle U_{jp} V_{lp} {}^{IJ}M_{ki}^{+} \right) & \text{for } \dim(\ker({}^{IJ}\mathbf{M})) = 1 \\ {}^{IJ}\tilde{N} \sum_{ijkl} {}^{IJ}\langle ij||kl\rangle U_{iq} U_{jp} V_{kq} V_{lp} & \text{for } \dim(\ker({}^{IJ}\mathbf{M})) = 2 \\ 0 & \text{for } \dim(\ker({}^{IJ}\mathbf{M})) > 2 \end{cases} \tag{5.2.4} $$

where $i, j, k \ldots$ are occupied orbital indices, $p, q, r \ldots$ are indices of biorthogonalized orbitals with zero overlap between determinants I and J, $\dim(\ker({}^{IJ}\mathbf{M}))$ indicates the size of the null space (number of biorthogonalized orbitals with zero overlap) of the *oo* overlap matrix ${}^{IJ}\mathbf{M}$, which is computed as

$$ {}^{IJ}\mathbf{M} = {}^{I}\mathbf{C}_{\text{occ}}^{\dagger}\mathbf{S}\,{}^{J}\mathbf{C}_{\text{occ}} \tag{5.2.5} $$

${}^{IJ}\tilde{N}$ is the reduced overlap, computed from the pseudodeterminant of ${}^{IJ}\mathbf{M}$, ${}^{IJ}\mathbf{M}^{+}$ indicates the Moore-Penrose pseudoinverse of ${}^{IJ}\mathbf{M}$, h_{ij} and $\langle ij||jk\rangle$ are one-electron and antisymmetrized two-electron integrals in the MO basis respectively, and the matrices $\mathbf{U}$ and $\mathbf{V}$ are computed from singular value decomposition of ${}^{IJ}\mathbf{M}$

$$ {}^{IJ}\mathbf{M} = \mathbf{U}\,{}^{IJ}\boldsymbol{\sigma}\mathbf{V}^{\dagger} \tag{5.2.6} $$

Very recent work by Burton invoking a nonorthogonal generalized Wick's theorem has been shown to further reduce the scaling to be independent of system size entirely (224; 225). Although the generalized Wick's theorem approach requires storage of a large number of sets of transformed two-electron integrals and so has a greater memory cost than the MO basis calculation presented, the reduction in the cost of subsequently evaluating each matrix element from $\mathcal{O}(N_{\text{occ}}^4)$ to $\mathcal{O}(1)$ has the potential to significantly extend the size of NO-ASD determinant expansions.

A well-known issue with the selection of the active space based on occupation number thresholds is the presence of discontinuities in the PES. In fact, these discontinuities are present in all multiconfigurational calculations (204; 226). To minimize threshold-based discontinuities, the same approach could be used in NO-ASD as in UNO, in which natural orbitals are computed at the geometry which gives the largest active space, and then the identified active space used across the entire PES. Alternatively, natural orbitals of half-projected determinants may also ameliorate discontinuities (227). However, natural orbitals of individual symmetry broken SCF solutions typically display greater fractional occupation (lower levels of intermediate correlation) than the averaged density, and so NO-ASD is less likely to suffer from the choice of threshold than averaged density UNO methods (section S5.6). A related issue that leads to discontinuities is the disappearance of SCF solutions as the geometry changes, which is fundamentally related to changes in the correlation mechanisms that are acting at a given geometry. As the relevant SCF solutions are the same in UNO and NO-ASD, both methods are likely to be affected by disappearing solutions to the same extent. However, using holomorphic solutions (228; 229) or coupled-determinant orbital reoptimization (230) may provide a solution to resolve the effect of vanishing solutions.

In the remainder of this work, NO-ASD results are compared to average-density UNO-CI and UNO-CAS results. The goal is to establish the extent to which the decomposition in eq. 5.2.1 affects the performance with respect to results from large active space CASSCF and DMRG calculations. The systems studied are the highly multireference ozone molecule, and transition-metal containing species nickel-acetylene and ammonia μ-oxo dicopper ammonia (geometries can be found in tables 5.4-5.7). The cc-PVTZ basis set was used for ozone and ni-acetylene calculations and cc-PVDZ basis set was used for μ-oxo dicopper ammonia calculations. The for the occupation number thresholds for NO-ASD were 0.02-1.98 and 0.01-1.99 for ozone, 0.02-1.98 for ni-acetylene, and 0.02-1.98 for μ-oxo dicopper. The code was implemented in a standalone in-house code that utilizes the MQCPack library (197) as well as interfacing with a modified version of Gaussian 16 (89).

RESULTS

We first consider the ozone system, in which two stable UHF solutions differing by 0.085 Hartree describe the correlation mechanisms within the system (labeled UHF 1 and UHF 2 in table 5.8 which shows occupation numbers (ONs) of NOs of all methods discussed here). Both SCF solutions have two fractionally occupied NOs

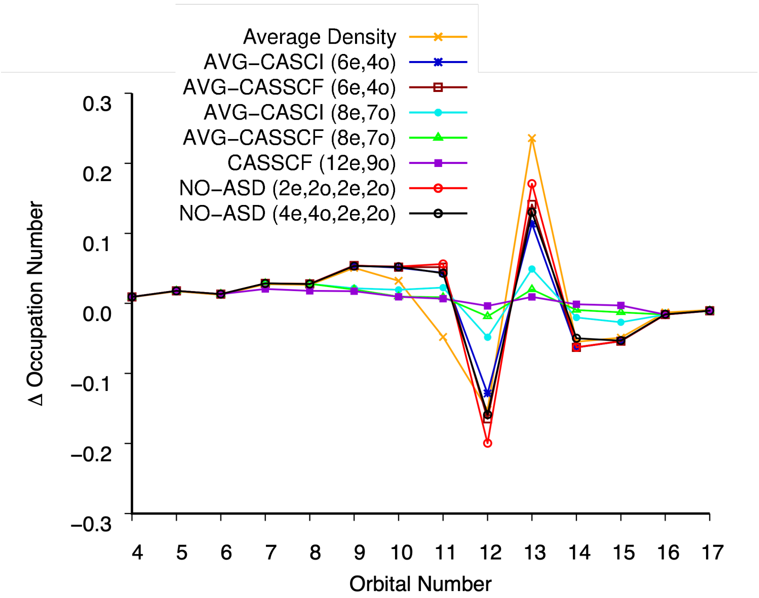

Figure 5.2. Occupation numbers of valence natural orbitals in ozone compared with a full valence DMRG for different methods indicated in the legend with the cc-pVTZ basis set.

(ONs between 0.02 and 1.98), although UHF 2 has more diradical character than UHF 1. As a result, the correlation mechanism described in UHF 1 is $n \rightarrow \pi^*$, while UHF 2 shows $\sigma \rightarrow \pi^*$ character (fig. 5.5). In contrast, the NOs of large active space CASSCF calculations (12 electrons in 9 orbitals) and DMRG calculations indicate that the fractionally occupied NO space contains 7 and 9 orbitals respectively. As discussed by Pulay (206), only two of these fractionally orbitals lie in the strong correlation regime, while the remaining orbitals have ONs close to the closed shell limit and so can be considered as intermediately correlated. ONs from the averaged density of the two SCF solutions indicate four fractionally occupied orbitals, where coupling of the two correlation mechanisms results in doubling of the required active space.

Fig. 5.2 illustrates how the ONs of the different methods examined compare with DMRG, where more positive (negative) ONs for low (high) orbital indices indicates a shift towards closed shell, and the HOMO orbital is index 12, while the LUMO orbital is index 13. The averaged density NO ONs (orange cross), show that orbitals 10 and 11 are the additional fractionally occupied NOs because their value is similar to or less than the DMRG NO. The resulting six electron in four orbital active space can be treated through either using complete active space configuration interaction (CASCI) (205) or CASSCF (204). Interestingly, the NO analysis of the CASCI (blue star) and CASSCF (brown open square) densities suggests that there are only three and two orbitals respectively in the correlated orbital space. Changing the criteria for fractionally occupied orbitals to ONs between 0.003 and 1.997 to capture additional intermediate correlation, leads to an eight electron in seven orbital active space (CASCI – cyan solid circles, CASSCF – green solid triangles). Including these additional orbitals gives ONs that are much closer to the DMRG and CASSCF using 12 electrons in 9 orbitals (purple solid square), with a seven orbital correlated space. Using the 0.02-1.98 NO criteria for the fractionally occupied orbitals leads to a NO-ASD(2e,2o;2e,2o) active space (red open circles), i.e. a two electron in two orbital expansion in the orbitals of UHF 1, and the same in the orbitals of UHF 2. Using NO 0.01-1.99 as the criteria leads to NO-ASD(4e,4o;2e,2o), with four orbitals from UHF 1 in the correlated space (black open circles). Both the NO-ASD calculations give NO ONs that are close to the CASCI(6,4) and CASSCF(6,4) results, with the NO-ASD(4e,4o;2e,2o) very closely reproducing the CASSCF(6,4) results.

Table 5.1 shows how the number of Hamiltonian matrix elements of each method correlates with the correlation energy remaining, assuming DMRG gives the exact result. Orbital reoptimization of CAS six electron in four orbital active space only reduces the energy by 2.6 kcal mol^{-1}, although with the eight electron in seven orbital active space, the difference was 28.2 kcal mol^{-1}, suggesting that the NOs of intermediate correlated orbitals change their shape to a greater extent than the strongly correlated orbitals. Increasing the active space from six electrons in four orbitals, to eight electron in seven orbitals increases the number of matrix elements from 10^2 to 10^6, with the correlation energy error decreasing by 49.4 kcal mol^{-1} for fixed orbitals, and 75.0 kcal mol^{-1} for reoptimized orbitals. Increasing the active space to twelve electrons in nine orbitals leads to an order of magnitude increase in the number of Hamiltonian matrix elements, while the correlation energy error decreases by only 8.4 kcal mol^{-1} and remains 157.8 kcal mol^{-1} compared to the full valence active space DMRG calculation. In comparison, the NO-ASD(2e,2o;2e,2o) method with only 64 Hamiltonian matrix elements gives results comparable to CAS(6e,4o), which is has four times as many elements. When the stricter criteria for determining fractional occupied orbitals are used, the NOASDC(4e,4o;2e,2o) reduces the correlation energy error by 10.2 kcal mol^{-1} even though the number of matrix elements increases just over six-fold.

The second system investigated is nickel-acetylene, which was identified by Keller and coworkers as possessing two correlation mechanisms (206). The two correlation mechanisms in nickel-acetylene are represented by two UHF solutions, that differ in energy by just 1.03 kcal mol^{-1} using the cc-PVTZ basis set (table 5.9). The higher energy solution (labelled UHF 1 in table 5.9) involves the bonding and antibonding orbital pair consisting of Ni d_{xy} and acetylene π^*_y orbital fragments. The UHF 2 correlation mechanism involves the interaction of orbitals from UHF 1 with the Ni d^2_z and Ni 3s orbitals (fig. 5.6). Fig. 5.3 shows how the ONs of NOs differ from a DMRG(18e,33o) calculation for the methods discussed in the remainder of this paragraph. Orbital 21 is the HOMO orbital index and orbital 22 is the LUMO orbital index. UHF 1 indicates a two electron in two orbital correlated space, while UHF 2 indicates a four electron in four orbital active space. The NO ONs of the DMRG calculation indicate a thirteen orbital correlated space is required, although all but four of these orbitals are in the intermediately correlated regime. The averaged density from the two UHF solutions (orange crosses) gives NO ONs that suggest a four electrons in four orbital correlated space. Performing CASCI(4e,4o) with the strongly

Method	# Hamiltonian matrix elements	ΔE (kcal mol^{-1})
^{a}DMRG 18e,32o	6.189x10^{29}	0.0
CASSCF 12e,9o	4.978x10^{7}	157.8
^{a}UNO-CASCI 8e,7o (AVG)	1.501x10^{6}	194.4
^{a}UNO-CASSCF 8e,7o (AVG)	1.501x10^{6}	166.2
^{a}UNO-CASCI 6e,4o (AVG)	256	243.8
^{a}UNO-CASSCF 6e,4o (AVG)	256	241.2
NO-ASD 2e,2o;2e,2o	64	242.4
NO-ASD 4e,4o;2e,2o	1,600	233.6

Table 5.1. Number of Hamiltonian matrix elements and error in correlation energy with respect to full valence DMRG calculation for different methods in the calculation of ozone using the cc-pVTZ basis set. ^{a}Results from ref. 206.

correlated NOs of the average density matrix (blue stars) leads to a density matrix with ONs that improve marginally on the UHF averaged density. Reoptimizing the orbitals in a CASSCF(4e,4o) calculation (green open squares), significantly improves the density, giving much closer agreement to DMRG in the ONs of the four strongly correlated NOs, although the intermediately correlated orbitals are not identified and remain closed shell. Capturing the intermediately correlated orbitals requires a twelve electron in fourteen orbital calculation, using an NO threshold of 0.001-1.999, in which there is no significant difference in the NO ONs regardless of whether fixed orbitals (cyan solid circles) or reoptimized orbitals (purple solid squares) are used. The NO-ASD(2e,2o;4e,4o) suggested by the NO ONs of the UHF solutions (red open circles) gives a significant improvement over the CASCI(4e,4o) calculation, indicating the additional two electron in two orbital active space in NO-ASD replicates orbital reoptimization in CASSCF(4e,4o), but does not capture intermediate correlated orbitals.

Analyzing the size of the Hamiltonian with respect to the error in the correlation energy (table 5.2), as was done above for ozone, it is apparent that the marginal increase in the size of the Hamiltonian of NO-ASD(2e,2o;4e,4o) with respect to CASCI(4e,4o) leads to an order of magnitude improvement in the correlation energy error (-23.9 kcal mol^{-1}) than orbital reoptimization with CASSCF(4e,4o) (-2.7 kcal mol^{-1}). To analyze where NO-ASD(2e,2o;4e,4o) lies in the hierarchy of increasing active space size, table 5.10 shows the energy of averaged density UNO-CASCI

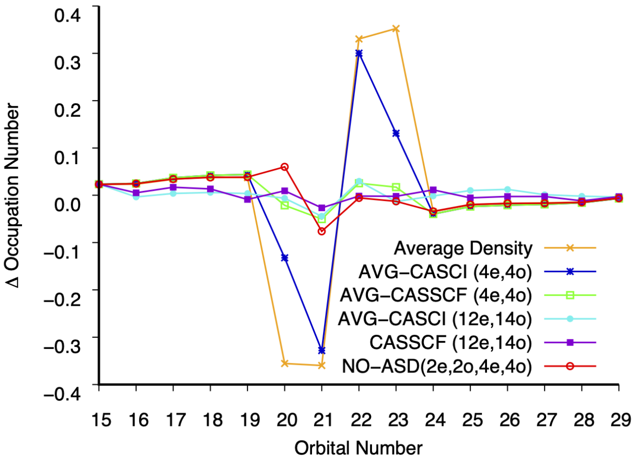

Figure 5.3. Occupation numbers of valence natural orbitals in nickel-acetylene compared with DMRG(18e,33o) for different methods indicated in the legend with the cc-pVTZ basis set.

with increasing active spaces. It can be seen that the NO-ASD(2e,2o;4e,4o) energy is slightly better than UNO-CASCI(8e,8o) despite comprising significantly fewer determinants. Including all the intermediate correlated orbitals increases the size of the Hamiltonian by 10^{10} matrix elements, and without orbital reoptimization still leaves 96.7 kcal mol^{-1} correlation energy error. The larger improvement in correlation energy upon orbital reoptimization with larger determinant expansions observed in ozone is also observed in nickel acetylene, reducing the error in correlation energy by 61.3 kcal mol^{-1}, again indicating that the intermediately correlated orbitals are more sensitive to orbital reoptimization than the strongly correlated orbitals.

Lastly, transition metal compounds containing $[Cu_2O_2]^{2+}$ are known to have high catalytic activity with biological relevance (231). Due to the variety of ways that copper(I) can bind to oxygen, there are several different possible structures that can exist in biological systems. Previous studies have shown that $[Cu_2O_2]^{2+}$ systems have significant multireference character and as a result, it is difficult to predict the relative energies of the different structures (232; 233; 234; 235). Here, we examine the μ-oxo dicopper ammonia complex, and the relative energies of the **bis** and **per** structures (fig. 5.4). The multireference character of the molecular wavefunction indicates large computationally infeasible active spaces are required. The two correlation mechanisms were represented by UHF solutions that were separated by 0.1201 Hartree in the **bis** geometry, and by 0.1000 Hartree in the **per** geometry. The two correlation mechanisms both include copper d_{xy} orbitals interacting with oxygen p_x and p_y orbitals in the first case, and with oxygen p_z in the second case (fig. 5.7 and 5.8). Natural orbital ONs at the **bis** geometry are shown in table 5.11, and for the **per** geometry are shown in table 5.12.

Examining the average density NOs indicates an eight electron in seven orbitals active space at the **bis** geometry, while at the **per** geometry, the indicated active

Methods	Number of Hamiltonian Elements	ΔE (kcal mol^{-1})
^{a}DMRG 18e,33o	2.212x10^{30}	0.0
CASSCF 12e,14o	8.132x10^{13}	35.4
^{a}UNO-CASCI 12e,14o (AVG)	8.132x10^{13}	96.7
^{a}UNO-CASCI 4e,4o (AVG)	1,296	188.3
^{a}UNO-CASSCF 4e,4o (AVG)	1,296	185.6
NO-ASD 2e,2o;4e,4o	1,600	164.4

Table 5.2. Number of Hamiltonian matrix elements and error in correlation energy with respect to full valence DMRG calculation for different methods in the calculation of nickel-acetylene using the cc-pVTZ basis set. ^{a}Results from ref. 206.

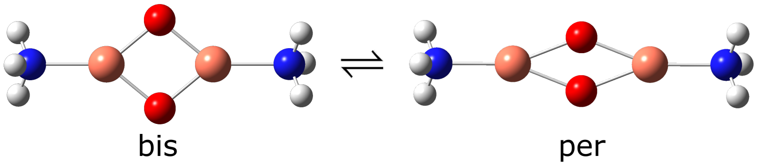

Figure 5.4. **Bis** and **per** isomers of μ-oxo dicopper ammonia complex.

space is six electrons in five orbitals, based on a threshold for strongly correlated orbitals of 0.01-1.99 (the NO with NO 0.00998 was also included at the **bis** geometry). The averaged density active spaces lead to Hamiltonian matrices with 10,000 matrix elements for (6e,5o) and 1.501×10^{6} matrix elements for (8e,7o) (table 5.3). For the NO-ASD calculation, a (4e,4o;4e,4o) active space containing Hamiltonian matrix containing 5184 matrix elements was used, which is 52% of the smaller (6e,5o) active space and < 1% of the larger (8e,7o) active space used with the average density NOs. Despite the smaller size of the NO-ASD Hamiltonian, the absolute energy for the **bis** isomer is energetically lower than that of the average density CASCI(6e,5o) calculation by 7.3 kcal mol^{-1}. One of the strongest demonstrations for the performance of NO-ASD is that the absolute energy for the **per** isomer it is lower than the average density CASCI(6e,5o) and CASCI(8e,7o) calculations by 4.2 and 4.0 kcal mol^{-1} respectively. Even the **bis** CASCI(8e,7o) calculation is 1.8 kcal mol^{-1} lower in energy than the NO-ASD(4e,4o;4e,4) calculation, while orbital reoptimization with CASSCF recovers a greater amount of correlation energy by 5.7 and 33.4 kcal mol^{-1} for the (6e,5o) and (8e,7o) active spaces respectively. NO ONs of NO-ASD, CASCI and CASSCF calculations all indicate four strongly correlated orbitals.

Examining the difference in energy between the two geometries, NO-ASD gives similar results to the average density CASCI of both size active spaces, in which the

Methods	Number of Hamiltonian Elements	E(**bis**) – E(**per**) (kcal mol^{-1})
[a]DMRG-CASPT2 24e,24o	5.347x10^{25}	22.6
[b]UNO-CASCI 8e,7o (AVG)	1.501x10^{6}	-8.9
[b]UNO-CASSCF 8e,7o (AVG)	1.501x10^{6}	8.2
[b]UNO-CASCI 6e,5o (AVG)	10,000	-0.1
[b]UNO-CASSCF 6e,5o (AVG)	10,000	9.4
NO-ASD 4e,4o;4e,4o	5,184	-3.2

Table 5.3. Relative energies between **bis** and **per** geometries of μ-oxo dicopper ammonia calculated using different methods with cc-PVDZ basis set, except DMRG calculation using ANO-RCC basis set. [a]Results taken from ref. 235. [b]Results are obtained from the methodology of ref. 206.

per geometry is lower in energy than the **bis** geometry. DMRG calculations indicate the opposite energy order of **bis** and **per** geometries (235). Allowing for orbital relaxation with CASSCF calculations yields energy ordering consistent with DMRG calculations, suggesting that orbital relaxation is important for properly describing the correct energy order, rather than the error in NO-ASD resulting from a breakdown of the correlation mechanism approximation.

Conclusions

In conclusion, we have introduced the concept of the NO-ASD methodology in which correlation mechanisms are used to partition strong correlation. NO-ASD was then assessed against average density CASCI and CASSCF calculations, as well as very large active space DMRG calculations. We demonstrated that NO-ASD gives results consistent with average density CAS expansions despite the smaller active space, indicating that the partitioning and recouping of strong correlation in the wavefunction by correlation mechanism can be used to avoid the computational expense of explicit entanglement of all orbitals. The methodology was assessed both in terms of NO ONs and correlation energy error with respect to DMRG calculations. Especially with larger determinant expansions, orbital reoptimization leads to improvements in the average density CAS calculations. As a result, nonorthogonal orbital reoptimization may provide a route to improve the NO-ASD method (230). While performing orbital reoptimization on the whole NO-ASD determinant expansion may not be computationally feasible, it is also possible to perform orbital reoptimization through a non-orthogonal multiconfigurational self-consistent field (NOMCSCF) calculation of the underlying SCF solutions that indicate the correlation mechanism. The subsequent reoptimized basis determinants used to partition the wavefunction and perform NO-ASD expansion are likely to capture correlation that is absent from the independently optimized SCF solutions.

SUPPORTING DOCUMENTS – APPLICATION OF NONORTHOGONAL METHODS FOR EFFICIENT MODELING OF STRONGLY CORRELATED SYSTEMS

5.5.1 Molecular geometries

5.5.1.1 Ozone [O_3]

O	0.8822749	0.6839687	0.0000000
O	0.1946029	-0.3909559	0.0000000
O	-1.0768778	-0.2930128	0.0000000

Table 5.4. Ozone cartesian coordinates

5.5.1.2 Nickel-actelyene [NiC_2H_2]

Ni	0.0000000	0.0000000	-1.5826858
C	0.6420065	0.0000000	0.1340163
H	-1.5920883	0.0000000	0.6573266
H	1.5920883	0.0000000	0.6573266
C	-0.6420065	0.0000000	0.1340163

Table 5.5. Ni-actylene cartesian coordinates

5.5.1.3 **Bis** (μ-oxo) dicopper ammonia [$(Cu(NH)_3)_2O_2$]

Cu	0.000000	1.400000	0.000000
Cu	0.000000	-1.400000	0.000000
O	0.000000	0.000000	1.150000
O	0.000000	0.000000	-1.150000
N	0.000000	3.400000	0.000000
N	0.000000	-3.400000	0.000000
H	-0.939693	3.742020	0.000000
H	0.939693	-3.742020	0.000000
H	0.469846	3.742020	0.813798
H	-0.469846	-3.742020	-0.813798
H	0.469846	3.742020	-0.813798
H	-0.469846	-3.742020	0.813798

Table 5.6. **Bis** (μ-oxo) dicopper ammonia cartesian coordinates

5.5.1.4 **Per** (μ-oxo) dicopper ammonia [$(Cu(NH)_3)_2O_2$]

Cu	0.000000	1.800000	0.000000
Cu	0.000000	-1.800000	0.000000
O	0.000000	0.000000	0.700000
O	0.000000	0.000000	-0.700000
N	0.000000	3.800000	0.000000
N	0.000000	-3.800000	0.000000
H	-0.939693	4.142020	0.000000
H	0.939693	-4.142020	0.000000
H	0.469846	4.142020	0.813798
H	-0.469846	-4.142020	-0.813798
H	0.469846	4.142020	-0.813798
H	-0.469846	-4.142020	0.813798

Table 5.7. Per (μ-oxo) dicopper ammonia cartesian coordinates

5.5.2 Total energies and occupation numbers

Methods	UHF 1	UHF 2	NO-ASD 2e,2o x 2e,2o	NO-ASD 4e,4o x 2e,2o	Average Density of UHF 1 and UHF 2	UNO-CASCI 6e,4o Average	UNO-CASSCF 6e,4o Average	UNO-CASCI 8e,7o Average	UNO-CASSCF 8e,7o Average	CASSCF 12e,9o	DMRG 18e,32o
Energy (Har.)	-224.3412647	-224.4261939	-224.4339198	-224.4478995		-224.4317326	-224.4358661	-224.5104361	-224.5553859	-224.5688159	-224.820227
Orb. 4	1.99999	1.99998	2.00000	2.00000	1.99963	2.00000	2.00000	2.00000	2.00000	2.00000	1.99070
Orb. 5	1.99990	1.99979	2.00000	2.00000	1.99939	2.00000	2.00000	2.00000	2.00000	2.00000	1.98215
Orb. 6	1.99978	1.99970	2.00000	1.99998	1.99890	2.00000	2.00000	2.00000	2.00000	2.00000	1.98673
Orb. 7	1.99973	1.99935	1.99999	1.99995	1.99887	2.00000	2.00000	2.00000	2.00000	1.99208	1.97144
Orb. 8	1.99897	1.99901	1.99994	1.99973	1.99856	2.00000	2.00000	2.00000	2.00000	1.99001	1.97208
Orb. 9	1.99887	1.99787	1.99980	1.99944	1.99683	2.00000	2.00000	1.96751	1.96573	1.96341	1.94598
Orb. 10	1.99600	1.99783	1.99975	1.99925	1.97943	1.99813	1.99886	1.96653	1.95692	1.95656	1.94717
Orb. 11	1.99000	1.99727	1.99734	1.98427	1.89314	1.98491	1.99286	1.96374	1.94981	1.94789	1.94114
Orb. 12	1.78975	1.28871	1.59032	1.63147	1.63809	1.66143	1.62528	1.74171	1.77146	1.78649	1.79002
Orb. 13	0.21025	0.71129	0.41243	0.37169	0.47757	0.35553	0.38300	0.29077	0.26150	0.25096	0.24165
Orb. 14	0.01000	0.00273	0.00020	0.01311	0.00812	0.00000	0.00000	0.04266	0.05334	0.06164	0.06281
Orb. 15	0.00400	0.00217	0.00016	0.00064	0.00493	0.00000	0.00000	0.02709	0.04125	0.05096	0.05394
Orb. 16	0.00113	0.00213	0.00003	0.00024	0.00289	0.00000	0.00000	0.00000	0.00000	0.00000	0.01589
Orb. 17	0.00103	0.00099	0.00002	0.00011	0.00111	0.00000	0.00000	0.00000	0.00000	0.00000	0.01052

Table 5.8. Ozone total energies and occupation numbers for NO-ASD, average density UNO-CAS(CI and SCF), CASSCF, and DMRG. DMRG results are directly taken from S. Keller *et al. J. Chem. Phys.* **2015**, 142, 244104. All calculations use the cc-PVTZ basis set.

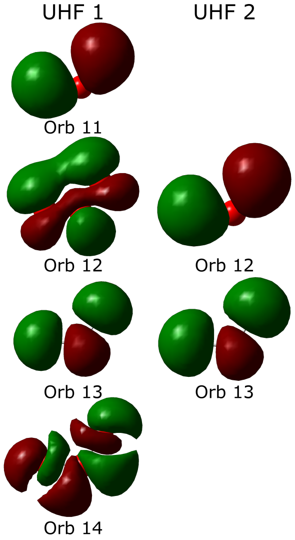
UHF 1
UHF 2
Orb 11
Orb 12
Orb 12
Orb 13
Orb 13
Orb 14

Figure 5.5. Pictorial Representation of the Natural Orbitals of Ozone's two UHF solutions

Methods	UHF 1	UHF 2	NO-ASD 4e,4o x 2e,2o	Average Density of UHF 1 and UHF 2	UNO-CASCI 4e,4o Average	UNO-CASSCF 4e,4o Average	UNO-CASCI 12e,14o Average	CASSCF 12e,14o	DMRG 18e,33o
Energy (Har.)	-1583.623755	-1583.625392	-1583.695693		-1583.657517	-1583.661859	-1583.803501	-1583.901295	-1583.957662
Orb. 15	1.99970	1.99970	1.99953	1.99928	2.00000	2.00000	2.00000	2.00000	1.97657
Orb. 16	1.99956	1.99970	1.99952	1.99836	2.00000	2.00000	1.97163	1.98026	1.97498
Orb. 17	1.99935	1.99949	1.99739	1.99692	2.00000	2.00000	1.96700	1.98017	1.96307
Orb. 18	1.99900	1.99926	1.99545	1.99624	2.00000	2.00000	1.96374	1.97127	1.95777
Orb. 19	1.99817	1.99658	1.99433	1.99325	2.00000	2.00000	1.95968	1.94729	1.95607
Orb. 20	1.99176	1.63678	1.98580	1.57026	1.79357	1.90443	1.91949	1.93524	1.92576
Orb. 21	1.51138	1.16270	1.80952	1.52607	1.55755	1.83540	1.84140	1.85911	1.88574
Orb. 22	0.48862	0.83730	0.13558	0.47151	0.44146	0.16661	0.17079	0.13946	0.14113
Orb. 23	0.00824	0.36322	0.06359	0.42896	0.20742	0.09356	0.06322	0.07438	0.07644
Orb. 24	0.00183	0.00342	0.00567	0.00506	0.00000	0.00000	0.03815	0.05094	0.03957
Orb. 25	0.00100	0.00074	0.00455	0.00371	0.00000	0.00000	0.03417	0.01862	0.02396
Orb. 26	0.00065	0.00051	0.00399	0.00369	0.00000	0.00000	0.03336	0.01840	0.02091
Orb. 27	0.00044	0.00030	0.00235	0.00303	0.00000	0.00000	0.02037	0.01659	0.01915
Orb. 28	0.00030	0.00030	0.00091	0.00143	0.00000	0.00000	0.01396	0.00421	0.01586
Orb. 29	0.00021	0.00025	0.00055	0.00115	0.00000	0.00000	0.00305	0.00407	0.00674

Table 5.9. Nickel-Actelyene total energies and occupation numbers for NO-ASD, average density UNO-CAS(CI and SCF), CASSCF, and DMRG. DMRG results are directly taken from S. Keller *et al.* *J. Chem. Phys.* **2015**, 142, 244104. All calculations use the cc-PVTZ basis set.

Method	Energy
NO-ASD 4e,4o x 2e,2o	-1583.695693
UNO-CASCI 4e,4o Average	-1583.657517
UNO-CASCI 6e,6o Average	-1583.685784
UNO-CASCI 8e,8o Average	-1583.693130
UNO-CASCI 10e,10o Average	-1583.721180
UNO-CASCI 12e,12o Average	-1583.769435

Table 5.10. Energy of NO-ASD(4e,4o;2e,2o) compared to averaged density UNO-CASCI with active spaces of increasing size.

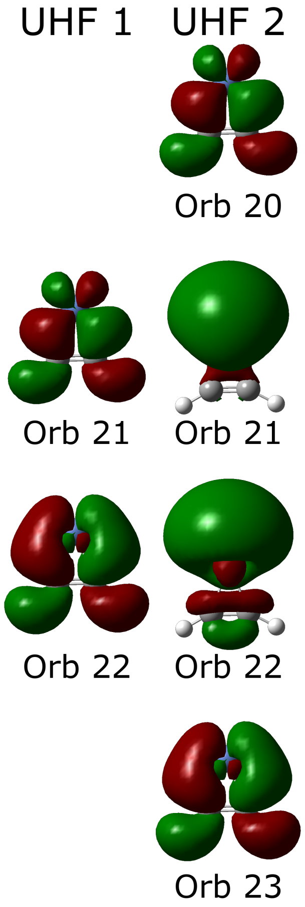
UHF 1
UHF 2
Orb 20
Orb 21
Orb 21
Orb 22
Orb 22
Orb 23

Figure 5.6. Pictorial Representation of the Natural Orbitals of Ni-Acetylene's two UHF solutions

Methods	UHF 1	UHF 2	NO-ASD 4e,4o x 4e,4o	Average Density of UHF 1 and UHF 2	UNO-CASCI 6e,5o Average	UNO-CASSCF 6e,5o Average	UNO-CASCI 8e,7o Average	UNO-CASSCF 8e,7o Average
Energy (Har.)	-3539.561699	-3539.441595	-3539.549569		-3539.538011	-3539.558614	-3539.552426	-3539.584802
Orb. 38	1.99973	1.99986	2.00000	1.99886	2.00000	2.00000	2.00000	2.00000
Orb. 39	1.99971	1.99986	2.00000	1.99662	2.00000	2.00000	2.00000	2.00000
Orb. 40	1.99947	1.99986	2.00000	1.99645	2.00000	2.00000	2.00000	2.00000
Orb. 41	1.99937	1.99948	1.99997	1.99373	2.00000	2.00000	2.00000	2.00000
Orb. 42	1.99864	1.99924	1.99994	1.99135	2.00000	2.00000	2.00000	2.00000
Orb. 43	1.99844	1.98857	1.99990	1.84150	2.00000	2.00000	1.98506	1.93111
Orb. 44	1.99832	1.98481	1.99842	1.77254	1.78410	1.99875	1.79674	1.83180
Orb. 45	1.09615	1.70607	1.52755	1.50557	1.04394	1.41574	1.03621	1.38719
Orb. 46	1.09522	1.17177	1.21582	1.23111	1.34492	1.35443	1.34672	1.68843
Orb. 47	0.90478	0.82823	0.81490	0.91937	0.95303	0.66487	0.97621	0.69147
Orb. 48	0.90385	0.29393	0.44283	0.73101	0.87400	0.56622	0.85260	0.45497
Orb. 49	0.00168	0.01519	0.00006	0.00998	0.00000	0.00000	0.00647	0.01503
Orb. 50	0.00156	0.01143	0.00001	0.00822	0.00000	0.00000	0.00000	0.00000
Orb. 51	0.00136	0.00076	0.00001	0.00102	0.00000	0.00000	0.00000	0.00000
Orb. 52	0.00063	0.00052	0.00000	0.00089	0.00000	0.00000	0.00000	0.00000

Table 5.11. Bis $\mu - oxo$ dicopper ammonia total energies and occupation numbers for NO-ASD and average density UNO-CAS(CI and SCF). All calculations use the cc-PVDZ basis set.

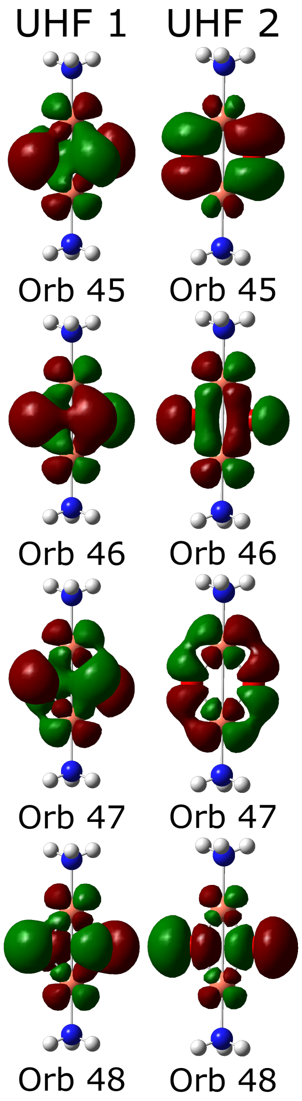
UHF 1
UHF 2
Orb 45
Orb 45
Orb 46
Orb 46
Orb 47
Orb 47
Orb 48
Orb 48

Figure 5.7. Pictorial Representation of the Natural Orbitals of **Bis** $\mu-oxo$ dicopper ammonia's two UHF solutions

Methods	UHF 1	UHF 2	NO-ASD 4e,4o x 4e,4o	Average Density of UHF 1 and UHF 2	UNO-CASCI 6e,5o Average	UNO-CASSCF 6e,5o Average	UNO-CASCI 8e,7o Average	UNO-CASSCF 8e,7o Average
Energy (Har.)	-3539.536109	-3539.435828	-3539.544548		-3539.537789	-3539.573556	-3539.538169	-3539.597849
Orb. 38	1.99990	1.99978	2.00000	1.99969	2.00000	2.00000	2.00000	2.00000
Orb. 39	1.99985	1.99957	2.00000	1.99918	2.00000	2.00000	2.00000	2.00000
Orb. 40	1.99985	1.99947	2.00000	1.99907	2.00000	2.00000	2.00000	2.00000
Orb. 41	1.99985	1.99880	1.99999	1.99733	2.00000	2.00000	2.00000	2.00000
Orb. 42	1.99985	1.99846	1.99997	1.99673	2.00000	2.00000	2.00000	2.00000
Orb. 43	1.99976	1.99812	1.99979	1.99652	2.00000	2.00000	1.99976	1.99995
Orb. 44	1.99975	1.99680	1.99221	1.98454	1.99363	1.99722	1.99355	1.97830
Orb. 45	1.99780	1.67970	1.97638	1.83637	1.97414	1.93995	1.97427	1.94307
Orb. 46	1.07825	1.08270	1.19583	1.08489	1.15786	1.19407	1.15965	1.17716
Orb. 47	0.92175	0.91730	0.80866	0.92619	0.84394	0.80847	0.84204	0.82448
Orb. 48	0.00220	0.32030	0.02423	0.17377	0.03043	0.06029	0.03053	0.05770
Orb. 49	0.00025	0.00320	0.00287	0.00209	0.00000	0.00000	0.00020	0.01934
Orb. 50	0.00024	0.00188	0.00001	0.00118	0.00000	0.00000	0.00000	0.00000
Orb. 51	0.00015	0.00154	0.00000	0.00089	0.00000	0.00000	0.00000	0.00000
Orb. 52	0.00015	0.00120	0.00000	0.00062	0.00000	0.00000	0.00000	0.00000

Table 5.12. Per $\mu - oxo$ dicopper ammonia total energies and occupation numbers for NO-ASD and average density UNO-CAS(CI and SCF). All calculations use the cc-PVDZ basis set.

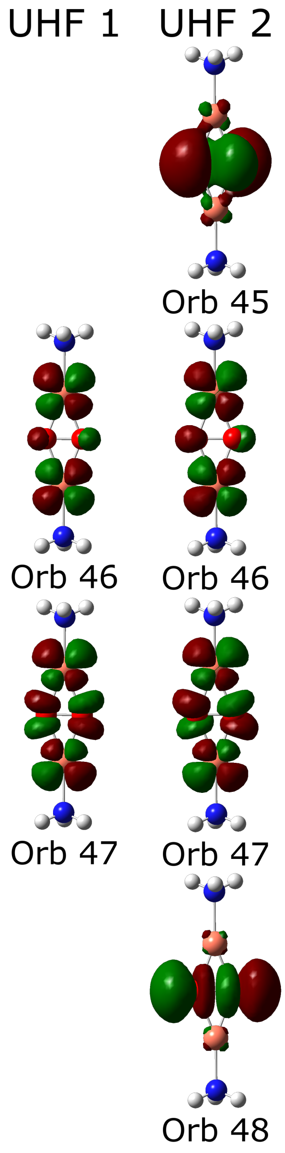
UHF 1
UHF 2
Orb 45
Orb 46
Orb 46
Orb 47
Orb 47
Orb 48

Figure 5.8. Pictorial Representation of the Natural Orbitals of **Per** $\mu-oxo$ dicopper ammonia's two UHF solutions

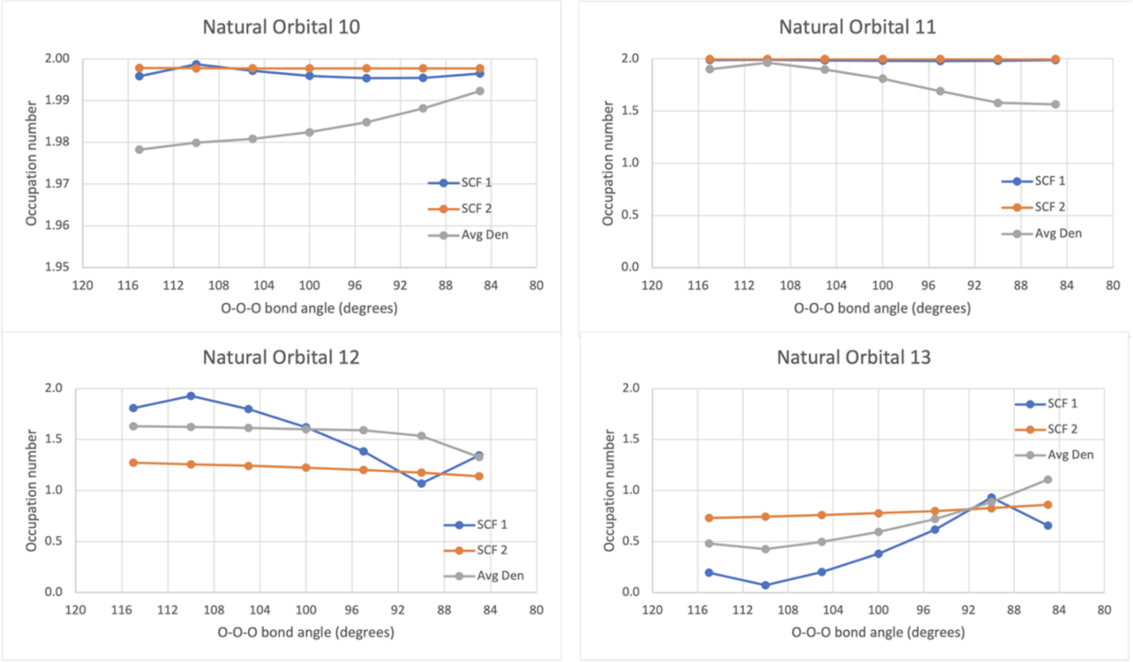

Figure 5.9. Selected natural orbital occupation numbers along the O-O-O bending coordinate of ozone.

EFFECT OF NATURAL ORBITAL OCCUPATION NUMBER THRESHOLDS ON ENERGY DISCONTINUITIES

To test the hypothesis that NO-ASD is less affected by the exact choice of threshold than averaged density UNO methods, we examined the SCF density and average density natural orbitals along the O-O-O bending coordinate for the two SCF determinants identified in this study (fig. 5.9). Using the 0.02-1.98 threshold, natural orbitals 12 and 13 are always included in the active space regardless of whether the density of SCF 1, SCF 2, or the averaged density is used. Natural orbital 11 is always outside the active using SCF 1 or SCF 2 densities, but inside the active space using the averaged density. Natural orbital 10 is always outside the active space using SCF 1 or SCF 2 density, but switches from being outside the active space at 105 degrees, to being inside the active space at 110 degrees. The average density show a much greater variation in occupation number of close-to-threshold natural orbitals 10 and 11 than the individual SCF densities, supporting the hypothesis that NO-ASD will suffer less from the effect of occupation number threshold crossing discontinuities.

CHAPTER 6

CONCLUSIONS

Throughout this work, we examined both preexisting and newly developed methodologies for the description of excited state systems to understand the photoreactivity in molecules like azobenzene.

The first work, in Chapter 3, demonstrated the utilization of preexisiting methodologies like CASSCF and TD-DFT for understanding electric field response to both unsubstituted and substituted azobenzene molecules for chemical control of the photochemical system. With unsubstituted azobenzene, significant findings were observed specifically in modification of the branching space of the CI with applied electric fields, demonstrating clear limitation or enhancement of the photoisomerization pathway through modification of the size and direction of an electric field. This was the first work to report a dipole inversion effect in which electric field response trends at strong fields were qualitatively different to that at weak fields allowing for the formation of new minima in the PES that did not exist in field free conditions. With the study of the substituted azobenzene we were interested in examining the effects of not just the applied electric field but also pH/deprotonation. We showed that with application of strong electric fields some of the thermal isomerization pathways become barrier-less. This result is significant because it can be used in systems where a fast thermal response is needed in which, with the application of a field, the trans molecule can be reproduced almost immediately without the need to overcome a transition barrier. We also examined the half-lives of the thermal barriers when the thermal pathways are competitive showing that there is a lower half-life when the pathways are energetically competitive.

Overall, the investigations of our first work of azobenzene with CASSCF and TD-DFT methodologies produced significant work detailing the reactions of azobenzene molecules with electric field control. With the continuation of this work, to enhance azobenzene properties further larger azobenzene systems became of interest. However, the examination of these systems is impossible with the methodologies utilized within the first work which is why we turned our focus onto the method development of SCF solution methodologies for excited states.

The first development we examined was that of the ΔSCF methodology in which the electronic states of interest are individually optimized. However, because the SCF solutions are individually optimized an issue arises with the unequal treatment of correlation between the ground and excited states. Thus, to allow for an equal treatment of correlation the ΔPAV-DH-DFT methodology was created in which the static correlation is achieved through symmetry breaking and projection and the dynamic correlation is achieved through DFT and MP2. Our first benchmarking of this methodology examined solely local excitations of small and medium sized molecules which demonstrated ΔPAV-DH-DFT methodology showed similar quality results to LR-CC2 and EOM-CCSD. This result is significant because the scaling of the ΔPAV-DH-DFT method is noniterative $\mathcal{O}(N^5)$, compared to iterative $\mathcal{O}(N^5)$ for LR-CC2 and iterative $\mathcal{O}(N^6)$ for EOM-CCSD. Meaning this methodology can give similar quality results to high performance pre-existing methodologies without the computational cost.

We expanded this work by examining the effect of HF exchange on describing a second benchmarking set consisting of local, charge transfer, and Rydberg states. It was observed that at low amounts of HF exchange several issues arise causing poor results for all excitations. Some issues are noted as: double counting of strong correlation, caused by the increase of DFT exchange in the description, and numerical issues caused by the reduced frontier orbital energy gap. Other issues were also observed at the opposite end of the HF exchange in which the projector fails due to increased contributions of higher order spin contaminating states. Implementation of a projector that can recouple all electron pairs would be needed to fix the issues at higher HF exchange values. Overall, the ΔPAV-DH-DFT methodology has many advantages however, it is still a single reference methodology thus, it fails at describing points of degeneracy and the entire PES however, it is very efficient for describing VEEs.

The second development of utilizing SCF solutions was in the NO-ASD approach where fragment wavefunctions are constructed and used to partition a CI active space. The NO-ASD was utilized in comparison to average-density UNO-(CI,CAS) for systems containing MCM. We demonstrated preliminary results with the NO-ASD methodology showing that we can achieve energies similar to that of an average-density UNO-(CI,CAS) calculation with substantially fewer Hamiltonian elements. This signifies the importance of nonorthognality on reducing computational cost just through nonorthogonality of the SCF solutions. It was observed with some systems orbital reooptimization is important for achieving accurate descriptions of energy. However, orbital optimization on the entire NO-ASD determinant expansion has a high computational cost but it is feasible to perform the optimization on the underlying SCF solutions.

The results indicated in this work demonstrates a limitation of current methodologies for studying excited state systems but also introduces and examines two newly developed methods for study of larger systems. This work provides new directions for excited state methodologies. While the newly developed methodologies are still in their elementary stages, this work provides a new perspective for examining excited states using SCF solutions.

REFERENCES

[1] Y.-C. Cheng and G. R. Fleming, “Dynamics of light harvesting in photosynthesis,” Annu. Rev. Phys. Chem. **60**, 241–262 (2009).

[2] C. N. Evrard, A. D. Mahler, and L. M. Thompson, “Excited state electronic structure of single-site vanadium oxide photocatalysts supported on mesoporous silica,” ACS Symp. Ser. Am. Chem. Soc. **1331**, 327–341 (2019).

[3] J. Neugebauer, “Subsystem-based theoretical spectroscopy of biomolecules and biomolecular assemblies,” ChemPhysChem **10**, 3148–3173 (2009).

[4] L. M. Thompson, A. Lasoroski, P. M. Champion, J. T. Sage, M. J. Frisch, J. J. v. Thor, and M. J. Bearpark, “Analytical harmonic vibrational frequencies for the green fluorescent protein computed with ONIOM: Chromophore mode character and its response to environment,” J. Chem. Theory Comput. **10**, 751–766 (2014).

[5] V. Coropceanu, X.-K. Chen, T. Wang, Z. Zheng, and J.-L. Brédas, “Charge-transfer electronic states in organic solar cells,” Nat. Rev. Mater. **4**, 689–707 (2019).

[6] S. U. Z. Khan, G. Londi, X. Liu, M. A. Fusella, G. D’Avino, L. Muccioli, A. N. Brigeman, B. Niesen, T. C. J. Yang, Y. Olivier, J. T. Dull, N. C. Giebink, D. Beljonne, and B. P. Rand, “Multiple charge transfer states in donor-acceptor heterojunctions with large frontier orbital energy offsets,” Chem. Mater. **31**, 6808–6817 (2019).

[7] J. Cornil, S. Verlaak, N. Martinelli, A. Mityashin, Y. Olivier, T. Van Regemorter, G. D’Avino, L. Muccioli, C. Zannoni, F. Castet, D. Beljonne, and P. Heremans, “Exploring the energy landscape of the charge transport levels in organic semiconductors at the molecular scale,” Acc. Chem. Res. **46**, 434–443 (2013).

[8] A. Dreuw and M. Head-Gordon, “Failure of time-dependent density functional theory for long-range charge-transfer excited states: The zincbacteriochlorin bacteriochlorin and bacteriochlorophyll spheroidene complexes,” J. Am. Chem. Soc. **126**, 4007–4016 (2004).

[9] S. Kümmel, “Charge-transfer excitations: a challenge for time-dependent density functional theory that has been met,” Adv. Energy Mater. **7**, 1700440 (2017).

[10] N. T. Maitra, “Charge transfer in time-dependent density functional theory,” J. Condens. Matter Phys. **29**, 423001 (2017).

[11] D. Hait, A. Rettig, and M. Head-Gordon, "Well-behaved versus ill-behaved density functionals for single bond dissociation: Separating success from disaster functional by functional for stretched h2," J. Chem. Phys. **150**, 094115 (2019).

[12] D. J. Tozer, "Relationship between long-range charge-transfer excitation energy error and integer discontinuity in kohn–sham theory," J. Chem. Phys. **119**, 12697–12699 (2003).

[13] M. Lundberg, T. Kawatsu, T. Vreven, M. J. Frisch, and K. Morokuma, "Transition states in a protein environment- oniom qm: Mm modeling of isopenicillin n synthesis," J. Chem. Theory Comput. **5**, 222–234 (2009).

[14] F. Segatta, L. Cupellini, M. Garavelli, and B. Mennucci, "Quantum chemical modeling of the photoinduced activity of multichromophoric biosystems: Focus review," Chem. Rev. **119**, 9361–9380 (2019).

[15] J. Tolle and J. Neugebauer, "The seamless connection of local and collective excited states in subsystem time-dependent density functional theory," J. Phys. Chem. Lett. **13**, 1003–1018 (2022).

[16] G. M. Barca, A. T. Gilbert, and P. M. Gill, "Simple models for difficult electronic excitations," J. Chem. Theory Comput. **14**, 1501–1509 (2018).

[17] A. T. Gilbert, N. A. Besley, and P. M. Gill, "Self-consistent field calculations of excited states using the maximum overlap method (mom)," J. Phys. Chem. A. **112**, 13164–13171 (2008).

[18] H.-Z. Ye, M. Welborn, N. D. Ricke, and T. Van Voorhis, "σ-scf: A direct energy-targeting method to mean-field excited states," J. Chem. Phys. **147**, 214104 (2017).

[19] H.-Z. Ye and T. Van Voorhis, "Half-projected σ self-consistent field for electronic excited states," J. Chem. Theory Comput. **15**, 2954–2965 (2019).

[20] L. Zhao and E. Neuscamman, "An efficient variational principle for the direct optimization of excited states," J. Chem. Theory Comput. **12**, 3436–3440 (2016).

[21] J. A. Shea and E. Neuscamman, "Size consistent excited states via algorithmic transformations between variational principles," J. Chem. Theory Comput. **13**, 6078–6088 (2017).

[22] X. Dong, A. D. Mahler, E. M. Kempfer-Robertson, and L. M. Thompson, "Global elucidation of self-consistent field solution space using basin hopping," J. Chem. Theory Comput. **16**, 5635–5644 (2020).

[23] D. A. McQuarrie and J. D. Simon, *Physical chemistry : a molecular approach* (University Science Books, Sausalito, Calif., 1997).

[24] A. Szabo and N. S. Ostlund, *Modern quantum chemistry: Introduction to advanced electronic structure theory* (Dover Publications, Inc., Mineola, 1996), 1st ed.

[25] E. Lewars, *Computational chemistry: Introduction to the theory and applications of molecular and quantum mechanics* (Springer Netherlands, 2010).

[26] J. L. Bao, L. Gagliardi, and D. G. Truhlar, "Self-interaction error in density functional theory: An appraisal," J. Phys. Chem. Lett. **9**, 2353–2358 (2018).

[27] S. Grimme, "Semiempirical hybrid density functional with perturbative second-order correlation," J. Chem. Phys. **124**, 034108 (2006).

[28] L. Goerigk and S. Grimme, "Double-hybrid density functionals," Wiley Interdiscip. Rev.: Comput. Mol. Sci. **4**, 576–600 (2014).

[29] T. Schwabe and S. Grimme, "Towards chemical accuracy for the thermodynamics of large molecules: new hybrid density functionals including non-local correlation effects," Phys. Chem. Chem. Phys. **8**, 4398–4401 (2006).

[30] L. Goerigk and S. Grimme, "A thorough benchmark of density functional methods for general main group thermochemistry, kinetics, and noncovalent interactions," Phys. Chem. Chem. Phys. **13**, 6670–6688 (2011).

[31] E. Brémond, J. C. Sancho-García, A. J. Pérez-Jiménez, and C. Adamo, "Communication: Double-hybrid functionals from adiabatic-connection: The QIDH model," J. Chem. Phys. **141**, 031101 (2014).

[32] F. D. Meo, P. Trouillas, C. Adamo, and J. C. Sancho-García, "Application of recent double-hybrid density functionals to low-lying singlet-singlet excitation energies of large organic compounds," J. Chem. Phys. **139**, 164104 (2013).

[33] A. Rubio and M. Marques, "Time-dependent density-functional theory," Phys. Chem. Chem. Phys. **11**, 4436–4436 (2009).

[34] S. Grimme and F. Neese, "Double-hybrid density functional theory for excited electronic states of molecules," J. Chem. Phys. **127**, 154116 (2007).

[35] N. Mehta, M. Casanova-Páez, and L. Goerigk, "Semi-empirical or non-empirical double-hybrid density functionals: which are more robust?" Phys. Chem. Chem. Phys. **20**, 23175–23194 (2018).

[36] R. Zare, "Laser control of chemical reactions," Science **279**, 1875–1879 (1998).

[37] A. Assion, T. Baumert, M. Bergt, T. Brixner, B. Kiefer, V. Seyfried, M. Strehle, and G. Gerber, "Control of chemical reactions by feedback-optimized phase-shaped femtosecond laser pulses," Science **282**, 919–922 (1998).

[38] O. Smirnova, S. Patchkovskii, Y. Mairesse, N. Dudovich, M. Y. Lvanov, and S. E. Harris, “Strong-field control and spectroscopy of attosecond electron-hole dynamics in molecules,” Proc. Natl. Acad. Sci. U.S.A. **106**, 16556–16561 (2009).

[39] S. N. Vogels, J. Onvlee, S. Chefdeville, A. van der Avoird, G. C. Groenenboom, and S. Y. T. van de Meerakker, “Imaging resonances in low-energy NO-He inelastic collisions.” Science **350**, 787–790 (2015).

[40] S. D. Deshmukh and Y. Tsori, “Communication: Control of chemical reactions using electric field gradients,” J. Chem. Phys. **144** (2016).

[41] A. Serrano-Jiménez, L. Bañares, and A. García-Vela, “Weak-field coherent control of photodissociation in polyatomic molecules,” Phys. Chem. Chem. Phys. **21**, 7885–7893 (2019).

[42] S. G. Boxer, I. T. Suydam, C. D. Snow, and V. S. Pande, “Electric fields at the active site of an enzyme: Direct comparison of experiment with theory,” Science **313**, 200–204 (2006).

[43] A. Warshel and A. Dryga, “Simulating electrostatic energies in proteins: Perspectives and some recent studies of pKas, redox, and other crucial functional properties,” Proteins: Struct., Funct., Bioinf. **79**, 3469–3484 (2011).

[44] S. Shaik, S. P. De Visser, and D. Kumar, “External electric field will control the selectivity of enzymatic-like bond activations,” J. Am. Chem. Soc. **126**, 11746–11749 (2004).

[45] S. Shaik, R. Ramanan, D. Danovich, and D. Mandal, “Structure and reactivity/selectivity control by oriented-external electric fields,” Chem. Soc. Rev. **47**, 5125–5145 (2018).

[46] S. Ciampi, N. Darwish, H. M. Aitken, I. Diez-Perez, and M. L. Coote, “Harnessing electrostatic catalysis in single molecule, electrochemical and chemical systems: a rapidly growing experimental tool box,” Chem. Soc. Rev. **47**, 5146–5164 (2018).

[47] F. Che, J. T. Gray, S. Ha, N. Kruse, S. L. Scott, and J.-S. McEwen, “Elucidating the roles of electric fields in catalysis: A perspective,” ACS Catal. **8**, 5153–5174 (2018).

[48] V. V. Welborn, L. R. Pestana, and T. Head-Gordon, “Computational optimization of electric fields for better catalysis design,” Nat. Catal. **1**, 1–7 (2018).

[49] R. Meir, H. Chen, W. Lai, and S. Shaik, “Oriented electric fields accelerate diels-alder reactions and control the endo/exo selectivity,” ChemPhysChem **11**, 301–310 (2010).

[50] Z. Wang, D. Danovich, R. Ramanan, and S. Shaik, “Oriented-external electric fields create absolute enantioselectivity in diels–alder reactions: Importance of the molecular dipole moment,” J. Am. Chem. Soc. **140**, 13350–13359 (2018).

[51] A. C. Aragones, N. L. Haworth, N. Darwish, S. Ciampi, N. J. Bloomfield, G. G. Wallace, I. Diez-Perez, and M. L. Coote, “Electrostatic catalysis of a diels–alder reaction,” Nature **531**, 88–91 (2016).

[52] X. Huang, C. Tang, J. Li, L.-C. Chen, J. Zheng, P. Zhang, J. Le, R. Li, X. Li, J. Liu, Y. Yang, J. Shi, Z. Chen, M. Bai, H.-L. Zhang, H. Xia, J. Cheng, Z.-Q. Tian, and W. Hong, “Electric field-induced selective catalysis of single-molecule reaction,” Sci. Adv. **5**, eaaw3072 (2019).

[53] K. Seki, S. D. Traytak, and M. Tachiya, “Rigorous calculation of electric field effects on the free energy change of the electron transfer reaction,” J. Chem. Phys. **118**, 669–679 (2003).

[54] P. M. De Biase, F. Doctorovich, D. H. Murgida, and D. A. Estrin, “Electric field effects on the reactivity of heme model systems,” Chem. Phys. Lett. **434**, 121–126 (2007).

[55] L.-J. Yu and M. L. Coote, “Electrostatic switching between $\mathrm{s_N}1$ and $\mathrm{s_N}2$ pathways,” J. Phys. Chem. A **123**, 582–589 (2019).

[56] Y. Wei, X. Wang, X. Wang, Z. Tao, Y. Cui, and M. Yang, “A theoretical study of the activation of nitromethane under applied electric fields,” RSC Adv. **6**, 24712–24718 (2016).

[57] L. D. Chen, M. Urushihara, K. Chan, and J. K. Nørskov, “Electric field effects in electrochemical CO_2 reduction,” ACS Catal. **6**, 7133–7139 (2016).

[58] M. Coote and G. Gryn’ova, “Directionality and the role of polarization in electric field effects on radical stability,” Aust. J. Chem. **70**, 367–372 (2017).

[59] N. Giuseppone and J. M. Lehn, “Electric-field modulation of component exchange in constitutional dynamic liquid crystals,” Angew. Chem. **45**, 4619–4624 (2006).

[60] C. F. Gorin, E. S. Beh, and M. W. Kanan, “An electric field-induced change in the selectivity of a metal oxide-catalyzed epoxide rearrangement,” J. Am. Chem. Soc. **134**, 186–189 (2012).

[61] B. Borca, T. Michnowicz, R. Pétuya, M. Pristl, V. Schendel, I. Pentegov, U. Kraft, H. Klauk, P. Wahl, R. Gutzler, A. Arnau, U. Schlickum, and K. Kern, “Electric-field-driven direct desulfurization,” ACS Nano **11**, 4703–4709 (2017).

[62] J. Wang, M. Yan, K. Zhao, X. Liao, P. Wang, X. Pan, W. Yang, and L. Mai, “Field effect enhanced hydrogen evolution reaction of MoS_2 nanosheets,” Adv. Mater. **29**, 1604464–6 (2016).

[63] N. S. Hill and M. L. Coote, “Internal oriented electric fields as a strategy for selectively modifying photochemical reactivity,” J. Am. Chem. Soc. **140**, 17800–17804 (2018).

[64] F. Knoch, D. Morozov, M. Boggio-Pasqua, and G. Groenhof, “Steering the excited state dynamics of a photoactive yellow protein chromophore analogue with external electric fields,” Comp. Theor. Chem. **1040-1041**, 120–125 (2014).

[65] S. Gozem, H. L. Luk, I. Schapiro, and M. Olivucci, “Theory and aimulation of the ultrafast double-bond isomerization of biological chromophores,” Chem. Rev. **117**, 13502–13565 (2017).

[66] B. G. Levine and T. J. Martinez, “Isomerization through conical intersections,” Annu. Rev. Phys. Chem. **58**, 613–634 (2007).

[67] M. Olivucci, G. Groenhof, M. Bouxin-Cademartory, B. Hess, S. P. de Visser, H. J. C. Berendsen, A. E. Mark, and M. A. Robb, “Photoactivation of the photoactive yellow protein: why photon absorption triggers a trans-to-cis Isomerization of the chromophore in the protein.” J. Am. Chem. Soc. **126**, 4228–4233 (2004).

[68] S. Shinkai, T. Nakaji, Y. Nishida, T. Ogawa, and O. Manabe, “Photoresponsive crown ethers. 1. Cis-trans isomerism of azobenzene as a tool to enforce conformational changes of crown ethers and polymers,” J. Am. Chem. Soc. **102**, 5860–5865 (1980).

[69] P. C. Knipe, S. Thompson, and A. D. Hamilton, “Ion-mediated conformational switches,” Chem. Sci. **6**, 1630–1639 (2015).

[70] W. Viricel, A. Mbarek, and J. Leblond, “Switchable lipids: Conformational change for fast pH-triggered cytoplasmic delivery,” Angew. Chem. **54**, 12743–12747 (2015).

[71] A. A. Beharry and G. A. Woolley, “Azobenzene photoswitches for biomolecules,” Chem. Soc. Rev. **40**, 4422–17 (2011).

[72] L. Dong, Y. Feng, L. Wang, and W. Feng, “Azobenzene-based solar thermal fuels: design, properties, and applications,” Chem. Soc. Rev. **47**, 7339–7368 (2018).

[73] A. Lennartson, A. Roffey, and K. Moth-Poulsen, “Designing photoswitches for molecular solar thermal energy storage,” Tetrahedron Lett. **56**, 1457–1465 (2015).

[74] J. R. Rumble, ed., *Physical constants of organic compounds* (CRC Press/Taylor & Francis, 2019), 100th ed.

[75] M. Alemani, M. V. Peters, S. Hecht, K.-H. Rieder, F. Moresco, and L. Grill, “Electric field-induced isomerization of azobenzene by STM ,” J. Am. Chem. Soc. **128**, 14446–14447 (2006).

[76] G. Füchsel, T. Klamroth, J. Dokić, and P. Saalfrank, “On the electronic structure of neutral and ionic azobenzenes and their possible role as surface mounted molecular switches.” J. Phys. Chem. B **110**, 16337–16345 (2006).

[77] P. Saalfrank, "Manipulation of adsorbates with electric fields," J. Chem. Phys. **113**, 3780–3791 (2000).

[78] Z. F. Liu, K. Hashimoto, and A. Fujishima, "Photoelectrochemical information storage using an azobenzene derivative," Nature **347**, 658–660 (1990).

[79] T. Enomoto, H. Hagiwara, D. A. Tryk, Z.-F. Liu, K. Hashimoto, and A. Fujishima, "Electrostatically induced isomerization of azobenzene derivatives in Langmuir—Blodgett films," J.. Phys. Chem. B **101**, 7422–7427 (1997).

[80] X. Tong, M. Pelletier, A. Lasia, and Y. Zhao, "Fast cis-trans isomerization of an azobenzene derivative in liquids and liquid crystals under a low electric field." Angew. Chem. **47**, 3596–3599 (2008).

[81] J. Wen, Z. Tian, and J. Ma, "Light- and electric-field-induced switching of thiolated azobenzene self-assembled monolayer," J. Phys. Chem. C **117**, 19934–19944 (2013).

[82] N. A. Davidenko, I. I. Davidenko, V. A. Pavlov, N. G. Chuprina, V. V. Tarasenko, and S. L. Studzinsky, "Adjustment of diffraction efficiency of polarization holograms in azobenzene polymers films using electric field," J. Appl. Phys. **122**, 013101 (2017).

[83] E. Diau, "A new trans-to-cis photoisomerization mechanism of azobenzene on the $s_1(n, \pi^*)$ surface," J. Phys. Chem. A **108**, 950–956 (2004).

[84] I. Conti, M. Garavelli, and G. Orlandi, "The different photoisomerization efficiency of azobenzene in the lowest nπ^* and $\pi\pi^*$ singlets: The role of a phantom state," J. Am. Chem. Soc. **130**, 5216–5230 (2008).

[85] J. Casellas, M. Bearpark, and M. Reguero, "Excited state decay in the photoisomerization of azobenzene: A new balance between mechanisms," ChemPhysChem. **17**, 3068–3079 (2016).

[86] F. Bernardi, M. Olivucci, and M. A. Robb, "Potential energy surface crossings in organic photochemistry," Chem. Soc. Rev. **25**, 321 (1996).

[87] V. Bonačić-Koutecký, J. Koutecky, and J. Michl, "Neutral and charged biradicals, zwitterions, funnels in S_1, and proton translocation: Their role in photochemistry, photophysics, and vision," Angew. Chem. **26**, 170–189 (1987).

[88] D. Yarkony, "Diabolical conical intersections," Rev. Mod. Phys. **68**, 985–1013 (1996).

[89] M. J. Frisch, G. W. Trucks, H. B. Schlegel, G. E. Scuseria, M. A. Robb, J. R. Cheeseman, G. Scalmani, V. Barone, G. A. Petersson, H. Nakatsuji, X. Li, M. Caricato, A. V. Marenich, J. Bloino, B. G. Janesko, R. Gomperts, B. Mennucci, H. P. Hratchian, J. V. Ortiz, A. F. Izmaylov, J. L. Sonnenberg, D. Williams-Young, F. Ding, F. Lipparini, F. Egidi, J. Goings, B. Peng,

A. Petrone, T. Henderson, D. Ranasinghe, V. G. Zakrzewski, J. Gao, N. Rega, G. Zheng, W. Liang, M. Hada, M. Ehara, K. Toyota, R. Fukuda, J. Hasegawa, M. Ishida, T. Nakajima, Y. Honda, O. Kitao, H. Nakai, T. Vreven, K. Throssell, J. A. Montgomery, Jr., J. E. Peralta, F. Ogliaro, M. J. Bearpark, J. J. Heyd, E. N. Brothers, K. N. Kudin, V. N. Staroverov, T. A. Keith, R. Kobayashi, J. Normand, K. Raghavachari, A. P. Rendell, J. C. Burant, S. S. Iyengar, J. Tomasi, M. Cossi, J. M. Millam, M. Klene, C. Adamo, R. Cammi, J. W. Ochterski, R. L. Martin, K. Morokuma, O. Farkas, J. B. Foresman, and D. J. Fox, "Gaussian 16 Revision A.03," (2016). Gaussian Inc. Wallingford CT.

[90] J. K. G. Watson, "Molecular rovibronic symmetries in electric and magnetic fields," Can. J. Phys. **53**, 2210–2220 (1975).

[91] I. K. Lednev, T. Q. Ye, P. Matousek, M. Towrie, P. Foggi, F. V. Neuwahl, S. Umapathy, R. E. Hester, and J. N. Moore, "Femtosecond time-resolved UV-visible absorption spectroscopy of trans-azobenzene: Dependence on excitation wavelength," Chem. Phys. Lett. **290**, 68–74 (1998).

[92] I. T. Suydam and S. G. Boxer, "Vibrational stark effects calibrate the sensitivity of vibrational probes for electric fields in proteins," Biochemistry **42**, 12050–12055 (2003).

[93] L. M. Thompson, A. Lasoroski, P. M. Champion, J. T. Sage, M. J. Frisch, J. J. van Thor, and M. J. Bearpark, "Analytical harmonic vibrational frequencies for the green fluorescent protein computed with ONIOM: Chromophore mode character and its response to environment," J. Chem. Theory Comput. **10**, 751–766 (2014).

[94] M. Liu, Y. Pang, B. Zhang, P. De Luna, O. Voznyy, J. Xu, X. Zheng, C. T. Dinh, F. Fan, C. Cao, F. P. G. de Arquer, T. S. Safaei, A. Mepham, A. Klinkova, E. Kumacheva, T. Filleter, D. Sinton, S. O. Kelley, and E. H. Sargent, "Enhanced electrocatalytic CO2 reduction via field-induced reagent concentration," Nature **537**, 382–386 (2016).

[95] S. D. Fried, S. Bagchi, and S. G. Boxer, "Measuring electrostatic fields in both hydrogen-bonding and non-hydrogen-bonding environments using carbonyl vibrational probes." J. Am. Chem. Soc. **135**, 11181–11192 (2013).

[96] S. D. Fried, L.-P. Wang, S. G. Boxer, P. Ren, and V. S. Pande, "Calculations of the electric fields in liquid solutions." J. Phys. Chem. B **117**, 16236–16248 (2013).

[97] S. D. Fried and S. G. Boxer, "Measuring electric fields and noncovalent interactions using the vibrational Stark effect," Acc. Chem. Res. **48**, 998–1006 (2015).

[98] O. Weingart, P. Altoe, M. Stenta, A. Bottoni, G. Orlandi, and M. Garavelli, "Product formation in rhodopsin by fast hydrogen motions." Phys. Chem. Chem. Phys. **13**, 3645–3648 (2011).

[99] M. M. T. El-Tahawy, A. Nenov, O. Weingart, M. Olivucci, and M. Garavelli, “Relationship between excited state lifetime and isomerization quantum yield in animal rhodopsins: Beyond the one-dimensional Landau-Zener model.” J. Phys. Chem. Lett. **9**, 3315–3322 (2018).

[100] C. Schnedermann, X. Yang, M. Liebel, K. M. Spillane, J. Lugtenburg, I. Fernández, A. Valentini, I. Schapiro, M. Olivucci, P. Kukura, and R. A. Mathies, “Evidence for a vibrational phase-dependent isotope effect on the photochemistry of vision.” Nat. Chem. **10**, 449–455 (2018).

[101] J. Griffiths, “II. Photochemistry of azobenzene and its derivatives,” Chem. Soc. Rev. **1**, 481 (1972).

[102] H. Rau and E. Lueddecke, “On the rotation-inversion controversy on photoisomerization of azobenzenes. Experimental proof of inversion,” J. Am. Chem. Soc. **104**, 1616–1620 (1982).

[103] F. Consoli, R. De Angelis, T. S. Robinson, S. Giltrap, G. S. Hicks, E. J. Ditter, O. C. Ettlinger, Z. Najmudin, M. Notley, and R. A. Smith, “Generation of intense quasi-electrostatic fields due to deposition of particles accelerated by petawatt-range laser-matter interactions.” Sci. Rep. **9**, 8551 (2019).

[104] J. A. Gámez, O. Weingart, A. Koslowski, and W. Thiel, “Cooperating dinitrogen and phenyl rotations in trans- azobenzene photoisomerization,” J. Chem. Theory Comput. **8**, 2352–2358 (2012).

[105] M. Azuki, K. Morihashi, T. Watanabe, O. Takahashi, and O. Kikuchi, “Ab initio GB study of the acid-catalyzed cis-trans isomerization of methyl yellow and methyl orange in aqueous solution,” Journal of Molecular Structure: THEOCHEM **542**, 255–262 (2001).

[106] N. J. Dunn, W. H. Humphries, A. R. Offenbacher, T. L. King, and J. A. Gray, “pH-Dependent cis ? trans Isomerization Rates for Azobenzene Dyes in Aqueous Solution,” J. Phys. Chem. A. **113**, 13144–13151 (2009).

[107] J. García-Amorós and D. Velasco, “Recent advances towards azobenzene-based lightdriven real-time information-transmitting materials,” Beilstein J. Org. Chem. **8**, 1003–1017 (2012).

[108] S. Samanta, A. Babalhavaeji, M. Dong, and G. A. Woolley, “Photoswitching of ortho-substituted azonium ions by red light in whole blood,” Angew. Chem. Int. Ed. **52**, 14127–14130 (2013).

[109] M. Dong, A. Babalhavaeji, M. J. Hansen, L. Kálmán, and G. A. Woolley, “Red, far-red, and near infrared photoswitches based on azonium ions,” Chem. comm. **51**, 12981–12984 (2015).

[110] S. Ludwanowski, M. Ari, K. Parison, S. Kalthoum, P. Straub, N. Pompe, S. Weber, M. Walter, and A. Walther, “pH tuning of water-soluble arylazopyrazole photoswitches,” Chem. Eur. J. **26**, 13203–13212 (2020).

[111] E. M. Kempfer-Robertson and L. M. Thompson, “Effect of oriented external electric fields on the photo and thermal isomerization of azobenzene,” J. Phys. Chem. A **124**, 3520–3529 (2020).

[112] I. Avdic, E. M. Kempfer-Robertson, and L. M. Thompson, “Oriented external electric field tuning of unsubstituted azoheteroarene thermal isomerization half-lives,” J. Phys. Chem. A **125**, 8238–8248 (2021).

[113] C. Cojocaru, A. Airinei, and N. Fifere, “Molecular structure and modeling studies of azobenzene derivatives containing maleimide groups,” SpringerPlus **2**, 1–19 (2013).

[114] M. Bouchouit, Y. Elkouari, L. Messaadia, A. Bouraiou, S. Arroudj, S. Bouacida, S. Taboukhat, and K. Bouchouit, “Synthesis, spectral, theoretical calculations and optical properties performance of substituted-azobenzene dyes,” Opt. Quantum Electron. **48**, 1–11 (2016).

[115] L. M. Thompson and H. P. Hratchian, “Spin projection with double hybrid density functional theory,” J. Chem. Phys. **141** (2014).

[116] I. T. Suydam, C. D. Snow, V. S. Pande, and S. G. Boxer, “Electric fields at the active site of an enzyme: Direct comparison of experiment with theory,” Science **313**, 200–204 (2006).

[117] T. Asano, T. Okada, S. Shinkai, K. Shigematsu, Y. Kusano, and O. Manabe, “Temperature and pressure dependences of thermal cis-to-trans isomerization of azobenzenes which evidence an inversion mechanism,” J. Am. Chem. Soc. **103**, 5161–5165 (1981).

[118] J. Garcia-Amorós, B. Maerz, M. Reig, A. Cuadrado, L. Blancafort, E. Samoylova, and D. Velasco, “Picosecond switchable azo dyes,” Chem. Eur. J. **25**, 7726–7732 (2019).

[119] C. R. Crecca and A. E. Roitberg, “Theoretical study of the isomerization mechanism of azobenzene and disubstituted azobenzene derivatives,” Journal of Physical Chemistry A **110**, 8188–8203 (2006).

[120] G. Füchsel, T. Klamroth, J. Dokić, and P. Saalfrank, “On the electronic structure of neutral and ionic azobenzenes and their possible role as surface mounted molecular switches,” J. Phys. Chem .B. **110**, 16337–16345 (2006).

[121] I. Conti, M. Garavelli, and G. Orlandi, “The different photoisomerization efficiency of azobenzene in the lowest nπ^* and $\pi\pi^*$ singlets: The role of a phantom state,” J. Am. Chem. Soc. **130**, 5216–5230 (2008).

[122] H. Lischka, D. Nachtigallová, A. J. A. Aquino, P. G. Szalay, F. Plasser, F. B. C. Machado, and M. Barbatti, "Multireference approaches for excited states of molecules," Chem. Rev. **118**, 7293–7361 (2018).

[123] M. Head-Gordon and A. Dreuw, "Single-reference ab initio methods for the calculation of excited states of large molecules," Chem. Rev. **105**, 4009–4037 (2005).

[124] S. Grimme, "Semiempirical hybrid density functional with perturbative second-order correlation," J. Chem. Phys. **124**, 034108 (2006).

[125] T. Schwabe and S. Grimme, "Towards chemical accuracy for the thermodynamics of large molecules: new hybrid density functionals including non-local correlation effects," Phys. Chem. Chem. Phys. **8**, 4398–4401 (2006).

[126] A. Ottochian, C. Morgillo, I. Ciofini, M. J. Frisch, G. Scalmani, and C. Adamo, "Double hybrids and time-dependent density functional theory: An implementation and benchmark on charge transfer excited states," J. Comput. Chem. **41**, 1242–1251 (2020).

[127] É. Brémond, M. Savarese, Á. J. Pérez-Jiménez, J. C. Sancho-García, and C. Adamo, "Speed-up of the excited-state benchmarking: double-hybrid density functionals as test cases." J. Chem. Theory Comput. **13**, 5539–5551 (2017).

[128] M. Alipour and N. Karimi, "Dissecting the accountability of parameterized and parameter-free single-hybrid and double-hybrid functionals for photophysical properties of TADF-based OLEDs," J. Chem. Phys. **146**, 234304–14 (2017).

[129] F. D. Meo, P. Trouillas, C. Adamo, and J. C. Sancho-García, "Application of recent double-hybrid density functionals to low-lying singlet-singlet excitation energies of large organic compounds," J. Chem. Phys. **139**, 164104–7 (2013).

[130] L. Goerigk and S. Grimme, "Assessment of TD-DFT methods and of various spin scaled CIS(D) and CC2 versions for the treatment of low-lying valence excitations of large organic dyes," J. Chem. Phys. **132**, 184103–10 (2010).

[131] L. Goerigk, J. Moellmann, and S. Grimme, "Computation of accurate excitation energies for large organic molecules with double-hybrid density functionals," Phys. Chem. Chem. Phys. **11**, 4611–12 (2009).

[132] S. Grimme and F. Neese, "Double-hybrid density functional theory for excited electronic states of molecules," J. Chem. Phys. **127**, 154116 – 19 (2007).

[133] G. Scuseria, C. A. Jiménez-Hoyos, T. M. Henderson, K. Samanta, and J. K. Ellis, "Projected quasiparticle theory for molecular electronic structure," J. Chem. Phys. **135**, 124108–17 (2011).

[134] C. A. Jiménez-Hoyos, T. M. Henderson, T. Tsuchimochi, and G. Scuseria, "Projected Hartree-Fock theory." J. Chem. Phys. **136**, 164109 (2012).

[135] D. L. Hill and J. A. Wheeler, “Nuclear constitution and the interpretation of fission phenomena,” Phys. Rev. **89**, 1102–1145 (1953).

[136] J. J. Griffin and J. A. Wheeler, “Collective motions in nuclei by the method of generator coordinates,” Phys. Rev. **108**, 311–327 (1957).

[137] J. K. Percus and A. Rotenberg, “Exact eigenfunctions of angular momentum by rotational projection,” J. Math. Phys. **3**, 928–6 (1962).

[138] R. Lefebvre and R. Prat, “On the projection of slater determinants,” Chem. Phys. Lett. **1**, 388–390 (1967).

[139] R. Lefebvre and R. F. Prat, “Etudes en methode de Hartree–Fock avec projection. I. Fonctions propres de S2. Evaluation de l’energie,” Int. J. Quant. Chem. **3**, 93–105 (1969).

[140] T. Tsuchimochi and T. van Voorhis, “Extended Møller-Plesset perturbation theory for dynamical and static correlations,” J. Chem. Phys. **141**, 164117–6 (2014).

[141] H. B. Schlegel, “Potential energy curves using unrestricted Møller-Plesset perturbation theory with spin annihilation,” J. Chem. Phys. **84**, 4530 (1986).

[142] C. Sosa and H. B. Schlegel, “Ab initio calculations on H + C2H2 → C2H3 using unrestricted Møller-Plesset perturbation theory with spin projection,” Int. J. Quant. Chem. **32**, 267–282 (1987).

[143] J. M. Wittbrodt and H. B. Schlegel, “Some reasons not to use spin projected density functional theory,” J. Chem. Phys. **105**, 6574 (1996).

[144] L. M. Thompson and H. P. Hratchian, “Spin projection with double hybrid density functional theory.” J. Chem. Phys. **141**, 034108 (2014).

[145] P.-O. Löwdin, “Quantum theory of many-particle systems. i. physical interpretations by means of density matrices, natural spin-orbitals, and convergence problems in the method of configurational interaction,” Phys. Rev. **97**, 1474–1489 (1955).

[146] G. E. Scuseria, C. A. Jiménez-Hoyos, T. M. Henderson, K. Samanta, and J. K. Ellis, “Projected quasiparticle theory for molecular electronic structure,” J. Chem. Phys. **135**, 124108 (2011).

[147] Z. Tóth and P. Pulay, “Finding symmetry breaking Hartree-Fock solutions: The case of triplet instability,” J. Chem. Phys. **145**, 164102 (2016).

[148] A. D. Mahler and L. M. Thompson, “Orbital optimization in nonorthogonal multiconfigurational self-consistent field applied to the study of conical intersections and avoided crossings,” J. Chem. Phys. **154**, 244101 (2021).

[149] J. Lee and M. Head-Gordon, “Regularized orbital-optimized second-order møller–plesset perturbation theory: A reliable fifth-order-scaling electron correlation model with orbital energy dependent regularizers,” J. Chem. Theory Comput. **14**, 5203–5219 (2018).

[150] R. J. Bartlett, “Coupled-cluster theory and its equation-of-motion extensions,” Wiley Interdiscip. Rev.: Comput. Mol. Sci. **2**, 126–138 (2011).

[151] J. F. Stanton and R. J. Bartlett, “The equation of motion coupled-cluster method. A systematic biorthogonal approach to molecular excitation energies, transition probabilities, and excited state properties,” J. Chem. Phys. **98**, 7029–7039 (1993).

[152] O. Christiansen, H. Koch, and P. Jørgensen, “The second-order approximate coupled cluster singles and doubles model CC2,” Chem. Phys. Lett. **243**, 409–418 (1995).

[153] M. Schreiber, M. R. Silva-Junior, S. P. A. Sauer, and W. Thiel, “Benchmarks for electronically excited states: CASPT2, CC2, CCSD, and CC3,” J. Chem. Phys. **128**, 134110–26 (2008).

[154] C. Azarias, C. Habert, Š. Budzák, X. Blase, I. Duchemin, and D. Jacquemin, “Calculations of n→π^* transition energies: Comparisons between TD-DFT, ADC, CC, CASPT2, and BSE/ GW descriptions,” J. Phys. Chem. A **121**, 6122–6134 (2017).

[155] D. J. Thouless, “Stability conditions and nuclear rotations in the hartree-fock theory,” Nucl. Phys. **21**, 225 – 232 (1960-11).

[156] B. O. Roos, K. Andersson, M. P. Fülscher, P. A. Malmqvist, L. Serrano-Andrés, K. Pierloot, and M. Merchan, “Multiconfigurational perturbation theory: Applications in electronic spectroscopy,” in “Advances in Chemical Physics,” (John Wiley & Sons, Inc., Hoboken, NJ, USA, 2007), pp. 219–331.

[157] H. J. Kulik, “Perspective: Treating electron over-delocalization with the DFT+U method,” J. Chem. Phys. **142**, 240901–11 (2015).

[158] S. Ghosh, P. Verma, C. J. Cramer, L. Gagliardi, and D. G. Truhlar, “Combining wave function methods with density functional theory for excited states,” Chem. Rev. **118**, 7249–7292 (2018).

[159] A. T. B. Gilbert, N. A. Besley, and P. M. W. Gill, “Self-consistent field calculations of excited states using the maximum overlap method (MOM).” J. Phys. Chem. A **112**, 13164 – 13171 (2008).

[160] É. Brémond, J. C. Sancho-García, Á. J. Pérez-Jiménez, and C. Adamo, “Communication: double-hybrid functionals from adiabatic-connection: the QIDH model.” J. Chem. Phys. **141**, 031101 (2014).

[161] S. Kozuch and J. Martin, "DSD-PBEP86: in search of the best double-hybrid DFT with spin-component scaled MP2 and dispersion corrections," Phys. Chem. Chem. Phys. **13**, 20104–4 (2011).

[162] S. Kozuch and J. Martin, "Spin-Component-Scaled Double Hybrids: An Extensive Search for the Best Fifth-Rung Functionals Blending DFT and Perturbation Theory," J. Comput. Chem. **34**, 2327–2344 (2013).

[163] E. M. Kempfer-Robertson, T. D. Pike, and L. M. Thompson, "Difference projection-after-variation double-hybrid density functional theory applied to the calculation of vertical excitation energies," J. Chem. Phys. **153**, 074103 (2020).

[164] E. J. Sundstrom and M. Head-Gordon, "Non-orthogonal configuration interaction for the calculation of multielectron excited states." J. Chem. Phys. **140**, 114103 (2014).

[165] D. J. Tozer and N. C. Handy, "On the determination of excitation energies using density functional theory," Phys. Chem. Chem. Phys. **2**, 2117–2121 (2000).

[166] N. Mardirossian and M. Head-Gordon, "ωb97X-V: A 10-parameter, range-separated hybrid, generalized gradient approximation density functional with nonlocal correlation, designed by a survival-of-the-fittest strategy," Phys. Chem. Chem. Phys. **16**, 9904–9924 (2014).

[167] M. A. Rohrdanz, K. M. Martins, and J. M. Herbert, "A long-range-corrected density functional that performs well for both ground-state properties and time-dependent density functional theory excitation energies, including charge-transfer excited states," J. Chem. Phys. **130**, 054112 (2009).

[168] R. A. Mendes, R. L. Haiduke, and R. J. Bartlett, "The devil's triangle of kohn–sham density functional theory and excited states," J. Chem. Phys. **154**, 074106 (2021).

[169] S. Nam, E. Cho, E. Sim, and K. Burke, "Explaining and fixing dft failures for torsional barriers," J. Phys. Chem. Lett. **12**, 2796–2804 (2021).

[170] V. Athavale, H.-H. Teh, and J. E. Subotnik, "On the inclusion of one double within CIS and TDDFT," J. Chem. Phys. **155**, 154105 (2021).

[171] J. F. Stanton and R. J. Bartlett, "The equation of motion coupled-cluster method. A systematic biorthogonal approach to molecular excitation energies, transition probabilities, and excited state properties," J. Chem. Phys. **98**, 7029–7039 (1993).

[172] L. Goerigk, J. Moellmann, and S. Grimme, "Computation of accurate excitation energies for large organic molecules with double-hybrid density functionals," Phys. Chem. Chem. Phys. **11**, 4436–4436 (2009).

[173] T. Schwabe and L. Goerigk, “Time-Dependent double-hybrid density functionals with spin-component and spin-opposite scaling,” J. Chem. Theory Comput. **13**, 4307–4323 (2017).

[174] L. Goerigk and S. Grimme, “Calculation of electronic circular dichroism spectra with time-dependent double-hybrid density functional theory,” J. Phys. Chem. A **113**, 767–776 (2008).

[175] L. Goerigk and S. Grimme, “Double-hybrid density functionals provide a balanced description of excited $^1\mathrm{L_a}$ and $^1\mathrm{L_b}$ states in polycyclic aromatic hydrocarbons,” J. Chem. Theory Comput. **7**, 3272–3277 (2011).

[176] L. Goerigk and S. Grimme, “Assessment of TD-DFT methods and of various spin scaled CIS(D) and CC2 versions for the treatment of low-lying valence excitations of large organic dyes,” J. Chem. Phys. **132**, 184103 (2010).

[177] A. Ottochian, C. Morgillo, I. Ciofini, M. J. Frisch, G. Scalmani, and C. Adamo, “Double hybrids and time-dependent density functional theory: An implementation and benchmark on charge transfer excited states,” J. Comp. Chem. **41**, 1242–1251 (2020).

[178] M. Casanova-Páez and L. Goerigk, “Global double hybrids do not work for charge transfer: A comment on “double hybrids and time-dependent density functional theory: An implementation and benchmark on charge transfer excited states”,” J. Comp. Chem. **42**, 528–533 (2021).

[179] É. Brémond, A. Ottochian, Á. J. Pérez-Jiménez, I. Ciofini, G. Scalmani, M. J. Frisch, J. C. Sancho-García, and C. Adamo, “Assessing challenging intra-and inter-molecular charge-transfer excitations energies with double-hybrid density functionals,” J. Comp. Chem. **42**, 970–981 (2021).

[180] D. Mester and M. Kállay, “A simple range separated double-hybrid density functional theory for excited states,” J. Chem. Theory Comput. **17**, 927–942 (2021).

[181] M. Casanova-Páez and L. Goerigk, “Assessing the Tamm-Dancoff approximation, singlet-singlet, and singlet-triplet excitations with the latest long-range corrected double-hybrid density functionals,” J. Chem. Phys. **153**, 064106 (2020).

[182] M. Casanova-Páez, M. B. Dardis, and L. Goerigk, “ωB2PLYP and ωB2GPPLYP: The first two double-hybrid density functionals with long-range correction optimized for excitation energies,” J. Chem. Theory Comput. **15**, 4735–4744 (2019).

[183] L. Goerigk and M. Casanova-Paéz, “The trip to the density functional theory zoo continues: Making a case for time-dependent double hybrids for excited-state problems,” Aust. J. Chem. **74**, 3 (2020).

[184] E. Brémond, A. J. Pérez-Jiménez, J. C. Sancho-García, and C. Adamo, "Range-separated hybrid and double-hybrid density functionals: A quest for the determination of the range-separation parameter," J. Chem. Phys. **152**, 244124 (2020).

[185] L. Wilbraham, C. Adamo, and I. Ciofini, "Communication: Evaluating non-empirical double hybrid functionals for spin-state energetics in transition-metal complexes," J. Chem. Phys. **148**, 041103 (2018).

[186] W. Chen and H. B. Schlegel, "Evaluation of S_2 for correlated wave functions and spin projection of unrestricted Møller–Plesset perturbation theory," J. Chem. Phys. **101**, 5957–5968 (1994).

[187] M.-P. Kitsaras and S. Stopkowicz, "Spin contamination in MP2 and CC2, a surprising issue," J. Chem. Phys. **154**, 131101 (2021).

[188] P. J. Knowles and N. C. Handy, "Convergence of projected unrestricted Hartee-Fock Møller-Plesset series." J. Phys. Chem. **92**, 3097–3100 (1988-06).

[189] N. C. Handy and P. J. Knowles, "Projected unrestricted Møller–Plesset second-order energies," J. Chem. Phys. **88**, 6991 (1988).

[190] M. J. G. Peach, P. Benfield, T. Helgaker, and D. J. Tozer, "Excitation energies in density functional theory: An evaluation and a diagnostic test," J. Chem. Phys. **128**, 044118 (2008).

[191] S. Grimme, "Improved second-order Möller-Plesset perturbation theory by separate scaling of parallel- and antiparallel-spin pair correlation energies," J. Chem. Phys. **118**, 9095 (2003).

[192] S. Kozuch and J. M. L. Martin, "DSD-PBEP86: in search of the best double-hybrid DFT with spin-component scaled MP2 and dispersion corrections," Phys. Chem. Chem. Phys. **13**, 20104–20107 (2011).

[193] S. Kozuch and J. M. Martin, "Spin-component-scaled double hybrids: an extensive search for the best fifth-rung functionals blending dft and perturbation theory," J. Comp. Chem. **34**, 2327–2344 (2013).

[194] G. M. J. Barca, A. T. B. Gilbert, and P. M. W. Gill, "Simple models for difficult electronic excitations," J. Chem. Theory Comput. **14**, 1501 – 1509 (2018).

[195] K. Carter-Fenk and J. M. Herbert, "State-Targeted Energy Projection: A Simple and Robust Approach to Orbital Relaxation of Non-Aufbau Self-Consistent Field Solutions," J. Chem. Theory Comput. **16**, 5067–5082 (2020).

[196] F. Neese, "The ORCA program system," Wiley Interdiscip. Rev.: Comput. Mol. Sci. **2**, 73–78 (2012).

[197] L. M. Thompson, X. Sheng, A. Mahler, D. Mullally, and H. P. Hratchian, "MQCpack 22.6," (2022). DOI: 10.5281/zenodo.6644196.

[198] E. J. Baerends, “Density functional approximations for orbital energies and total energies of molecules and solids,” J. Chem. Phys. **149**, 054105 (2018).

[199] G. Santra and J. M. L. Martin, “Do double-hybrid functionals benefit from regularization in the PT2 term? Observations from an extensive benchmark,” J. Phys. Chem. Lett. **13**, 3499–3506 (2022).

[200] L. M. Thompson and H. P. Hratchian, “On approximate projection models,” Mol. Phys. **310**, 1–9 (2019).

[201] M. E. Casida, C. Jamorski, K. C. Casida, and D. R. Salahub, “Molecular excitation energies to high-lying bound states from time-dependent density-functional response theory: Characterization and correction of the time-dependent local density approximation ionization threshold,” J. Chem. Phys. **108**, 4439–4449 (1998).

[202] L. M. Thompson, “Global elucidation of broken symmetry solutions to the independent particle model through a Lie algebraic approach.” J. Chem. Phys. **149**, 194106 (2018).

[203] V. Veryazov, P. Malmqvist, and B. O. Roos, “How to select active space for multiconfigurational quantum chemistry?” Int. J. Quantum Chem. **111**, 3329–3338 (2011).

[204] J. M. Bofill and P. Pulay, “The unrestricted natural orbital-complete active space (uno-cas) method: An inexpensive alternative to the complete active space-self-consistent-field (cas-scf) method,” J. Chem. Phys. **90**, 3637–3646 (1989).

[205] P. Pulay and T. P. Hamilton, “Uhf natural orbitals for defining and starting mc-scf calculations,” J. Chem. Phys. **88**, 4926–4933 (1988).

[206] S. Keller, K. Boguslawski, T. Janowski, M. Reiher, and P. Pulay, “Selection of active spaces for multiconfigurational wavefunctions,” J. Chem. Phys. **142**, 244104 (2015).

[207] S. M. Parker, T. Seideman, M. A. Ratner, and T. Shiozaki, “Communication: Active-space decomposition for molecular dimers,” J. Chem. Phys. **139**, 021108 (2013).

[208] Y. Mo and S. D. Peyerimhoff, “Theoretical analysis of electronic delocalization,” J. Chem. Phys. **109**, 1687–1697 (1998).

[209] Y. Mo and J. Gao, “An ab initio Molecular Orbital–Valence Bond (MOVB) method for simulating chemical reactions in solution,” J. Phys. Chem. A **104**, 3012–3020 (2000).

[210] T. P. Straatsma, R. Broer, A. Sánchez-Mansilla, C. Sousa, and C. d. Graaf, "GronOR: Scalable and accelerated nonorthogonal configuration interaction for molecular fragment wave functions," J. Chem. Theory Comput. **18**, 3549–3565 (2022).

[211] Q. Wu, C.-L. Cheng, and T. van Voorhis, "Configuration interaction based on constrained density functional theory: A multireference method," J. Chem. Phys. **127**, 164119–10 (2007).

[212] G. K. Chan, "Low entanglement wavefunctions," Wiley Interdisciplinary Reviews: Computational Molecular Science **2**, 907–920 (2012).

[213] Y. Lu, R. Zhao, J. Zhang, M. Liu, and J. Gao, "Minimal active space: NOSCF and NOSI in multistate density functional theory," J. Chem. Theory Comput. **18**, 6407–6420 (2022).

[214] Y. Lu and J. Gao, "Fundamental variable and density representation in multistate DFT for excited states," J. Chem. Theory Comput. **18**, 7403–7411 (2022).

[215] Y. Lu and J. Gao, "Multistate density functional theory of excited states," J. Phys. Chem. Lett. **13**, 7762–7769 (2022).

[216] H. G. A. Burton and D. J. Wales, "Energy landscapes for electronic structure," J. Chem. Theory Comput. **17**, 151–169 (2020).

[217] H. G. A. Burton, "Energy landscape of state-specific electronic structure theory," J. Chem. Theory Comput. **18**, 1512–1526 (2022).

[218] A. T. B. Gilbert, N. A. Besley, and P. M. W. Gill, "Self-consistent field calculations of excited states using the maximum overlap method (MOM)," J. Phys. Chem. A **112**, 13164–13171 (2008).

[219] A. J. W. Thom and M. Head-Gordon, "Locating multiple self-consistent field solutions: An approach inspired by metadynamics," Phys. Rev. Lett. **101**, 193001 – 4 (2008).

[220] G. M. J. Barca, A. T. B. Gilbert, and P. M. W. Gill, "Simple models for difficult electronic excitations," J. Chem. Theory Comput. **14**, 1501–1509 (2018).

[221] L. M. Thompson, "Global elucidation of broken symmetry solutions to the independent particle model through a Lie algebraic approach," J. Chem. Phys. **149**, 194106 (2018).

[222] I. Mayer, *Simple Theorems, Proofs, and Derivations in Quantum Chemistry* (Springer New York, NY, 2003).

[223] A. J. W. Thom and M. Head-Gordon, "Hartree-fock solutions as a quasidiabatic basis for nonorthogonal configuration interaction," J. Chem. Phys. **131**, 124113 (2009).

[224] H. G. A. Burton, “Generalized nonorthogonal matrix elements: Unifying wick’s theorem and the slater-condon rules,” J. Chem. Phys. **154**, 144109 (2021).

[225] H. G. A. Burton, “Generalized nonorthogonal matrix elements for arbitrary excitations,” arXiv (2022). 2208.10208, ver. 1 (accessed 2022-10-16).

[226] A. S. d. Meras, M.-B. Lepetit, and J.-P. Malrieu, “Discontinuity of valence casscf wave functions around weakly avoided crossing between valence configurations,” Chem. Phys. Lett. **172**, 163–168 (1990).

[227] R. G. A. Bone and P. Pulay, “Half-projected Hartree–Fock natural orbitals for defining CAS–SCF active spaces,” Int. J. Quant. Chem. **45**, 133–166 (1993).

[228] H. G. A. Burton and A. J. W. Thom, “Holomorphic Hartree-Fock theory: An inherently multireference approach.” J. Chem. Theory Comput. **12**, 167 – 173 (2016).

[229] H. G. A. Burton, M. Gross, and A. J. W. Thom, “Holomorphic Hartree-Fock theory: The nature of two-electron problems.” J. Chem. Theory Comput. **14**, 607 – 618 (2018).

[230] L. M. Thompson and A. D. Mahler, “Orbital optimization in nonorthogonal multiconfigurational self-consistent field applied to the study of conical intersections and avoided crossings,” J. Chem. Phys. **154** (2021).

[231] L. Q. Jr. and W. B. Tolman, “Bis(μ-oxo)dimetal "Diamond" cores in copper and iron complexes relevant to biocatalysis,” Angew. Chem. Int. Ed. **41**, 1114–1137 (2002).

[232] C. J. Cramer, M. Włoch, P. Piecuch, C. Puzzarini, and L. Gagliardi, “Theoretical models on the Cu_2O_2 torture track: Mechanistic implications for oxytyrosinase and small-molecule analogues,” J. Phys. Chem. A **110**, 1991–2004 (2006).

[233] B. F. Gherman and C. J. Cramer, “Quantum chemical studies of molecules incorporating a ${Cu_2O_2}^{2+}$ core,” Coord. Chem. Rev. **253**, 723–753 (2009).

[234] D. G. Liakos and F. Neese, “Interplay of correlation and relativistic effects in correlated calculations on transition-metal complexes: The $(Cu_2O_2)^{2+}$ core revisited,” J. Chem. Theory Comput. **7**, 1511–1523 (2011).

[235] Q. Wang, J. Zou, E. Xu, P. Pulay, and S. Li, “Automatic construction of the initial orbitals for efficient generalized valence bond calculations of large systems,” J. Chem. Theory Comput. **15**, 141–153 (2018).

Appendix A: Commonly Used Acronyms

Commonly Used Acronyms in text, organized alphabetically.

ΔDFT: Difference Density Functional Theory
ΔDH-DFT: Difference Double-Hybrid Density Functional Theory
ΔHF: Difference Hartree-Fock
ΔMP2: Difference Second Order Møller-Plesset Perturbation Theory
ΔPAV-DFT: Difference Projection-after-Variation Density Functional Theory
ΔPAV-DH-DFT: Difference Projection-after-Variation Double-Hybrid Density Functional Theory
ΔPAV-HF: Difference Projection-after-Variation Hartree-Fock
ΔSCF: Difference Self Consistent Field
AS: Active Space
AO: Atomic Orbital
CAS: Complete Active Space
CASCI: Complete Active Space Configuration Interaction
CASPT2: Complete Active Space Second Order Perturbation Theory
CASSCF: Complete Active Space Self Consistent Field
CSFs: Configuration State Functions
CDFTCI: Constrained Density Functional Theory Configuration Interaction
CC: Coupled Cluster
CCS: Coupled Cluster Singles
CCSD: Coupled Cluster Singles and Doubles
CC2: Coupled Cluster Singles and Approximate Doubles
CI: Configuration Interaction
CIS: Configuration Interaction Singles
CI: Conical Intersection
DFT: Density Functional Theory
DFT+U: Density Functional Theory with Modified On-Site Repulsion
DH: Double-Hybrid
DH-DFT: Double-Hybrid Density Functional Theory
DIIS: Direct Inversion of the Iterative Subspace
DMRG: Density Matrix Renormalization Group
EOM-CCSD: Equation-of-Motion Coupled Cluster Singles and Doubles
FCI: Full Configuration Interaction
GGA: Generalized Gradient Approximation
HF: Hartree-Fock
KS: Kohn-Sham
LCAO: Linear Combination of Atomic Orbitals
LDA: Local Density Approximation

LR: Linear Response
LR-CC: Linear Response Coupled Cluster
LR-CC3: Linear Response Coupled Cluster Singles, Doubles, and approximate Triples
LR-CC2: Linear Response Singles and Approximate Doubles
MCM: Multiple Correlation Mechanism
MO: Molecular Orbital
MOM: Maximum Overlap Method
MP: Møller-Plesset Perturbation Theory
MP2: Second Order Møller-Plesset Perturbation Theory
MRCI: Multireference Configuration Interaction
NO: Natural Orbitals
NO-ASD: Nonorthogonal Active Space Decomposition
NOCI: Nonorthogonal Configuration Interaction
NOMCSCF: Nonorthogonal Multiconfigurational Self Consistent Field
OEEFs: Oriented External Electric Fields
NO: Occupation Numbers
oo: Occupied-Occupied
ov: Occupied-Virtual
PAV: Projection-after-Variation
PAV-DH-DFT: Projection-after-Variation Double-Hybrid Density Functional Theory
PES: Potential Energy Surface
RHF: Restricted Hartree-Fock
RR: Real Restricted
RU: Real Unrestricted
STM-BJ: Scanning Tunneling Microscopy Break Junction
SCF: Self Consistent Field
SD: Slater Determinant
SIE: Self-Interaction Error
STEP: State-Targeted Energy Projection
SVD: Singular Value Decomposition
TD-DFT: Time Dependent Density Functional Theory
TDDHDFT: Time Dependent Double-Hybrid Density Functional Theory
TS: Transition Structure(s)
2ERIs: Two-Electron Integrals
UHF: Unrestricted Hartree-Fock
UNO: Unrestricted Natural Orbitals
VEE: Vertical Excitation Energy
vv: Virtual-Virtual

CURRICULUM VITA

Emily M. Kempfer (Kempfer-Robertson)
Email: emilykempfer95@gmail.com

EDUCATION

University of Louisville Louisville, KY, USA
Ph.D. Candidate in Computational Physical Chemistry Aug 2020–EXP:Mar 2023

- Advisor: Dr. Lee Thompson
- Thesis: "Excited State Methodologies with Application to Controlled Azobenzene Isomerization"

University of Louisville Louisville, KY, USA
M.S. in Computational Physical Chemistry Aug 2018–Aug 2020

- Advisor: Dr. Lee Thompson
- Original Research Proposal: "Controlling Photochemical and Thermal Reactivity of Multiazobenzene Systems Through Internal and External Modifications"

Missouri State University Springfield, MO, USA
M.S. in Organic Chemistry/ 9 credit hours completed Aug 2016–May 2017

- Thesis: "Organic Study of Chitosan Solubility for Application in Gene Replication"

Missouri State University Springfield, MO, USA
B.S. in Chemistry Aug 2013–May 2017

- Emphasis in Graduate Study

AWARDS AND HONORS

- **2021-2022 Student Champion** 2022
  Student Nominated Award for teaching
- **Presdier at ACS Fall 2022**, Chicago, IL 2022
  Presider for Division of Computers in Chemistry Quantum Mechanics Session for ACS National Conference
- **University of Louisville Arnos Spatola Fellowship Award** 2022–2023
  Departmental Graduate Fellowship Awarded for Research and Career Aspirations
- **University of Louisville Doctoral Fellowship** 2018–2020
  University Fellowship Provided to Most Promising First Year Graduate Students
- **ACS Organic Division Undergraduate Award** 2017
  American Chemical Society Award, Awarded for Research and Teaching done in Organic Chemistry
- **Outstanding Inorganic Chemistry Student Award** 2016
  Award for Top Student in Inorganic Chemistry Class

PROFESSIONAL DEVELOPMENT

- **Nonorthogonal Configuration Interaction Workshop** May 2022
  Attended week-long course virtually organized by Tjerk Straatsma from Oak Ridge National Laboratory and Coen de Graaf from Universitat Rovira I Virgili detailing the NOCI-F methodology and the GronOR code.
- **Scientific Programming Workshop with MolSSI** May 2019
  Attended 2-Day course with Molecular Sciences Software Institute (MolSSI) detailing the usage of python in chemistry.

SKILLS

- **Computer Programming:** Fortran, MATLAB, Perl, Python
- **Molecular Simulation:** Gaussian and Molpro
- **Computational Methodologies:** CASSCF, CASPT2, HF, ONIOM, and DFT
- **Productivity Applications:** TEX(LATEX), Vim, Microsoft Office, Git, GNUPlot

UNDERGRADUATE ADVISING

Andrew Bovill May 2022–May 2023
University of California, Merced
- University of California, Merced PhD graduate student
- First author on current study with me as second author

Erin Pidcock January 2023–March 2023
University of Louisville
- On final projects at the University of Louisville
- Looking for a career in industry

Jonathan Bersson May 2022–December 2022
University of Louisville
- Research Experience for Undergraduates (REU) student, in which I advised his own project
- Wants to continue in academia

Meagan Hasse January 2021–May 2023
University of Louisville
- Included as second or third author on three of my first author papers
- Looking for a career in industry

Irma Avdic May 2020–May 2021
University of Louisville
- University of Chicago Chemistry PhD graduate student
- Published first author paper, including me as second author and included as second or third author on two of my first author papers

Thomas Dane Pike August 2019–May 2020
University of Louisville
- University of Louisville Anthropology PhD graduate student
- Included as second on two of my first author papers

TEACHING

Graduate Teaching Assistant Louisville, KY, USA
University of Louisville August 2018–May 2022

- Leading physical chemistry recitation classes to junior-senior undergraduates classes averaging 15 students
- Teaching general chemistry labs to freshman-junior undergraduates with class sizes of 20 students

Graduate Teaching Assistant Springfield, MO, USA
Missouri State University January 2017–May 2017

- Teaching organic chemistry labs to sophomore-senior undergraduates with class sizes of 20 students.

Peer Assisted Study Session Leader Springfield, MO, USA
Missouri State University August 2016–December 2016

- Leading recitation classes for sophomore-senior undergraduates in organic chemistry with class sizes of over 100 students

INDUSTRY EXPERIENCE

Buckeye International St. Louis, MO, USA
Quality Control Specialist June 2017–July 2018

- Ensured the quality of the chemicals made in the factory each day
- Managed customer relations of product complaints

City Utilities of Springfield Missouri Springfield, MO, USA
Water Laboratory Quality Control Co-Op July 2015–December 2016

- Ensured quality of public water through chemical analysis
- Wrote and followed standard operating procedures (SOPs)
- Graphed control charts of laboratory performance weekly and reported results in a timely manner

St. Louis Metropolitan Police Department St. Louis, MO, USA
Drug Chemistry Summer Intern May 2014–August 2014

- Assisted lab technicians by testing and analyzing narcotics
- Performed several experiments to characterize the illegal state of the narcotic

ORAL PRESENTATIONS

- **ACS Fall 2022** Chicago, IL August 2022
  Title: Unrestricted Natural Orbital Active Space Decomposition Method through Nonorthogonal Determinant Block Interactions
- **Oak Ridge National Laboratory (invited talk)** Oak Ridge, TN (in-person) August 2022
  Title: Excited State Methodologies for Modeling Multistate Chemical Processes
- **WATOC 2020** Vancouver, BC, CA July 2022
  Title: Compact Wavefunction Descriptions for Modeling Excited State Processes
- **University of Munster** Munster, DE (invited virtual talk) June 2022
  Title: Excited State Methodologies for Modeling Multistate Chemical Processes

- **SERMACS 2021** Birmingham, AL November 2021
  Title: Direct Reference Excited State Methodologies for Modeling Multistate Chemical Processes
- **ACS Spring 2021** (virtual) April 2021
  Title: Difference Projection-After-Variation Double-Hybrid Density Functional Theory Applied to the Calculation of Vertical Excitation Energies
- **Graduate Student Regional Research Conference** (virtual) March 2021
  Title: Difference Projection-After-Variation Double-Hybrid Density Functional Theory Applied to the Calculation of Vertical Excitation Energies

POSTER PRESENTATIONS

- **WATOC 2020** Vancouver, BC, CA July 2022
  Title: Unrestricted Natural Orbital Active Space Decomposition Method through Nonorthogonal Determinant Block Interactions
- **SETCA 2019** Knoxville, TN May 2019
  Title: Control of Photo and Thermal Isomerization Pathways in Azobenzene with Oriented External Electric Fields

PUBLICATIONS

Kempfer-Robertson, E.M.; Avdic, I.; Haase, M.N.; Pike, T. D.; Thompson, L. M. Protonation State Control of Electric Field Induced Molecular Switching Mechanisms, *Phys. Chem. Chem. Phys.*, **25**, 5251, (2023).

Kempfer-Robertson, E.M.; Haase, M.N.; Thompson, L. M. Nonorthogonal active space decomposition of wavefunctions with multiple correlation mechanisms, *J. Phys. Chem. Lett.*, **13**, 12041 (2022).

Kempfer-Robertson, E.M.; Haase, M.N.; Avdic, I.; Thompson, L. M. Role of exact exchange in difference projection-after-variation double-hybrid density functional theory, *J. Phys. Chem. A.*, **126**, 8058 (2022)

Avdic, I.; **Kempfer-Robertson, E.M.**; Thompson, L. M. Oriented external electric field tuning of unsubstituted azoheteroarene thermal isomerization half-lives, *J. Phys. Chem. A*, **125**, 8238, (2021).

Kempfer-Robertson, E. M.; Pike, T. D.; Thompson, L. M. Difference projection-after-variation double-hybrid density functional theory applied to the calculation of vertical excitation energies, *J. Chem. Phys.*, **153**, 074103, (2020).

Dong, X.; Mahler, A. D.; **Kempfer-Robertson, E.M.**; Thompson, L. M. Global Elucidation of Self-Consistent Field Solution Space Using Basin Hopping, *J. Chem. Theory Comput.*, **16**, 5635 (2020).

Kempfer-Robertson, E. M.; Thompson, L. M. Control of Photo and Thermal Isomerization Pathways in Azobenzene with Oriented External Electric Fields, *J. Phys. Chem. A*, **124**, 3520, (2020).